Active Layer Control for High Efficiency Perovskite Solar Cells

Giles E. Eperon

Oriel College

University of Oxford

Thesis submitted in fulfilment of the requirements for the degree of

Doctor of Philosophy at the University of Oxford.

Trinity Term, 2015

Active Layer Control for High Efficiency Perovskite Solar Cells

Giles E. Eperon, Oriel College, University of Oxford

Thesis submitted in fulfilment of the requirements for the degree of Doctor of Philosophy at the University of Oxford. Trinity Term, 2015

Abstract

The work documented in this thesis concerns the control and modification of semiconducting perovskite thin films for their use in perovksite solar cells (PSCs). PSCs are a promising new thin-film technology, offering both high solar to electricity conversion efficiencies and cheap fabrication costs. Herein, the boundaries of perovskite solar cell research are pushed further by tackling several challenges important to the field.

Initially, this work focuses on understanding why the best PSCs made so far have been mesostructured devices, with the perovskite infiltrated into a scaffold. It is shown that this can be seen as simply a fabrication aid; without the scaffold, thin films easily dewet from the substrate. By understanding the crucial parameters important in carefully controlling this dewetting, it is minimised, and it is shown that scaffold-free planar heterojunction devices with high efficiencies can be fabricated.

This work leads on to the next section; the development of semi-transparent perovskite solar cells. In their present state, PSCs cannot compete with silicon as stand-alone modules. Here, the morphological control has been leveraged to realise a different embodiment – semi-transparent perovskite devices for use in building-integrated photovoltaics. Competitive efficiency and transparency are demonstrated. Moreover, a hybrid self-tinting power-generating window concept is fabricated, by combining the photovoltaic and electrochromic technologies.

In the third section of the thesis, the limitations of the most studied perovskite material, methylammonium lead halide, are addressed: its overly wide bandgap and thermal instability. To address these, the chemical constituents of the perovksite are altered, and the development of more efficient and more stable materials are reported. These are likely to be important for perovskite modules to pass international certification requirements for commercialisation.

Finally, an in-depth study on the effect of ambient moisture, relevant for considering scale-up and the fabrication environment needed, is carried out. It is shown that the presence of some moisture during film fabrication allows a reduction of defect states in the perovskite material, enhancing device performance and film quality.

Acknowledgements

First and foremost, I wish to thank my supervisor, Professor Henry J. Snaith (FRS), for giving me the opportunity to work on perovskites during their golden era, and more importantly, allowing me boundless freedom in my research during my time at Oxford. His sheer excitement and enthusiasm for science has been a constant source of inspiration, and I couldn't hope for a better example. I have always left his office with at least seventeen more exciting ideas than I went in with.

I would like to thank all the other Snaithlings, both current and past, for making life in the lab not just productive but also a lot of fun. It's been great to work with you all. Special thanks go to Severin, Tomas, Sam, and Martina. I'd also like to thank Ed and Pablo for getting me started with research at Oxford. I highly appreciate the work of all my other collaborators, both at Oxford and elsewhere, who have been essential in making the work presented here happen and are all great people to work with. In particular, thanks to Nakita Noel, Sandeep Pathak, Antonio Abate, The Ballster, Jacob Wang, Max Hoerantner, Clara Beck, Ye Zhang, David McMeekin, Konrad Wojciechowski, Rebecca Sutton, Tom Green, Christian (bearded), Victor Burlakov, Michael Johnston, Laura Herz, Amir Abbas Haghighirad, James Beilsten-Edmands, Dane deQuilettes, Darren Neo, the UCL guys (Giuseppe, Andrea, Franco), the Swansea guys (Joel, Dan, Trystan), the Eindhoven guys (Bardo, Koen, Hans), the Bath guys (Adam, Petra, Laurie) and the Italians (Alessandro, Giulia, Annamaria).

I'd like to thank all my other friends in Oxford, in particular the residents of 54 Morrell Avenue, for all the board games, beer brewing, tasty food, balloon-based pranks, and generally being a great household. A further thanks to everyone I've been on climbing adventures with, for some of the best parts of life outside the lab.

Without the continual encouragement and support of my family, I wouldn't be here now. I appreciate very much being encouraged to ask questions during my upbringing; I'm sure my path was set from the moment Dad explained constructive and destructive interference on the surface of oil slicks to a 7-year old me.

Finally, I thank Charlie, for being the other half of my life team. You mean everything.

Publications

* Denotes equal contribution authorships.

1. Eperon, G. E.; Burlakov, V. M.; Docampo, P.; Goriely, A.; Snaith, H. J. Morphological Control for High Performance, Solution-Processed Planar Heterojunction Perovskite Solar Cells. *Adv. Funct. Mater.* **2013**, *24*, 151–157.

2. Docampo, P.; Ball, J. M.; Darwich, M.; Eperon, G. E.; Snaith, H. J. Efficient Organometal Trihalide Perovskite Planar-Heterojunction Solar Cells on Flexible Polymer Substrates. *Nat. Commun.* **2013**, *4*, 2761.

3. Leijtens, T.; Eperon, G. E.; Pathak, S.; Abate, A.; Lee, M. M.; Snaith, H. J. Overcoming Ultraviolet Light Instability of Sensitized TiO2 with Meso-Superstructured Organometal Tri-Halide Perovskite Solar Cells. *Nat. Commun.* **2013**, *4*, 2885.

4. Eperon, G. E.; Burlakov, V. M.; Goriely, A.; Snaith, H. J. Neutral Color Semitransparent Microstructured Perovskite Solar Cells. *ACS Nano* **2014**, *8*, 591–598.

5. Eperon, G. E.; Stranks, S. D.; Menelaou, C.; Johnston, M. B.; Herz, L. M.; Snaith, H. J. Formamidinium Lead Trihalide: A Broadly Tunable Perovskite for Efficient Planar Heterojunction Solar Cells. *Energy Environ. Sci.* **2014**, *7*, 982–988.

6. Wehrenfennig, C.; Eperon, G. E.; Johnston, M. B.; Snaith, H. J.; Herz, L. M. High Charge Carrier Mobilities and Lifetimes in Organolead Trihalide Perovskites. *Adv. Mater.* **2014**, *26*, 1584–1589.

7. Burlakov, V. M.; Eperon, G. E.; Snaith, H. J.; Chapman, S. J.; Goriely, A. Controlling Coverage of Solution Cast Materials with Unfavourable Surface Interactions. *Appl. Phys. Lett.* **2014**, *104*.

8. Noel, N. K.; Stranks, S. D.; Abate, A.; Wehrenfennig, C.; Guarnera, S.; Haghighirad, A.; Sadhanala, A.; Eperon, G. E.; Pathak, S. K.; Johnston, M. B.; *et al.* Lead-Free Organic-Inorganic Tin Halide Perovskites for Photovoltaic Applications. *Energy Environ. Sci.* **2014**, *7*, 3061–3068.

9. Snaith, H. J.; Abate, A.; Ball, J. M.; Eperon, G. E.; Leijtens, T.; Noel, N. K.; Stranks, S. D.; Wang, J. T.; Wojciechowski, K.; Zhang, W. Anomalous Hysteresis in Perovskite Solar Cells. *J. Phys. Chem. Lett.* **2014**, *5*, 1511–1515.

10. Leijtens, T.; Lauber, B.; Eperon, G. E.; Stranks, S. D.; Snaith, H. J. The Importance of Perovskite Pore Filling in Organometal Mixed Halide Sensitized TiO 2 -Based Solar Cells. *J. Phys. Chem. Lett.* **2014**, *5*, 1096–1102.

11. Leijtens, T.; Stranks, S. D.; Eperon, G. E.; Lindblad, R.; Johansson, E. M. J.; McPherson, I. J.; Rensmo, H.; Ball, J. M.; Lee, M. M.; Snaith, H. J. Electronic Properties of Meso-Superstructured and Planar Organometal Halide Perovskite Films: Charge Trapping, Photodoping, and Carrier Mobility. *ACS Nano* **2014**, *8*, 7147–7155.

12. Habisreutinger, S. N.; Leijtens, T.; Eperon, G. E.; Stranks, S. D.; Nicholas, R. J.; Snaith, H. J. Carbon Nanotube/polymer Composite as a Highly Stable Charge Collection Layer in Perovskite Solar Cells. *Nano Lett.* **2014**, *14*, 5561–5568.

13. Habisreutinger, S. N.; Leijtens, T.; Eperon, G. E.; Stranks, S. D.; Nicholas, R. J.; Snaith, H. J. Enhanced Hole Extraction in Perovskite Solar Cells Through Carbon Nanotubes. *J. Phys. Chem. Lett.* **2014**, *5*, 4207–4212.

14. Grancini, G.; Marras, S.; Prato, M.; Giannini, C.; Quarti, C.; Angelis, F. De; Bastiani, M. De; Eperon, G. E.; Snaith, H. J.; Manna, L.; *et al.* The Impact of the Crystallization Processes on the Structural and Optical Properties of Hybrid Perovskite Films for Photovoltaics. *J. Phys. Chem. Lett.* **2014**, *5*, 3836–3842.

15. Filip, M. R.; Eperon, G. E.; Snaith, H. J.; Giustino, F. Steric Engineering of Metal-Halide Perovskites with Tunable Optical Band Gaps. *Nat. Commun.* **2014**, *5*, 5757.

16. Eperon, G. E.; Bryant, D.; Troughton, J.; Stranks, S. D.; Johnston, M. B.; Watson, T.; Worsley, D. a; Snaith, H. J. Efficient, Semitransparent Neutral-Colored Solar Cells Based on Microstructured Formamidinium Lead Trihalide Perovskite. *J. Phys. Chem. Lett.* **2015**, *6*, 129-138.

17. *Zhang, Y.; *Liu, M.; Eperon, G. E.; Leijtens, T. C.; McMeekin, D.; Saliba, M.; Zhang, W.; Bastiani, M. de; Petrozza, A.; Herz, L. M.; *et al.* Charge Selective Contacts, Mobile Ions and Anomalous Hysteresis in Organic–inorganic Perovskite Solar Cells. *Mater. Horiz.* **2015**, *2*, 315–322.

18. *Cannavale, A.; *Eperon, G. E.; Cossari, P.; Abate, A.; Snaith, H. J.; Gigli, G. Perovskite Photovoltachromic Cells for Building Integration. *Energy Environ. Sci.* **2015**, *8*, 1578–1584.

19. Zhang, W.; Saliba, M.; Moore, D. T.; Pathak, S. K.; Hörantner, M. T.; Stergiopoulos, T.; Stranks, S. D.; Eperon, G. E.; Alexander-Webber, J. A.; Abate, A.; *et al.* Ultrasmooth Organic–inorganic Perovskite Thin-Film Formation and Crystallization for Efficient Planar Heterojunction Solar Cells. *Nat. Commun.* **2015**, *6*, 6142.

20. Pockett, A.; Eperon, G. E.; Peltola, T.; Snaith, H. J.; Walker, A.; Peter, L. M.; Cameron, P. J. Characterization of Planar Lead Halide Perovskite Solar Cells by Impedance Spectroscopy, Open-Circuit Photovoltage Decay, and Intensity-Modulated Photovoltage/Photocurrent Spectroscopy. *J. Phys. Chem. C* **2015**, *119*, 3456–3465.

21. Beilsten-Edmands, J.; Eperon, G. E.; Johnson, R. D.; Snaith, H. J.; Radaelli, P. G. Non-Ferroelectric Nature of the Conductance Hysteresis in $CH_3NH_3PbI_3$ Perovskite-Based Photovoltaic Devices. *Appl. Phys. Lett.* **2015**, *106*, 173502.

22. Quilettes, D. W. de; Vorpahl, S. M.; Stranks, S. D.; Nagaoka, H.; Eperon, G. E.; Ziffer, M. E.; Snaith, H. J.; Ginger, D. S. Impact of Microstructure on Local Carrier Lifetime in Perovskite Solar Cells. *Science* **2015**, *348*, 683–686.

23. Eperon, G. E.; Paternò, G. M.; Sutton, R. J.; Zampetti, A.; Haghighirad, A. A.; Cacialli, F.; Snaith, H. J. Inorganic Caesium Lead Iodide Perovskite Solar Cells. *J. Mat. Chem. A.* **2015**, *3*, 19688-19695.

24. Eperon, G. E.; Habisreutinger, S. N.; Leijtens, T.; Bruijnaers, B. J.; Franeker, J. J. van; deQuilettes, D. W.; Pathak, S. K.; Sutton, R. J.; Grancini, G.; Ginger, D.; *et al.* The Importance of Moisture in Hybrid Lead Halide Perovskite Thin Film Fabrication. *ACS nano* **2015**, *9*, 9380-9393.

Table of Contents

1. INTRODUCTION

1.1 Background and motivation

As the population of the world grows and we become ever hungrier for energy, total energy consumption on the planet has risen dramatically. In the last 40 years global energy consumption has more than doubled, now standing at over 105,000 terawatt-hours (TWh) per year, equivalent to a sustained power consumption of more than 12 terawatts (TW).[1] To compensate for losses in transformation and conversion processes, realistically this requires a primary supply of 155,000 TWh, or more than 17 TW. It is expected that by 2040, demand will grow by a further 37%.[2] However, the vast majority of energy generation today, more than 66%, is produced by burning coal, natural gas and oil. Carbon dioxide produced as an unavoidable byproduct of fossil fuel combustion has already led to rising global temperatures and climate change, and if we continue using these fuel sources, disastrous consequences will arise from continuing global temperature increases.[3] Weather patterns will change, sea levels will rise, whole civilisations will become flooded, and human society as we know it will have an uncertain future. In addition to the critical issue of climate change, longer term energy generation must be considered. Fossil fuels are in limited supply, and the discovery of new reserves and extraction methods cannot continue forever.

Clearly fossil fuels cannot continue to be burned indefinitely, both for the sake of mitigating catastrophic climate change and as a practical consideration as supplies dwindle. Therefore, the need for an energy source that is abundant, does not produce carbon dioxide, and that can supply a large fraction of the world's needs is of the utmost importance if society is to continue its current energy consumption habits. Candidates as

renewable energy sources include wind power, solar power, geothermal power, tidal power and hydropower. Of these, as shown in Figure 1.1, that with the greatest available energy source by far is solar power.

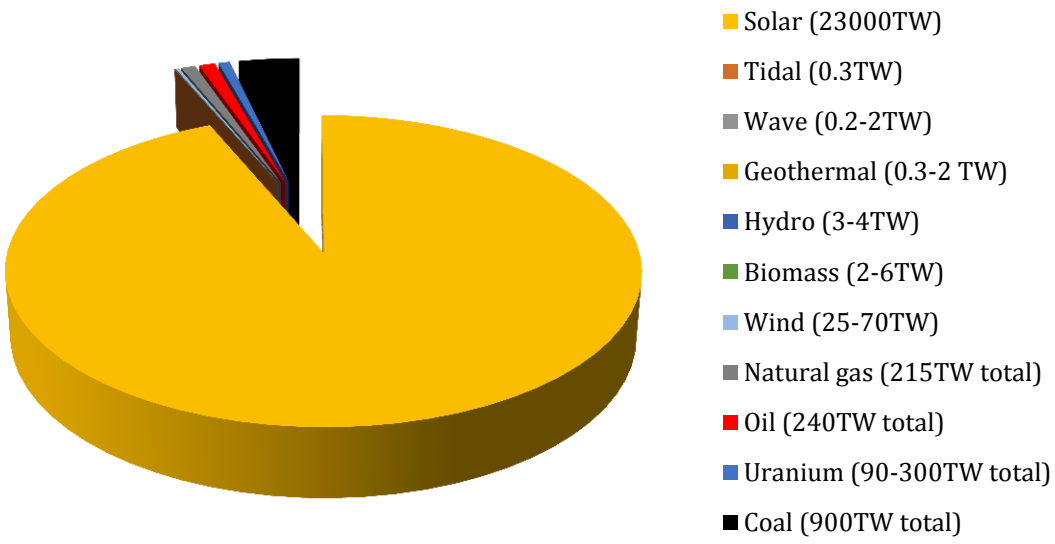

Figure 1.1: Pie chart showing a comparison of the potential for finite and renewable energy sources. Renewable sources show average yearly potential and finite resources show the estimated total amount remaining (as of 2010).[4]

A huge number of photons from the sun, carrying a huge amount of energy, hit the earth every day. Tapping into only a fraction of this vast available solar flux would allow the whole planet to easily be powered. The most promising way of converting solar energy into usable power is by using photovoltaic devices, which convert incoming photons directly into usable electrical power. Enough power to supply the whole world could be generated by covering just 0.3-0.4% of the Earth's surface with such devices, assuming 20% conversion efficiency for sunlight into electrical power.

Such efficiency is not infeasible for these devices. Efficiencies for photovoltaics are governed by the so-called Shockley-Queisser limit, stating that a maximum power conversion efficiency (PCE) of 31-33% is possible for a single semiconductor junction device.[5] The highest efficiencies reported in a real single junction device are over 28%, attained with gallium arsenide semiconductors.[6] Furthermore, by stacking materials in a multi-junction device, circumventing the single-junction efficiency limit, efficiencies of over 38% have been achieved. These high efficiency devices are however extremely

expensive to process and fabricate, so are used only in niche applications. Most solar cells fabricated and installed today are made from silicon, with efficiencies of up to 25% in a single junction. However, even silicon requires high temperature processing and various expensive and toxic treatments to fabricate high quality devices, meaning that the production is still expensive and environmentally unfriendly. This means that there is a long payback time to make installing modules worthwhile, limiting uptake in comparison to other established energy technologies.

Therefore, there is a real and urgent need to develop even lower cost solar cells with high efficiencies that can be mass-produced rapidly. An option to reduce processing costs is to employ materials which can be formed via solution-based processing. This refers to processes where the required material is deposited from solution, including techniques such as inkjet printing, blade coating, spin-coating, spray coating and slot-dye coating. Such techniques do not typically require high vacuum or high temperatures and thus are much faster and cheaper than conventional wafer processing or vacuum deposition. They also allow compatibility with flexible substrates for roll-to-roll processing, which could significantly increase throughput of a production facility. Solution-processed materials have already shown promise as light-emitting diodes (LEDs), lasers, photodetectors, sensors and transistors.

Therefore, in recent years, solution processed photovoltaics have emerged as a field of significant interest and intense research. The first of these to be developed was the dye-sensitized solar cell (DSSC), emerging in 1991, based upon the use of a light-harvesting dye anchored upon semiconductor nanoparticles.[7] These devices have now increased in efficiency to over 12% PCE using only low cost materials and solution processing. Additionally, organic photovoltaics and quantum dot photovoltaics, based upon organic semiconductors and quantum-confined semiconductor nanocrystals respectively, now display around 10% power conversion efficiency.[6]

More recently, emerging from these fields, hybrid organic-inorganic perovskite semiconductors have attracted a great deal of interest. These materials are cheap, solution-processable, and have ideal properties for their incorporation into photovoltaics. Their high material quality and versatility has enabled a meteoric rise in efficiencies, making them the fastest developing photovoltaic technology yet and a prime candidate for a low-cost, high efficiency photovoltaic technology to address the energy problems of the world.

1.2 Aims of this thesis

This thesis broadly focuses on the development of high efficiency perovskite solar cells by control and modification of the perovksite semiconductor. A particular emphasis is placed on solving the big challenges in the field via chemical, physical and material modification. Namely, these are removing the necessity for a mesostructure, moving the perovskite's bandgap closer to that optimal for solar energy conversion, realising a commercial application for the perovskites in their present form, and understanding the atmospheric conditions needed to make the best devices.

Initial reports of perovskite solar cells were based on the dye-sensitized solar cell structure, with a thin layer of the perovskite acting merely as a sensitizer, coating the large surface area of a mesoporous oxide.[8,9] In this architecture, photoexcited electrons are rapidly injected into the semiconducting oxide and diffuse through this to be extracted at the electrode. It was realised in latter reports however that the perovskite itself could function as both an absorber and a charge transporting material; by replacing the semiconducting oxide with an inert scaffold, forcing electron transport through the perovskite itself, the solar cell was in fact able to function more effectively.[10] The working principles of perovskite solar cell operation will be described in more detail in Chapter 2.

Despite the more efficient operation of the solar cells based on an inert scaffold, it appeared that the scaffold was still necessary to fabricate working devices.[11] In theory this should not be the case; it is electronically inert and thus represents an unnecessary processing step. In Chapter 4 this issue will be tackled, and it will be demonstrated that the role of the scaffold is simply as a processing aid. Without the scaffold, a low quality perovskite film with many small holes and poor surface coverage is attained. An experimental study is undertaken to understand why this happens, and then to establish processing conditions necessary for fabrication of high coverage and high quality films. It will then be demonstrated that this allows the removal of the mesoporous scaffold in solar cells, and successfully result in the first planar perovskite solar cells with efficiencies above 10%.

This concept of intelligently controlling processing conditions in order to control surface coverage and morphology will also form the basis for Chapter 5 and 6. Here, it will be shown that arrays of perovskite 'islands' can be formed, with controllable size. These self-assembling arrays of microstructured islands can form visibly transparent and neutral-coloured films. These show promise for an industrially relevant application: perovskite solar cells for building integration. In their current incarnations, perovskite solar cells will struggle to compete with silicon modules for significant market share, however here the

versatility of solution processing becomes important. Currently available semi-transparent solar cells, designed for incorporation into windows of buildings and automobiles, suffer from a difficulty to fabricate a neutral-coloured film with respectable efficiency or at low cost. This renders them architecturally or economically non-viable. The solution-processed perovskites offer a solution to this. Application of these films in perovskite solar cells will be shown to produce neutral-coloured and semi-transparent working solar cells with impressive efficiency to transparency ratios, which represent an important potential application for the perovksite technology. In Chapter 6 the use of these semi-transparent devices in a photovoltachromic device will be detailed, namely a combination of solar cell and 'smart' tinted window. 'Smart' windows with controllable colouration normally require an external power source to activate the tinting, but the transparent solar cells developed allow the integration of these two devices together on one substrate, which would significantly reduce processing costs. The solar cell powers the tinting of the device with no need for external power, and excess electricity can be used elsewhere.

In Chapter 7, 8 and 9 the development of novel perovskite materials will be discussed. The previous commonly used perovskite, namely methylammonium lead iodide, has a semiconducting bandgap that is somewhat too wide for the optimum for solar energy conversion, limiting its maximum efficiency. By changing the composition of the perovskite structure itself, replacing the methylammonium organic cation with formamidinium, a slightly larger cation, it will be demonstrated that the bandgap can be narrowed. This results in a material even better suited to photovoltaic uses, providing higher efficiency planar devices. This material is incorporated into the semitransparent solar cell architecture in chapter 8, again increasing device efficiencies due to its narrower bandgap, and together with the application of a novel transparent electrode the performance to transparency ratio reaches impressive levels. In Chapter 9 the first fully inorganic perovskite solar cells will be presented. All effective perovskite solar cells developed previously have been hybrid organic-inorganic devices, but here it will be shown that the organic cation can be exchanged for an inorganic component, caesium, and working devices still fabricated. These materials show promise for being more thermally stable.

Finally, a photophysical study will be presented concerning the effect of atmospheric moisture on perovskite films. The previous work has demonstrated several ways in which perovskite solar cells may be commercialised, but a key concern is how easily they can actually be scaled up for mass production; can they be processed in ambient air or is a

controlled environment needed? This is addressed in Chapter 10. It will be shown that atmospheric moisture does play a significant role in perovskite film fabrication, but that it is in fact beneficial, allowing even higher quality films to be formed.

1.3 References

1. International Energy Agency, *2014 Key World Energy Stat.*, 2014.

2. International Energy Agency, *World Energy Outlook Exec. Summ.*, 2014.

3. T. F. Stocker, G.-K. D. Qin, L. V. Plattner, S. K. Alexander, N. L. Allen, F.-M. Bindoff, J. a. Bréon, U. Church, S. Cubasch, P. Emori, P. Forster, N. Friedlingstein, J. M. Gillett, D. L. Gregory, E. Hartmann, B. Jansen, R. Kirtman, K. Knutti, P. Krishna Kumar, J. Lemke, V. Marotzke, G. a. Masson-Delmotte, I. I. Meehl, S. Mokhov, V. Piao, D. Ramaswamy, M. Randall, M. Rhein, C. Rojas, D. Sabine, L. D. Shindell, D. G. Talley and V. and S.-P. Xie, *Clim. Chang. 2013 Phys. Sci. Basis. Contrib. Work. Gr. I to Fifth Assess. Rep. Intergov. Panel Clim. Chang.*, 2013, 33–115.

4. R. Perez and M. Perez, *IEA SHC Sol. Updat.*, 2009, **50**, 2–3.

5. W. Shockley and H. J. Queisser, *J. Appl. Phys.*, 1961, **32**, 510.

6. NREL, *Best Research-Cell Efficiencies, http://www.nrel.gov/ncpv/images/efficiency_chart.jpg*, 2015.

7. B. O'Regan and M. Grätzel, *Nature*, 1991, **353**, 737-740.

8. Im Jeong-Hyeok, C.-R. Lee, J.-W. Lee, Park Sang-Won and N.-G. Park, *Nanoscale*, 2011, **3**, 4088–4093.

9. A. Kojima, K. Teshima, Y. Shirai and T. Miyasaka, *J. Am. Chem. Soc.*, 2009, **131**, 6050–6051.

10. M. M. Lee, J. Teuscher, T. Miyasaka, T. N. Murakami and H. J. Snaith, *Science*, 2012, **338**, 643–647.

11. J. M. Ball, M. M. Lee, A. Hey and H. J. Snaith, *Energy Environ. Sci.*, 2013, **6**, 1739–1743.

2. BACKGROUND

This chapter presents on overview of the background knowledge required for understanding of the rest of the thesis. It will include an overview of semiconductor physics, solar cell device operation, perovskites and perovskite solar cells, and some more specific topics.

2.1 Semiconductors

Semiconductors form the basis of operation for solar cells. In this chapter, a brief description of semiconductors, and why they are integral in forming solar cells, will be given.

A semiconductor is a material which can conduct electricity well under some conditions but not others. They are effectively somewhere in between a metal and an insulator. This can be understood in terms of the quantum energy states present in these materials, each of which can be occupied by only two electrons (one of each spin) due to the Pauli Exclusion Principle. These states arise from the atomic orbitals of the individual atoms (where energy levels are found by solving Schrödinger's equation) brought together into a solid material with repeating structure. It is then necessary to solve the equation for a periodic array of atomic potentials. This gives rise to a periodic electron probability distribution, with the delocalised electrons forming continua, or bands, of levels. The probability distribution is thus a combination of a periodic component, related to the crystal structure, and a plane wave component, representing the wavefunction of an electron in free space. Without going into too much detail, solving the Schrödinger equation then gives energies as a function of $\boldsymbol{k}$, the wave vector. The resulting distribution $E(\boldsymbol{k})$ is known as the crystal's *band structure*. This is also dependent on the lattice directions in the crystal. Band structure is normally plotted for the most important crystal directions, and with k varied from 0 to π/a, with a being the spacing of atomic planes in that direction, as shown in Figure 2.1. The energy distribution repeats for $k > \pi/a$ since for a wave with period a, the values are the same for multiples of $2\pi/a$. $E(\boldsymbol{k})$ is identical *to* $E(-\boldsymbol{k})$ in the same lattice direction, due to the symmetry of the crystal.

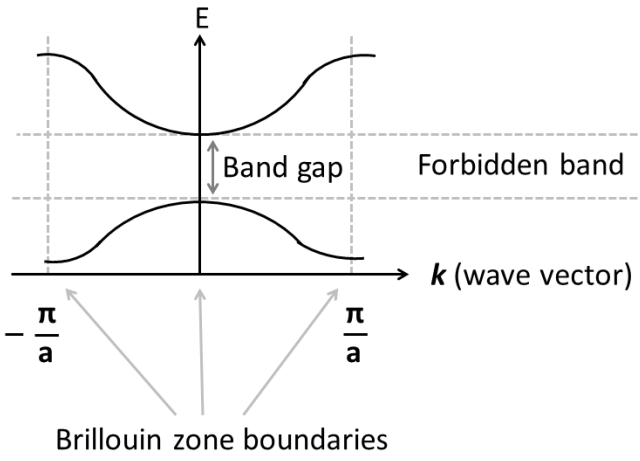

Figure 2.1: Schematic band structure diagram showing *E(k)* within a Brillouin zone for one lattice direction.

The interaction of electrons behaving as waves in a lattice spaced by lattice constant a means that electrons effectively diffract from the periodic lattice – the direct implication being that there are some energy levels which are forbidden, because the electron waves cancel each other out. This is the physical origin of band gaps, and these wave vectors occur at $\boldsymbol{k} = \pm\pi/a$. The point $\boldsymbol{k} = \pi/a$ is called the Brillouin zone boundary; here, the gradient of $E(\boldsymbol{k})$ becomes zero and a maximum or minimum of energy is reached. Considering this picture, it is clear that the crystal spacing and symmetry will directly affect the material's band structure, most notably its band gaps.

The energetic distribution of these bands forms the electronic band structure of the material. Typical band structures of different types of material are illustrated simply in Figure 2.2.

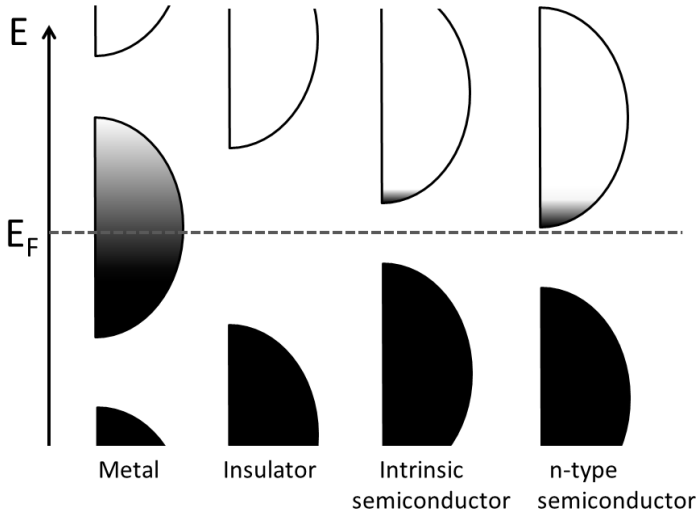

Figure 2.2: Diagram of filling of density of states for different types of material with different band structures. The vertical axis displays energy, and the horizontal axis represents the density of available states in the bands. Black represents filled states, white unfilled. The Fermi level is shown; it is within a band for a metal, in between bands for semiconductors and insulators. In a semiconductor the bands are close enough to allow some populating of the upper bands with electrons.

The Fermi level (E_F) of a material as illustrated in a band structure diagram represents the hypothetical energy level with a 50% probability of being occupied by an electron at any given time at thermal equilibrium. For electrical conduction to occur, the Fermi level must lie within a band with delocalised electron states. This is the case in a metal; there are a large number of states near to the Fermi level that are available to carry current. In an insulator, the Fermi level lies within a large band gap between states, meaning that there are no available states for conduction at this energy. In a semiconductor, the band

structure has a band gap, but it is much smaller than that in an insulator. The Fermi level typically resides within this bandgap and thus significant numbers of electrons can be excited to cross the bandgap. The distribution of electrons in available levels is given by the Fermi-Dirac distribution:

$$\boldsymbol{n(E) = \frac{1}{e^{\frac{E-E_F}{kT}}+1}} \qquad \textbf{2.1}$$

Where *n(E)* represents the average number of electrons at a certain energy state *E* at given temperature *T*, where *k* is the Boltzmann constant.

The deeper (lower energy) band is typically termed the valence band (VB) and the higher band the conduction band (CB). When electrons are excited into the conduction band they are able to move easily due to the large number of states available, so these electrons can carry current. Electron vacancies in the valence band, referred to as 'electron-holes' or simply 'holes', that remain behind when an electron is excited into the conduction band, are able to move in a similar way through the valence band, and are normally treated as a particle equivalent to an electron but positively charged.

Electrons can be excited into the conduction band in a number of ways, including by heat or by light – basically any energy input enough to excite an electron across the bandgap. As can be seen from Equation 2.1, at absolute zero and in the dark, all electrons will be in the VB and hence there will be no conductivity. As temperature is raised, more and more electrons will be able to be excited across the gap and so conductivity will rise. In an insulator, with enough heating, conduction is also possible – the only real difference between an insulator and a semiconductor is the magnitude of the energy gap with no available states in. Practically speaking, the definition of a semiconductor tends to mean materials with a bandgap of less than 3eV.

In addition to thermal excitation, electrons can be excited optically, by absorbing photons with energy greater than the bandgap. This can free the electron from the valence band and move it to the conduction band, where it is then mobile and free to conduct electricity. Conductivity achieved in this way is called photoconductivity and is the process at the core of photovoltaic materials.

Conductivity can also be influenced by shifting the position of the Fermi level within the bandgap. This can be changed by adding impurities with different numbers of valence electrons or different bond energies, which can allow electrons or holes to be freed more easily from these impurities, thereby increasing the number of carriers available for conduction. This effectively adds electrons or holes to levels near to the conduction or

valence bands, and is called doping (n-doping or p-doping for electrons or holes respectively). The case of an n-doped semiconductor is shown in Figure 2.3. The additional electrons easily excited into the CB from the impurities shift the Fermi level closer to the CB. Therefore this material will be more conductive for electrons.

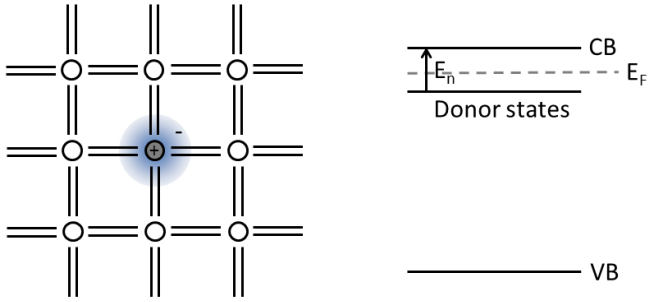

Figure 2.3: Diagram of n-type impurity doping in the crystal bonding (left) and in the band diagram (right). An extra electron is loosely bound to the donor atom (delocalised negative charge in blue). The Fermi level is shifted to much closer to the conduction band, and when the ionisation energy of E_n is supplied electrons are excited from the donor states into the conduction band, becoming completely delocalised and free to carry current.

Doping is normally achieved by substituting an atom in the crystal lattice with one with a different number of outer orbital electrons (valence electrons). One with too many electrons is known as a donor and with too few, an acceptor. The surplus electrons from a donor atom are bound weakly as they are not needed for the structural bonds, so have a low energy to ionise into the conduction band, meaning these impurities add an extra state in the band diagram close to the conduction band. This means that the fermi level lies between this level and the conduction band as all these new states are occupied at zero temperature. In the case of an acceptor dopant, the new atom takes an electron away from another bond, which is then bound more tightly than normal. This effectively creates a weakly bound hole. The hole can be lowered into the valence band easily (delocalised completely) so an acceptor level is created close to the valence band. Therefore, the Fermi level is shifted to lie between this new level and the valence band.

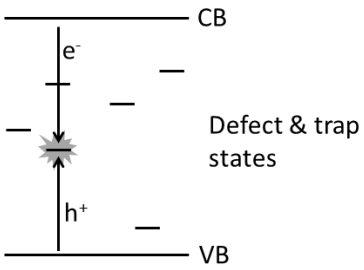

Figure 2.4: Diagram showing some defect levels in the bandgap. These can provide sites for easier recombination for electrons and holes, as shown.

As well as intentional incorporation of dopant defects into the crystal structure, semiconductors can contain other defects which introduce unwanted levels into the band gap. Even the most crystalline semiconductor is likely to have a few broken bonds and interface states, and in a polycrystalline semiconductor, grain boundaries are a particular source of defect sites. Non-stoichiometric regions, strained regions, and impurities in the materials used for fabrication can all result in defect states within the bandgap. Especially in solution-processed materials, due to the less controlled nature of fabrication, there can be many such defects. The impact of such defects depends on the nature of the state. Some are benign, but often they can act as recombination centres – a state in the middle of the bandgap makes a recombination event between an electron and a hole much more likely. Some act as trap states, capturing a free electron or hole and impeding mobility. This trapped electron or hole can then either eventually escape or recombine. Large numbers of defect states can result in a fermi level pinning, where the density of defects is so high that the fermi level is fixed amongst them, as they are not all ionised at room temperature. Therefore, the role of defects plays a highly significant role in semiconductor quality and solar cell operation.

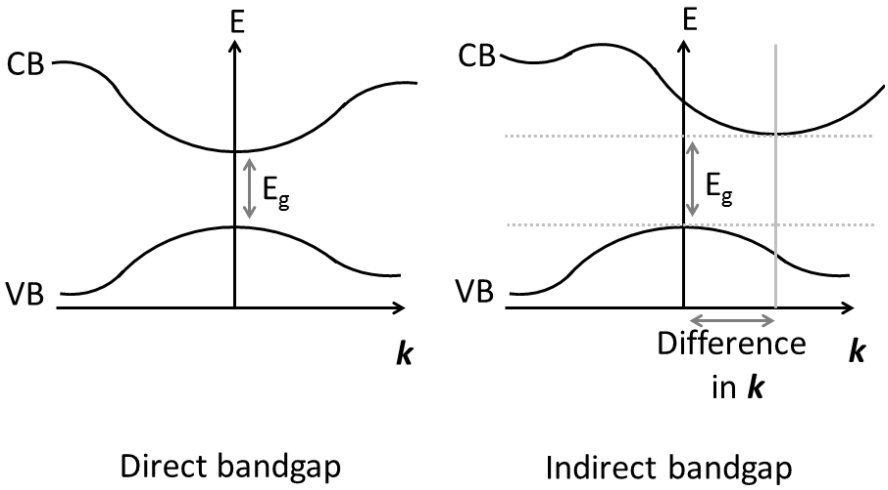

Figure 2.5: Diagram of direct and indirect bandgap materials, represented in *k*-space. The CB minimum and VB maximum take have the same *k* values in a direct gap material, and different ones in an indirect gap material.

The bandgap of a semiconductor can either be described as direct or indirect. Without going into too much detail, this refers to whether there must also be a transfer of phonon (crystal lattice vibration) momentum involved in an absorption or emission process. If no momentum transfer is necessary, the material is said to be direct bandgap, if there must also be a momentum transfer event, it is an indirect gap material. Phonon momentum is described in ***k-space***, related to the Fourier transform of the periodicity of the lattice in real space. In a direct bandgap material, the CB minimum and VB maximum have the same value of ***k***, in an indirect bandgap material they differ, as shown in Figure 2.5. The type of bandgap has severe implications for optoelectronic devices; absorption and radiative recombination (see later for more details about recombination processes) require momentum transfer in an indirect bandgap material, meaning the processes are less likely – this means absorption is weaker. Therefore, indirect bandgap material solar cells normally must be thicker to absorb enough photons, whereas a direct bandgap material can be much thinner.

2.2 Solar cell operation[1]

In its simplest form, a solar cell can be described as a light absorbing material connected to an external circuit in an asymmetrical manner, allowing physical separation of photoexcited charge carriers to generate current and voltage.

The light absorbing material is normally a semiconductor; upon illumination, electrons are excited from the valence band into the conduction band where they are mobile, and due to

an asymmetry that can be achieved in several ways they flow out of the cell in a preferred direction.

The different methods of achieving an asymmetry will be discussed later. First, the basic general operating characteristics of photovoltaic devices will be summarised.

At the core of photovoltaic operation is the generation of current and voltage under illumination. The current produced when the two terminals are connected (i.e. the voltage between them is zero) is known as the short-circuit current (I_{sc}); the voltage when the terminals are isolated (i.e. there is no current flow) is known as the open-circuit voltage (V_{oc}). For an intermediate load connected with resistance R, the cell will produce a voltage V (between 0 and V_{oc}) and a current I (between 0 and I_{sc}) such that $V = IR$, where the current-voltage relation $I(V)$ is described by the current-voltage characteristics of the solar cell under that specific illumination. Hence, the current-voltage characteristic of a particular solar cell determines its functionality and is the most important metric when characterising a photovoltaic device. Typically, currents (I) are expressed as current densities (J) as the current is generally proportional to area of the device.

The amount of current that can be generated by a given solar cell depends on the incident light spectrum and the amount of this light that the solar cell can absorb. The absorption of a particular semiconductor is determined by its bandgap. Photons with energy greater than the bandgap can be absorbed, exciting an electron from the VB to the CB or a higher energy state. Photons with energy less than the bandgap can in general not be absorbed, as there is no state suitable for an electron to be excited from the VB into. Therefore, solar cells typically can only absorb usefully light below a certain wavelength. It then may appear as though the smallest bandgap possible would be ideal, but this is not the case: photons excited to states higher than the CB will rapidly thermalize back down to the CB due to energetic considerations; the excess energy will simply be lost as heat. The voltage generated by the solar cell is given by the energy an extracted electron will have (with the definition $U = qV$); thus this is at best equal to the bandgap of the material. This is shown schematically in Figure 2.6.

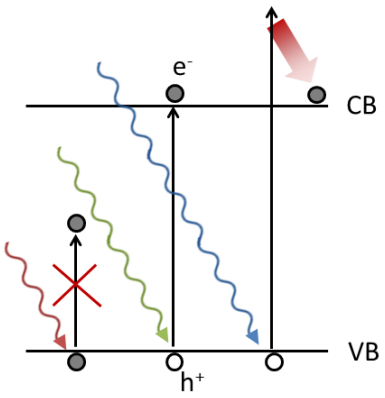

Figure 2.6: Photon absorption in a semiconductor. Photons with energy lower than E_g cannot promote an electron and so are not absorbed (left). Photons with energy = E_g promote an electron with no energy wastage, leaving a hole in the valence band (centre). Photons with energy > E_g promote an electron to a higher state, which then rapidly thermalizes to the band edge, losing the excess energy as heat (right).

Because the number of photons absorbed is hence clearly dependent on the incident energy spectrum, a fixed reference is defined. The solar spectrum is that which we are interested in for photovoltaic energy conversion, and this is different depending on where and when it is measured in the world. Therefore a fixed reference spectrum is defined, representing the solar spectrum at ground level for mid-latitude regions at a solar zenith angle of 48°. This is a good representation of the overall yearly average for mid-latitudes and is referred to as the Air Mass 1.5 spectrum (AM1.5). A total irradiance is also required, and for the same average criteria this is 100mWcm^{-2}. The AM1.5 spectrum is shown in Figure 2.7, shaded to represent the photons that could be usefully absorbed and those not absorbed by a material with a bandgap of around 1.4eV (equivalent to wavelength of 900nm).

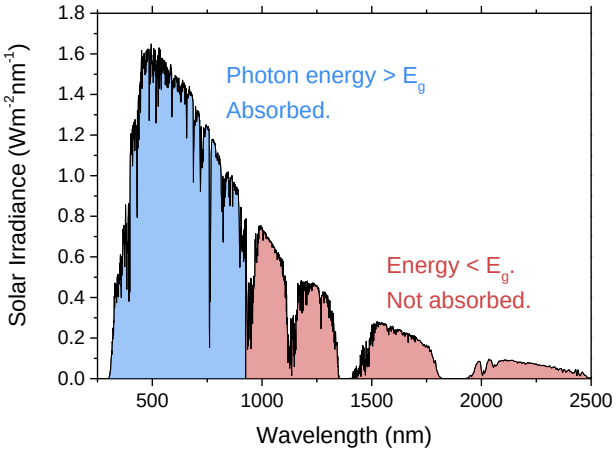

Figure 2.7: Solar spectral irradiance at AM1.5. For a semiconductor with a bandgap of 1.4eV, wavelengths where photons have enough energy to excite an electron across the bandgap, so can be absorbed, are shaded blue, whereas those which do not have enough energy to excite an electron and so are not absorbed, are shaded red.[2]

In addition to having a bandgap that will allow absorption of photons, it is also important to know the absorption coefficient of the material at particular energies – how effectively photons are absorbed per unit length in the material. Semiconductors typically have an absorption spectrum that increases from the bandgap energy, due to the energetic shape of the density of states. This is represented by Fermi's Golden Rule, stating that the probability of an energetic transition is related to the number of available states and the strength of the interaction. Generally, the absorption coefficient $\alpha(E)$ will be related to the integral of the product of the density of states in the CB and VB, so for a direct gap semiconductor, where the densities of states $g(E)$ in each band vary as $(E_{v0}-E)^{1/2}$ and $(E-E_{c0})^{1/2}$ (where $E_{c0,v0}$ are the energies of the onset of the CB and VB respectively) for the VB and CB respectively, it is given by:

$$\boldsymbol{\alpha(E) = A(E - E_g)^{1/2}} \qquad \textbf{2.2}$$

Where A is a constant dependent on the material. For an indirect bandgap material, a phonon of the necessary energy must be present too, and as a result, the absorption coefficient is given by:

$$\boldsymbol{\alpha(E) = A(E - E_g)^{2}} \qquad \textbf{2.3}$$

This is shown schematically for a direct gap material in Figure 2.8. A simple way to increase the absorption of a particular material is to make it thicker, but this is not always

possible, given that photoexcited carriers must be extracted from the material – see later for a discussion of this.

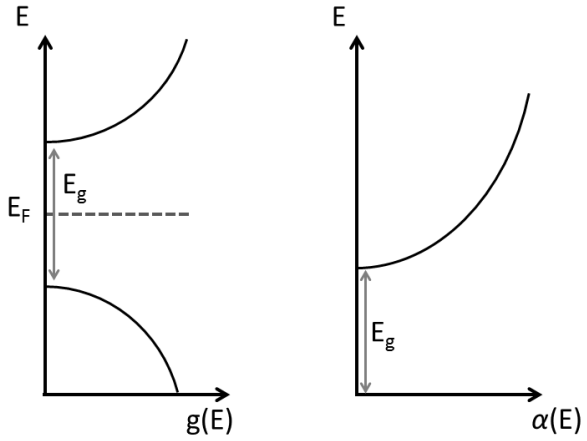

Figure 2.8 Simple density of states diagram for a semiconductor (left) and corresponding absorption coefficient spectrum (right).

It is now possible to calculate the total photons absorbed in a material, by integrating the product of the absorbance of a particular material and the AM1.5 spectrum. However, this is not equivalent yet to the total current that a solar cell can generate. To determine the current generated, it is also necessary to know how effectively photoexcited electrons are separated and collected, which will be discussed in more detail later. The overall efficiency of the process for a given energy is described by the External Quantum Efficiency (EQE(E)). This is the probability of an incident photon of energy E delivering one electron to the external circuit. Thus it takes into account absorption, charge separation and charge collection. The total short-circuit current density (J_{sc}) generated by the cell is then given by integrating the product of this and the solar spectrum:

$$\boldsymbol{J_{SC} = q \int EQE(E)\Phi_{AM1.5}(E)dE} \qquad \textbf{2.4}$$

For example, if it is assumed that the 1.4eV material illustrated in Figure 2.7, for example, has an EQE of 100% for all photons above its bandgap (the best possible case, and quite unlikely!), a short circuit photocurrent of 32.9mAcm^{-2} could be generated.

In addition to this photogenerated current, when a solar cell is under load it generates a voltage. The potential difference between electrodes provided by this voltage causes some current to flow in the opposite way to the photocurrent, i.e. in the wrong way compared to useful current generation. In the case of the open-circuit voltage, this reverse current would equal the forwards photocurrent, providing a net zero current. Since the photovoltaic device will exhibit this reverse current even in the dark, with no

photogenerated current, it is termed the 'dark current'. Most photovoltaic devices behave like a diode in the dark, as a consequence of the asymmetry mentioned earlier that is necessary to achieve charge separation and collection. Thus, the dark current normally follows an ideal diode equation:

$$J_{dark} = J_0(e^{\frac{qV}{k_BT}} - 1) \quad \textbf{2.5}$$

where J_0 is a constant, k_B is Boltzmann's constant, and T is the temperature in Kelvin.

The overall current under illumination can then be approximated by the sum of the (reverse) dark current and the (forwards) short circuit photocurrent. This becomes, for an ideal diode,

$$J = J_{SC} - J_0(e^{\frac{qV}{k_BT}} - 1) \quad \textbf{2.6}$$

Realistically however, under bias, parasitic resistances have a significant effect on the current-voltage characteristics. These are generally split into two types of resistance: series resistance and shunt resistance. Series resistance (R_s) arises from resistance of the cell materials to current flow and from contact resistance. This is particularly a problem at high charge densities or high illumination levels. Shunt, or recombination, resistances (R_{sh}) arise due to leakage channels such as pinholes and recombination at badly selective contacts. Furthermore, the ideal diode behaviour is not often seen in real materials; a more realistic approach is to include an 'ideality factor' *m* in the diode equation, representing a different dependence of current on bias. This arises due to additional recombination mechanisms in different materials. We can add all these modifications into the diode equation, to now get a realistic current-voltage dependence for a solar cell:

$$J = J_{SC} - J_0\left(e^{\frac{q(V+JAR_S)}{mk_BT}} - 1\right) - \frac{V+JAR_S}{R_{sh}} \quad \textbf{2.7}$$

where A is the area of the device. This current voltage relation can now well describe the behaviour of most solar cells. This equation can be more intuitively represented by an electrical circuit diagram, which is shown in Figure 2.9. There is a current generation source, related to the semiconductor photoexciting charge, a diode in parallel, related to the asymmetry within the device that is necessary to extract charge selectively, and resistors in parallel and series representing the shunt and series resistances respectively.

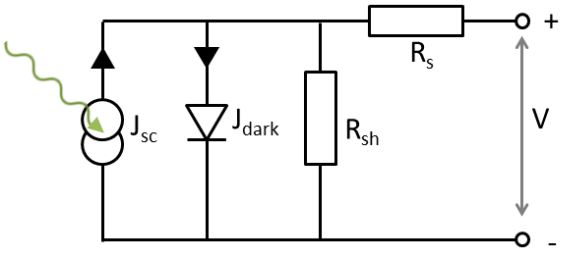

Figure 2.9: Solar cell equivalent circuit diagram. J_{sc} represents current generated from absorbed photons, and J_{dark} represents the diode dark current that would flow in the opposite direction.

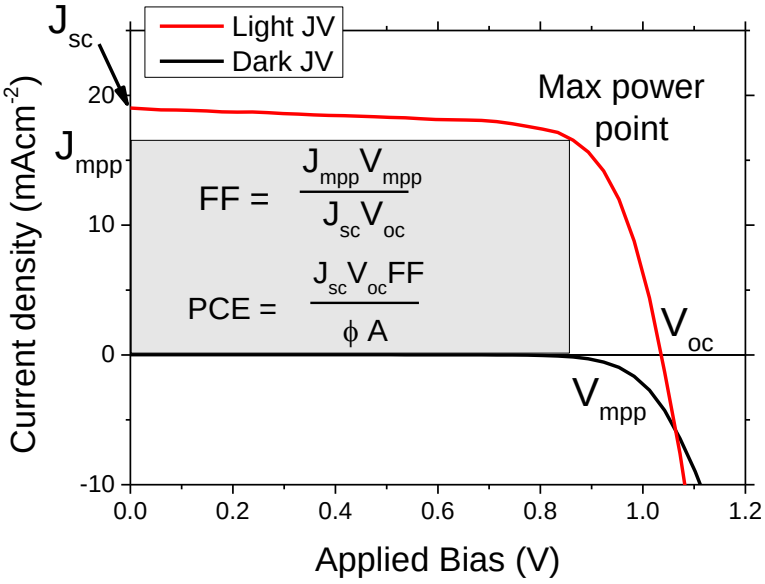

Figure 2.10: Current-voltage curve for photovoltaic device under illumination (red) and in the dark (black). The shaded area represents the maximum power attainable.

A typical current-voltage (*JV*) relation for a real solar cell measured in the light and dark is shown in Figure 2.10. The previously defined short-circuit current, defined as positive, is observed where the light curve intersects V=0, and the open-circuit voltage where J=0. The photovoltaic device is producing power in the whole region where J and V are positive, in the standard convention. Power density is given by $P = JV$; the point at which this product is maximum is called the maximum power point. This power (P_{mpp}) occurs at a particular voltage V_{mpp} and current density J_{mpp}. The ratio of this product to the theoretically ideal power J_{sc} x V_{oc} is defined as the 'fill factor' (*FF*), which describes the 'squareness' of the JV curve, representing the severity of resistive and recombination losses:

$$FF = \frac{J_{mpp}V_{mpp}}{J_{SC}V_{OC}} \quad \textbf{2.8}$$

The power conversion efficiency (PCE or η) is defined as the ratio of the power density produced to the incident light power density (P_I):

$$PCE = \frac{J_{mpp}V_{mpp}}{P_I} \quad \textbf{2.9}$$

which can be reformulated in terms of the incident light intensity φ, cell area, and the FF:

$$PCE = \frac{J_{SC}V_{OC}FF}{\varphi A} \quad \textbf{2.10}$$

The quantities J_{sc}, V_{oc}, FF and PCE, extracted from the JV curve, are the key performance parameters of a solar cell and are for the purposes of comparison are generally measured under standard test conditions: 25°C and 100mWcm^{-2} AM1.5 illumination as described above.

2.3 Types of solar cell

There are several common types, or architectures, of solar cell. They all rely upon in some way creating an asymmetry forcing directional extraction of carriers. A brief description of some of the most important architectures will be given here.

2.3.1 p-n junction

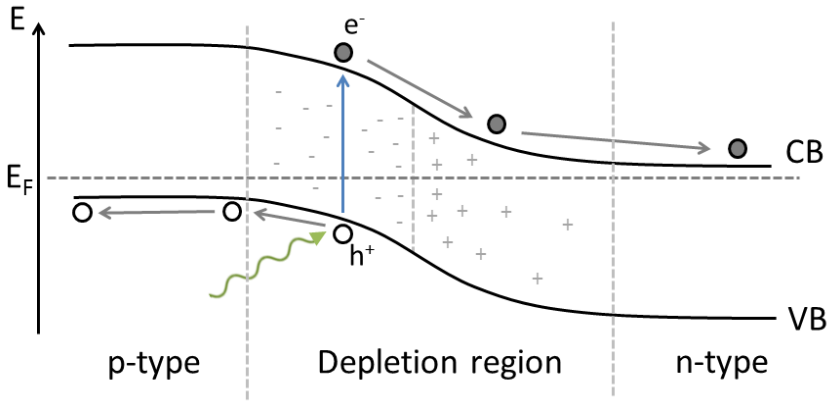

Figure 2.11: Schematic representation of a p-n junction solar cell under open circuit conditions.

The p-n junction is the classical model of an archetypal solar cell, and is the basis for most silicon solar cells in mass manufacture today. It has been around since the 1950s. It consists of an interface between p-type and n-type semiconductors. As illustrated in Figure 2.11, by bringing the two differently doped materials into contact, the excess holes

from the p-type and excess electrons from the n-type material will be attracted to the interface region and recombine. This then leaves an excess of ionized dopant atoms in each material (positive in the n-type and negative in the p-type, which create a so-called depletion region, which is depleted of free carriers. This creates a bending of the bands resulting in an energetic gradient in between the two materials. Upon photoexcitation, photogenerated electrons in the depletion region and throughout the bulk are attracted 'downwards' in energy towards the n-type material, and holes towards the p-type material. This creates a 'built-in field', providing the asymmetry in this device.

2.3.2 p-i-n junction

A p-i-n junction is similar to a p-n junction, but with an intrinsic (undoped) semiconductor between the p and n regions. The same built-in potential is established as a p-n junction, but it is extended throughout the bulk by the intrinsic region. This is useful in materials where the carrier diffusion length is short. Depending on the intrinsic material's dielectric constant, the field may be screened in the intrinsic region; in this case it can be a useful architecture for materials with a long diffusion length but uncontrollable doping, instead requiring p and n type materials different from the intrinsic material to provide the built in field.

2.3.3 Organic solar cells

Organic solar cells are comprised of a junction between two molecular semiconductors, normally referred to as an electron donor and an electron acceptor. These are organic molecules that are able to be excited in a way analogous to a semiconductor; instead of being excited between conduction and valence bands, electrons are excited between molecular orbitals, with an effective bandgap appearing between the highest occupied molecular orbital (HOMO) and the lowest unoccupied molecular orbital (LUMO). Upon photoexcitation, electron-hole pairs, referred to as excitons, are strongly bound, only splitting when coming into contact with a material with different work function. Since they do not diffuse very far before recombining, a distributed junction approach between two materials with different work function is normally used, by blending materials to reduce path length to the interface at any point in the cell. Once split, electrons and holes travel through the acceptor or donor respectively to reach the electrodes. These cells are limited by the energy required to drive efficient exciton splitting at the interface; there is always a significant loss in energy between the open-circuit voltage and the bandgaps of the materials used.

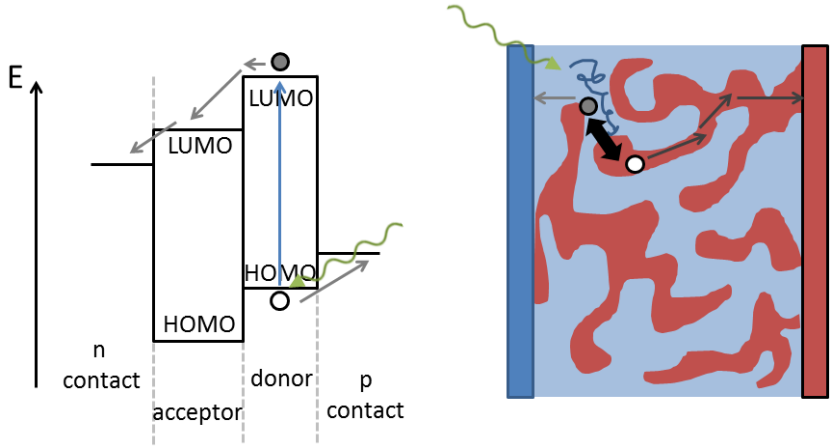

Figure 2.12: Schematic representation of organic solar cell operation. Left: energy level diagram. Right: schematic of distributed junction approach between an acceptor material (blue) and a donor material (red). Upon photoexcitation, an exciton is formed, diffusing until it reaches the interface. It can then split into an electron and a hole, which travel through the respective materials to the contacts.

2.3.4 Dye-sensitized solar cells

The dye-sensitized solar cell, first developed in 1991 by O'Regan and Gratzel,[3] effectively separates the processes of charge generation and transport into separate materials. A thin layer of sensitizing dye is anchored to a mesoporous wide bandgap semiconductor, providing a large surface area for excitation. This is contacted by a liquid redox electrolyte, which is capable of transporting charge by transferring electrons between ions in different oxidation states. Typical operation is illustrated in Figure 2.13. Electron-hole pairs, in the form of an exciton, are excited in the dye, and subsequently the electron is rapidly transferred into the n-type semiconductor (normally TiO_2) and the hole into the electrolyte. The electron and hole then travel through the mesoporous semiconductor and electrolyte to the collection electrodes. The built-in field in this case arises from the energetic difference between conduction band in the semiconductor and the reduction level in the electrolyte; electrons cannot transfer into the electrolyte nor holes to the semiconductor, due to the choice of materials.

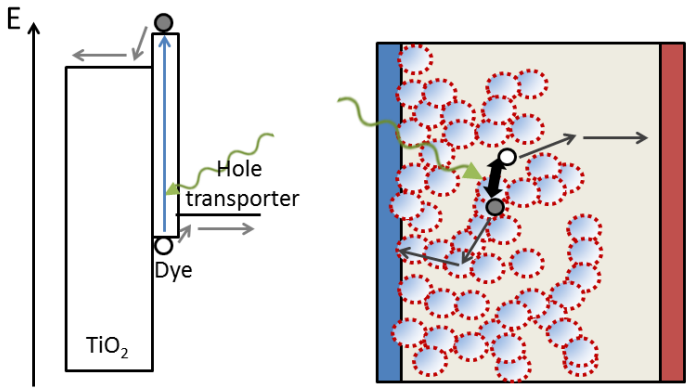

Figure 2.13: Dye sensitized solar cell operation. Left: energy level diagram. Right: schematic of operation. Upon excitation of an exciton in the dye, electrons are rapidly transferred into the TiO_2 and holes to the hole transporter, either an electrolyte or a solid state hole transporter. These materials then transport the charge to the electrodes.

In recent years, to overcome stability concerns, a solid-state version of the dye-sensitized solar cell has been developed.[4] This replaces the liquid electrolyte with a solid-state hole transporting material, normally a small-molecule organic semiconductor, where holes can be transported by 'hopping' between neighbouring molecules.

2.4 Perovskites

Perovskites are a class of materials that are defined as those that have the same crystal structure as calcium titanate, $CaTiO_3$. This takes the form ABX_3, where A and B are two cations of different sizes, and X is an anion that bonds to both. The B cation, smaller than the A cation, is surrounded by corning-sharing octahedra of X anions, with the A cation in between the octahedra. This structure is illustrated in Figure 2.14.

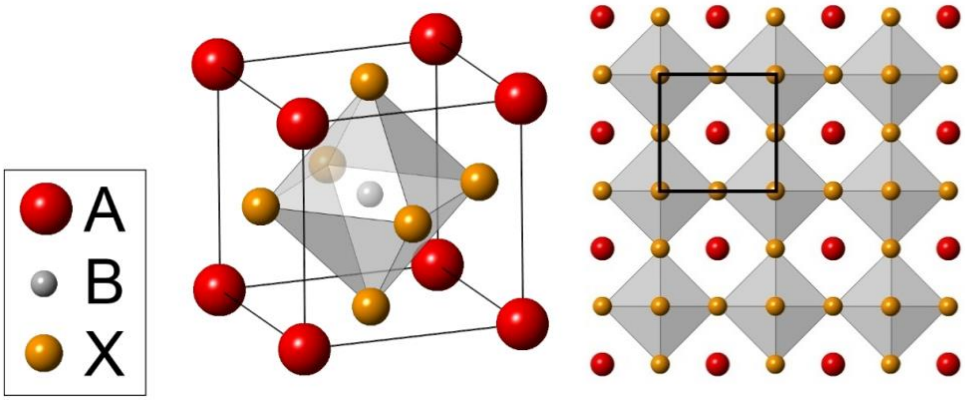

Figure 2.14: Perovskite crystal structure. Left: unit cell for a cubic ABX_3 perovskite lattice. Right: view along one crystallographic axis of a greater number of unit cells, with the unit cell outlined in black.

This three-dimensional perovskite lattice structure can only form for certain combinations of anions and cations, depending on their ionic radius. To define the allowed compositions, there exists a 'tolerance factor', which is defined as:[5]

$$t = \frac{r_A + r_X}{\sqrt{2}(r_B + r_X)} \qquad \textbf{2.11}$$

Where r_A, r_B, and r_X are the ionic radii of the A, B, and X components of the perovskite lattice. t = 1 would correspond to a perfectly packed structure, having a cubic lattice structure, and it can be varied only in a restricted range. In practice, a cubic 3D structure will likely form if $0.8 \leq t \leq 1$. However, distorted lower symmetry perovskites that take tetragonal, trigonal, rhombahedral, or hexagonal structures can form when $0.7 \leq t \leq 0.8$. When the tolerance factor is greater than 1, the structure will likely form a 2-dimensional perovskite analogue, where sheets of B-X octahedra are separated by large A cations.

The perovskites of interest for photovoltaic applications are halide-based perovskites. There are a number of A, B, and X ions that have been investigated in the halide perovskite family. Typical A site cations that can form 3D perovskites include Li^+, Na^+, Rb^+, K^+, Cs^+ and the organic cations $CH_3NH_3^+$ (MA) and $H_2NCNH_2^+$ (FA).[5,6] Larger organic molecules have been used to force the perovksite structure into the 2D layered structures.[7] The B site can be occupied by any divalent metal cation, and indeed a large range of transition metals have been explored, but the most relevant for optoelectronic applications are Sn^{2+}, Ge^{2+}, Pb^{2+} and Eu^{2+}.[5] The practically useful halides suitable for the X site are I^-, Br^-, Cl^- and F^-.

The halide perovskites are generally solution-processable semiconductors that require only low temperature processing to form high quality crystalline materials.[5] Therefore,

they are of significant interest for cheap and efficient photovoltaics. The most commonly employed perovskite for optoelectronic purposes is methylammonium lead halide, $CH_3NH_3PbX_3$ (X=I, Br, Cl) ($MAPbX_3$). Different choices of halide, X, give materials with different bandgaps, as will be discussed further in Chapter 7.[8] $MAPbI_3$ is most interesting for photovoltaic energy conversion, with a bandgap of 1.57eV. With an EQE of 100%, this material could generate a short-circuit current density of up to 26mAcm^{-2}, and more in-depth calculations give an efficiency limit of 31% PCE, close to the Shockley-Quiesser maximum.[9] This perovskite has a tetragonal structure at room temperature, caused by a distortion of the cubic lattice, with lattice constants a=b=8.85Å, c=12.64Å. This structure has a tolerance factor of ~0.84. The Sn^{2+} analogue has been shown to forms similar compounds with theoretically more ideal bandgaps, but instability due to the ease of oxidation limits its practical use.[10,11]

The lead halide perovskites have been demonstrated to have high luminescence efficiency,[12] carrier mobility,[13] and slow non-radiative recombination rates.[14,15] These beneficial properties mean that in addition to its use in photovoltaic devices, they have now been incorporated as the active material into light-emitting devices,[16–18] lasers,[12,19–21] and transistors.[22,23]

2.5 Perovskite solar cell operation

2.5.1 The evolution of the perovskite solar cell

The perovskite solar cell field has exploded into being over the last 3 years, during the time in which the work described in this thesis was being carried out, and thus the understanding of perovskite solar cell operation has grown along with developments in the field. The evolution of the perovskite solar cell will thus be briefly described, along with the advances in understanding gained along the way.

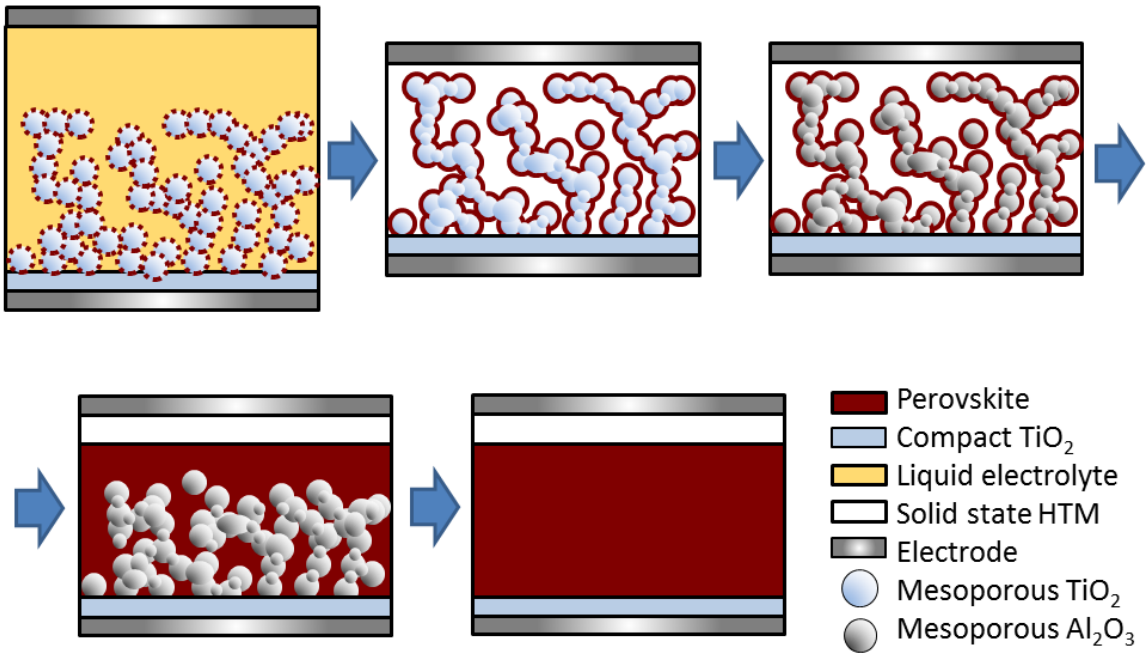

Figure 2.15: Diagram of the evolution of the perovskite solar cell, as described in this section. From top left to bottom right: Sensitized perovskite solar cell with liquid electrolyte, solid-state sensitized perovskite solar cell, mesosuperstructured perovskite solar cell, mesostructured solar cell with thick perovskite capping layer, planar perovskite solar cell. The examples of compact TiO_2 and a solid state HTM (Hole Transporting Material) are used as the hole-blocking and electron blocking layers respectively; however there are many other materials suitable for these purposes at the present time.

Interest in halide perovskites dates back more than a century,[24] but it was the more recent work of Mitzi and co-workers that exposed these materials to the broader community.[5] Work was carried out mainly on light-emitting devices and transistors, but no photovoltaic devices were reported.[7,25–27]

The first report of a solar cell incorporating halide perovskites was in 2009, when Miyasaka et al incorporated a thin layer of $MAPbI_3$ nanoparticles onto the surface of mesoporous TiO_2 for use as a 'dye' in a dye-sensitized solar cell configuration, with hole transport provided by a liquid electrolyte.[28] It was thought here that the perovskite was simply acting as a dye, with no long-range transport possible; electrons and holes quickly extracted from the perovskite into the TiO_2 and electrolyte respectively. A *PCE* of 3.8% was achieved in this initial report. This work was taken further by Park et al in 2011, achieving a noteworthy *PCE* of 6.5%.[29] However, the perovskite nanoparticles dissolved in

the liquid electrolyte in a matter of minutes, rendering the cells difficult to reproduce or measure.

This instability was addressed in 2012 almost simultaneously by the groups of Snaith and Gratzel, by replacing the problematic liquid electrolyte with a solid-state hole transporting material, Spiro-OMeTAD (2,2',7,7'-tetrakis-(N,N-di-4-methoxyphenylamino)-9,9'-Spirobifluorene), previously used in solid-state dye sensitized solar cells.[30,31] This not only solved the stability issue but also improved the efficiency to 9.7%, in this 'solid-state sensitized solar cell' configuration. However, a more important finding was reported by Snaith et al: it was found that the mesoporous TiO_2 could in fact be replaced with an inert material, Al_2O_3, which is incapable of transporting charge. Solar cells made with this material instead of TiO_2 displayed even higher efficiencies (10.9%), which demonstrated that long-range electron transport must be occurring within a continuous layer of perovskite on the surface of the mesoporous structure. This provided the first evidence that the perovskite material itself may have not only favourable absorption properties, but also be a high-quality semiconducting material. This architecture, using the mesoporous layer only as a scaffold, was termed a 'meso-superstructured solar cell'.[31] Shortly afterwards, it was shown by Etgar et al that the perovskite could also transport holes; the Spiro-OMeTAD was replaced by simply a thick capping layer of perovskite, and such hole-transporter-free cells exhibited reasonable efficiencies.[32]

The realisation that $MAPbX_3$ could effectively transport both electrons and holes for hundreds of nanometres led to a flurry of activity on understanding the material better. It was shown via terahertz spectroscopy and other methods that the mobilities of electrons and holes in the $MAPbX_3$ perovskites have exceptionally high values of $\sim 20 cm^2 V^{-1} s^{-1}$, one of the highest observed for a solution-processed material.[13,15,33,34] In combination with this, they were shown to exhibit very low recombination rates, both radiative and non-radiative.[15]

The diffusion length is an important parameter in a semiconductor; it describes the distance that an average charge can diffuse before recombining. This represents the depth from which charge can easily be extracted in a device made from a pure block of this material, so if it is longer than the absorption depth (the distance over which most light is absorbed) for relevant wavelengths, all generation and charge can take place in this material, and a planar device made from this material should be the most efficient. There would be no need for charge to be extracted into other materials in the way that occurs in the sensitized devices. It can be extracted from the mobility and lifetime measurements, but in addition it was directly shown, by using a time-resolved photoluminescence

quenching technique, that the diffusion length for both photoexcited electrons and holes in such perovskites could be up to over a micrometer.[35,36] Compared to an absorption depth of 100-200nm, this clearly indicates that the material should be capable of functioning effectively in a planar device architecture.

Another relevant parameter is the exciton binding energy. As discussed, in organic materials electrons and holes are strongly bound in an exciton once excited, and further energy input is needed to split them – this extra energy is the exciton binding energy. A high exciton binding energy would detrimentally affect the *PCE* achievable, as extra energy would have to be lost in splitting the exciton. In most inorganic semiconductors, exciton binding energy is typically small, meaning that most photoexcited species are present as free charge. Since the halide perovskites investigated are organic-inorganic hybrid materials, it was unclear whether there would be a high or low exciton binding energy. Initial optical spectroscopic techniques suggested that the excitonic binding energy in $MAPbI_3$ was <50meV, but recently more direct magneto-optic measurements have revealed it to be only a few meV at room temperature.[37–40] With room temperature thermal energy being 26meV, this would result in the majority of photoexcited carriers being present as free charge, not excitons, in the perovskite. Therefore the exciton binding energy should not be a limiting factor for the *PCE*.

All these observations led to the conclusion that $MAPbX_3$ and related perovskites are effectively very high quality semiconductors, which can be solution-processed at low temperatures and yet retain high crystallinity and excellent optoelectronic properties. Therefore it was realised that planar perovskite devices, with a bulk layer of perovskite sandwiched between selective contacts, should be the optimum architecture. These had not been explored previously due to deposition issues. The work carried out in Chapter 4 will discuss these issues, how to solve them by carefully control of the deposition and annealing conditions, and describe the development of planar perovskite solar cells with the scaffold completely eliminated, with efficiencies above 10% for the first time.[41,42]

Further jumps in efficiency were achieved by the incorporation of solid perovskite capping layers into the mesoporous titania architecture, moving towards the planar junction approach.[8,43] It was also shown by two groups that vacuum deposition of the perovskite in a planar architecture was possible.[44,45]

The highest efficiencies to date have been achieved by incorporating narrower-bandgap perovskites, based on replacing the methylammonium cation with a slightly larger formamidinium cation. The development of the formamidinium lead halide perovskite material will be discussed in depth in Chapters 7 and 8.[46] Devices incorporating this

material in a hybrid structure (thin TiO_2 mesoporous layer plus thick perovskite capping layer) have now demonstrated efficiencies of above 20%, and the increases in efficiency show no sign of slowing down.[47–49] Notably though, devices with a reported 19% efficiency use the completely planar architecture, demonstrating that the most efficient possible architecture has not been decided on by the community just yet.[50]

2.5.2 Operating mechanism

An operating mechanism for a perovskite solar cell can now be suggested. Thick layers of perovskite with selective contacts (including thin mesoporous TiO_2 in that definition) appear to be the most efficient architecture, and the one most discussed in this thesis.

Firstly it should be noted that it is thought that doping in the halide perovskites is generally small but also uncontrollable, due to the solution-processing deposition techniques employed. Therefore, doping will effectively be ignored, as it is not thought to play a major role in device operation.[51–53] It should be mentioned that a common chloride-assisted deposition of $MAPbI_3$, often denoted as $MAPbCl_xI_{3-x}$ or similar, may incur trace residues of chloride, but that it is not thought to be incorporated within the crystal lattice nor 'dope' in the conventional sense.[54–56]

The operating mechanism is simple, as illustrated in Figure 2.16. It is effectively a p-i-n junction with a material with a long diffusion length and no controlled doping profile, as discussed in section 2.3.2 above. Its operation can be split into three stages:

1. Light is absorbed in the bulk of the perovskite, exciting electrons and holes into the CB and VB respectively.
2. These immediately separate, due to the low exciton binding energy, and diffuse around the material.
3. When a carrier reaches the correct selective contact, it is energetically driven to be extracted into the contact material, and travels through the selective material to the electrode. Carriers reaching the wrong selective contact are blocked from being extracted.

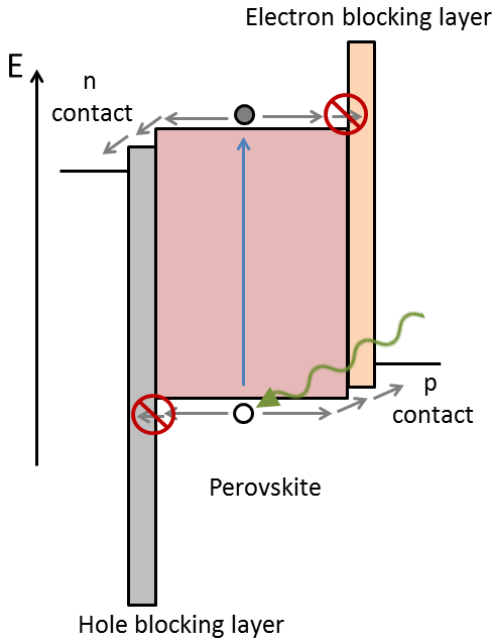

Figure 2.16: Operating mechanism of planar perovskite solar cell, as described above.

It should be noted that this is described for the open circuit condition, and furthermore no band bending at the interfaces is considered. This is a simplistic picture and for some contact materials there will inevitably be some energetic interaction between the perovskite and the contact material.

Based on this operating model, some criteria for a high-performing perovskite solar cell can be established:

- Perovskite has close to the ideal bandgap for solar energy conversion (see Section 2.2)
- Long diffusion length in perovskite (ideally more than absorption depth, as discussed earlier). This encompasses:
    - Long photoexcited carrier lifetime
    - High mobility in perovskite material
    - Slow recombination rates
- High quality of perovskite material, i.e. few defects or trap sites
- Good carrier selectivity of contacts
- Efficient carrier extraction at the selective contacts with little energy loss
- Little non-radiative recombination
- High radiative recombination (this will be discussed later)

- No pinholes in perovskite film allowing recombination (i.e. uniform and continuous film of perovskite)

2.5.3 Hysteresis in perovskite solar cells

It is worth noting that recently a phenomenon has become apparent in perovskite solar cells whereby current-voltage characteristics can exhibit hysteresis, with the solar cell parameters being different depending on scan direction and rate of voltage sweep (i.e. from forwards bias to reverse bias or vice versa).[57–59] This can result in artificially inflated *PCE* values. By holding the solar cell at forward bias before measuring, an enhanced efficiency can be attained, while a reduced efficiency is attained by holding the cell at reverse bias or even short circuit before measuring.[59] Moreover, the magnitude of the observed hysteresis depends on the scan rate of the current-voltage sweep. It appears that a very fast scan, if initially held at forward bias, will demonstrate high efficiencies in both scan directions and little hysteresis, a mid-rate scan will demonstrate high efficiency in the scan from forward bias and low efficiency from short circuit, and a very slow scan will display little hysteresis. In this slow scan, which approaches the steady state condition, often lower efficiencies are measured in both directions. Typical hysteresis behaviour for a planar perovskite solar cell is shown in Figure 2.17. It can be concluded that the problem arises when the current-voltage sweep is carried out at a faster rate than the device can respond, which seems to be on the timescale of seconds.

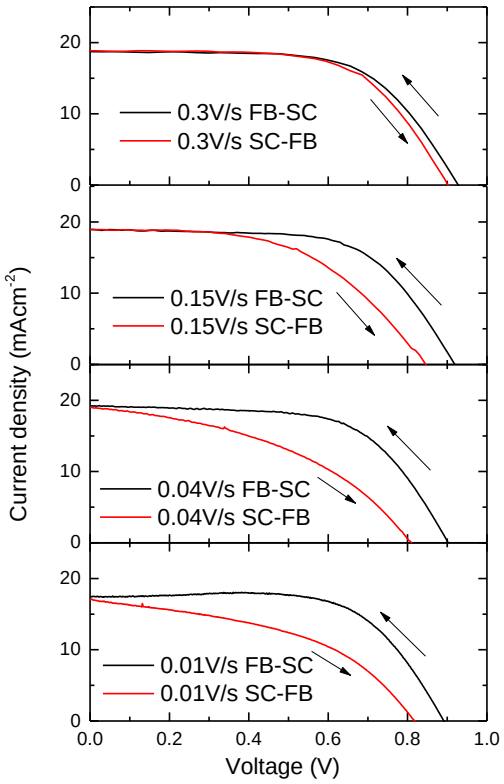

Figure 2.17: Hysteresis in a planar-structured methylammonium lead iodide perovskite solar cell. FB-SC refers to scanning voltage from forward bias to short circuit, and SC-FB vice versa. Typically, the highest efficiencies are extracted from the FB-SC scans, and hysteresis is most extreme at intermediate speed scans (0.04V/s here). The scan rates depicted here do not go down to low enough speeds to observe a reduction of hysteresis at very low scan speeds.

The slowest scan rate would thus be most accurate for measuring real efficiency, as it approaches the steady state condition.[58] However, we often do not know exactly how slow we need to scan – and the rate of the hysteretic process occurs on different timescales in solar cells prepared in different architectures and via different fabrication routes.[57] Moreover, scanning a cell very slowly is often impractical when screening a number of parameters. The question arises of how to practically measure the 'real' efficiency of a device. The most commonly employed solution to this has been established as holding the device at its maximum power point voltage and measuring photocurrent (and hence PCE) over time, until a steady state value is reached. Since the behaviour is very different from that expected from rate dependent capacitive current, this is a more accurate method of attaining a real efficiency than taking the average of the forward and reverse scans.[60]

The cause of this current-voltage hysteresis is still under debate; this will be elaborated upon in Chapter 9. Based on the results that will be shown in Chapter 9, however, it can be concluded that the dominant mechanism responsible for inducing hysteretic behaviour is likely to be mobile ions and defects in the perovskite material, though trap states at the interfaces may also be important. By applying a bias to a perovskite film, it can be polarised temporarily, with photovoltaic function being possible in either direction.[61] It appears that poling in this way creates a temporary asymmetry in the device, meaning that selective contacts are not even necessary on short timescales (tens of seconds).[62] The likely mechanism is that under applied bias, charged mobile ions (vacancies, interstitial defects, or even some of the ions making up the material itself) move to screen the applied field, building up charge at the interface. Upon release of the field, this charge may be compensated by photoexcited electrons and holes, meaning that there is an excess of various defects at each interface, which can then act as dopants.[61] The exact mechanism is still under debate, but in some way this ionic motion is able to set up a built-in field in the device, dissipating upon release of the field over tens of seconds.[63,64] The built-in field encourages charge separation to either side of the device, effectively increasing the carrier drift velocities and minimizing recombination. This allows non-selective devices to function temporarily, and allows 'normal' devices to function in some cases better than they would otherwise be able, since there is an additional field assisting charge extraction at the correct contacts. This effectively allows carriers to last longer in the material before recombining, giving them an increased chance of being extracted. The proposed mechanism for hysteresis is shown in Figure 2.18.

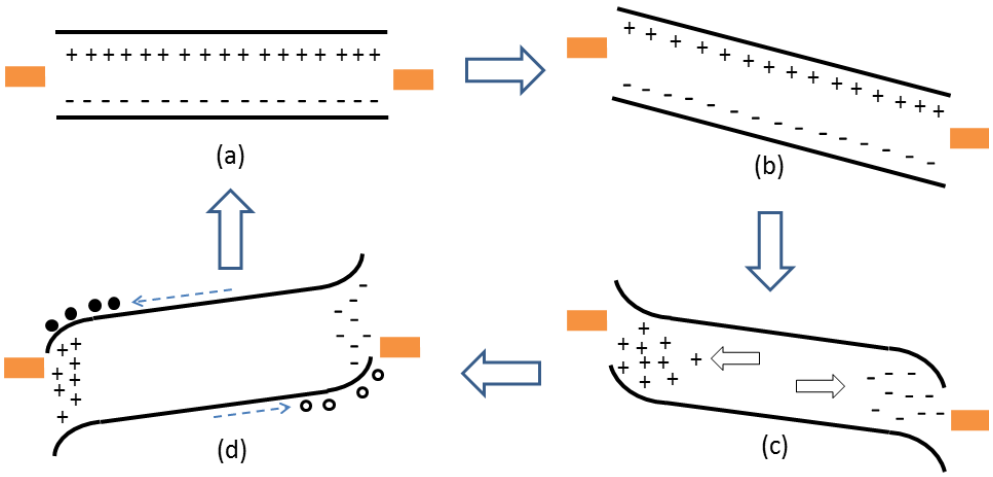

Figure 2.18: Proposed mechanism for hysteresis. Here it is assumed field extends uniformly across the whole film, which is the simplest case. a) Under no bias, charged ions/defects present throughout the film, flat field profile. b) Under bias, uniform field present throughout the film. c) Mobile charged ions/defects move to compensate the applied field, resulting in a flattening of the field profile. d) When bias released, the doping or charge buildup from the mobile ions results in field across the film, encouraging separation of charge and selective extraction at the contacts. Eventually the charged ions will dissipate back to a uniform distribution throughout the bulk, and the field disappear, as in a).

2.6 Photoluminescent characterisation of perovskites for solar cells

In addition to measuring JV curves, it is useful to be able to characterise a material for its use in a solar cell without making a full device.

Since the majority of this thesis focuses on planar-structured perovskite devices, material quality is of paramount importance, since the perovskite will be doing the light absorption and charge transport. As discussed above, some criteria have been established that are necessary to make a good perovskite solar cell.

Importantly, these include a long diffusion length, slow recombination rates, and more radiative than non-radiative recombination. These criteria can be established by photoluminescence methods.

Recombination is an important part of solar cell materials. Recombination, the loss of mobile electrons and holes by a number of removal mechanisms, can be divided into

avoidable and unavoidable recombination processes. The unavoidable processes are a part of the fundamental nature of a semiconducting material, and include radiative recombination (also known as spontaneous emission), stimulated emission, and auger recombination. Radiative recombination is the relaxation of an electron across the bandgap, resulting in the emission of a photon- effectively the reverse of photoexcitation of an electron. Stimulated emission is generally not relevant at solar fluences. Auger recombination is an electron-electron or hole-hole interaction resulting in the decay of one carrier across the bandgap and energy transfer to the other carrier. This is mainly important in materials with high carrier densities or at high fluences, and it is not very important for the perovskite cells discussed herein under 1 sun illumination.

Avoidable processes normally involve non-radiative recombination between an electron in the CB and a hole in the VB via a trap state, due to the presence of defects as discussed above. The energy lost is converted to heat. This is especially prevalent at surfaces due to surface trap states. Non-radiative recombination is always detrimental to the performance of a semiconductor in a solar cell - a high non-radiative decay rate means that the diffusion length for excited carriers will be reduced.

On the other hand, radiative recombination is not necessarily detrimental. A high radiative decay rate for a particular material would also reduce the diffusion length however, so the ideal solar cell material would have a long radiative lifetime in order that excited carriers can be collected before being lost as photons (though note that some of these photons can be re-absorbed).

Somewhat counter-intuitively, it can also be shown that a high radiative efficiency is actually crucial to attaining the best solar cell performance. A good solar cell should also be a good LED.[65,66] This is due to the fact that at open circuit, when they cannot be extracted electrically, ideally *all* excited electrons would eventually recombine radiatively, rather than non-radiatively. A high *rate* of radiative recombination is not necessary, rather a high *efficiency.* When a bias is applied, and the cell is under load, the amount of radiative emission will depend on the competition between extraction rate and radiative decay rate; ideally here the radiative decay rate is long enough that all carriers can be extracted. However, the open-circuit voltage will indeed depend on the radiative efficiency, in simplified terms:[67]

$$\boldsymbol{V_{OC} = V_{OC\,ideal} - \frac{kT}{q} |\ln \eta_{ext}|} \qquad \textbf{2.12}$$

where η_{ext} is the external luminescence efficiency. The latter term thus represents a loss in V_{OC} when the luminescence efficiency is less than 1 (i.e. less than perfect). The external

luminescence efficiency in a device is related directly to the photoluminescence efficiency of the semiconductor. Thus to attain the highest open-circuit voltages, a material should be used with as high as possible photoluminescence efficiency. This is a metric which can easily be quantified, by a photoluminescent quantum efficiency measurement.

Regarding the radiative decay rate, as previously mentioned, a high decay rate would mean that even if the photoluminescence was very high, excited carriers would decay radiatively before being extracted, so a slow radiative decay is ideal for a photovoltaic material. A material with slow radiative and non-radiative decay rates will have a long excited carrier lifetime. This can be probed by measuring the time-resolved photoluminescence: fitting the photoluminescent decay of excited species over time after a pulsed excitation gives a measure of the average lifetime of an excited carrier. It is even possible to estimate diffusion lengths using photoluminescent decay techniques, and this will be discussed in more detail in Chapters 3 and 7.

To conclude, the ideal photoluminescent properties of a material for use in solar cells would be:

- High (as close to unity as possible) photoluminescence quantum efficiency
- Long photoluminescent lifetime.

These criteria will be considered throughout this thesis, in particular in Chapter 10 where material quality is brought to the forefront.

2.7 Dewetting

The concept of dewetting plays an important part of the work undertaken in this thesis. Dewetting refers to the retraction of a film from a surface; the opposite of spreading. This is often an unwanted process as it ruptures the film; however in some cases control of dewetting has been used to form structures or arrays of particles.[68] Dewetting can occur both in the liquid state and in the solid state. Here, an introduction to the mechanisms of both types of dewetting is given, with a particular view to establish the important experimental parameters in a dewetting system.

2.7.1. Liquid state dewetting

Dewetting of a liquid from a solid substrate is of particular importance during deposition processes such as spin-coating, or during annealing processes in which the film is still in the liquid state or at temperatures above its melting point. Whilst the film remains liquid, it is governed by hydrodynamics, as the fluid layer can easily flow. The hydrodynamic

equations governing dewetting kinetics are complex, but they are now well-understood.[69,70] Wetting or dewetting is driven by surface energy considerations. If a drop of liquid on a solid substrate, in thermal and mechanical equilibrium, is considered, as shown in Figure 2.19, it can be seen that there are three surface tensions that should be considered: solid-liquid, liquid-gas, and solid-gas.

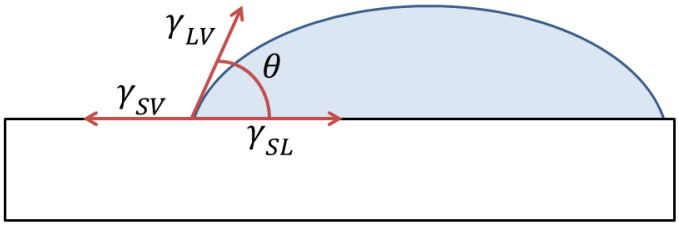

Figure 2.19: Mechanical equilibrium leading to Young's equation: surface tensions (free energies per unit area) acting on the contact line between a liquid drop (blue) and a solid substrate (white).

The contact angle that the drop in equilibrium makes with the surface is given by Young's equation:[69]

$$\boldsymbol{\gamma_{SV} = \gamma_{SL} + \gamma_{LV} cos\theta} \qquad \textbf{2.13}$$

where γ_{SV} denotes the solid-vapour surface tension, γ_{SL} the solid-liquid tension and γ_{LV} the liquid-vapour surface tension. These tensions are free energies per unit area, or forces, and the equation follows from balance of forces. If these tensions are known, then it can be determined whether the fluid will be driven to wet or de-wet; if $\gamma_{SV} < \gamma_{SL} + \gamma_{LV}$, then the lowest energy state will be that where the contact angle is finite and the fluid will partially wet in equilibrium, whereas if $\gamma_{SV} = \gamma_{SL} + \gamma_{LV}$, the contact angle must be zero and equilibrium will be such that a uniform layer of fluid covers the surface complete – complete wetting. A 'spreading coefficient' S can be defined, representing γ_{SV} compared to its value for complete wetting:

$$\boldsymbol{S = \gamma_{LV}(cos\theta - 1) = \gamma_{SV} - \gamma_{SL} - \gamma_{LV}} \qquad \textbf{2.14}$$

If $S \geq 0$, then spreading will be favourable, whereas if $S < 0$, dewetting will be. However, upon deposition of the liquid upon a substrate, it will not be immediately in equilibrium. Spin-coating a film, for example, can produce a continuous film initially, even if $S < 0$. Such a film can either be in a metastable state (not at the free energy minimum, but an energy barrier is present preventing it from reaching that state without more energy input) or an unstable state, and this dictates how dewetting generally occurs.

To clarify the distinction between stable, metastable and unstable films, the interface potential $\varphi(h)$ can be plotted, defined as the free energy taken to bring two interfaces from infinity to a distance h.[71] Here the interfaces are the solid-liquid interface and the liquid-air interface, with h the initial thickness of the film. This is shown in Figure 2.20 for the three cases. In curve 1, $\varphi(h) > 0$ and the minimum will be at infinite film thickness – in this case the film is stable, the force needed to push the interfaces together continues to increase as they approach. In curve 2, there is a minimum of $\varphi(h)$ at a certain value of h. The system can thus gain energy by changing the film thickness to this value, so if the initial thickness is greater than it, it will dewet - this film is unstable. In curve 3, as the interfaces approach, force first increases and then decreases before reaching a minimum; a free energy barrier must be surmounted. The film is unstable for small film thicknesses, but for larger thicknesses, another perturbation would be needed to drive the film towards dewetting. Here, the film is called metastable.

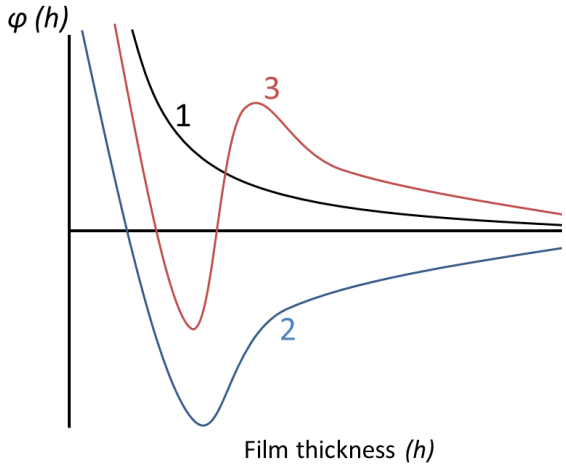

Figure 2.20: Effective interface potential as function of film thickness for stable (1), unstable (2) and metastable (3) films.

A dewetting liquid film will destabilise to expose dry patches, occurring via the formation of holes. Practically, the formation of holes can be considered to occur in one of three routes.[71] If the system is perturbed by surface defects (dust or other inhomogeneities), these can form the nucleation point for a hole in the film, known as heterogeneous nucleation. If hole nucleation is driven by thermal noise, it is termed homogeneous nucleation. These mechanisms are the relevant ones for metastable films.

If the system is unstable, it can destabilise spontaneously. This situation leads to what is known as spinodal dewetting, where a regular array of holes with an effective wavelength forms in the film.[72] It is named this in analogy to the spinodal decomposition occurring in an unstable mixture of two phases. It is observed in regimes where $\varphi''(h) < 0$, which

normally occurs for very thin films of material.[71] The patterns formed by the different types of dewetting are shown diagrammatically in Figure 2.21.

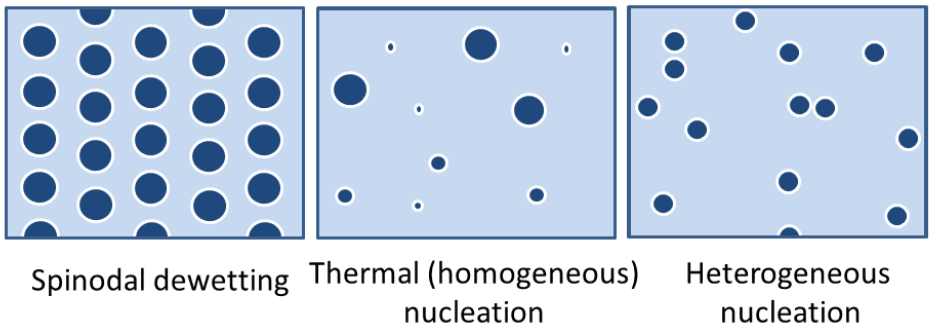

Figure 2.21: Simplified diagram of dewetting patterns that would be observed from spinodal dewetting, homogeneous and heterogeneous nucleation processes.[71]

The critical parameters influencing the magnitude and type of dewetting in the liquid state can thus be summarised. Due to the dependence of stability on film thickness, this is of critical importance. The surface tensions involved, related in particular to those of the substrate and the fluid, will alter the spreading coefficient and thus control the whole process. Due to the influence of thermal noise-based nucleation, and the possibility to overcome energy barriers by addition of thermal energy, temperature will be an important parameter too. By modifying the substrate and film thickness, all 3 dewetting regimes have been observed in a single fluid system.[71]

Once the film has formed initial holes, these holes will then grow in a way governed by hydrodynamics. Generally they will move towards the equilibrium wetted state from the initial state; this may involve at some point the holes become large enough to impinge, which will result in the formation of islands of material.

Thus far, the kinetics of dewetting processes have not been considered. Knowing the initial type of hole nucleation and the various surface potentials of a system, mathematical models can be constructed to understand the dynamics of liquid dewetting. This is not detailed extensively here, aside from to mention that temperature will generally be the most important parameter on the rate of dewetting. There are many considerations to take into effect to accurately model the dynamics of dewetting systems; such a system will be complicated by incorporating other effects that may be present in realistic systems such as slip, viscoeleasticity, gravity, phase changes, and non-newtonian effects.

2.7.2. Solid state dewetting

Dewetting of material in the solid state is more complex and less well understood than in the liquid state. Solid state dewetting typically occurs when films are heated at temperatures below their melting point. The driving force is the same as for liquid state – minimisation of surface energies.

However, importantly, in a solid film the crystallinity of the material plays an important role. Crystalline films will not form a 'bead' in a similar way to the liquid films, with uniform surface tension over the material, rather they have facets, with different surface tensions for the different crystal facets. It has been shown that flat isotropic solid surfaces are also generally stable to small perturbations, so another process is needed to explain hole formation.

If the crystal has non-isotropic surface energy, it is important to know the surface energy of the different facets; this can be described by a gamma plot as shown in the left of Figure 2.22. Here the surface energy is represented by a vector as a function of angle of the normal with respect to a specific crystal orientation. In the simple 2D example shown there are 8 points with minimum surface energy; these correspond to the facets on the preferred crystal shape. This can then be used along with the knowledge of the interface energy to determine the equilibrium shape of the crystal on the substrate, as on the right of Figure 2.22.[73]

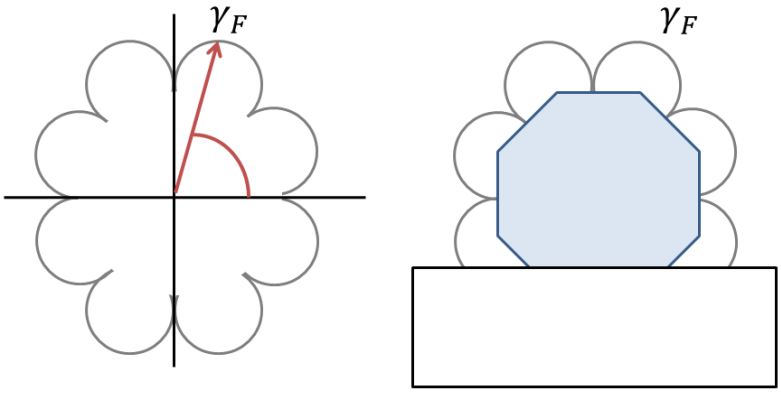

Figure 2.22: Left: gamma plot showing magnitude of surface energy of crystal as a vector plotted as a function of angle of the normal with respect to a specific orientation. Right: Equilibrium shape of the crystal (blue) on a substrate (white).

The other key difference to liquid dewetting is that Instead of being subject to hydrodynamic flow, solid films cannot flow easily. In order to restructure themselves, films must be subject to some process that allows mobility of the components of the lattice. This could be via bulk diffusion, evaporation-condensation, or surface diffusion; it

is now generally accepted that in most cases surface diffusion is the dominant transport mechanism.[74] The mobility of the lattice components via surface diffusion is strongly temperature-dependent, so temperature will be a critical parameter in the rate of material flow and hence dewetting.

Solid films can generally be either polycrystalline, single crystalline, or amorphous. Amorphous and polycrystalline films will behave similarly whereas single crystals tend to exhibit somewhat different dewetting characteristics as discussed later.

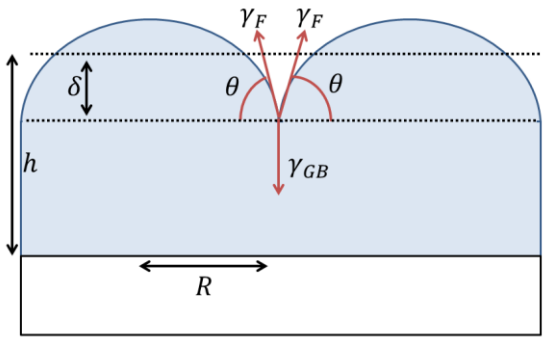

Figure 2.23: Hole growth at a grain boundary in a film with grain radius R. Height of the film *h* represents what the height would be if the film were flat. Here, the groove depth δ is less than the height so it does not form a complete hole.

In polycrystalline films, grain boundaries are present between crystallites, and have energy γ_{GB}. For an isotropic γ_F (film surface energy), force balance in a simple 1D case leads to the shape shown in Figure 2.23. It can be shown that θ is given by:[75]

$$\boldsymbol{\theta = sin^{-1}\frac{\gamma_{GB}}{2\gamma_F}} \qquad \textbf{2.15}$$

If the depth of the groove, δ, is greater than the film thickness *h*, the groove will contact the substrate and become a hole that is able to grow to initiate dewetting. In this simple approximation this depends on the grain radius *R*, and it can be shown that the film will rupture if:

$$\boldsymbol{R > R_C = \frac{3sin^3\theta}{h(2-cos\theta+cos^3\theta)}} \qquad \textbf{2.16}$$

So it can be seen that the number of holes will increase when there are high energy grain boundaries, when the thickness *h* is small, the film surface energy γ_F small, and grain boundary radius R large. Extending this analysis to a real 3D case, boundaries between 3

grains would have the highest energy and holes would be most likely to form there.[75] Another consideration in a real film is crystal stress; if a hole is able to relax a strain in a crystal it is more likely to form. The rate of hole formation will impact the overall dewetting rate, if new holes are forming during the process. It will depend on the rate of hole formation and the rate of hole growth. For a kinetic process, it can be shown to scale with the thickness of the film and the surface self-diffusivity. [76]

The next step is to consider the rate of hole growth. Once a hole has formed, capillary forces will drive retraction of the edge and the hole can grow. If a hole is formed with a sharp edge initially, material will be transported away from the corner to reduce the curvature. The curvature will always be greater than the flat surface of the film so material will continue to flow over the rim towards the main film. This builds into a larger rim, so the curvature lessens and flow slows. In some cases, a valley forms behind the rim, and can 'pinch-off' to form a separate island.[74] The retraction of an edge is shown schematically in Figure 2.24. In addition to 'pinch-off', a growing hole can form 'fingering instabilities', where its edge reaches an unstable shape and breaks up into 'fingers'.[77] This can be related to grain boundaries.

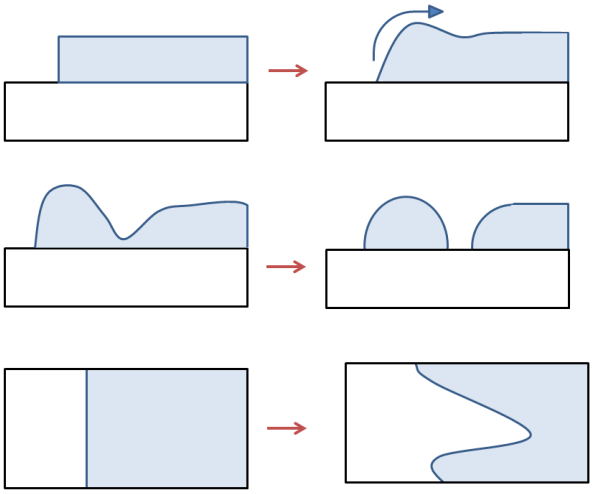

Figure 2.24: Dewetting processes in solid films. Top: Edge retraction of a straight-sided pore to form a rim. Surface diffusion driven by curvature is shown by the arrow. Middle: Pinch-off due to deepening of the valley behind the rim. Bottom: Fingering instability (viewed from top) due to a perturbation in the retracting edge of the film.

In both pinch-off and fingering cases, the strands formed will be subject to the so-called Rayleigh-Plateau instability, and tend to break up into islands.[78]

The overall dewetting rate can now thus be considered. The previous discussions indicate that a series of kinetic processes govern the overall dewetting rate. Firstly, a pre-existing number of holes can grow, or there is a timescale over which new holes form, via for example, grooving. New holes can form throughout the process. The edges of formed holes retract to form dewet areas. When holes impinge, much of the original film may be uncovered, but the dewetting processes continue via strands breaking up into islands.

In a simple case, the dependence of exposed area upon dewetting time, can be given by:

$$\boldsymbol{A_{dewet} = 1 - \exp(-\int_{\tau}^{t} 2\pi \dot{r}^2_{dewet} \dot{N}(t - t')dt')} \qquad \textbf{2.17}$$

where $\dot{N}$ is the rate of formation of new holes, $\dot{r}_{dewet}$ is a constant hole growth rate, and τ is the time that the first holes appear. This results in curves of the shape shown in Figure 2.25.[68] It can be established that experimentally, $\dot{r}_{dewet} \propto D/h^3$, where D is the surface diffusivity, and the other most critical parameters contributing to the rate of dewetting are the activation energy for surface diffusion and the temperature.[77]

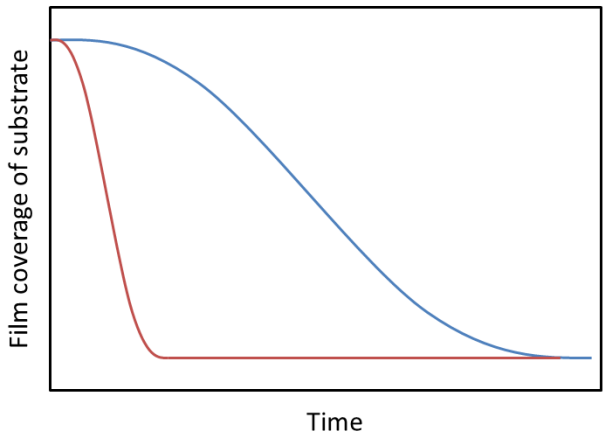

Figure 2.25: Diagrammatic plot of film coverage as a function of time due to dewetting, for two temperatures (red is higher temperature than blue).

Single crystal films are also subject to dewetting, especially when they are very thin. There are some differences compared to polycrystalline or amorphous films, though the overall picture is similar. The main difference is that they do not have grain boundaries that can initiate pinhole formation. Another mechanism is thus required to explain observed initial dewetting; no clear dominant mechanism is obvious. The main ways in which pinholes could be initiated are: pinholes in the initial film, topographical irregularities on the substrate surface (especially important when the film is thin), impurities or particles on the substrate or film surface, or crystal defects such as dislocations.

The crystallography will also affect the shape of opening pores, which will tend to be more regular in shape, with straight edges along crystallographic planes. Rims formed around single crystal holes will be faceted, which will increase in height and width over time in a similar manner to the polycrystalline example, and these will generally grow more slowly at the corners, due to mass diffusion away from a corner being able to happen in more than one direction (whereas it is constrained in one direction at the edges). This results in a modification of the initial faceted shape of the hole. The uneven growth can result in fingering instabilities at the edges near the corners and pinch-off forming strands, normally along crystallographic planes at the edges, which will then bead up due to the Rayleigh-Plateau instability. An example of expected pore growth in a single crystal film is shown in Figure 2.26.

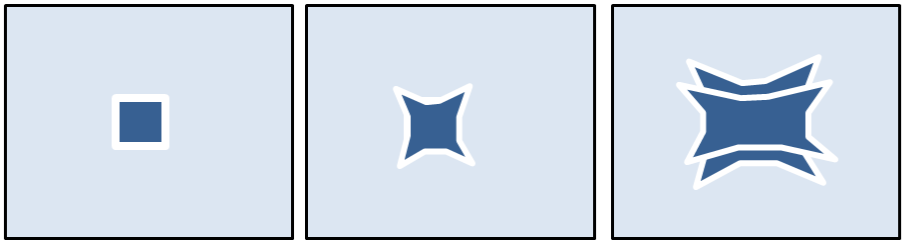

Figure 2.26: Left to right: diagram of the growth of a hole in a single crystal film.

From the above discussion on both liquid and solid state dewetting, it can be concluded that there are a small number of experimental parameters that will have the highest importance on how dewet a film is. These are:

- initial film thickness
- initial pinholes in the film
- temperature
- time

Finally, some additional complications that can be present in real dewetting films are mentioned. These will be elaborated upon in Chapter 4.

All the mechanisms discussed above have assumed that material is retained during dewetting, i.e. there is no material evaporation. This would significantly complicate the situation – as well as material movement by surface diffusion, in a solid, it could also evaporate, so the same rim formation may not arise. In a liquid, where flow is facile, it will result in uniform reduction in size of the film thickness and island size as dewetting occurs, complicating any dynamical models.

Secondly, a change in phase from liquid to solid or vice versa will complicate the situation. One would have to treat each phase separately and couple them together in the middle, so any final holes in a solid film at the point when the transition occurs would be the initial pores in a liquid form, for example.

2.8 Electrochromism

Electrochromism is the phenomenon of some materials to reversibly change colour upon application of a bias, normally in the presence of an additional species. Electrochromics are of interest for their application in 'smart' windows, able to control the throughput of solar radiation into buildings, and thus controlling human comfort as well as allowing greater heating / cooling energy efficiency. Such technologies are already becoming commercially deployed and offer the potential for a significant drop in energy wasted in the population's homes and workplaces. It is estimated that as much as 30-40% of all primary energy is spent in buildings, for purposes of heating, cooling, lighting and ventilation.[79] Intelligent control of irradiance though windows would allow needs to be met in a much more efficient manner.

There are several types of electrochromic materials, the most common and most studied being the oxides. Specifically, tungsten oxide, WO_3, has received most research effort and is of relevance for this thesis, so will be described here.

It was observed experimentally in the 1950s and 1960s that upon insertion of protons, or lithium ions, into WO_3, the colour changed.[79] This could be achieved by placing the oxide into contact with an electrolyte containing these species, and applying a bias. The reason for the colour change has been widely debated, but it is now thought that it is related to a change in electronic band structure upon Li^+/H^+ intercalation into the lattice. The insertion of Lithium ions, driven by the applied bias, is accompanied by a balancing insertion of electrons:

$$\boldsymbol{WO_3 + Li^+ + e^- \overset{bias}{\longleftrightarrow} Li_xWO_3} \qquad \textbf{2.18}$$

Where practically, for reversibility, $x < 0.5$. In terms of the band structure, the crystal structure has a wide bandgap between the highest filled band and the next band, rendering it transparent. Inserting and extracting charge leads to a change in the Fermi level, giving partial filling of the next band, allowing absorption at low photon energies, as depicted in .

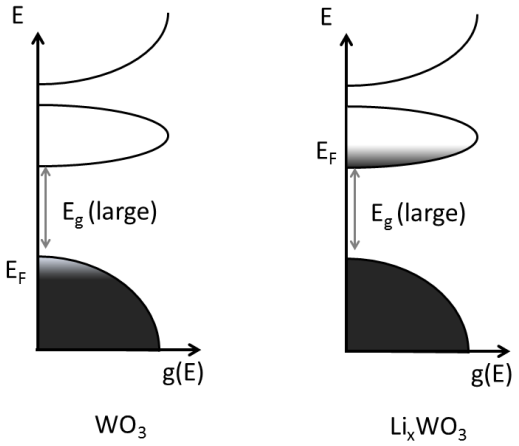

Figure 2.27: Diagram of density of states for WO_3 with and without lithium intercalation. Black represents filled states.

The inserted electrons are localised on W sites, changing some from W^{6+} to W^{5+}. Photon absorption can then take place via so-called polaron absorption:

$$W_a^{5+} + W_b^{6+} + photon \rightarrow W_a^{6+} + W_b^{5+} \qquad 2.19$$

Where a and b denote different W atoms; an electron is transferred between sites.

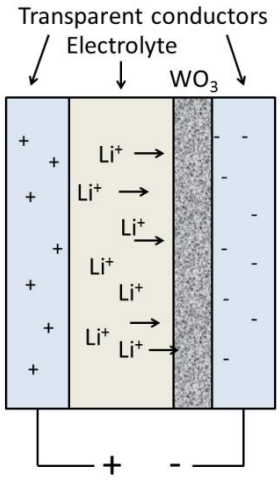

Figure 2.28: Diagram of WO_3 / Li^+ based electrochromic device.

In terms of device design, a typical electrochromic device architecture is shown in Figure 2.28. The electrochromic film, contacted by an ion-conducting electrolyte (which should also be able to store ions), is sandwiched between two transparent conductors; on application of bias, Li ions are inserted from the electrolyte into the electrochromic, and charge balance is maintained by a counter-flow of electrons in the external circuit, injecting also into the electrochromic. Reversing the voltage returns the device to its original state.

2.9 References

1. J. Nelson, *The Physics of Solar Cells*, Imperial College Press, 2004.

2. NREL, *Ref. Sol. Spectr. Irradiance Air Mass 1.5*.

3. B. O'Regan and M. Grätzel, *Nature*, 1991.

4. U. Bach, D. Lupo, P. Comte, J. E. Moser, F. Weissörtel, J. Salbeck, H. Spreitzer and M. Grätzel, *Nature*, 1998, **395**, 583–585.

5. D. B. Mitzi, *Progress in Inorganic Chemistry, vol. 48*, 1999.

6. a.S. Verma, V. K. K. Jindal, a. S. Verma and V. K. K. Jindal, *J. Alloys Compd.*, 2009, **485**, 514–518.

7. D. B. Mitzi, S. Wang, C. A. Feild, C. A. Chess and A. M. Guloy, *Science*, 1995, **267**, 1473–1476.

8. J. H. Noh, S. H. Im, J. H. Heo, T. N. Mandal and S. Il Seok, *Nano Lett.*, 2013, **13**, 1764–1769.

9. W. E. I. Sha, X. Ren, L. Chen and W. C. H. Choy, *Appl. Phys. Lett.*, 2015, **106**, 221104.

10. N. K. Noel, S. D. Stranks, A. Abate, C. Wehrenfennig, S. Guarnera, A. Haghighirad, A. Sadhanala, G. E. Eperon, S. K. Pathak, M. B. Johnston, A. Petrozza, L. Herz and H. Snaith, *Energy Environ. Sci.*, 2014, **7**, 3061–3068.

11. F. Hao, C. C. Stoumpos, D. H. Cao, R. P. H. Chang and M. G. Kanatzidis, *Nat. Photonics*, 2014, **8**, 489–494.

12. F. Deschler, M. Price, S. Pathak, L. Klintberg, D. D. Jarausch, R. Higler, S. Huettner, T. Leijtens, S. D. Stranks, H. J. Snaith, M. Atature, R. T. Phillips and R. H. Friend, *J. Phys. Chem. Lett.*, 2014, **5**, 1421–1426.

13. T. Leijtens, S. D. Stranks, G. E. Eperon, R. Lindblad, E. M. J. Johansson, I. J. McPherson, H. Rensmo, J. M. Ball, M. M. Lee and H. J. Snaith, *ACS Nano*, 2014, **8**, 7147–7155.

14. S. D. Stranks, G. E. Eperon, G. Grancini, C. Menelaou, M. J. P. Alcocer, T. Leijtens, L. M. Herz, A. Petrozza and H. J. Snaith, 2013, **342**, 341–344.

15. C. Wehrenfennig, G. E. Eperon, M. B. Johnston, H. J. Snaith and L. M. Herz, *Adv. Mater.*, 2014, **26**, 1584–1589.

16. Z.-K. Tan, R. S. Moghaddam, M. L. Lai, P. Docampo, R. Higler, F. Deschler, M. Price, A. Sadhanala, L. M. Pazos, D. Credgington, F. Hanusch, T. Bein, H. J. Snaith and R. H. Friend, *Nat. Nanotechnol.*, 2014, **9**, 1–6.

17. M. F. Aygüler, M. D. Weber, B. M. D. Puscher, D. D. Medina, P. Docampo and R. D. Costa, *J. Phys. Chem. C*, 2015, **119**, 12047–12054.

18. O. A. Jaramillo-Quintero, R. S. Sánchez, M. Rincón and I. Mora-Sero, *J. Phys. Chem. Lett.*, 2015, **6**, 1883–1890.

19. H. Zhu, Y. Fu, F. Meng, X. Wu, Z. Gong, Q. Ding, M. V. Gustafsson, M. T. Trinh, S. Jin and X.-Y. Zhu, *Nat. Mater.*, 2015, 636–642.

20. R. Dhanker, a. N. Brigeman, a. V. Larsen, R. J. Stewart, J. B. Asbury and N. C. Giebink, *Appl. Phys. Lett.*, 2014, **105**, 151112.

21. B. R. Sutherland, S. Hoogland, M. M. Adachi, C. T. O. Wong and E. H. Sargent, *ACS Nano*, 2014, **8**, 10947–10952.

22. X. Y. Chin, D. Cortecchia, J. Yin, A. Bruno and C. Soci, *Arxiv Prepr.*, 2015.

23. Y. Mei, O. D. Jurchescu, C. Zhang and Z. V. Vardeny, *MRS Commun.*, 2015, 1–5.

24. M. A. Green, A. Ho-Baillie and H. J. Snaith, *Nat. Photonics*, 2014, **8**, 506–514.

25. D. B. Mitzi, *J. Chem. Soc. Dalt. Trans.*, 2001, 1–12.

26. K. Chondroudis and D. B. Mitzi, *Chem. Mater.*, 1999, **11**, 3028–3030.

27. D. B. Mitzi, K. Chondroudis and C. R. Kagan, *IBM J. Res. Dev.*, 2001, **45**, 29–45.

28. A. Kojima, K. Teshima, Y. Shirai and T. Miyasaka, *J. Am. Chem. Soc.*, 2009, **131**, 6050–6051.

29. J.-H. Im, C.-R. Lee, J.-W. Lee, S.-W. Park and N.-G. Park, *Nanoscale*, 2011, **3**, 4088–4093.

30. H.-S. Kim, C.-R. Lee, J.-H. Im, K.-B. Lee, T. Moehl, A. Marchioro, S.-J. Moon, R. Humphry-Baker, J.-H. Yum, J. E. Moser, M. Grätzel and N.-G. Park, *Sci. Rep.*, 2012, **2**, 591.

31. M. M. Lee, J. Teuscher, T. Miyasaka, T. N. Murakami and H. J. Snaith, *Science*, 2012, **338**, 643–647.

32. L. Etgar, P. Gao, Z. Xue, Q. Peng, A. K. Chandiran, B. Liu, M. K. Nazeeruddin and M. Grätzel, *J. Am. Chem. Soc.*, 2012, **134**, 17396–17399.

33. H. Oga, A. Saeki, Y. Ogomi, S. Hayase and S. Seki, *J. Am. Chem. Soc.*, 2014, **136**, 13818–13825.

34. C. S. Ponseca, T. J. Savenije, M. a. Abdellah, K. Zheng, A. P. Yartsev, T. Pascher, T. Harlang, P. Chabera, T. Pullerits, A. Stepanov, J.-P. P. Wolf, V. Sundström and V. Sundstrom, *J. Am. Chem. Soc.*, 2014, **136**, 5189–5192.

35. S. D. Stranks, G. E. Eperon, G. Grancini, C. Menelaou, M. J. P. Alcocer, T. Leijtens, L. M. Herz, A. Petrozza and H. J. Snaith, *Science*, 2013, **342**, 341–344.

36. G. Xing, N. Mathews, S. Sun, S. S. Lim, Y. M. Lam, M. Grätzel, S. Mhaisalkar and T. C. Sum, *Science*, 2013, **342**, 344–347.

37. V. D'Innocenzo, G. Grancini, M. J. P. Alcocer, A. R. S. Kandada, S. D. Stranks, M. M. Lee, G. Lanzani, H. J. Snaith and A. Petrozza, *Nat. Commun.*, 2014, **5**, 3586.

38. C. Sheng, C. Zhang, Y. Zhai, K. Mielczarek, W. Wang, W. Ma, A. Zakhidov and Z. V. Vardeny, *Phys. Rev. Lett.*, 2015, **114**, 116601.

39. A. Miyata, A. Mitioglu, P. Plochocka, O. Portugall, J. T.-W. Wang, S. D. Stranks, H. J. Snaith and R. J. Nicholas, *Nat. Phys.,* 2015, **11**, 582–587.

40. T. J. Savenije, C. S. Ponseca, L. T. Kunneman, M. A. Abdellah, K. Zheng, Y. Tian, Q. Zhu, S. E. Canton, I. G. Scheblykin, T. Pullerits, A. P. Yartsev, V. Sundström and V. Sundstrom, *J. Phys. Chem. Lett.*, 2014, **5**, 2189–2194.

41. G. E. Eperon, V. M. Burlakov, P. Docampo, A. Goriely and H. J. Snaith, *Adv. Funct. Mater.*, 2014, **24**, 151–157.

42. J. M. Ball, M. M. Lee, A. Hey and H. J. Snaith, *Energy Environ. Sci.*, 2013, **6**, 1739–1743.

43. J. Burschka, N. Pellet, S.-J. J. Moon, R. Humphry-Baker, P. Gao, M. K. Nazeeruddin, M. Grätzel and M. Gratzel, *Nature*, 2013, **499**, 316–319.

44. O. Malinkiewicz, A. Yella, Y. H. Lee, G. M. M. Espallargas, M. Graetzel, M. K. Nazeeruddin and H. J. Bolink, *Nat. Photonics*, 2013, **8**, 128–132.

45. M. Liu, M. B. Johnston and H. J. Snaith, *Nature*, 2013, **501**, 395–398.

46. G. E. Eperon, S. D. Stranks, C. Menelaou, M. B. Johnston, L. M. Herz and H. J. Snaith, *Energy Environ. Sci.*, 2014, **7**, 982–988.

47. N. J. Jeon, J. H. Noh, W. S. Yang, Y. C. Kim, S. Ryu, J. Seo and S. Il Seok, *Nature*, 2015, **517**, 476–480.

48. W. S. Yang, J. H. Noh, N. J. Jeon, Y. C. Kim, S. Ryu, J. Seo and S. I. Seok, *Science*, 2015, **348**, 1234–1237.

49. J.-W. Lee, D.-J. Seol, A.-N. Cho and N.-G. Park, *Adv. Mater.*, 2014, **26**, 4991–4998.

50. H. Zhou, Q. Chen, G. Li, S. Luo, T. -b. Song, H.-S. Duan, Z. Hong, J. You, Y. Liu and Y. Yang, *Science*, 2014, **345**, 542–546.

51. T. Shi, W.-J. Yin, F. Hong, K. Zhu and Y. Yan, *Appl. Phys. Lett.*, 2015, **106**, 103902.

52. A. Guerrero, E. J. Juarez-perez, J. Bisquert, I. Mora-sero and G. Garcia-belmonte, *Appl. Phys. Lett.*, 2014, **105**, 133902.

53. A. Pockett, G. E. Eperon, T. Peltola, H. J. Snaith, A. Walker, L. M. Peter and P. J. Cameron, *J. Phys. Chem. C*, 2015, **119**, 3456–3465.

54. S. Colella, E. Mosconi, P. Fedeli, A. Listorti, F. Orlandi, P. Ferro, T. Besagni, A. Rizzo, G. Calestani, G. Gigli, F. De Angelis, R. Mosca and F. Gazza, *Chem. Mater.*, 2013, **25**, 4613.

55. G. Grancini, S. Marras, M. Prato, C. Giannini, C. Quarti, F. De Angelis, M. De Bastiani, G. E. Eperon, H. J. Snaith, L. Manna and A. Petrozza, *J. Phys. Chem. Lett.*, 2014, **5**, 3836–3842.

56. E. L. Unger, A. R. Bowring, C. J. Tassone, V. Pool, A. Gold-Parker, R. Cheacharoen, K. H. Stone, E. T. Hoke, M. F. Toney and M. D. McGehee, *Chem. Mater.*, 2014, **26**, 7158–7165.

57. H. J. Snaith, A. Abate, J. M. Ball, G. E. Eperon, T. Leijtens, N. K. Noel, S. D. Stranks, J. T. Wang, K. Wojciechowski and W. Zhang, *J. Phys. Chem. Lett.*, 2014, **5**, 1511–1515.

58. E. L. Unger, E. T. Hoke, C. D. Bailie, W. H. Nguyen, A. R. Bowring, T. Heumuller, M. G. Christoforo and M. D. McGehee, *Energy Environ. Sci.*, 2014, **7**, 3690–3698.

59. W. Tress, N. Marinova, T. Moehl, S. M. Zakeeruddin, M. K. Nazeeruddin and M. Grätzel, *Energy Environ. Sci.*, 2015, **8**, 995–1004.

60. N. J. Jeon, J. H. Noh, Y. C. Kim, W. S. Yang, S. Ryu and S. Il Seok, *Nat. Mater.*, 2014, **13**, 1–7.

61. Z. Xiao, Y. Yuan, Y. Shao, Q. Wang, Q. Dong, C. Bi, P. Sharma, A. Gruverman and J. Huang, *Nat. Mater.*, 2015, **14**, 193–198.

62. Y. Zhang, M. Liu, G. E. Eperon, T. C. Leijtens, D. McMeekin, M. Saliba, W. Zhang, M. de Bastiani, A. Petrozza, L. M. Herz, M. B. Johnston, H. Lin and H. J. Snaith, *Mater. Horiz.*, 2015, **2**, 315–322.

63. Y. Zhao, C. Liang, H. min Zhang, D. Li, D. Tian, G. Li, X. Jing, W. Zhang, W. Xiao, Q. Liu, F. Zhang and Z. He, *Energy Environ. Sci.*, 2015, **8**, 1256–1260.

64. H. min Zhang, C. Liang, Y. Zhao, M. Sun, H. Liu, J. Liang, D. Li, F. Zhang and Z. He, *Phys. Chem. Chem. Phys.*, 2015, **17**, 9613–9618.

65. O. D. Miller, E. Yablonovitch and S. R. Kurtz, *IEEE J. Photovoltaics*, 2012, **2**, 303–311.

66. U. Rau, *Phys. Rev. B - Condens. Matter Mater. Phys.*, 2007, **76**, 1–8.

67. R. T. Ross, *J. Chem. Phys.*, 1967, **46**, 4590.

68. C. V Thompson, *Annu. Rev. Mater. Res.*, 2012, **42**, 399–434.

69. R. Blossey, *Thin Liquid Films: Dewetting and Polymer Flow*, Springer, 2012.

70. D. Bonn, J. Eggers, J. Indekeu and J. Meunier, *Rev. Mod. Phys.*, 2009, **81**, 739–805.

71. R. Seemann, S. Herminghaus and K. Jacobs, *Phys. Rev. Lett.*, 2001, **86**, 5534–5537.

72. R. Xie, A. Karim, J. F. Douglas, C. C. Han and R. A. Weiss, 1998, 1251–1254.

73. W. . Winterbottom, *Acta Metall.*, 1967, **15**, 303–310.

74. D. J. Srolovitz and S. A. Safran, *J. Appl. Phys.*, 1986, **60**, 255.

75. D. J. Srolovitz and S. A. Safran, *J. Appl. Phys.*, 1986, **60**, 247.

76. W. W. Mullins, *J. Appl. Phys.*, 1957, **28**, 333.

77. E. Jiran and C. V. Thompson, *Thin Solid Films*, 1992, **208**, 23–28.

78. F. a. Nichols and W. W. Mullins, *J. Appl. Phys.*, 1965, **36**, 1826.

79. C. G. Granqvist, *Thin Solid Films*, 2014, **564**, 1–38.

3. METHODS

Here the generally applicable methods and fabrication procedures used in this thesis are outlined. More specialised procedures are described in the individual chapters of relevance.

Unless otherwise stated, all chemicals were purchased from Sigma-Aldrich or Alfa Aesar and used as received. All solvents used were anhydrous.

3.1 Perovskite preparation

3.1.1 Chloride-assisted methylammonium lead halide perovskite ($MAPbI_{3-x}Cl_x$)

Methylamine iodide was prepared by reacting methylamine, 33 wt% in ethanol, with hydroiodic acid (HI) 57 wt% in water, at room temperature. HI was added dropwise while stirring. Upon drying at 100°C, a white powder was formed, which was dried overnight in a vacuum oven before use.

To form the non-stoichiometric $MAPbI_{3-x}Cl_x$ precursor solution, methylammonium iodide and lead (II) chloride are dissolved in anhydrous *N*,*N*-dimethylformamide (DMF) at a 3:1 molar ratio of MAI to $PbCl_2$, with final concentrations 0.88M lead chloride and 2.64M methylammonium iodide. This solution is stored under a dry nitrogen atmosphere.

To form a film of this perovskite, this precursor was spin-coated on an oxygen plasma-cleaned substrate in a nitrogen-filled glovebox at 2000rpm for 45 seconds, then allowed to dry at room temperature for 20-30 minutes. It was then annealed on a hotplate in the glovebox at 90°C for 150 minutes then at 120°C for 20 minutes.

3.1.2 Methylammonium lead iodide perovksite (1:1 $MAPbI_3$)

1:1 $MAPbI_3$ precursor was prepared by dissolving equimolar amounts of methylammonium iodide and PbI_2 in DMF at 0.5M, in a nitrogen-filled glovebox.

To form a film of this perovskite, this precursor was spin-coated in a nitrogen-filled glovebox at 2000rpm and annealed at 100°C for 5 minutes.

3.1.3 Formamidinium lead halide perovskite ($H_2NCH_2NH_2PbI_{3y}Br_{3(1-y)}$)

Formamidinium iodide (FAI) and formamidinium bromide (FABr) were synthesised by dissolving formamidinium acetate powder in a 1.5x molar excess of 57%w/w hydroiodic acid (for FAI) or 48%w/w hydrobromic acid (for FABr). After addition of acid, the solution was left stirring for 10 minutes at 50°C. Upon drying at 100°C, a yellow-white powder is formed. This was then washed with diethyl ether and recrystallized twice with ethanol, to form white needle-like crystals. Before use, it was dried overnight in a vacuum oven.

To form $FAPbI_3$ and $FAPbBr_3$ precursor solutions, FAI and PbI_2 or FABr and $PbBr_2$ were dissolved in anhydrous N,N-dimethylformamide in a 1:1 molar ratio, at 0.88M of each reagent, to give a 0.88M perovskite precursor solution.

To form a film of this perovskite, the precursors were diluted down to 0.55M in DMF. For uniform and continuous film formation, just before spin-coating, 38µl of hydroiodic acid (57%w/w) was added to 1ml of the 0.55M $FAPbI_3$ precursor solution and 32µl of hydrobromic acid (48%w/w) to the 0.55M $FAPbBr_3$ solution. To form $FAPbI_{3y}Br_{3(1-y)}$ perovskite precursors, mixtures were made of the $FAPbI_3$ and $FAPbBr_3$ solutions in the required ratios. The precursor with added acid was spin-coated in a nitrogen-filled glovebox at 2000rpm for 45 seconds, on a substrate heated to 85°C. The films were then annealed in air at 170°C for 10 minutes. This gave a very uniform layer ~400nm thick of $FAPbI_{3y}Br_{3(1-y)}$.

3.1.4 Caesium lead halide perovskite ($CsPbI_3$)

To form the $CsPbI_3$ precursor solution, CsI and PbI_2 were dissolved in anhydrous N,N-dimethylformamide in a 1:1 molar ratio, at 0.48M of each reagent. For the low-temperature processing route described in Chapter 9, immediately prior to spin-coating, 33µl of hydroiodic acid (57%w/w) was added to 1ml of the 0.48M precursor solution to enable a low-temperature phase transition.

To form films, the precursor was then spin-coated in a nitrogen-filled glovebox at 2000rpm for 45s, and annealed at 100°C for 10 minutes. For the high-temperature route, no hydroiodic acid was added and films were annealed at 335°C for 5 minutes.

3.1.5 Semi-transparent perovskite films

Semi-transparent $MAPbI_3$ perovskite layers were deposited by spin-coating a non-stoichiometric precursor solution of methylammonium iodide and lead chloride (3:1 molar ratio, final concentrations 0.88M lead chloride, 2.64M MAI) in anhydrous dimethylsulfoxide (DMSO). Spin-coating was carried out at 2000rpm in a nitrogen-filled glovebox. The films were then annealed at 130°C for 20 minutes in the glovebox.

Semi-transparent $FAPbI_3$ perovskite layers were deposited by spin-coating a non-stoichiometric precursor solution of formamidinium iodide, methylammonium iodide and lead chloride (1:2:1 molar ratio, final concentrations 0.88M lead chloride, 1.76M MAI and 0.88M FAI) in anhydrous DMSO. Spin-coating was carried out at 2000rpm in a nitrogen-filled glovebox. The films were then annealed at 130°C for 20 minutes in the glovebox, and then at 170°C for 10 minutes in air.

3.2 Solar cell fabrication

3.2.1 Substrate preparation

Devices were fabricated on fluorine-doped tin oxide (FTO) coated glass (Pilkington, 7Ω $\square^{-1}$) substrates. Initially FTO was removed from regions under the anode contact, to prevent shunting upon contact with measurement pins, by etching the FTO with 2M HCl and zinc powder. Substrates were then cleaned sequentially in 2% hallmanex detergent, acetone, propan-2-ol and oxygen plasma.

3.2.2 Hole-blocking (electron extracting) layer deposition

A ~50nm hole-blocking layer of compact TiO_2 was deposited by spin-coating a mildly acidic solution of titanium isopropoxide in ethanol (350µl in 5ml ethanol with 0.013M HCl), and annealed at 500°C for 30 minutes, ramping from room temperature over 45 minutes. Spin-coating was carried out at 2000rpm for 60 seconds.

3.2.3 Alumina scaffold deposition

For mesosuperstructured perovskite devices, an alumina mesoporous scaffold was then deposited by spin-coating (at 2500 rpm for 60s) a colloidal dispersion of 20nm Al2O3 nanoparticles in isopropanol, at a dilution of 1:2 stock solution to isopropanol, followed by drying at 150°C for 10 minutes.

3.2.4 Hole transporter (electron-blocking) layer deposition

A hole-transporting layer was then deposited in air via spin-coating a 0.0788M solution of 2,2',7,7'-tetrakis-(N,N-di-p-methoxyphenylamine)9,9'-spirobifluorene (Spiro-OMeTAD) (purchased from Borun Chemicals Ltd) in chlorobenzene (96.5mg/ml), with additives of 0.0184M lithium bis(trifluoromethanesulfonyl)imide (Li-TFSI) and 0.0659M 4-tert-butylpyridine. The lithium salt, pre-dissolved at 170mg/ml in 1-butanol, is added as a catalyst for p-doping. Upon exposure to oxygen, Li-TFSI reacts with oxygen and Spiro-OMeTAD to form lithium oxides and Spiro-OMeTAD(TFSI), which is a p-dopant for Spiro-OMeTAD.[1] The role of tert-butylpyridine additive is currently unclear; it assists in film formation but may also play an important role in perovskite film surface passivation.[2]

This solution was spin-coated at 2000rpm for 45 seconds. Devices were then left overnight in air for the Spiro-OMeTAD to dope via oxidation.

3.2.5 Contact deposition

Finally, 50-100nm gold or silver electrodes were thermally evaporated under vacuum of ~10^{-6} Torr, at a rate of ~0.1nm/s, to complete the devices.

3.2.6 Transparent conductive laminate cathode (TLC)

A transparent nickel grid laminate electrode is employed for some of the semi-transparent devices described in Chapter 8. This is described in full detail elsewhere.[3] To fabricate the TLC, a commercially available poly(3,4-ethylenedioxythiophene) polystyrene sulfonate (PEDOT:PSS) blend (EL-P3145 AGFA) and acrylic microemulsion pressure sensitive adhesive (F46 Styccobond) were mixed such that the final volume fraction of the PEDOT:PSS in the dry transparent conductive adhesive film was 0.0175. This corresponded to a 1:1.34 Styccobond:PEDOT:PSS ratio by weight. This mix was then tape cast onto sheets of commercially available flexible nickel microgrid sheets (Epimesh 300 from Epigem) at a thickness of ~90 μm. The films were dried for 15 minutes at 60 ^{o}C followed by 5 minutes at 120 ^{o}C leaving final dried transparent conductive adhesive films of ~30 μm thick. Cells to which the TCC was to be applied had a solution of PEDOT:PSS (Hereaus GSD1330S) mixed with ethanol and isopropanol in a 1:1:1 ratio by volume sprayed onto the HTL surface whilst the cell was held on a 50°C hotplate and left for 10 seconds post spraying. This left a layer of PEDOT:PSS approximately 50nm thick. The TLC fabricated as described above was then laminated onto the PEDOT:PSS surface of the cells using finger pressure.

3.2.7 Inverted perovskite solar cell fabrication

For 'inverted' devices, which refer to those where electrons are extracted from the top electrode, devices are fabricated in the reverse order, with the hole-transporting (electron-blocking) layer before the perovskite and a hole-blocking (electron extracting) layer afterwards. For these devices, indium tin oxide (ITO) (Colorado Concept Coatings LLC, ~20 $\Omega\square^{-1}$) substrates were used. An electron-blocking layer of PEDOT:PSS (Heraeus Al4083) was deposited by spin-coating at 4000rpm in air and annealing in nitrogen at 140^{o}C for 15 minutes. Perovskite precursor was deposited as described above. The electron-extracting layer was deposited by spin-coating a 20mg/ml solution of Phenyl-C61-butyric acid methyl ester (PCBM) in chlorobenzene and annealing at 100^{o}C for 30 mins. Electrodes for the inverted devices were calcium (20nm) followed by aluminium (100nm), thermally evaporated under vacuum of ~10^{-6} Torr, at a rate of 0.03 nm/s and ~0.1nm/s respectively, to complete the devices.

3.3 Solar cell characterisation

3.3.1 Current-voltage characterisation

The current density–voltage (JV) curves were measured under simulated AM 1.5 sunlight at 100 mWcm^{-2} irradiance generated by an Abet Class AAB sun 2000 simulator, with the intensity calibrated with an NREL calibrated KG5 filtered Si reference cell. The light intensity was checked at the start of each measurement by a reference diode. JV curves were recorded with a Keithley 2400 sourcemeter integrated with a computer running a Labview program developed in-house. The mismatch factor, determining the accuracy of the solar spectrum, was calculated to be 0.99%-1.2% between 400 and 1100nm during the course of this thesis.[4] The solar cells were masked with a metal aperture to define the active area, and measured in a light-tight sample holder to minimize any edge effects. Defining the active are a with a mask is a crucial step to avoid unwanted contributions to charge collection from a wider area than the device area.[4]

For fast JV scans, cells were scanned from forwards bias to short-circuit at a rate of 0.38V/s after holding under illumination at 1.4V for 5 seconds. Maximum power point voltage was determined from these fast JV scans and current measured holding at this voltage for the stabilised power output scans.

3.3.2 External Quantum Efficiency - Fourier transform photocurrent spectroscopy

External quantum efficiency was measured via fourier-transform photocurrent spectroscopy, a fast and sensitive spectral characterization method.[5] This was carried out using the modulated beam of a Bruker Vertex 80v Fourier Transform Interferometer with tungsten lamp source and a Stanford Research SR570 current preamplifier. Samples were calibrated to a Newport-calibrated reference silicon solar cell with known external quantum efficiency. The solar cells were masked with a metal aperture to define the active area.

3.4 Optical characterisation

3.4.1 Absorption measurements

Absorption, transmittance and reflectance spectra were collected with a Varian Cary 300 UV-Vis spectrophotometer with an internally coupled integrating sphere.

3.4.2 Tauc plot bandgap estimation

An optical bandgap can be estimated for the perovskite materials by assuming it follows the relation described in Section 2.1. For a direct bandgap material, this is:

$$\boldsymbol{\alpha(E) = A(E - E_g)^{1/2}} \qquad \textbf{3.1}$$

Based on this relation, E_g can be determined from an absorbance coefficient spectrum, by plotting $(\alpha h\nu)^2$ against energy in eV, known as a Tauc plot.[6] The estimated bandgap is determined from the extrapolation of the linear region to the energy-axis intercept. Absorption coefficient α is determined from absorption spectra collected with an integrating sphere. An example absorption spectrum and Tauc plot are shown below.

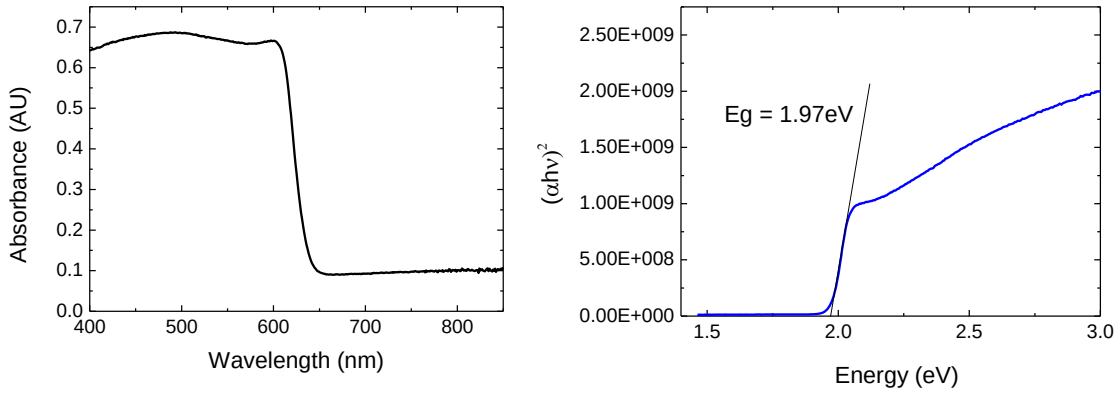

Figure 3.1: Left, absorbance spectrum of a $FAPbI_yBr_{3(1-y)}$ perovskite (where y=0.3). Right, Tauc plot assuming direct bandgap, showing determination of estimated bandgap from intercept.

3.4.3 Active layer transmittance measurements

In particular for the semi-transparent perovskite devices described in Chapters 5 and 8, it is necessary to accurately calculate the transmittance of a perovskite film. This becomes non-trivial when considering a perovskite film that is formed upon an FTO-coated glass substrate, for example, and being interested in calculating the transmittance of only the photovoltaic region, or the 'active layer'.

To calculate the active layer transmittance, the exact definition is first described. Because it is the properties of *only* the active layer that are of interest, the active layer transmittance is defined as being the percentage light intensity which is not absorbed in a single pass through it. Hence, interfacial reflections and absorbance in other layers of the cell are excluded.

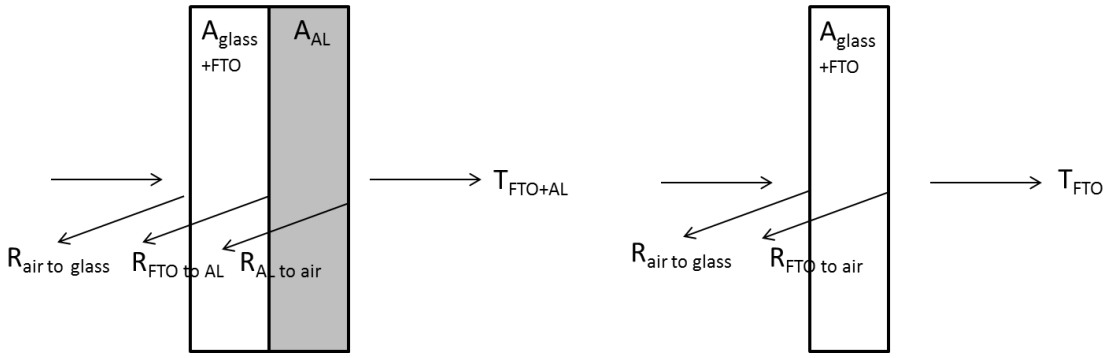

Figure 3.2: Diagrams showing transmittances and reflectances involved in measuring the active layer transmittance. Left: optical processes in a sample on FTO-coated glass, right: for FTO-coated glass only. FTO would comprise a thin layer on the right side of the glass. It is noted that the arrows represent total transmittance/reflectance, including scattered transmission, as there measurements were taken with an integrating sphere.

The transmittance of active layers formed on FTO-coated glass, and the transmittance of FTO-coated glass only, was measured using an integrating sphere. Any optical effects between glass and FTO were ignored. As seen in Figure 3.2, the reflections from these films will be different. The dominant reflection, at the air-glass interface, will be the same. However, the semi-transparent perovskite cell has a second reflection at the FTO-active layer interface, and a third reflection at the perovskite-air interface. The FTO-coated glass sample has a second reflection at the FTO-air interface. One can calculate the effect the reflections have on the transmittances measured:

$$T_{FTO} = (1-R_{air\ to\ glass})(1-A_{glass+FTO})(1-R_{FTO\ to\ air}) \quad \textbf{3.2}$$

$$T_{FTO+AL} = (1-R_{air\ to\ glass})(1-A_{glass+FTO})(1-R_{FTO\ to\ AL})(1-A_{AL})(1-R_{AL\ to\ air}) \quad \textbf{3.3}$$

Where *T, R*, and *A* are the fractional transmittance, reflectance and absorption within a layer or at an interface. "AL" is the abbreviation used for the active layer.

The active layer transmittance has been defined as $(1-A_{AL})$, so rearranging for this term, several components can be cancelled:

$$1-A_{AL} = \frac{T_{FTO+AL}(1-R_{FTO\ to\ air})}{T_{FTO}(1-R_{FTO\ to\ AL})(1-R_{AL\ to\ air})} \quad \textbf{3.4}$$

So if the reflections from FTO to air, FTO to the active layer, and the active layer to air can be quantified, the active layer transmittance can be found from the measured transmittances.

In order to measure these, the assumption is made that the angle of incidence is small, and that interference effects and more than two multiple reflections can be ignored. Then, from the Fresnel equations, the reflectance is the same from both sides of an interface (i.e. $R_{AL\ to\ air} \sim R_{air\ to\ AL}$). The necessary reflectances can then be determined as shown below.

The reflectance from the active layer side of a sample is given by:

$$R_{AL+FTO} = R_{air\ to\ AL} + (1 - R_{air\ to\ AL})(1-A_{AL})^2 R_{AL\ to\ FTO} + \ldots \textit{(smaller terms)} \qquad 3.5$$

If the assumption is made that the second term is small compared to the first term (it is attenuated twice by the active layer absorption, and the reflectance from the active layer to FTO is likely <20% based on expected indices of refraction), then $R_{air\ to\ AL}$ can be obtained.

The reflectance from the glass side of the same sample is given by:

$$R_{FTO+AL} = R_{air\ to\ glass} + (1 - R_{air\ to\ glass})(1-A_{FTO+glass})^2 R_{FTO\ to\ AL} + \ldots \textit{(smaller terms)} \qquad 3.6$$

$R_{air\ to\ glass}$ can be measured, and $A_{FTO+glass}$ can be measured (using $A = 1 - T - R$). Thus, $R_{FTO\ to\ AL}$ can be determined. Finally, $R_{FTO\ to\ air}$ is needed, which can be measured via $R_{air\ to\ FTO}$.

The requisite reflectances were measured for a range of samples, mounted on an 8° wedge at the exit port of an integrating sphere. Figure 3.3 shows the magnitudes of the reflectances measured/calculated for a typical semi-transparent film.

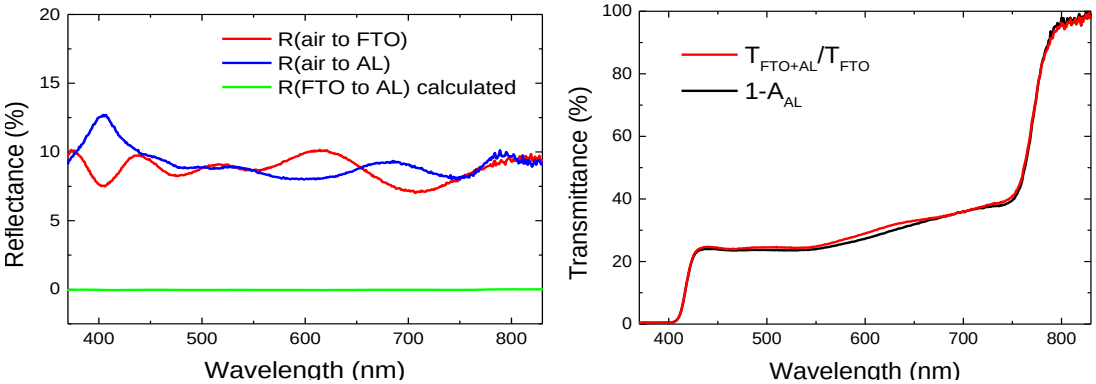

Figure 3.3: Left, Reflectance spectra of the relevant reflections for determining active layer transmittance. Right, Transmittance spectra showing the impact of factoring in reflective differences between FTO and FTO+sample to the calculated active layer transmittance.

It is observed that the FTO to active layer reflectance is negligibly small. This occurs due to the fact that the reflectances R_{FTO+AL} and $R_{air\ to\ glass}$ measured are similar, and $(1-A_{FTO+glass})$ is almost 1, so a small number is divided by a significantly larger number.

Because this is the case, only the reflectances from FTO and the active layer to air make a significant impact on the transmittance calculation. However, these reflectances are also quite similar. Figure 3.3 shows the two curves, $\frac{T_{FTO+AL}}{T_{FTO}}$ and $\frac{T_{FTO+AL}(1-R_{FTO\ to\ air})}{T_{FTO}(1-R_{FTO\ to\ AL})(1-R_{AL\ to\ air})}$.

It can be observed that factoring the differing reflections into the calculation has only a small effect on the calculation of the active layer transmittance. This is due to the fact that reflectances from the active layer and FTO to air are similar, and the FTO to active layer reflectance negligible. Calculating the average visible transmittance from these plots gives 38.19% for the full calculation and 39.18% for $\frac{T_{FTO+AL}}{T_{FTO}}$.

Due to the fact that this difference is small, and within the margins of error introduced by differences between different regions of the same sample, the more simple calculation below can be used with the introduction of only small errors.

$$\boldsymbol{1\text{-}A_{AL} \sim \frac{T_{FTO+AL}}{T_{FTO}}} \qquad \textbf{3.7}$$

This definition is used for the calculations of active layer transmittance in the following chapters.

3.4.4 Photoluminescence measurements

Steady-state photoluminescence measurements were carried out using a Horiba Scientific Fluorolog spectrofluorometer, with a monochromated xenon light source.

3.4.5 Photoluminescence quantum yield measurements

Steady-state photoluminescence quantum efficiency (PLQE) values were determined using a 532 nm CW laser excitation source (Suwtech LDC-800) to illuminate a sample in an integrating sphere (Oriel Instruments 70682NS) and the laser scatter and PL collected using a fiber-coupled detector (Ocean Optics MayaPro). The spectral response of the fiber-coupled detector setup was calibrated using a spectral irradiance standard (Oriel Instruments 63358). PLQE calculations were carried out using established techniques.[7] Unless otherwise stated, the excitation intensity was 180mWcm^{-2}.

3.4.6 Time-resolved photoluminescence

Time-resolved PL measurements were acquired using a time-correlated single photon counting (TCSPC) setup (FluoTime 300, PicoQuant GmbH). Film samples were

photoexcited using a 507nm laser head (LDH-P-C-510, PicoQuant GmbH) pulsed at frequencies between 0.3-10MHz, with a pulse duration of 117ps and fluence of ~3μJ/cm^2 - 30nJ/cm^2. The PL was collected using a high resolution monochromator and hybrid photomultiplier detector assembly (PMA Hybrid 40, PicoQuant GmbH).

3.4.7 Diffusion length calculation

Diffusion length in a bulk material can be estimated by a reasonably simple quenching method.[8,9] Three films are measured: a neat film (on glass), a film with a hole quencher spin-coated on top, and a film with an electron quencher spin-coated on top. Upon photoexcitation, photoexcited carriers will diffuse through the material. In the quenched films, when an electron/hole diffuses into the quenching layer, it is rapidly transferred to that material and can no longer contribute to photoluminescence. By comparing the photoluminescence decay rates, indicative of how many carriers are radiatively decaying *within* the material (not the quencher) at a given time after an excitation pulse, and fitting the rates to a diffusion equation, it is possible to estimate the diffusivity and hence diffusion length of each carrier separately in the material.

In this thesis, quenching layers of Spiro-OMeTAD (for holes) at 50mg/ml and PCBM (for electrons) at 30mg/ml in chlorobenzene were spin-coated on top of samples at 2000rpm and 1000rpm respectively.

The diffusion modelling was carried out by Christopher Menelaou of the University of Oxford and is summarised below. For more details, see reference [8].

The PL decay dynamics were modeled by calculating the number and distribution of excitations in the film *n(x,t)* according to the 1-D diffusion equation,

$$\frac{\partial n(x,t)}{\partial t} = D\frac{\partial^2 n(x,t)}{\partial x^2} - k(t)n(x,t) \qquad \textbf{3.8}$$

where D is the diffusion coefficient and $k(t)$ is the PL decay rate in the absence of any quencher material.[9] The total decay rate, $k = 1/k_f + 1/k_{nr} = \beta\tau^{-\beta}t^{\beta-1}$, (where k_f and k_{nr} are fluorescent and non-radiative rates respectively) was determined by fitting a stretched exponential decay to TCSPC data measured from perovskite layers with PMMA and assumed independent of the capping material. The effect of the quenching layer was included by assuming that all carriers which reach the interface are quenched with unit efficiency ($n(L,t)=0$, where $x=0$ at the glass/perovskite interface and L is the perovskite film thickness). As the excitation pulse was from the glass substrate side of the samples, the initial distribution of excitons was taken to be $n(x,0)=n_0exp(-\alpha x)$, where $\alpha=A/L$ (absorbance at 507 nm / perovskite layer thickness). Any deviation from this distribution

due to reflection of the laser pulse at the perovskite/quencher interface was assumed to be negligible. In order to calculate the diffusion length L_D, the diffusion coefficient was varied to minimize the reduced chi-squared value,

$$\chi_r^2 = \frac{1}{(n-p-1)} \sum \frac{(y(t)-y_c(t))^2}{y(t)} \quad \textbf{3.9}$$

where $y(t)$ and $y_c(t)$ are the measured and calculated PL intensities at time t, n is the number of data points and p is the number of fitting parameters.[10] The equation was solved numerically using the Crank-Nicholson algorithm and the number of carriers integrated across the entire film in order to determine the total PL intensity at time t.

3.4.8 Angle-dependent photocurrent

Angle-dependent photocurrent was measured by carrying out JV sweeps with a Keithley 2636 SourceMeter upon illumination of the device with a 532nm CW laser, spot size 0.1cm^2, with the beam appropriately attenuated to produce similar currents as when the devices were under AM1.5 solar simulated illumination. Extra-large gold electrodes were evaporated onto devices fabricated as described previously. The spot was kept within the bounds of the device region at all times, and the device was rotated on a calibrated stage, taking measurements every 5^o.

3.4.9 CIE colour perception calculation

Colour perception was quantified using the CIE (International Commission on Illumination) 1931 xy colour space, designed to represent human colour perception.[11] The CIE colour space represents a colour by three parameters: x, y, and Y, where x and y provide the colour co-ordinates specifying a hue, or chromaticity, and Y specifies the luminance of that colour. Chromaticity values can be plotted on a colour space diagram as a visual representation of the hue.

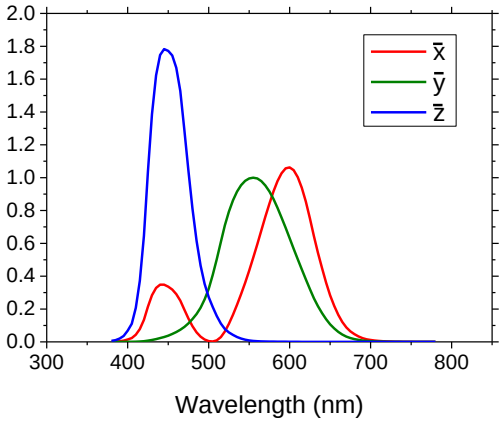

Figure 3.4: CIE colour matching functions. Y axis has no units.

The x and y colour coordinates are obtained from the tristimulus values, which represent the response of the cone cells in a human eye to particular wavelengths. The tristimulus values are obtained by integrating the product of the spectrum of the coloured light in question ($I(\lambda)$) with the CIE colour matching functions ($\bar{x}, \bar{y}, \bar{z}$) shown in Figure 3.4, between 380 and 780nm, being the approximate wavelength range of the human eye. The colour matching functions represent the response of the different types of cone cells in the eye to different wavelengths. The tristimulus values are given by:

$$\boldsymbol{X} = \int_{380}^{780} \boldsymbol{I(\lambda)\bar{x}(\lambda)d\lambda} \qquad \textbf{3.10}$$

$$\boldsymbol{Y} = \int_{380}^{780} \boldsymbol{I(\lambda)\bar{y}(\lambda)d\lambda} \qquad \textbf{3.11}$$

$$\boldsymbol{Z} = \int_{380}^{780} \boldsymbol{I(\lambda)\bar{z}(\lambda)d\lambda} \qquad \textbf{3.12}$$

The x and y colour coordinates are then given by functions of the tristimulus values:

$$\boldsymbol{x} = \frac{\boldsymbol{X}}{\boldsymbol{X+Y+Z}} \qquad \textbf{3.13}$$

$$\boldsymbol{y} = \frac{\boldsymbol{Y}}{\boldsymbol{X+Y+Z}} \qquad \textbf{3.14}$$

and the co-ordinate (x,y) can then be plotted on the chromaticity diagram shown in Figure 3.5 below.

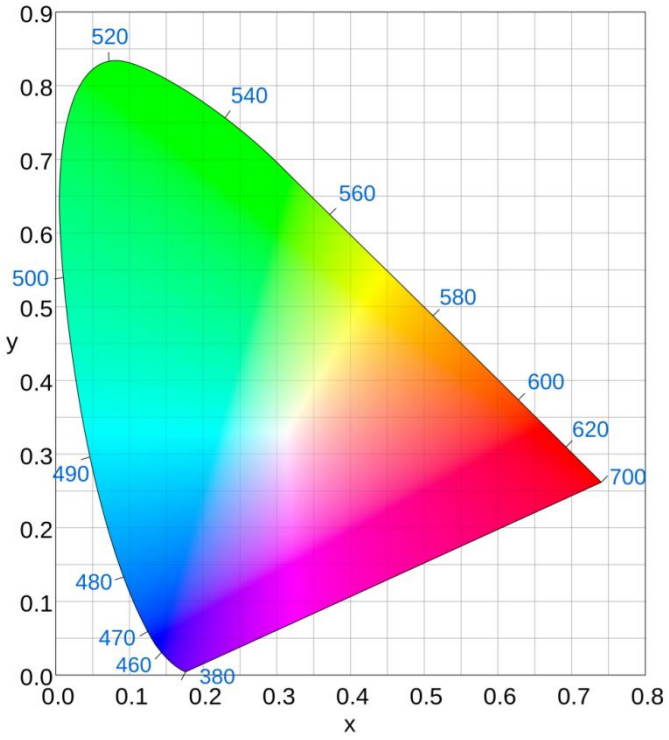

Figure 3.5: CIE 1931 colour space chromaticity plot

To quantify the perceived colour of a semi-transparent solar cell in daylight, the relevant spectrum is the product of the AM1.5 solar spectrum and the transmission spectrum of the active layer in question. This is the $I(\lambda)$ used in the chromaticity calculations above to obtain the colour co-ordinates for a semi-transparent solar cell layer.

The CIE has defined 'standard daylight illuminants' representing daylight illumination, and the commonly used illuminant D65, representing mid-day sun in Europe, has colour co-ordinates of (0.313, 0.329). The AM1.5 spectrum itself has colour co-ordinates of (0.332, 0.343) so is very close to the D65 illuminant.

3.4.10 In-situ absorbance

In-situ absorbance measurements were carried out by Bardo Bruijnaers and Jacobus J. van Franeker of the Technical University of Eindhoven. After spin coating a perovskite film, the sample was left to dry in an enclosed container for 45 minutes. During this time the relative humidity of the glovebox was adjusted by releasing water into the atmosphere. When the correct humidity was reached, the sample was transferred to a hot plate at 90°C and the absorbance measurement was started immediately. The light source for the

absorbance measurement was a halogen light (Philips Brilliantline 14619) incident on the sample at a 60° angle. The light transmitted through the sample is scattered by the white hot plate below the sample. This scattered light is transmitted again through the sample and then collected by a fibre optic cable, connected to a fibre optic spectrometer (Avantes Avaspec-2048_14).

3.4.11 Photoluminescence mapping

Photoluminescence mapping was carried out by Tomas Leijtens of the Italian Institute of Technology in Milan. The photoluminescence maps were recorded using a home built set-up. The modulated pump laser beam (650 nm) was focused onto the sample with sub-micron resolution using a confocal microscope objective. The transmitted light was re-columnated by a similar objective, collected in an optical fibre, and detected using an InGaAs photodiode. The signal was measured with a lock-in amplifier set to the same frequency and phase as the excitation pump. To collect a map, the sample position was varied with a piezo electric stage. The excitation intensity was varied from approximately 10^{20} cm^{-2} to 2 x 10^{21} cm^{-2}.

3.5 Material characterisation

3.5.1 Scanning Electron Microscopy

A Hitachi S-4300 field emission scanning electron microscope was used to acquire SEM images. For cross-sections, devices were scribed with a diamond-tipped pen and snapped cleanly in half, before sputter-coating 5nm of platinum to prevent sample charging during imaging.

3.5.2 Surface coverage analysis

The program ImageJ was used to calculate film surface coverages. Perovskite films typically show as brighter than the substrate, so a threshold brightness was set visually and the regions below and above the threshold quantified by the program, to calculate the percentage of substrate area covered.[12]

3.5.3 X-ray diffraction

X-ray diffraction spectra were obtained using a Panalytical X'Pert Pro x-ray diffractometer, using the copper K-alpha wavelength of 0.154nm. Spectra were obtained from thin films on glass or full devices with the electrodes removed.

3.5.4 Thickness measurement

Sample thicknesses were measured using a Veeco Dektak 150 surface profileometer.

3.6 References

1. A. Abate, T. Leijtens, S. Pathak, J. Teuscher, R. Avolio, M. E. Errico, J. Kirkpatrik, J. M. Ball, P. Docampo, I. McPherson and H. J. Snaith, *Phys. Chem. Chem. Phys.*, 2013, **15**, 2572–9.

2. N. K. Noel, A. Abate, S. D. Stranks, E. S. Parrott, V. M. Burlakov, A. Goriely and H. J. Snaith, *ACS Nano*, 2014, **8**, 9815–9821.

3. D. Bryant, P. Greenwood, J. Troughton, M. Wijdekop, M. Carnie, M. Davies, K. Wojciechowski, H. J. Snaith, T. Watson and D. Worsley, *Adv. Mater.*, 2014, **26**, 7499–7504.

4. H. J. Snaith, *Energy Environ. Sci.*, 2012, **5**, 6513.

5. K. Vandewal, L. Goris, I. Haeldermans, M. Nesládek and K. Haenen, 2008, **516**, 7135–7138.

6. J. Tauc, R. Grigorovic and a. Vancu, *Phys. Status Solidi*, 1966, **15**, 627–637.

7. J. C. de Mello, H. F. Wittmannn and R. H. Friend, *Adv. Mater.*, 1997, **9**, 230.

8. S. D. Stranks, G. E. Eperon, G. Grancini, C. Menelaou, M. J. P. Alcocer, T. Leijtens, L. M. Herz, A. Petrozza and H. J. Snaith, *Science*, 2013, **342**, 341–344.

9. P. E. Shaw, A. Ruseckas and I. D. W. Samuel, *Adv. Mater.*, 2008, **20**, 3516–3520.

10. J. R. Lakowicz, *Principles of Flurescence Spectroscopy*, Spinger London Ltd, 2007.

11. T. Smith and J. Guild, *Trans. Opt. Soc.*, 1931, **33**, 73–134.

12. M. D. Abràmoff, P. J. Magalhães and S. Ram, *Biophotonics Int.*, 2004.

4. MORPHOLOGICAL CONTROL ENABLING HIGH PERFORMANCE PLANAR PEROVSKITE SOLAR CELLS

The work presented in this chapter has been published in:

- G. E. Eperon, V. M. Burlakov, P. Docampo, A. Goriely and H. J. Snaith, "Morphological control for high performance, solution-processed planar heterojunction perovskite solar cells", *Adv. Funct. Mater.*, 2014, **24**, 151–157.

- V. M. Burlakov, G. E. Eperon, H. J. Snaith, S. J. Chapman and A. Goriely, "Controlling coverage of solution cast materials with unfavourable surface interactions", *Appl. Phys. Lett.*, 2014, **104**, 091602.

4.1 Context and summary

Organic-inorganic lead halide perovskite based solar cells have exhibited the highest efficiencies to-date when incorporated into mesostructured composites. However, thin solid films of a perovskite absorber should be capable of operating at the highest efficiency in a simple planar heterojunction configuration. In this chapter, it is shown that film morphology is a critical issue in planar heterojunction CH3NH3PbI$_{3-x}$Cl$_x$ solar cells. Dewetting occurring during the annealing process is responsible for forming discontinuous films. The parameters critical for controlling dewetting are established. By varying these, the morphology of perovskite films is varied, and it is demonstrated that the highest photocurrents are attainable only with the highest perovskite surface coverages. With optimized solution based film formation, power conversion efficiencies of up to 11.4% are achieved, the first instance of efficiencies above 10% in fully thin-film solution processed perovskite solar cells with no mesoporous layer.

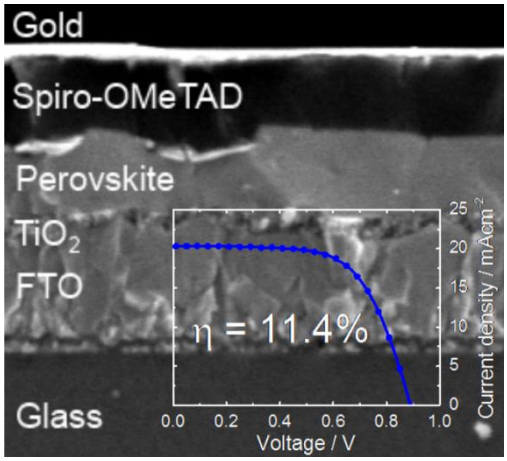

4.2 Introduction

As described in Chapter 2, the halide perovskites have been shown to exhibit ambipolar transport, allowing them to replace the hole or electron transporter in hybrid cells,[1–3] making this family of materials suitable for solution-processable thin-film solar cells. Particularly, the perovskite $MAPbI_{3-x}Cl_x$ has been demonstrated to function in a quasi-thin-film architecture, with a layer of bulk crystalline perovskite formed over a mesoporous alumina scaffold.[4] In this previous work, planar perovskite *p-i-n* heterojunctions with no mesoporous layer gave power conversion efficiencies of only up to 4.9%, while the highest power conversion efficiencies were shown in mesostructured solar cell configurations with the perovksite fully infiltrating a porous scaffold. However, internal quantum efficiencies of almost 100% for the planar configuration pointed towards its promise as an ultimately more efficient architecture.[4] It is also beneficial from a production point of view to simplify the cell architecture. Hence, high efficiency cells with simply a single solution processed solid absorber layer would be advantageous.

It has been proposed that the planar thin-film architecture's lower performance may arise from pin-hole formation, incomplete coverage of the perovskite resulting in low-resistance shunting paths and lost light absorption in the solar cell; as in other technologies the issue of film formation is likely to be extremely important in the planar junction.[5] It is well-known that as-fabricated thin films are often thermodynamically unstable, and likely to dewet or agglomerate upon annealing, as predicted from energetic considerations.[6] In this chapter it is shown that by following the previously reported fabrication protocol for perovskite solution coating on flat substrates, significant dewetting is observed, leading to incomplete coverage and non-uniform film thickness. With optimised film formation, primarily controlling the atmosphere, annealing temperature and film thickness, it is possible to form via solution casting uniform thin perovskite films with "full coverage" with no mesoporous layer. Doing so, the previously reported maximum power conversion efficiency in this configuration is more than doubled. This matches the best performing hydrazine processed CZTSSe thin film solar cell,[7] and represents the first report of over 10% efficiency in this new fully thin-film solution processed perovskite technology.

4.3 Role of the mesoporous layer

The perovskite MSSCs studied are effectively a distributed heterojunction. The $MAPbI_{3-x}Cl_x$ perovskite, infiltrated within an alumina scaffold, acts as the intrinsic absorber and electron transporter, and Spiro-OMeTAD as the p-type hole transporter. Previously, the highest efficiencies have been obtained in this "infiltrated" architecture.[2,4] A typical MSSC

cell would have short-circuit current of 17-20mAcm^{-2}, open-circuit voltage of 1.0-1.1V, and fill factor of 0.6-0.7, which combine to result in power conversion efficiencies of above 10%.

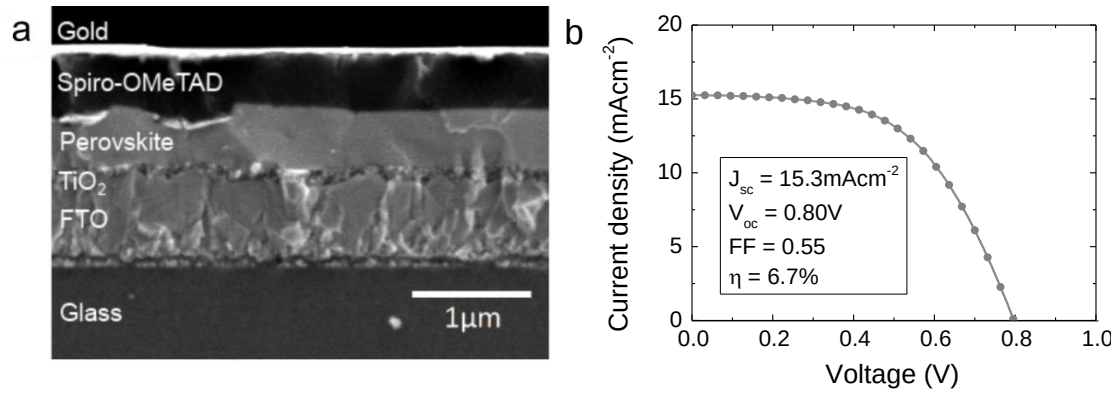

Figure 4.1: (a) Cross-sectional SEM micrograph showing device architecture of the planar heterojunction solar cells. (b) Average current-voltage characteristics from a batch of 10 non-optimised planar heterojunction solar cells, prepared according to the published procedure,[4] measured under simulated AM1.5 sunlight. It is noted that the presented JV curve is a numerical average of ten different JV curves, not simply a representative JV curve.

In the planar heterojunction configuration, illustrated in Figure 4.1a), J_{sc}, V_{oc}, and fill factor are lower, as shown in the current voltage curve presented in Figure 4.1b). The significant drop in these parameters may be a result of poor coverage of perovskite films. The effects of poor coverage would be twofold: Firstly, if there are regions of no perovskite coverage, light will pass straight through without absorption, decreasing the available photocurrent; secondly, insufficient coverage results in a high frequency of "shunt paths" allowing contact between Spiro-OMeTAD and the TiO_2 compact layer. Any such contact will act as a parallel diode in the solar cell equivalent circuit, causing a drop in V_{oc} and fill factor, and accordingly power conversion efficiency.[8,9]

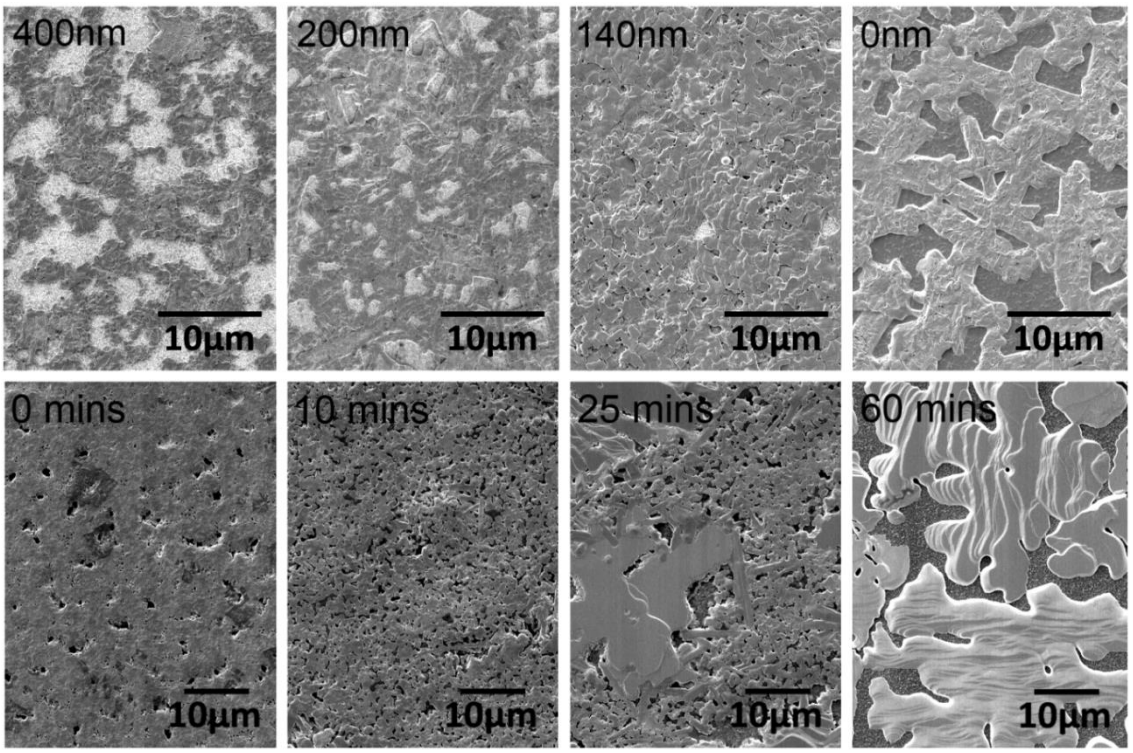

Figure 4.2: Top row: SEM micrographs of the top surfaces of $MAPbI_{3-x}Cl_x$ films formed on alumina scaffolds of thickness shown. Bottom row: SEM micrographs of perovskite films on compact TiO_2-coated FTO glass with 100°C anneal times shown on SEM images, prepared in a nitrogen atmosphere.

To investigate whether surface coverage is indeed an issue in this type of solar cell, scanning electron microscope (SEM) images of the surface morphology of perovskite films were taken, with increasingly reduced thickness of mesoporous Al_2O_3, transitioning from the MSSC infiltrated configuration to the thin-film planar heterojunction. These SEM images are shown in Figure 4.2; the samples were prepared in air according to the published procedure. As previously shown,[4] it is observed that in addition to perovskite crystallization within the mesoporous layer, a perovskite "capping layer" is also formed. The surface coverage of the capping layer is not complete however, and increases with decreasing alumina thickness (Figure 4.2). However, when the alumina is fully removed, the perovskite film forms differently, as seen in Figure 4.2. It appears to have dewet from the substrate to some extent. The fractional surface coverage of perovskite can be estimated, by simply setting a brightness threshold on the image and calculating the area above and below threshold. For the films with no mesoporous layer, the surface coverage unexpectedly drops to values of ~75%, indicating that one of the main roles of the alumina layer is to control film formation in such a way as to produce a high coverage capping layer. When no alumina is present, the reduced perovskite coverage likely leads to the

reduced J_{sc}, V_{oc} and fill factor as suggested above. If this coverage could be increased, higher performances would be expected, possibly exceeding those of the MSSC structure.

To understand why these voids are present in the perovskite layers coated on flat films, a time-series of the perovskite anneal process was studied, with SEM images shown in Figure 4.2. Since films are extremely moisture-sensitive until fully crystallized, here the films were processed in a dry nitrogen-filled glovebox to enable characterisation of the pre-crystallized films. Rapid degradation of non-annealed films in moist atmospheres was observed, likely due to the hygroscopicity of the methylammonium cation.[10] Straight after spin-coating, film coverage is high, with a number of small pores. Upon annealing, many additional small pores form rapidly (Figure 4.2, 10mins), and then either increase in size or close up until the final crystalline phase is reached (Figure 4.2, 60 mins). Upon formation of stable crystals, pore evolution was observed to cease, likely due to evaporation and mass transport no longer being energetically favourable. The morphology of samples prepared in an inert atmosphere is notably different from the air-processed samples, likely due to the lack of moisture, which otherwise attacks the surface as the film forms. It is suggested that the change in the film morphology upon annealing is driven by surface energy minimisation and is facilitated by mass loss.[6] A precursor solution with an excess of methylammonium and halide compared to the lead content is used, and upon spin-coating, an organic and halide-rich film is formed (3:1:5 organic:metal:halide by moles). As the thermal annealing process takes place, it is likely to be energetically favourable for the excess organic and halide to evaporate, once a temperature threshold is reached. This would continue until a crystal with equimolar amounts of organic, metal and halide (1:1:3 organic:metal:halide by moles) is left. The loss of the excess material has been discussed in more detail by Unger et al and Williams et al, and it is generally though that the reaction proceeds thusly:[11,12]

$$\boldsymbol{3CH_3NH_3I + PbCl_2 \rightarrow CH_3NH_3PbI_3 + 2CH_3NH_2 + 2HCl} \qquad \textbf{4.1}$$

with the reaction proceeding at temperatures of above 80°C. Once the perovskite is crystallized as $MAPbI_3$, mass loss ceases since a low-energy state has been reached.

4.4 Dewetting considerations

Depending on the conditions, pores present in a film were observed to either in general increase or decrease in size, resulting in a smaller number of large pores under the standard annealing conditions. Overall, the film appears to have dewet the substrate.

In order to stop this happening it would be instructional to understand the dewetting process of a perovskite film during annealing, with the aim of minimising dewetting. A detailed introduction to dewetting has been given in Chapter 2; here the application of this theory to the experimental observations is considered.

As shown in Figure 4.2, several processes appear to be happening concurrently. Based on the observations made it is possible to summarise some postulations about the dewetting of the perovskite system, in order to begin to understand how it may behave upon annealing:

- There is an initial distribution of holes already present after spin-coating
- During annealing, more holes form
- Some holes open and some appear to close
- During annealing, crystallisation occurs (then becoming a solid state system)
- Some holes impinge
- There is significant mass loss in the system (see Equation 4.1)

And the considerations relevant to dewetting that there is no known information on are:

- Is the film liquid or solid before crystallisation?
- What are the surface energies of the material and how does this depend upon annealing time and phase?
- What is the relation between material loss and crystallisation?
- What is the diffusivity in the various states of the material and how does it change over time?

The initial hole distribution in the perovksite film was studied to determine if it had a characteristic pattern for spinodal dewetting during spin-coating, which would show a characteristic pore size and spacing. However, as shown in Figure 4.3, the pore radius distribution shows a wide range of pore sizes in the initial film, before annealing. It is thus impossible to determine how these pores originated – whether through thermal nucleation in liquid state, or heterogeneous nucleation from a rough substrate or surface inhomogeneities in either liquid or solid state, or both. The FTO substrate is very rough, so this will likely serve as many nucleation points for holes to form at.

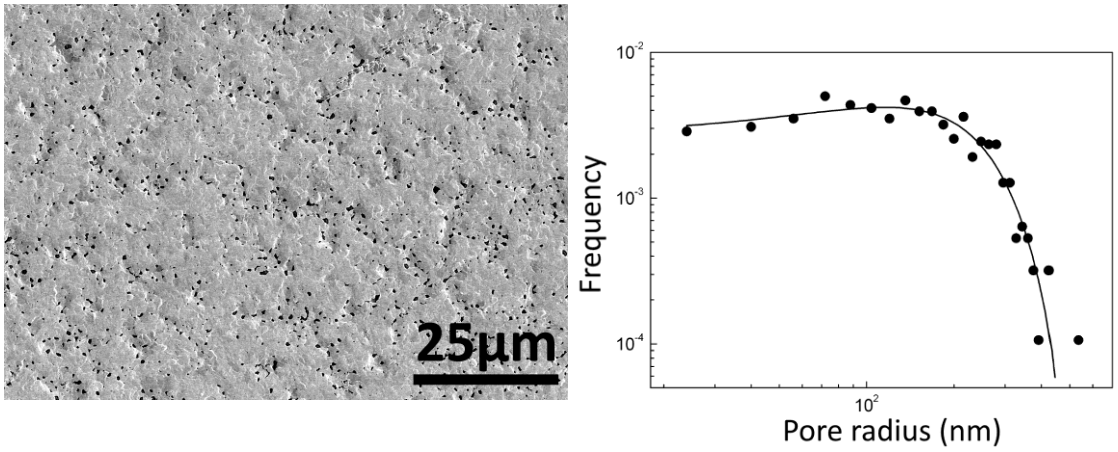

Figure 4.3: Left, typical SEM image of an unannealed perovskite film. Right, typical initial pore radius distribution averaged over 10 unannealed perovskite film samples.

More importantly, so little is known about this system that we cannot conclusively say that the initial film will behave as a solid or a liquid material at typical annealing temperatures. It is known that material loss of some components occurs via evaporation, but it is unknown whether this is sublimation on decomposition or due to changing phase from liquid to gas. The observations could support either state – it could be a viscous liquid or an amorphous solid. It is also unknown whether there is significant solvent remaining in the film after spin-coating. The mass loss will complicate any analysis as it would alter the expected dynamics significantly. Instead of being forced to create rims (if the material is solid state), material could just evaporate from the pore edges. It can be safely assumed that when crystallisation has occurred, the material is in the solid state. It is likely that crystallisation is facilitated by the mass loss – the material will only crystallise once it reaches bulk stoichiometry. According to observations, dewetting does not play a large role after crystallisation. Single crystal dewetting can thus be ruled out.

The problem can be summarised thusly: a material with unknown phase and an initial distribution of holes dewets upon heating, whilst at the same time undergoing mass loss and crystallisation, with unknown activation energies. In order to attain a film with high coverage, it will be necessary to minimise dewetting whilst still driving mass loss and crystallisation.

While the ideal situation would be to develop a model accounting for all these factors, there are many complexities of this system compared to dewetting modelling studies in the literature.[6,13] The unknown phase, mass loss, and diffusivity complicate the formulation of an accurate model so here this route is not pursued.

Therefore, to establish if it is possible to control dewetting, an experimental study is more appropriate. As concluded in Chapter 2, Section 2.6, there are a number of parameters that will have most impact on a dewetting process, whether it is in the solid or liquid state. These were:

- initial film thickness
- initial pinholes in the film
- temperature
- time

The initial pinhole distribution was held fixed, as although it could possibly by varied by changing substrate and spin coating parameters, this opens a very large parameter space and it is unlikely that they could be completely eliminated; the dewetting process is dominated by the later effects. Experimentally it was determined, in studies not detailed herein, that for a given annealing temperature, the annealing time should be optimised to attain a fully crystalline perovskite if a functioning solar cell is to be fabricated. Annealing for too long resulted in degradation; annealing for insufficiently long time resulting in a large degree of amorphous material prone to rapid degradation. Time was therefore fixed to the optimum time for each anneal temperature, based on experimental optimisation, to attain a crystalline material.

This then leaves two parameters of importance that can be well-controlled in experiment: initial film thickness and annealing temperature. $CH_3NH_3PbI_{3-x}Cl_x$ perovskite films are typically annealed at 100°C, with an initial thickness of ~600nm. This only provides a final surface coverage of about 70%, as experimentally observed. Thus, a study was undertaken to minimise dewetting by varying these two parameters.

It should also be mentioned that the amount of solvent present in the film initially could be varied by changing the solvent used and hence vapour pressure, changing the initial diffusivity of the components and possibly changing the onset of the liquid-solid transition. This will certainly change dewetting dynamics and its temporal evolution so will likely have an impact on dewetting although it is not mentioned specifically in the dewetting introduction, which focuses on constant liquid or solid phases.

4.5 Controlling surface coverage

In order to determine if these predictions were attainable, perovskite films were fabricated and analysed. Annealing temperature and initial thickness were varied, and the

resulting crystallized perovskite coverage measured using the image analysis software ImageJ[14].

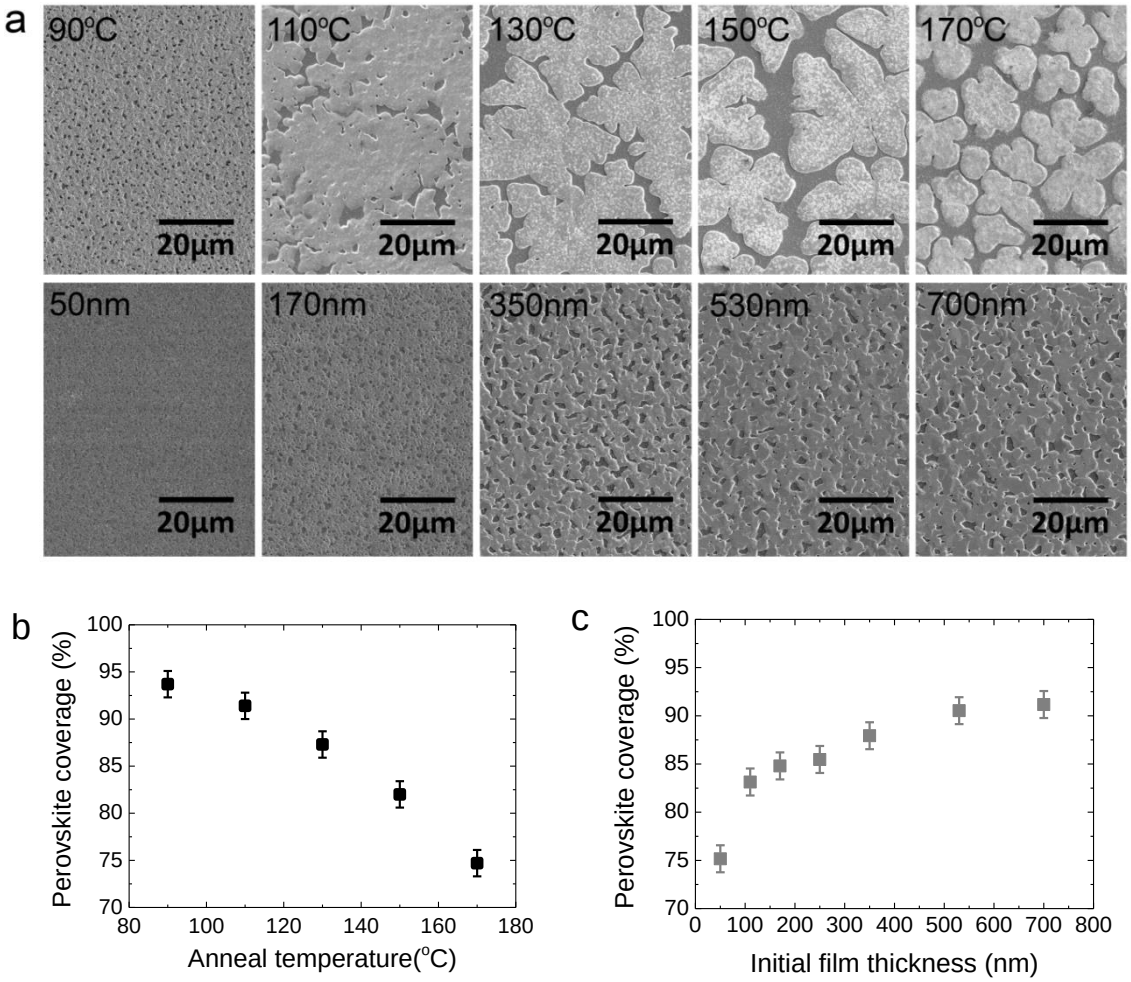

Figure 4.4: a) Top row: SEM micrographs showing dependence of perovskite coverage on annealing temperature, temperature shown on images, holding initial film thickness fixed at 650±50nm. Bottom row: effect of initial perovskite film thickness, shown on images, with annealing temperature fixed at 95°C. (b and c) Perovskite surface coverage as a function of (b) anneal temperature and (c) initial film thickness, calculated from SEM images.

SEM images of representative perovskite films are shown in Figure 4.4a), and the calculated coverages plotted in Figure 4.4b) and Figure 4.4c). The effect of varying temperature on the wetting of the thin film is shown in (a). As anneal temperature increases, the number of pores in the final film decreases, but their size increases and the morphology transitions from continuous layers into discrete islands of perovskite. This has the effect of reducing surface coverage, as seen in (b). Previously, annealing has been carried out at 100°C; however this data suggests as low a temperature as possible should

be used to attain maximum coverage whilst still enabling full crystallisation of the perovskite absorber.

The influence of thickness variation whilst holding the temperature fixed at 95°C is also shown in Figure 4.4. It can be seen that with increasing initial film thickness, the average pore size increases, though there are fewer pores per unit area. The effect on coverage is thus not obvious; image analysis reveals that thicker initial films result in marginally greater coverages, as seen in Figure 4.4c). The previous standard protocol used a thickness of around 500-700nm. This is within the expected region of high coverage; the primary factors of importance when understanding the photovoltaic behaviour for these perovskite films of >200nm thickness becomes a balance between full photon absorption and electron and hole diffusion length throughout the bulk perovskite. An experimental optimisation (not detailed herein) of devices suggested thicknesses between 400 and 800nm were suitable for attaining high efficiency devices.

To establish if increasing the perovskite coverage solves the decreases in performance seen previously, planar heterojunction devices with a range of perovskite coverages were fabricated.

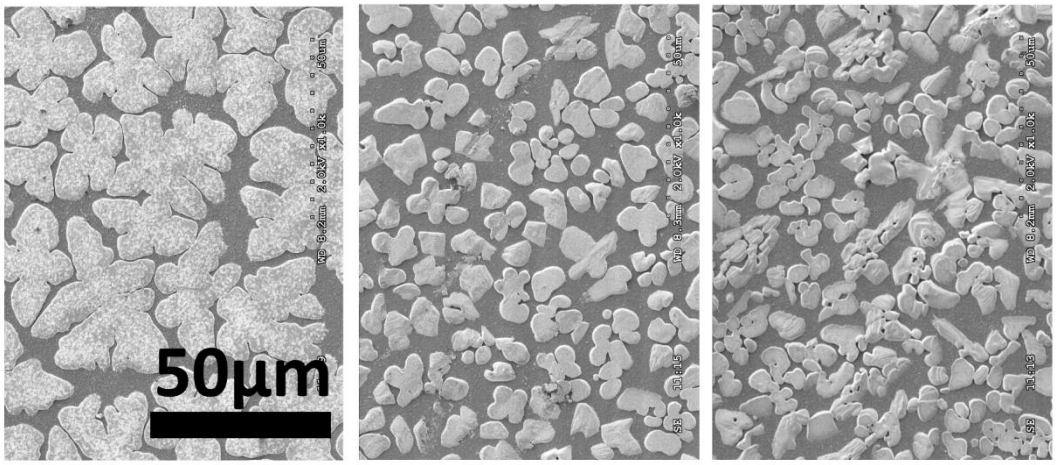

Figure 4.5: SEM images of perovskite films fabricated from precursors dissolved in different solvents. Left; DMF; centre, DMSO; right, NMP. All films are annealed at 150°C for 10 minutes. The boiling points respectively are 153°C, 189°C, and 202°C. The scale is the same in all images.

Anneal temperature was varied, and additionally the solvent used was varied to obtain the lowest coverages. Employing more slowly-evaporating solvents, DMSO and n-methyl-2-pyrrolidone (NMP), instead of DMF, reduces the surface coverage, as shown in Figure 4.5. Solvent evaporation rate affects the onset of the transition from high diffusivity to low diffusivity; a lower solvent evaporation rate allows the system more time for pores to

grow/shrink, so in the regions where pores will generally open it will result in even lower surface coverages.

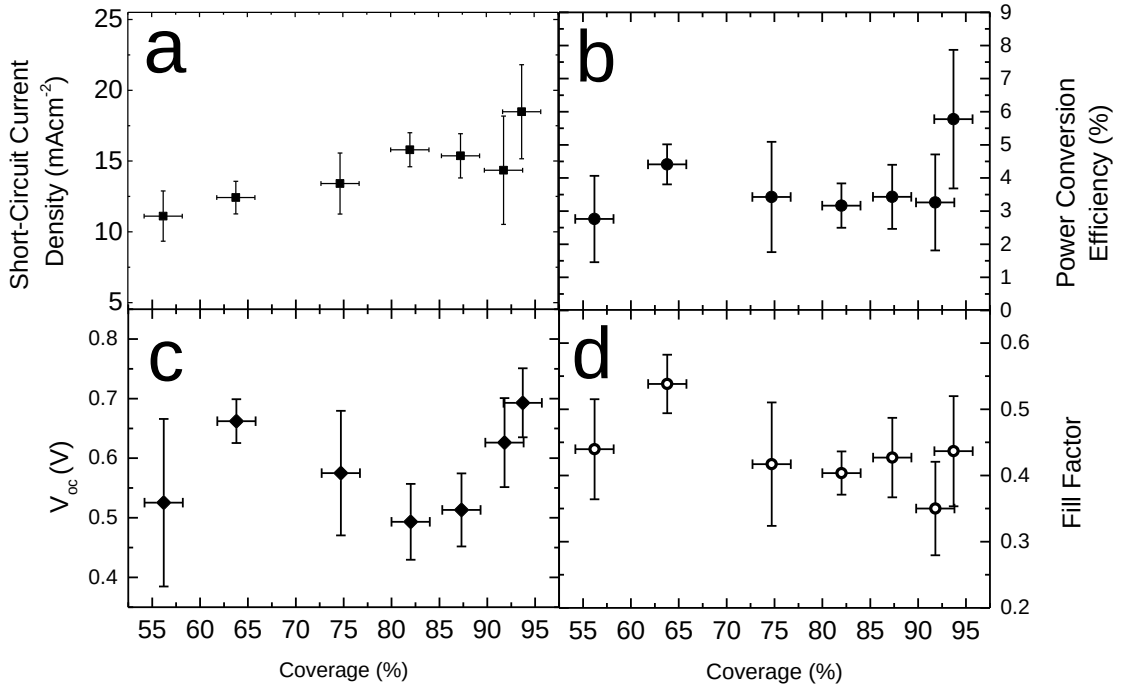

Figure 4.6: Dependence of the (a) short-circuit current density, (b) power conversion efficiency, (c) open-circuit voltage and (d) fill factor on perovskite coverage, extracted from solar cells illuminated under simulated AM1.5 sunlight of 100 mWcm^{-2} irradiance. Each data point represents the mean from a set of 9 or more individual devices.

Mean device parameters for a single batch of devices, extracted from current-voltage curves under simulated AM1.5, 100 mWcm^{-2} sunlight are shown in Figure 4.6. Short-circuit photocurrent shows a clear trend with coverage. At coverages of ~56%, average J_{sc} is around 11 mAcm^{-2}. As the coverage increases up to ~94%, J_{sc} increases linearly, up to average values of around 18 mAcm^{-2}. The best performing individual cells show J_{sc} above 21mAcm^{-2}, matching the highest currents reported in the perovskite solar cells to date. The effect of coverage on power conversion efficiency, shown in Fig 4.6(b), is not so clear. Despite the trend in photocurrent, fill factor and V_{oc} do not follow easily understandable trends with coverage. It is likely that the changing morphology of the film additionally results in varying electronic and physical contact between hole transporter--perovskite, hole transporter-TiO_2 layer and perovskite- TiO_2 layer, which complicates the situation. However, the lowest average efficiencies are observed for the lowest coverages, and the highest average efficiencies are observed for the highest coverages. Though the

intermediate behaviour is not clear, this study supports the logical conclusion that high coverage is the optimum configuration for high power generation.

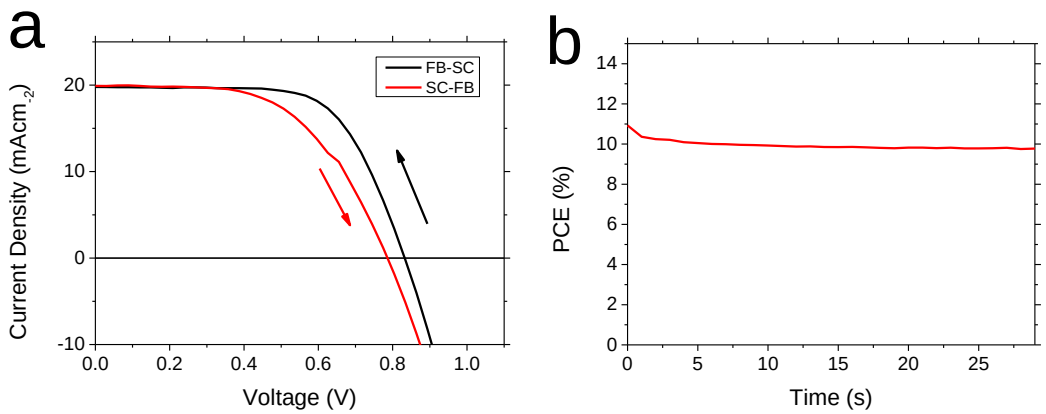

Figure 4.7: Hysteresis in high coverage planar heterojunction solar cells. a) Current-voltage scans for a typical device, measured at 0.38V/s scan speed. FB-SC refers to scanning voltage from forward bias to short circuit; SC-FB vice versa. The calculated efficiencies from the JV curve are ~11% and ~8.8% for FB-SC and SC-FB respectively. b) Stabilised power output measured holding the cell under AM1.5 illumination at 0.6V (MPP for the FB-SC scan). The cell stabilises at ~9.7% PCE.

As discussed in Chapter 2, planar methylammonium lead halide devices display current-voltage hysteresis. Accordingly, it is necessary to also measure the stabilised power output to determine the real PCE of such a device. Such measurements were taken on the high-coverage planar perovskite devices; data from a representative device is shown in Figure 4.7. It can be seen that hysteresis in JV curves is present, with different PCEs extracted depending on the scan direction. The stabilised power output reaches a steady value less than the PCE extracted from the best JV curve, indicating that the issue of hysteresis is important for these devices and solving it will be necessary for stabilising devices at the highest PCEs. This will be discussed further in Chapter 9.

4.6 Changing the film-substrate interaction

Motivated by this simple principle, and given that it proved impossible to attain 100% coverage by optimization of temperature and thickness alone, an attempt was made to achieve full coverage by varying the film-substrate interaction energy. This was achieved by altering the thickness of the TiO_2 compact layer. Indeed, it was observed that by using thicker TiO_2 compact layers, increased coverage was attained.

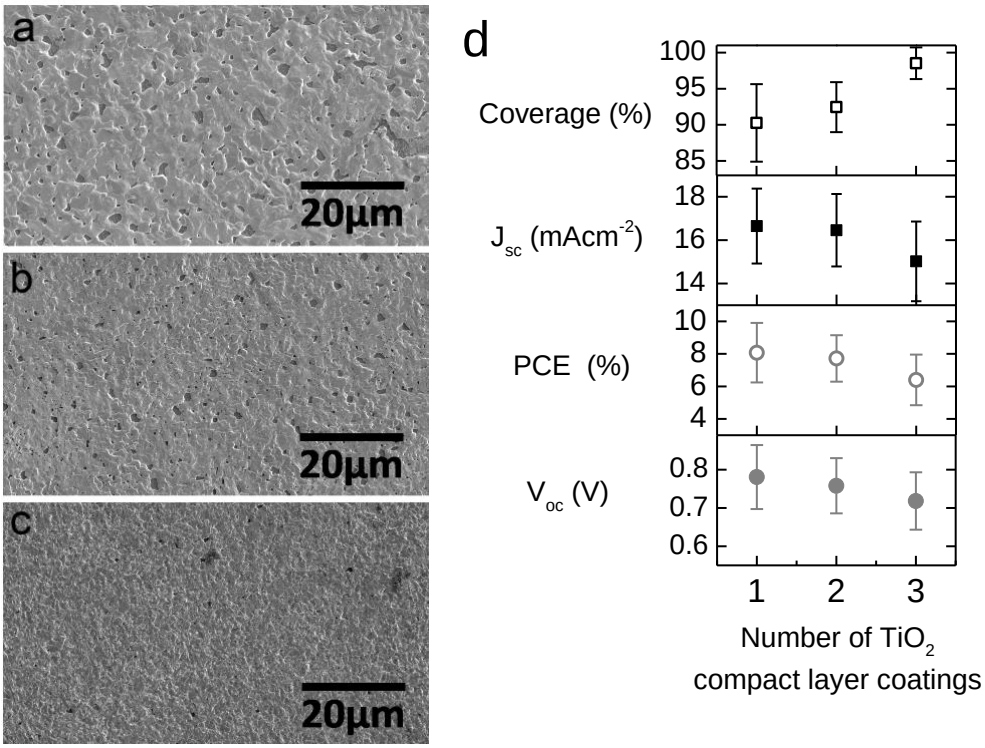

Figure 4.8: (a)-(c) SEM micrographs of perovskite films formed on (a) ~75nm (b) ~150nm and (c) ~225nm thick TiO_2 compact layers coating FTO substrates. (d) Dependence of perovskite coverage and device parameters on the thickness of the TiO_2 compact layers, in a single batch of devices. Each data point represents the mean from 32 or more individual devices, with the exception of coverage, which is based on 3 measurements per data point.

Representative films are shown in Figure 4.8. This discovery enabled the production of full-coverage perovskite films. it is proposed that the n-type compact layer interacts electronically with the perovskite film during formation; possibly a thicker layer is able to transfer more electronic charge to the perovskite assisting its formation near the surface due to differing electrostatics.

Devices were fabricated from a range of TiO_2 compact layer thicknesses, and perovskite coverage and device parameters were measured to determine if any additional gains in efficiency were observed compared to 90%+ coverage. TiO_2 compact layer thickness was varied by repeatedly spin-coating more layers of the TiO_2 precursor solution. A single spin-coated layer was measured to be approximately 75nm thick. Figure 4.8d) shows the dependence of perovskite coverage, J_{sc}, power conversion efficiency and V_{oc} on increased TiO_2 compact layer thickness. With thicker TiO_2 layers, an increase in perovskite coverage is seen; however, disappointingly J_{sc} and V_{oc} both drop, resulting in lower device efficiencies. A TiO_2 compact layer of increased thickness is likely to have a significant effect

upon device performance since the relatively resistive TiO_2 layer is critical to electron collection. Thick TiO_2 compact layers have been shown previously to hinder charge extraction in dye-sensitized solar cells due to increased series resistance;[15] this is likely the reason for the observed decrease in performance.

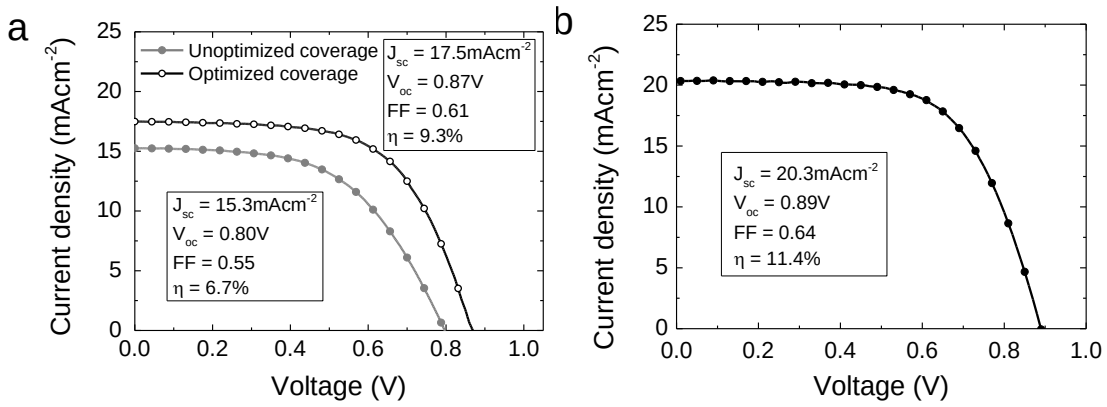

Figure 4.9: Current-voltage characteristics measured under simulated AM1.5 sunlight of (a) the average of a batch of 11 solar cells produced using the optimized high coverage planar heterojunction configuration, compared to the previously shown unoptimized batch and (b) the best performing solar cell based on the planar heterojunction configuration.

Despite not achieving further improvements in efficiency with full coverage based on thicker TiO_2 compact layers, due to series resistance limitations, impressive efficiencies were obtained with the highest perovskite coverages on the thinnest TiO_2 layer. This was achieved by annealing at a lower temperature of 90°C, with an initial perovskite film thickness of 450-550nm. The improvement in average current-voltage characteristics, and hence overall performance resulting from this process is shown in Figure 4.9a). The current-voltage curve corresponding to the most efficient device measured is shown in Figure 4.9b). The efficiency of the most efficient device is 11.4%, which represents greater than a two-fold improvement over the previous report of solution processed planar heterojunction perovskite solar cells.[4] Improvements are due to increased J_{sc}, V_{oc} and fill factor, and are likely to stem from two effects resulting from improved perovskite coverage. Firstly, it has enabled collection of a higher fraction of incident photons, increasing useful current generated. Secondly, the increased coverage has reduced contact area between the hole transporter and the hole-blocking layer, which removes a shunt path previously leading to leakage currents.[16] Reduction of these shunt paths would therefore be expected to enhance the fill factor and V_{oc} as has been observed in this chapter. Full elimination of shunt paths may be expected to increase V_{oc} up to levels seen in the MSSC configuration (~1.1V). Additionally, further tuning of the interaction energy

between the TiO_2 compact layer and the perovskite, whilst still employing thin TiO_2 films, could enable 100% perovskite coverage upon electronically optimal layers, resulting in further enhanced performance.

4.7 Outlook and conclusion

By understanding and controlling morphology of perovskite films originating from a non-stoichiometric composition of precursor salts, the critical role of uniform perovskite film formation in planar heterojunction perovskite solar cells has been demonstrated. The highest efficiencies are achievable only with the highest surface coverages. Planar heterojunction cells were fabricated at low temperatures with efficiencies of up to 11.4%, the first instance of a fully thin-film solution processed perovskite solar cell with no mesoporous layer with efficiency above 10%. This indicates that a mesoporous layer is no longer necessary to achieve high efficiency perovskite cells. Simplification of the cell architecture in this way increases the versatility of such cells, and can enable easier and cheaper manufacturing on a large scale. The work described in this chapter paves the way for future developments and those described in upcoming chapters, demonstrating for the first time that the planar heterojunction architecture is capable of generating power conversion efficiencies as high, if not eventually higher than, the mesoporous architectures.

4.8 References

1. I. Chung, B. Lee, J. He, R. P. H. Chang and M. G. Kanatzidis, *Nature*, 2012, **485**, 486–489.

2. M. M. Lee, J. Teuscher, T. Miyasaka, T. N. Murakami and H. J. Snaith, *Science*, 2012, **338**, 643–647.

3. L. Etgar, P. Gao, Z. Xue, Q. Peng, A. K. Chandiran, B. Liu, M. K. Nazeeruddin and M. Grätzel, *J. Am. Chem. Soc.*, 2012, **134**, 17396–17399.

4. J. M. Ball, M. M. Lee, A. Hey and H. J. Snaith, *Energy Environ. Sci.*, 2013, **6**, 1739–1743.

5. W. Jaegermann, A. Klein and T. Mayer, *Adv. Mater.*, 2009, **21**, 4196–4206.

6. C. V Thompson, *Annu. Rev. Mater. Res.*, 2012, **42**, 399–434.

7. D. A. R. Barkhouse, O. Gunawan, T. Gokmen, T. K. Todorov and D. B. Mitzi, *Prog. Photovoltaics Res. Appl.*, 2012, **20**, 6–11.

8. P. Docampo and H. J. Snaith, *Nanotechnology*, 2011, **22**, 225403.

9. L. Han, N. Koide, Y. Chiba and T. Mitate, *Appl. Phys. Lett.*, 2004, **84**, 2433–2435.

10. J. H. Noh, S. H. Im, J. H. Heo, T. N. Mandal and S. Il Seok, *Nano Lett.*, 2013, **13**, 1764–1769.

11. E. L. Unger, A. R. Bowring, C. J. Tassone, V. Pool, A. Gold-Parker, R. Cheacharoen, K. H. Stone, E. T. Hoke, M. F. Toney and M. D. McGehee, *Chem. Mater.*, 2014, **26**, 7158–7165.

12. S. T. Williams, F. Zuo, C.-C. Chueh, C.-Y. Liao, P.-W. Liang and A. K.-Y. Jen, *ACS Nano*, 2014, **8**, 10640–10654.

13. V. M. Burlakov, G. E. Eperon, H. J. Snaith, S. J. Chapman and A. Goriely, *Appl. Phys. Lett.*, 2014, **104**, 091602.

14. M. D. Abràmoff, P. J. Magalhães and S. Ram, *Biophotonics Int.*, 2004.

15. B. Peng, G. Jungmann, C. Jäger, D. Haarer, H.-W. Schmidt and M. Thelakkat, *Coord. Chem. Rev.*, 2004, **248**, 1479–1489.

16. H. J. Snaith, N. C. Greenham and R. H. Friend, *Adv. Mater.*, 2004, **16**, 1640–1645.

5. NEUTRAL-COLOURED, SEMI-TRANSPARENT PEROVSKITE SOLAR CELLS

The work presented in this chapter has been published in:

- G. E. Eperon, V. M. Burlakov, A. Goriely and H. J. Snaith, "Neutral color semitransparent microstructured perovskite solar cells ", *ACS Nano*, 2014, **8,** 591–598.

5.1 Context and summary

Neutral-coloured semi-transparent solar cells are commercially desired to integrate solar cells into the windows and cladding of buildings and automotive applications. In the previous chapter it was shown that in a planar perovskite solar cell, high surface coverage of the perovskite on the substrate is desired to fabricate the highest efficiency devices. The important parameters to allow predictable control were determined, experimentally, allowing surface coverage to be intelligently controlled by carefully controlling deposition parameters. In this chapter, an important use for the low-coverage perovskite films is realised. The spontaneous dewetting that occurs to form the lowest coverage films is taken advantage of to create micro-structured arrays of perovskite 'islands', on a length-scale small enough to appear continuous to the eye yet large enough to enable unattenuated transmission of light between the islands. The islands are thick enough to absorb most visible light and the combination of completely absorbing and completely transparent regions results in neutral transmission of light. Using these films, thin-film solar cells are fabricated with respectable power conversion efficiencies. Remarkably, it is found that such discontinuous films still have good rectification behaviour and relatively high open-circuit voltages due to inherent rectification between the n- and p-type charge collection layers. Furthermore, the ease of "colour-tinting" such micro-structured perovksite solar cells with no reduction in performance is demonstrated, by incorporation of a dye within the hole transport medium.

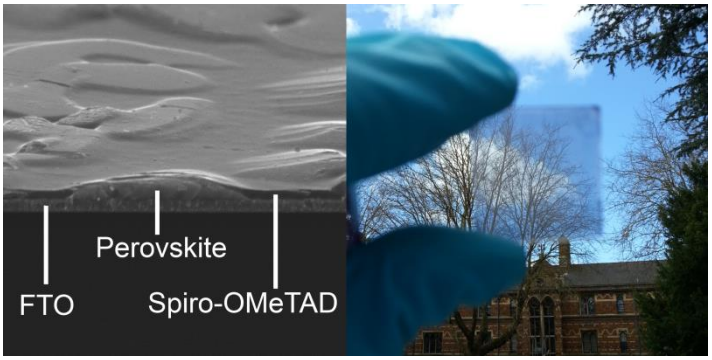

5.2 Introduction

Building-integrated photovoltaics (BIPV) are an attractive concept for economic generation of solar power.[1] Integration of semi-transparent solar cells into windows is of particular interest since it opens the prospect of employing the entire façade of a building for solar power generation, rather than simply employing the limited roof space. In order for such solar glazing to be practical, costs must be low, and ideally they can be manufactured through existing coating methods employed in the glazing industry. They need to generate significant power, whilst still having good transparency. Furthermore, whilst coloured windows are interesting for novel applications, and a "splash" of colour is desirable, the largest demand is for neutral-colour tinted windows with controllable levels of transparency.

Some of the most successful approaches to achieve semi-transparency in solar cells have used organic or dye-sensitized solar cells (OPV and DSSC respectively).[2–7] These technologies are solution-processable, representing a low-cost production method and easy scalability.[8] Impressive recent progress has been made with neutral coloured OPV.[7,9,10] However, their efficiencies are unlikely to reach those of crystalline technologies in the near future, due to large energy losses occurring at charge transfer interfaces.[11,12] To attain colour-neutrality with organics, the active materials must be chosen carefully, often at a loss to overall efficiency.[3,4,13] An option with thin-film solar technologies, where the solar cell comprises a solid absorber layer, is to simply reduce the thickness of the absorber layer to allow transparency. Indeed, this is precisely what is done with amorphous silicon, currently being installed in BIPV applications. However, due to the nature of the density of states in the conduction and valence band in a crystalline semiconductor, as discussed in detail in Section 2.1, to the absorption coefficient increases continuously from the band gap, and thin films will assume a red or brown tint. Even though "bronze" is a choice for solar glazing, it does not represent the most desirable option.

High-efficiency $MAPbI_{3-x}Cl_x$ perovskite solar cells can be produced at low temperatures and in a fully planar thin-film architecture, reducing fabrication steps and simplifying the design, as has been discussed in Chapter 4.[15] These characteristics make such perovskites ideal materials for fabrication of semi-transparent windows. However, they fall firmly within the thin-film category and a thin continuous perovskite film suffers from the same reddish-brown tint as conventional semiconductors.

A methodology to control the fractional surface coverage of $MAPbI_{3-x}Cl_x$ perovskite films was described in the previous chapter of this thesis, with the target of obtaining uniform

and complete coating. Perovskite films are deposited from spin-coating a precursor with a molar excess of organic and halide components and typically contain several small pores as-cast. Upon annealing, mass loss of the solvent and excess organic (MA) and halide (I or Cl) components allows morphological change due to minimisation of surface energy. The evolution of morphology depends upon several parameters. An experimental investigation of the evolution of pores upon annealing was carried out; pores could either be energetically driven to close, allowing high surface coverage, or open, effectively dewetting the material from the substrate. It was found that by controlling parameters such as the initial film thickness, annealing temperature, atmosphere, and solvent vapour pressure, control could be exerted over whether pores in general opened or closed, thus close to 100% surface coverage was achieved, and correspondingly highly efficient planar heterojunction solar cells fabricated.

In addition to maximising surface coverage, incomplete surface coverage can be exploited. In this chapter, dewetting of such films is leveraged to form micro-structured arrays of perovskite "islands". The perovskite islands are thick enough to absorb all visible light, whereas the "dewet" regions (absent of perovskite) are visibly transparent. Therefore, a semi-transparent layer is formed whilst avoiding the brown tint observed in thin semiconductor films; the overall optical appearance of such a film is neutral-coloured. By varying the extent of dewetting, the transparency of the film is controlled, resulting in tuneable and efficient semi-transparent solar cells. This work endows the perovskite technology with the neutral uniform colouration previously exclusive to organics, but at lower cost and high efficiency.

5.3 Controlling coverage to control transparency

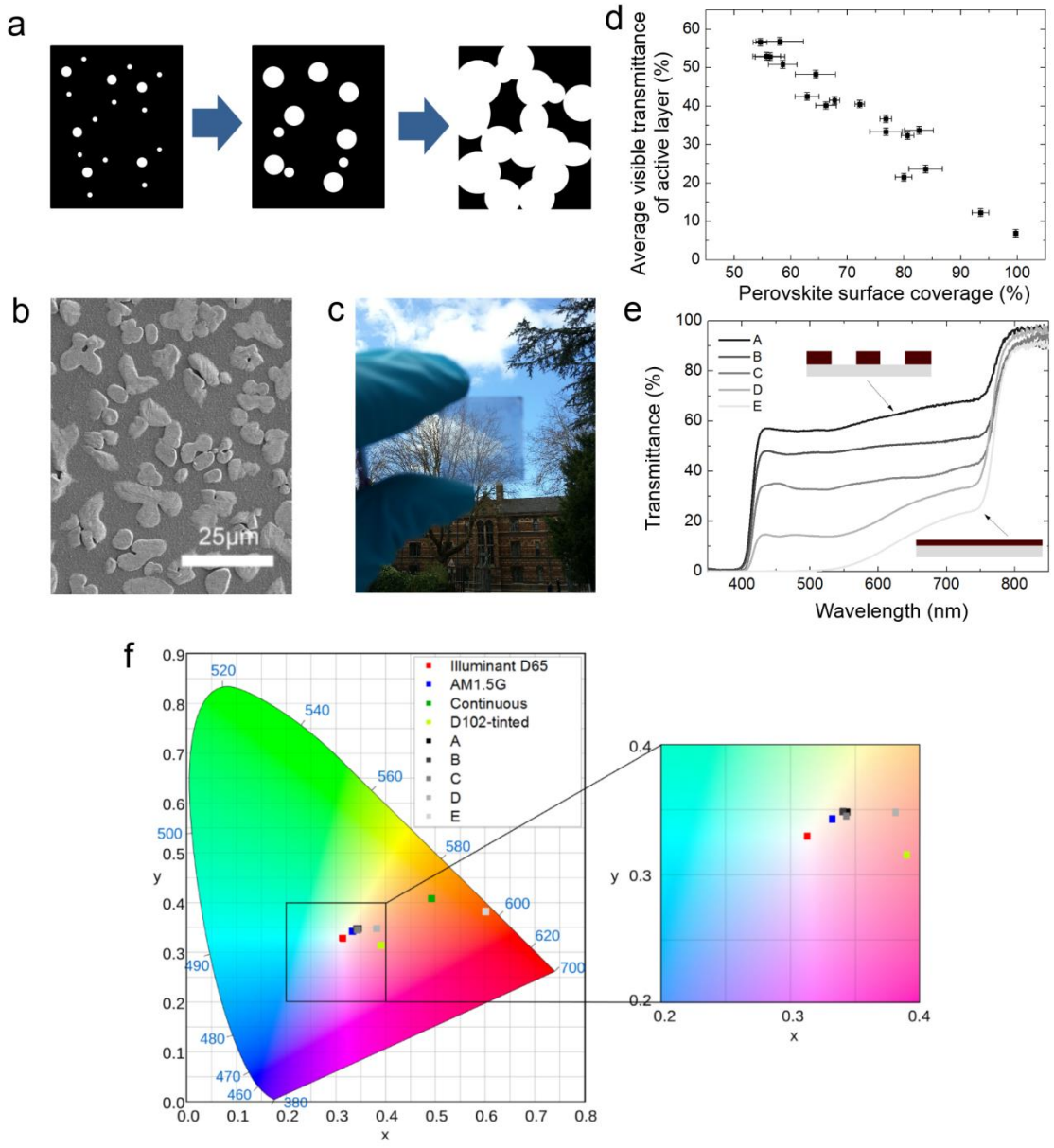

Figure 5.1: Controlled dewetting to vary transmittance of a perovskite film. a) Schematic of the film dewetting process showing morphology change over time, from as-cast film to discrete "islands". Perovskite material is represented with black, pores by white. b) Scanning electron micrograph of the top surface of a representative film of perovskite "islands" (paler regions) on a TiO_2-coated FTO substrate. c) Photograph through a typical semi-transparent perovskite film formed on glass, demonstrating neutral colour and semi-transparency. d) Dependence of average visible transmittance of the active layer on perovskite surface coverage e) Transmittance spectra of active layers of a selection of dewet perovskite devices. Diagrammatical representations of the most and least transparent films are shown

as insets. f) colour coordinates of the films with transmittance spectra shown in (d) under AM1.5 illumination, on the CIE xy 1931 chromacity diagram, and the enlarged central region. Colour coordinates of a thin continuous perovskite film, a D102 dye-tinted cell (described later), the D65 standard daylight illuminant and AM1.5 illumination are also shown.

In Figure 5.1a, a schematic of the dewetting process to produce discontinuous regions of the perovskite absorber $MAPbI_{3-x}Cl_x$ is shown. This has been described in more detail in Chapter 4. Over time, pore growth, controllable through processing conditions such as temperature and film thickness, dictates the final morphology of the polycrystalline film. In Figure 5.1b, an SEM image of a representative semi-transparent perovksite film formed to maximise open area is shown. The "islands" were measured to be >1μm in height. Visibly, such films appeared neutral-coloured (Figure 5.1c)- a 1μm film of perovksite absorbs effectively all light at energies above its bandgap, which is 1.55eV.[16] A continuous 1μm film would hence appear black, but because the perovskite film is formed of discontinuous islands, it appears semi-transparent and of neutral colour. For neutral colour to be achieved, it is a prerequisite that the absorption onset of the absorber is in the near infra-red. In order to characterise such films for their use in working solar cells, it is the optical behaviour of not just the perovskite, but the whole active layer necessary to produce a working solar cell, that is of interest. Here, the device architecture is a planar heterojunction of perovskite between an n-type compact TiO_2 layer and Spiro-OMeTAD. Therefore, from here the "active layer" is defined as the structure: compact TiO_2/perovskite/Spiro-OMeTAD. Furthermore, as the application for semi-transparent solar cells is for visible aesthetics, it is the visible wavelengths, between 370 and 740nm, that are of interest. The average visible transmittance (AVT) is defined as the mean transmittance of a film between these wavelengths. Based on the insight gained in Chapter 4, perovskite films were fabricated on compact TiO_2-coated FTO glass under a range of processing conditions in order to achieve a wide range of transparencies (see Table 5.1). Annealing temperature, solvent, and atmosphere were varied to achieve an AVT range from ~7-57%. The perovskite surface coverage was measured via analysis of SEM images, then the Spiro-OMeTAD layer applied and the AVT measured with an integrating sphere, as described in detail in Section 3.4.3. In Figure 5.1d, the dependence of AVT on perovskite surface coverage is shown. A linear trend demonstrates the ease of controlling the transparency of such films by careful choice of solvent and processing temperature. A selection of representative active layer transmittance spectra are shown in Figure 5.1e. Encouragingly flat spectra across the majority of the visible spectrum are observed,

especially for the more transmissive samples. This implies that these films should have very neutral colouration. For the less transmissive samples (especially D and E in Figure 5.1e), there is a higher perovskite surface coverage, or less dewetting. For the same amount of starting material, the final film volume should be the same regardless of the extent of dewetting, hence the regions of perovskite in the films with more coverage are thinner, and evidentially not thick enough to fully absorb the light at the red end of the spectrum. This is seen in Figure 5.1d, where even with 100% perovskite coverage, AVT is not 0%. The more dewet films comprise thicker perovskite islands and hence have flatter spectra. Diagrams of the cross-section of high and low transmission films are shown as an inset to Figure 5.1e.

Is it noted that the measured absorbances were taken using an integrating sphere, thus including scattered light as well as specular transmission. If there was significant surface roughness at an interface between two materials with significantly different refractive index, significant haze would be present. This would obviously be non-ideal for building integration (aside from in situations where a hazy window is desired) as it would affect the clarity of the view through the window. When rough perovskite is coated on glass with no HTM, this is the case and a film will indeed appear hazy, distorting passing light. However, when coated with Spiro-OMeTAD, the haze is much reduced and distortion minimal. This is presumably due to the fact that the perovskite and Spiro-OMeTAD have similar refractive indices, and the top surface of the Spiro interface with air is smoother than a perovskite air interface. From literature, the refractive indices at optical wavelengths of perovskite and Spiro-OMeTAD are ~2.4,[17], and ~1.9,[18] compared to the refractive index of air at 1.0. The smaller the difference, the less refraction at an interface, hence the less scatter if the interface is rough. The value for Spiro-OMeTAD is between those of perovskite and air, hence, Spiro-OMeTAD will act to effectively reduce haze by 'graduating' the refractive index at this interface, explaining why the films with HTM are not very hazy.

Active layer AVT (%)	AVT error (%)	Solvent	Anneal temperature (°C)	Anneal time (mins)	Atmosphere
6.92	0.07	DMF	90	120	Dry N_2
12.31	0.84	DMF	110	45	Dry N_2
21.54	0.60	DMSO	90	120	Dry N_2
23.69	0.20	DMF	130	20	Dry N_2
32.38	0.02	DMF	90	120	Air
33.35	0.28	NMP	90	120	Dry N_2
33.69	0.30	DMSO	110	45	Dry N_2
36.70	0.53	DMF	110	45	Air
40.16	1.19	NMP	110	45	Dry N_2
40.56	0.13	DMF	130	20	Air
41.51	0.46	NMP	130	20	Dry N_2
42.53	0.31	DMSO	130	20	Dry N_2
48.32	0.01	DMSO	110	45	Air
50.91	0.54	NMP	110	45	Air
52.88	0.29	NMP	130	20	Air
53.02	1.00	NMP	90	120	Air
56.62	0.03	DMSO	90	120	Air
56.87	0.27	DMSO	130	20	Air

Table 5.1: Parameters used to achieve a certain active layer AVT for one batch of samples. Errors in AVT are determined from the standard deviation in taking multiple measurements across the same film.

To quantify the colour-neutrality of the active layers, colour perception indices were calculated using the CIE 1931 xy colour space, designed to represent human visual colour perception. Details of this calculation are given in Section 3.4.9. The appearance of transmitted light is represented by the product of the AM1.5 solar spectrum and the transmission spectrum of the active layer in question. x and y colour parameters were calculated for the samples labelled A-E in Figure 5.1e, and the results displayed on the CIE 1931 xy chromaticity diagram in Figure 5.1f. A ~200nm thick continuous perovskite film, the reference daylight illuminant D65, and the AM1.5 spectrum are also plotted. The colour co-ordinates of the most transmissive active layers (A, B, C) are located very close

to the AM1.5 spectrum and the D65 reference in the low colour region of the chromaticity diagram, representing excellent colour-neutrality. At lower transmittances, films move towards the red-brown side of the chromacity diagram, where the thin continuous perovskite film is positioned.

5.4 Semi-transparent planar heterojunction solar cells

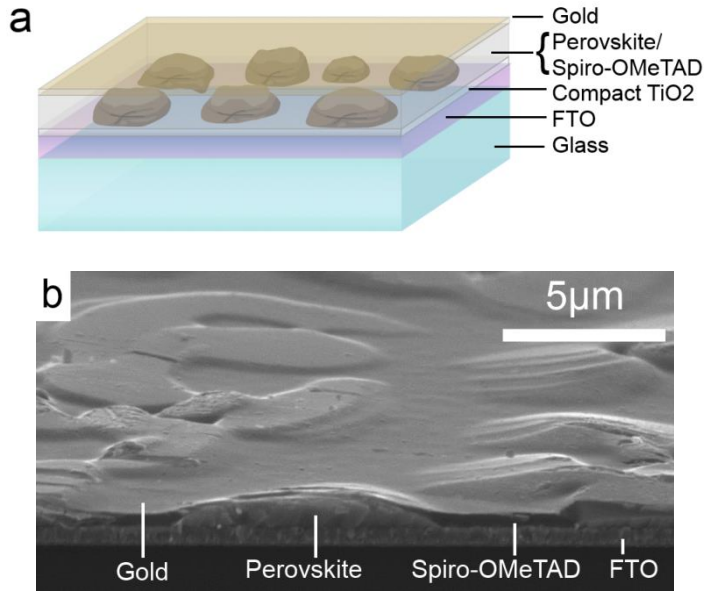

Figure 5.2: Semi-transparent neutral-coloured perovskite solar cells. a) Diagram showing the architecture of the dewet planar perovskite heterojunction solar cell. This diagram was designed by Maximilian Hoerantner of Oxford University. b) Tilted cross-sectional SEM image of a full semi-transparent solar cell showing the perovskite "islands" coated with Spiro-OMeTAD.

Having demonstrated that it is possible to fabricate perovskite films with a wide range of transparencies, with neutral colour attainable at the higher transparencies, planar heterojunction solar cells with a range of transmittances were fabricated, with the architecture shown in Figure 5.2a. An SEM image of a cross section of a full device is shown in Figure 5.2b. The perovskite islands can be clearly seen, with the Spiro-OMeTAD infiltrating the spaces between and also coating the islands with a thin layer.

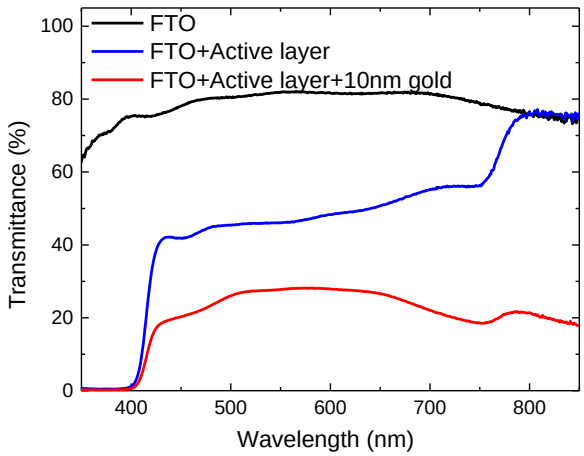

Figure 5.3: Transmittance spectra of the components of a representative semi-transparent cell, showing the transmission of the FTO-glass, the FTO-glass plus active layer, and the whole cell including a semi-transparent gold electrode.

Ideally, extremely transparent and conductive electrodes would be employed on both sides in order to maintain high transparencies. However, full optimisation of the electrodes is beyond the scope of this study, and here fluorine doped tin oxide (FTO) was used as the anode and a thin (~10nm) layer of gold as the cathode. Such devices are reasonably transparent, though the gold electrode is a major source of transmittance loss, as we show in Figure 5.3. This will clearly be a major limitation to the transparency of a final working device; this problem is addressed later in this thesis, in Chapter 8.

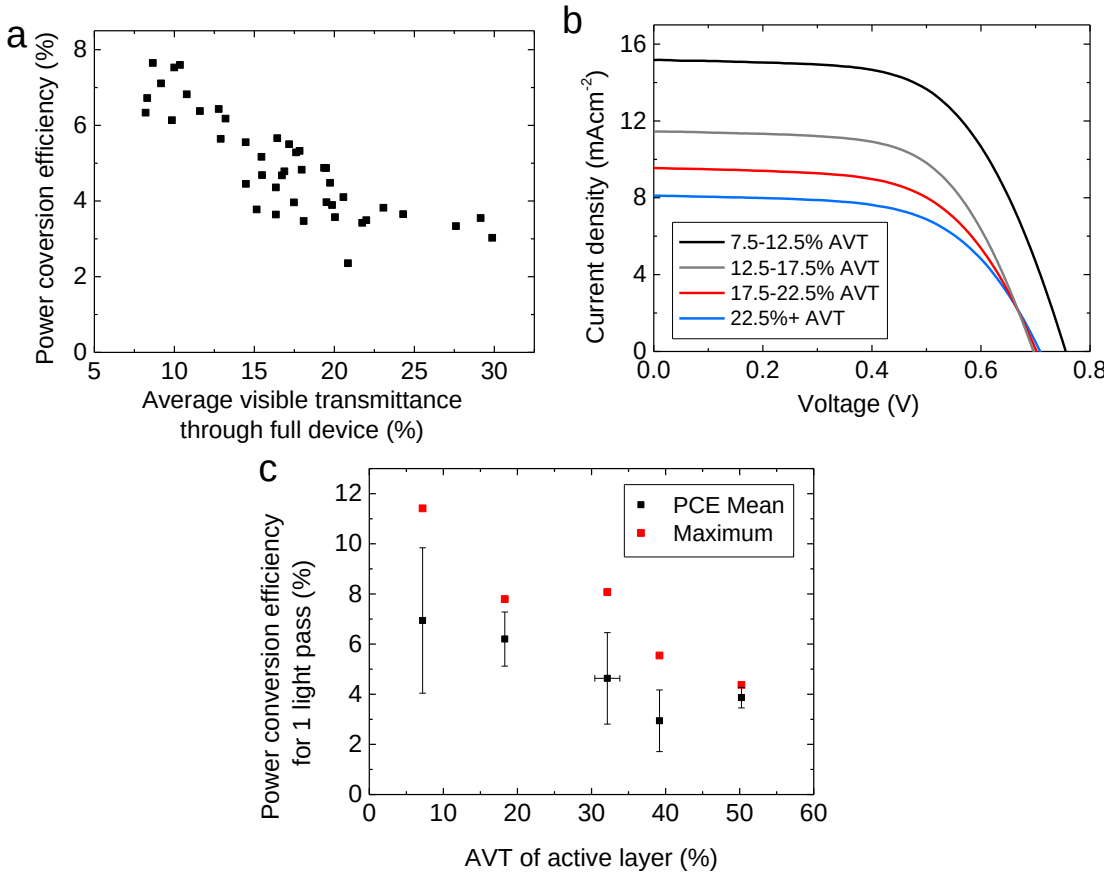

Figure 5.4: Semi-transparent solar cell device performance. a) Power conversion efficiencies for a batch of individual solar cells with ~10nm Au electrodes, plotted as a function of full device AVT. b) Average current density-voltage (JV) characteristics for the cells plotted in (a). The curves are numerical averages of the current-voltage characteristics for individual cells split into the AVT intervals shown, with 5-15 cells per interval. c) Power conversion efficiency plotted as a function of active layer AVT, for a different batch of cells with thicker gold electrodes. The PCE plotted represents that which is attainable with an entirely transparent cathode (not a thick gold cathode). It has been corrected to remove current generated in the second pass (see Section 5.7 for details on calculation). Each point represents the mean of at least 14 individual devices, and the maximum PCE for the champion device in each interval is plotted. In all cases PCE was extracted from current-voltage measurements performed under 100mWcm^{-2} AM1.5 illumination. Full performance data for all devices in this Figure are shown in Table 5.2 and Table 5.3.

AVT interval (%)	Number of devices	Mean AVT (%)	Mean J_{sc} (mAcm^{-2})	Mean V_{oc} (V)	Mean FF	Mean PCE (%)	Min PCE (%)	Max PCE (%)
7.5-12.5	9	9.66	15.2	0.76	0.61	6.9	6.1	7.6
12.5-17.5	15	15.4	11.4	0.70	0.62	5.0	3.6	6.4
17.5-22.5	14	19.6	9.6	0.71	0.61	4.1	2.4	5.3
22.5+	5	26.8	8.1	0.71	0.61	3.5	3.0	3.8

Table 5.2: Performance parameters extracted from current-voltage characteristics measured under 100mWcm^{-2} AM1.5 simulated sunlight for the full semi-transparent solar cells plotted in Figure 5.4a and b.

Mean active layer AVT (%)	No. of devices	Mean J_{sc} measured (mAcm^{-2})	J_{sc} (no second pass) (mAcm^{-2})	Mean V_{oc} (V)	Mean FF	Corrected mean PCE (%)	Corrected min PCE (%)	Corrected max PCE (%)
7.2	16	10.1	9.6	0.88	0.68	7.0	1.0	11.4
18.3	26	14.8	13.8	0.80	0.56	6.2	4.0	7.8
32.1	17	13.3	12.1	0.75	0.53	4.6	1.8	8.1
39.2	20	9.7	8.7	0.72	0.47	2.9	0.8	5.5
50.3	14	9.7	8.5	0.76	0.60	3.9	3.1	4.3

Table 5.3: Performance parameters extracted from current-voltage characteristics measured under 100mWcm^{-2} AM1.5 simulated sunlight for the batch of semi-transparent cells shown in Figure 5.4c, with the correction described later applied to remove current generated in the second pass.

The power conversion efficiencies as a function of AVT of the whole device (including 10nm gold electrode) from a single batch of devices, extracted from current density-voltage curves measured under simulated AM1.5, 100mWcm^{-2} sunlight, are shown in Figure 5.4a. A clear trend is observed; at the lowest transmittances in this batch (AVT ~7%) power conversion efficiencies approach 8%, and as transmittance increases, the efficiency decreases. The most transparent cells, with AVTs of ~30%, show power conversion efficiencies of around 3.5%. In Figure 5.4b average current density-voltage curves from the same devices are shown, split into intervals of AVT. A reduction in photocurrent is observed for the higher transmittance devices, as expected as more light passes straight through the device. Remarkably, it is found that that device yield in these highly discontinuous films does not suffer from critical shunting, as might be expected

based on other thin film solar cells. Although there is a significant spread in device efficiency at similar transmittances, few devices were entirely non-functioning, and the lower coverage films did not show a greater spread. An interesting observation is that open-circuit voltage is similar at ~0.7V for all but the least transmissive set of cells, where it is raised to ~0.75V. It is proposed that greater perovskite coverage reduces Spiro-OMeTAD-compact TiO_2 contact area and that these regions represent a parallel diode to the photoactive regions, with a lower shunt resistance and diode turn-on voltage. Hence, increasing the perovskite coverage increases the overall shunt resistance and increases the V_{oc}. From these JV curves it appears that for the higher transmittances (i.e. lower perovskite coverage), the V_{oc} reaches a minimum of ~0.7V.

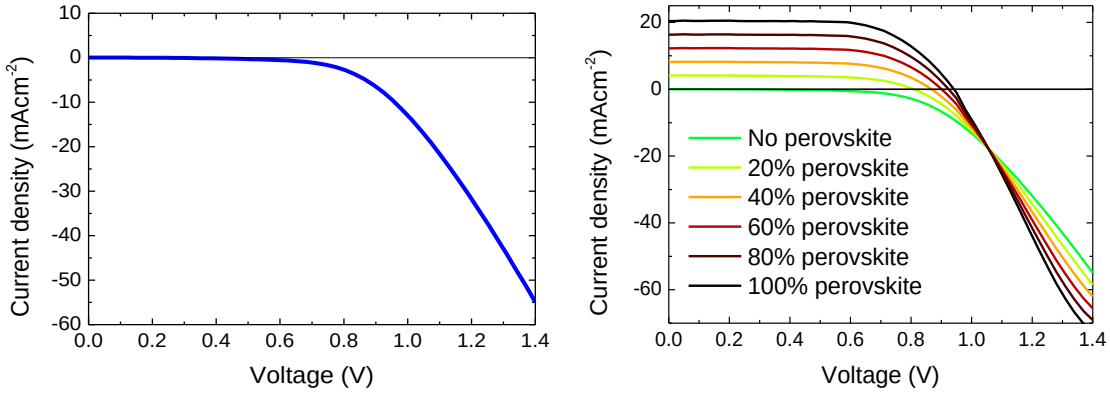

Figure 5.5: Left, Current-voltage characteristics for a Spiro-OMeTAD-compact TiO_2 diode, fabricated in the same way as the perovskite solar cells but with no perovskite layer. Right, Mathematically determined fractional averages between the light current-voltage characteristics of a measured high-performance perovskite planar heterojunction solar cell, and the Spiro-OMeTAD-compact TiO_2 diode.

To further understand this, and understand how even the discontinuous perovskite films can show good rectification behaviour, Spiro-OMeTAD-compact TiO_2 diodes (with no perovskite layer at all) were fabricated and tested. A typical JV curve is shown in Figure 5.5a.Their diode characteristics show a dark current turn-on at also about ~0.7V. A discontinuous layer of perovskite sandwiched between compact TiO_2 and Spiro-OMeTAD is effectively then a combination of such Spiro-OMeTAD-compact TiO_2 diodes and the Spiro-OMeTAD-perovskite-compact TiO_2 solar cell diodes. To simply model current-voltage characteristics that would be expected under illumination with different perovskite coverages, current-voltage characteristics were fractionally averaged between a measured highly efficient planar heterojunction perovskite solar cell (with full perovskite coverage, so no Spiro-OMeTAD-compact TiO_2 parallel diode behaviour) and the Spiro-OMeTAD-compact TiO_2 diode. Modelled current-voltage characteristics are shown in

Figure 5.5. Good rectification behaviour at all fractions of perovskite is observed, and that the V_{oc} would decrease from ~1V to 0.7V, as is observed in measured devices.

It is noted that the percentages of perovskite modelled do not represent the perovskite coverage, simply the mathematical fraction of the full coverage perovskite solar cell current-voltage characteristics versus the Spiro-OMeTAD diode. Varying material thicknesses and resistances make it difficult to more precisely model the exact behaviour of a device with a given perovskite coverage (a mathematical or computational model with two discrete diodes in parallel would need to be used), but it is the trend of V_{oc} dropping from ~1V to ~0.7V, consistent with experiment, which is enlightening here. It can be concluded that even in the case of there being minimum perovskite coverage, we would not expect the diode turn-on voltage to be any lower than 0.7V, and hence this sets a lower limit on the open-circuit voltage. With higher perovskite coverage, the fraction of Spiro-OMeTAD-perovskite-compact TiO_2 diode area compared to Spiro-OMeTAD-compact TiO_2 will increase, and the effective turn-on voltage of these parallel diodes should increase from 0.7V to >1V, as seen.

The electrodes used (FTO and 10nm thick gold) are non-optimum transparent electrodes. Much work is being undertaken to develop highly transmissive and conductive electrodes for semi-transparent solar cells and other applications.[19] In light of this, the best performance that could be achieved from these solar cells, if an entirely transparent cathode was used, was determined. Devices were fabricated with a number of different active layer AVTs, between 5% and 50%, and thicker gold electrodes deposited to minimise electrode resistance. The power conversion efficiency was determined from measuring current-voltage characteristics, and then the photocurrent corrected to remove the fraction of current generated by the second pass of reflected light from the gold electrode (See Section 5.7 for details of calculation). The PCE that could be attained from devices with entirely transparent cathodes was thus determined (Figure 5.4c). It is noted that the measured photocurrent has not been increased to account for light absorbed in the FTO and all the "corrected" photocurrents are lower than the measured photocurrents (Table 5.3). Even so, it can be seen that significantly improved performance could be achieved in comparison to the devices employing the thin gold electrodes, at a given active layer AVT. Notably, ~30% AVT active layers could still generate power conversion efficiencies of over 8%, which is a transparency and a performance that is compatible with commercial applications, being better than currently offered by a-Si, and would represent the best semi-transparent neutral-coloured solar cell efficiency to date. Once the lower open-circuit voltages in these micro-structured perovskite solar cells have been resolved,

the V_{oc} should be able to be pushed up towards the 1.1V which is achievable in uniform planar heterojunction solar cells,[20] which would result in another 20 to 30% increase in relative efficiency. In addition, FTO coated glass was employed here, which is not the most transmissive conducting layer- further improvements are still possible by simply employing a more transparent anode and an antireflective coating. An estimation of the further increases in efficiency possible are discussed in Section 5.8 of this chapter.

5.5 Colour-tinting semi-transparent solar cells

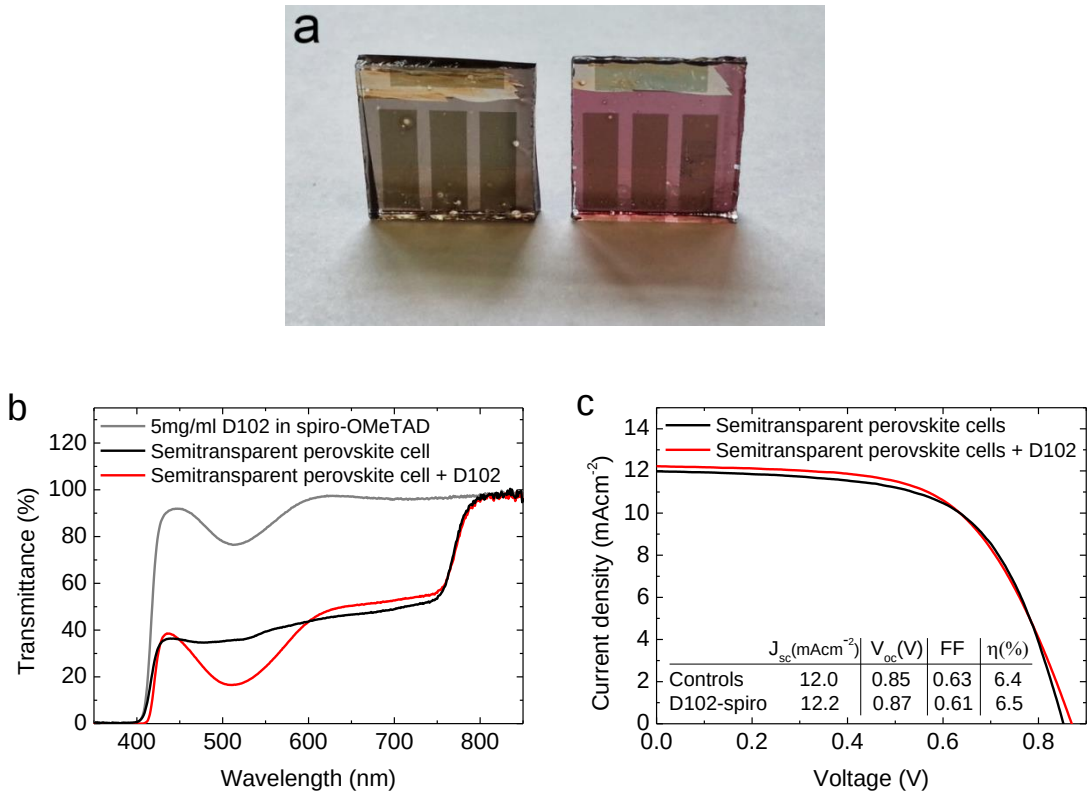

Figure 5.6: a) Photographs of semi-transparent perovskite solar cells without (left) and with (right) D102 dye included in the Spiro-OMeTAD layer, with 10nm gold electrodes. b)Transmittance spectra of the active layer of such cells. c) Average current density-voltage characteristics of such solar cells, demonstrating effectively no change in performance with inclusion of the dye. Device performance parameters are shown in the inset. Averages are numerical averages from 9 D102 doped and 12 control cells.

Having demonstrated a new and versatile means to form neutral-coloured semi-transparent solar cells, an aspect of further interest would be the prospect for lightly colour-tinting such cells, to allow further architectural flexibility and add appeal for

specialised applications. With the micro-structured architecture, it can be envisaged that it should be easy to optically modify the semi-transparent cells by incorporation of a dye or pigment into the regions where light passes through. Here, an indolene dye termed D102 was simply dissolved into the Spiro-OMeTAD solution, and upon application to typical semi-transparent cells it produced "rose-tinted" devices (Figure 5.6a).[21] Plotting this tinted active layer on the chromacity diagram in Figure 5.1f shows these films lie in the pale pink region. As shown in Figure 5.6b, the absorption peak of the dye in addition to the perovskite attenuation is apparent in the transmittance spectrum. While light absorbed by the dye will not contribute to photocurrent, device performance should remain unaltered, provided the dye has not introduced any detrimental electronic artefacts. The current-voltage curves of such devices are shown in Figure 5.6c which confirms this; on average the rose-tinted cells perform similarly to the control cells.

Another way of providing semi-transparency would be to use a wider bandgap perovskite, of which there are many known examples.[22,23] This would allow through light of lower energy than the bandgap, as described in Chapter 2. However, this system would be restricted to the range of colours attainable with such a semiconductor (yellow, though red, to brown); the advantage of dye-tinting a neutral-coloured 'base' is that any colour of dye or pigment could be incorporated, those with proven resilience to long term exposure to light, and even colours typically challenging to achieve with semiconductors, such as green or blue.

There is no 'ideal' semi-transparent solar cell since it depends upon the colour desired. For an application requiring colours achievable with a semiconductor, a continuous layer of wider bandgap perovksite might be preferable. However, the novelty of the approach presented in this chapter is that neutral-coloured semi-transparent solar cells have been fabricated. For colour-neutrality, a bandgap of ~1.6eV or lower is necessary, so that a thick layer absorbs all visible light and hence looks black. This configuration also allows the addition of *any* colour to the grey 'base', providing much greater flexibility in terms of independence of colour and semi-transparency.

As discussed briefly earlier, more transparent electrodes are necessary, specifically the cathode, for fully optimised semi-transparent perovskite solar cells. For this purpose, low temperature processable, and ideally solution processable electrodes need to be developed, which have towards 90% AVT with the order of 10 Ω/□ sheet resistivity and exhibit good ohmic contact to the hole-transporter. Solutions may come from transparent conducting oxides, carbon nanotubes, graphene or metallic nanowires, such as

silver.[6,24,25,26,27] One particular solution to this problem will be discussed further in Chapter 8.

A key concern for an application such as architectural glass is that of long-term stability. Power-generating glass must have a long functional lifetime to avoid the expense of replacing it regularly. The methylammonium lead halide perovskite is hygroscopic, indicating that substantive sealing form the atmosphere is required, facilitated by sealing between two glass sheets. Recent preliminary work on stability has in fact shown that even with rudimentary sealing from the atmosphere, such solar cells are already relatively robust to prolonged exposure and operation under full spectrum sun light. [28,29] Ensuring the materials and solar cell composites are capable of attaining operational lifetimes of over 25 years will prove to be an important consideration, and is likely to be a surmountable challenge.

5.6 Outlook and conclusion

In summary, in this chapter a new concept for the fabrication of neutral-coloured semi-transparent solar cells has been developed, by creating micro-structured layers of organometal halide perovskite by partial dewetting of solution cast films. Complete devices show good efficiencies at reasonable levels of transparencies, with significant scope for further improvement by implementing electrodes with higher transparencies, and enhancing the open-circuit voltage. Furthermore, is has been demonstrated that the micro-structured perovskite film concept can be easily adapted to integrate colour into semi-transparent devices, with no loss in efficiency. This work now enables perovskite solar cells to not only compete for high efficiency opaque applications, but to also offer an ideal solution to building integrated photovoltaics- neutral colour semi-transparency at comparatively high efficiency.

5.7 Additional methods: correction to remove second pass of light reflected from electrodes

In order to account for and remove the extra current generated in the back reflection from the semi-transparent gold contact, the reflectance at a semi-transparent gold-Spiro-OMeTAD contact and the active layer absorption were used to determine what percentage of the current was due to the second pass of light.

The possible current generated in the first pass is from light which is neither reflected nor absorbed in the FTO-coated glass, and is then absorbed in the perovskite. The current generated in the second pass is generated from any light that is not absorbed in the first

pass through the active layer, is reflected at the gold electrode, and is absorbed in the perovskite.

The fraction of current that comes from just the first pass is that which is of interest for a device with transparent electrodes. The total generated current can be multiplied by this factor to get current in the first pass only. This can be expressed as:

$$\frac{J_1}{J_1+J_2} = \frac{\int \varphi T_{FTO} A_{perov}\, d\lambda}{\int \varphi T_{FTO} A_{perov}\, d\lambda + \int \varphi T_{FTO} (1-A_{active\ layer}) R_{spiro-gold} A_{active\ layer}\, d\lambda} \qquad \textbf{5.1}$$

In which φ represents AM1.5 photon flux, and *R*, *A* and *T* are fractional reflectance, absorptions and transmittances. The internal quantum efficiency and the area of the device determine the exact values for generated current, but these factors simply cancel out.

It is noted that light passes through the perovskite *before* the Spiro-OMeTAD in the active layer (for other calculations the distinction has been ignored, but here it is relevant), so for the first pass the absorbance of Spiro-OMeTAD is excluded. This is done by extrapolating the active layer absorption at 500nm to wavelengths below that (typically a flat spectrum is observed for perovskite absorption at these wavelengths, so this assumption is valid) – Spiro-OMeTAD absorbs strongly below 420nm. For the second pass, some light at these wavelengths has now been absorbed in the Spiro-OMeTAD so the whole active layer absorption is used for the total light absorption in the first pass.

The reflectance from a Spiro-OMeTAD-gold semi-transparent contact was measured separately with a gold-Spiro contact on glass, using an integrating sphere.

An example of the calculation is demonstrated in Figure 5.7. The first pass useful absorption (Figure 5.7a, black curve) is simply determined using an integrating sphere, and extrapolated to remove the influence of Spiro-OMeTAD. The second pass useful absorption (Figure 5.7a, blue curve) is determined from the product of the first pass transmittance, including Spiro-OMeTAD absorption (Figure 5.7a, green curve), the reflectance at the Spiro-OMeTAD-gold contact (Figure 5.7a, red curve), and the absorption of the perovskite. In Figure 5.7b, the available AM1.5 photon flux is shown before and after passing through FTO glass. The product of this with the first and second pass absorption (as shown in Figure 5.7a) respectively gives the photon flux absorbed in each pass, which is shown in Figure 5.7c. Integrating these graphs gives the maximum current that could be generated (per m^2, with 100% internal quantum efficiency) in each pass, so as described in Equation 5.1 we can determine the current that could be generated in the first pass only. For the example shown, the integrated values are 8.33 photons $s^{-1}m^{-2}$ and 1.25

photons $s^{-1}m^{-2}$ for the first and second passes respectively, so 87.0% of the measured photocurrent comes from the first pass.

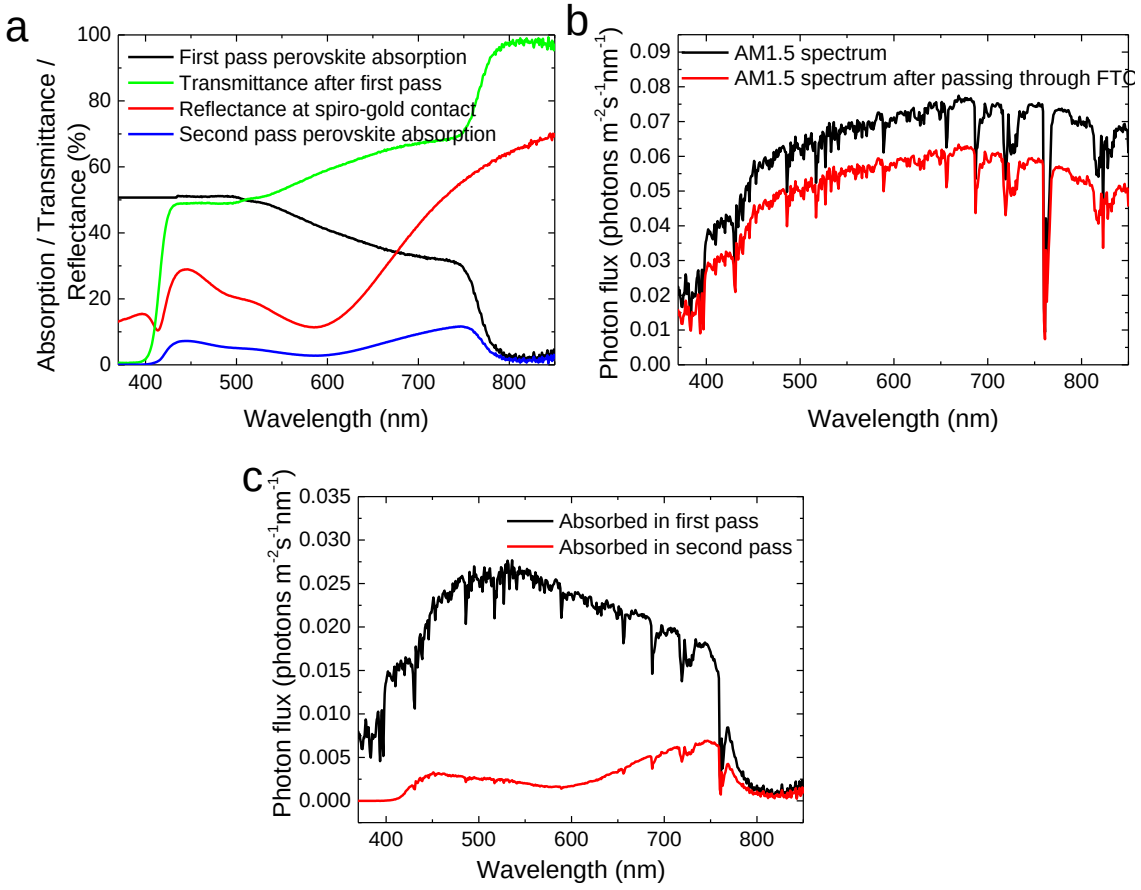

Figure 5.7: a) Example data for a representative semi-transparent perovskite solar cell showing first pass perovskite absorption, and second pass perovskite absorption calculated from the first pass transmittance and gold contact reflectance, also shown. b) The available photon flux before and after passing through FTO. c) Absorbed photon flux in the first and second passes. The ratio of the integrals of these curves gives the ratio of current generated in the first and second passes.

5.8 Additional methods: Estimation of extra photocurrent available with a fully transparent, non-reflective anode

In addition to removing the influence of the second pass, to remove the effect of a non-transparent anode (i.e. FTO coated glass), the extra current available to a semi-transparent solar cell if the anode is also perfectly transparent and non-reflective can be estimated. Using the same method as previously, the total photon flux available for conversion to current (in a single pass) with the product of the AM1.5 solar spectrum can be determined,

either including or excluding the losses (reflective and absorptive) imparted in transmission through the FTO-glass (see Figure 5.7b), with the absorption of the perovskite layer in question. Determining the ratio between the integrals of the resultant graphs (an example is shown in Figure 5.8a) gives a conversion factor for the photocurrent and PCE, to increase it to what it would be if there was no absorption or reflection from the anode. This factor was determined for the devices shown in Figure 5.4c, and the new maximum efficiencies are shown in Figure 5.8b. The conversion factor was approximately 1.25 in all cases, meaning PCE could increase by another 25%. This calculation does neglect any possible discrepancies that may arise due to measured FTO-glass absorption including losses as scatter at near-90° angles, so large that the integrating sphere cannot detect it, which may in fact contribute to photocurrent in a device. Thus this represents a maximum efficiency gain rather than a realistic one.

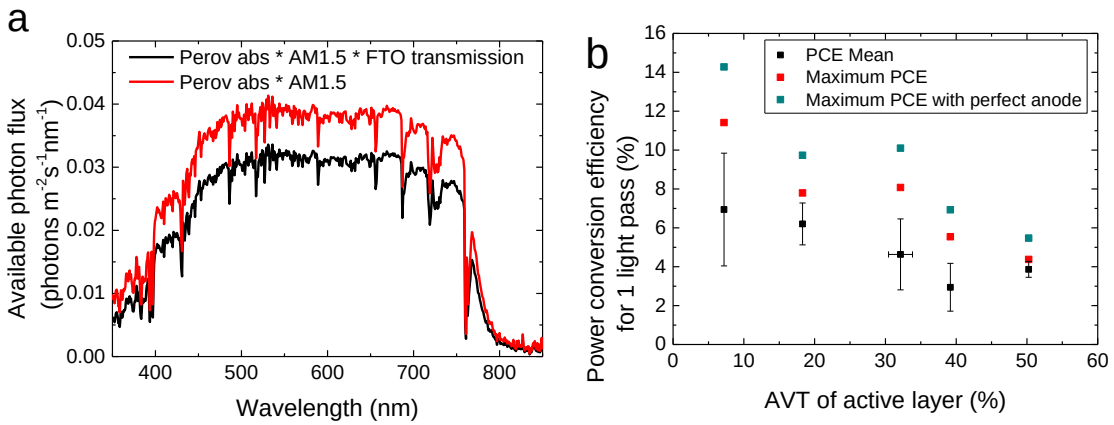

Figure 5.8: a) The available photon flux for a representative semi-transparent perovskite film, determined by multiplying the AM1.5 solar spectrum with the perovskite's absorption, and also the transmittance of the FTO glass for the FTO-inclusive plot. b) The data from Figure 5.4c, with the additional current that could be attained with no absorption or reflection at the FTO-glass taken into account.

5.9 References

1. A. Henemann, *Renew. Energy Focus*, 2008, **9**, 14,16–19.

2. M. G. Kang, N. G. Park, Y. J. Park, K. S. Ryu and S. H. Chang, *Sol. Energy Mater. Sol. Cells*, 2003, **75**, 475–479.

3. K.-S. Chen, J.-F. Salinas, H.-L. Yip, L. Huo, J. Hou and A. K.-Y. Jen, *Energy Environ. Sci.*, 2012, **5**, 9551.

4. Y.-F. Chiang, R.-T. Chen, A. Burke, U. Bach, P. Chen and T.-F. Guo, *Renew. Energy*, 2013, **59**, 136–140.

5. C.-C. Chueh, S.-C. Chien, H.-L. Yip, J. F. Salinas, C.-Z. Li, K.-S. Chen, F.-C. Chen, W.-C. Chen and A. K.-Y. Jen, *Adv. Energy Mater.*, 2013, **3**, 417–423.

6. C. Chen, L. Dou, R. Zhu, C. Chung, T. Song, Y. B. Zheng, S. Hawks, G. Li, P. S. Weiss and Y. Yang, *ACS Nano*, 2012, **6**, 7185–7190.

7. R. F. Bailey-Salzman, B. P. Rand and S. R. Forrest, *Appl. Phys. Lett.*, 2006, **88**, 3–5.

8. F. C. Krebs, T. Tromholt and M. Jørgensen, *Nanoscale*, 2010, **2**, 873–886.

9. A. Colsmann, A. Puetz, A. Bauer, J. Hanisch, E. Ahlswede and U. Lemmer, *Adv. Energy Mater.*, 2011, **1**, 599–603.

10. C.-C. Chen, L. Dou, J. Gao, W.-H. Chang, G. Li and Y. Yang, *Energy Environ. Sci.*, 2013, **6**, 2714–2720.

11. H. J. Snaith, *Adv. Funct. Mater.*, 2010, **20**, 13–19.

12. T. Kirchartz, K. Taretto, U. Rau, V. Ief-photo and F. Ju, 2009, **1**, 17958–17966.

13. T. Ameri, G. Dennler, C. Waldauf, H. Azimi, A. Seemann, K. Forberich, J. Hauch, M. Scharber, K. Hingerl and C. J. Brabec, *Adv. Funct. Mater.*, 2010, **20**, 1592–1598.

14. G. E. Eperon, V. M. Burlakov, P. Docampo, A. Goriely and H. J. Snaith, *Adv. Funct. Mater.*, 2014, **24**, 151–157.

15. J. M. Ball, M. M. Lee, A. Hey and H. J. Snaith, *Energy Environ. Sci.*, 2013, **6**, 1739–1743.

16. M. M. Lee, J. Teuscher, T. Miyasaka, T. N. Murakami and H. J. Snaith, *Science*, 2012, **338**, 643–647.

17. J. M. Ball, S. D. Stranks, M. T. Hörantner, S. Hüttner, W. Zhang, E. J. W. Crossland, I. Ramirez, M. Riede, M. B. Johnston, R. H. Friend and H. J. Snaith, *Energy Environ. Sci.*, 2015, **8**, 602–609.

18. P. Docampo, A. Hey, S. Guldin, R. Gunning, U. Steiner and H. J. Snaith, *Adv. Funct. Mater.*, 2012, **22**, 5010–5019.

19. K. Ellmer, *Nat. Photonics*, 2012, **6**, 808–816.

20. M. Liu, M. B. Johnston and H. J. Snaith, *Nature*, 2013, **501**, 395–398.

21. L. Schmidt-Mende, U. Bach, R. Humphry-Baker, T. Horiuchi, H. Miura, S. Ito, S. Uchida and M. Grätzel, *Adv. Mater.*, 2005, **17**, 813–815.

22. C. H. Nh, J.-H. J. Im, J. Chung, S. S. S.-J. Kim and N. N. N.-G. Park, *Nanoscale Res. Lett.*, 2012, **7**, 353.

23. J. H. Noh, S. H. Im, J. H. Heo, T. N. Mandal and S. Il Seok, *Nano Lett.*, 2013, **13**, 1764–1769.

24. W. Gaynor, G. F. Burkhard, M. D. McGehee and P. Peumans, *Adv. Mater.*, 2011, **23**, 2905–2910.

25. J. Krantz, T. Stubhan, M. Richter, S. Spallek, I. Litzov, G. J. Matt, E. Spiecker and C. J. Brabec, *Adv. Funct. Mater.*, 2013, **23**, 1711–1717.

26. D. Yang, G. Meng, S. Zhang, Y. Hao, X. An, Q. Wei, M. Ye and L. Zhang, *Chem. Commun. (Camb).*, 2007, **1**, 1733–1735.

27. L. Hu, H. S. Kim, J. Y. Lee, P. Peumans and Y. Cui, *ACS Nano*, 2010, **4**, 2955–2963.

28. T. Leijtens, G. E. Eperon, S. Pathak, A. Abate, M. M. Lee and H. J. Snaith, *Nat. Commun.*, 2013, **4**, 2885.

29. J. Burschka, N. Pellet, S.-J. J. Moon, R. Humphry-Baker, P. Gao, M. K. Nazeeruddin, M. Grätzel and M. Gratzel, *Nature*, 2013, **499**, 316–319.

6. SEMI-TRANSPARENT PHOTOVOLTACHROMIC CELLS FOR SELF-TINTING, POWER GENERATING, SOLAR WINDOWS

The work presented in this chapter has been published in:

- A. Cannavale*, G. E. Eperon*, P. Cossari, A. Abate, H. J. Snaith and G. Gigli, "Perovskite photovoltachromic cells for building integration" *Energy Environ. Sci.*, 2015, **8**, 1578–1584.

  *These authors contributed equally to this work.

6.1 Context and summary

In this chapter a new application of the semi-transparent perovskite solar cells is presented. By incorporating an electrochromic component, a dual function 'photovoltachromic' device is fabricated. Such a device has neutral colour and visible transparency but can be switched to a tinted state, allowing a dynamically controllable transparent or opaque device where the power required for the tinting is supplied by the photovoltaic component. Upon irradiation with the sun's light, this device can switch from neutral colour semi-transparent to dark blue-tinted in a matter of seconds; once switched, the photovoltaic component can then provide power to an external circuit as per normal. The combination of a semi-transparent perovskite photovoltaic and solid-state electrochromic cells enables fully solid-state photovoltachromic devices with 26% (or 16%) average visible transmittance and 3.7% (or 5.5%) maximum power conversion efficiency. Upon activating the self-tinting, the average visible transmittance drops to 8.4% (or 5.5%). Such stand-alone, self-powered devices are of commercial interest for integration into windows and surfaces of buildings and vehicles. The results presented in this chapter represent a significant step towards the commercialization of photovoltachromic building envelopes.

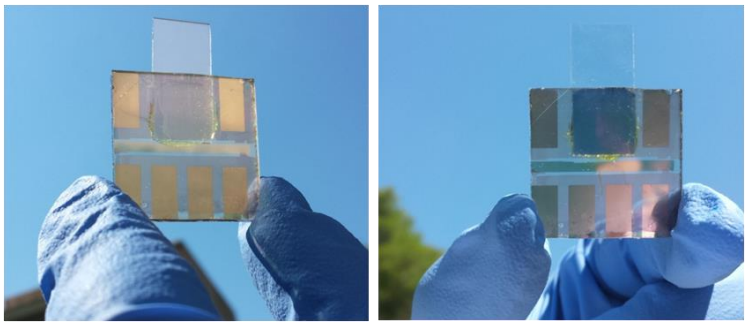

6.2 Introduction

In addition to simply being able to generate power from a neutral-tinted window, as described in the previous chapter, the transparency and the colouring of building glazing envelopes are critical to control the indoor thermal and visual comfort.[1,2] Electrochromic devices have been described in Chapter 2. Such devices, currently available on the market, can modulate their throughput of light and thereby heat by applying an external voltage bias, resulting in a change in transparency which does not require continuous voltage input.[3,4] Bechinger and co-workers first proposed self-powered electrochromic windows, namely photoelectrochromic cells (PECs), where the colouration process is generated by the cell itself, adaptively changing with the external light condition.[5] This is similar process to that in photochromics, as found in self-tinting glasses – while light can switch the transparency, it is not controllable. In this original architecture, PECs formed of photoactive and the chromogenic electrodes on two separate glass substrates were separated by a liquid electrolyte.[6,7] The photoactive electrode was made from a dye-sensitized titanium dioxide layer and the chromogenic electrode with tungsten oxide (WO_3). Upon short-circuiting the device, photoexcited electrons from the sensitized TiO_2, and lithium ions from the electrode, are driven into the WO_3 resulting in a change to Li_XWO_3 which as described earlier has a deep bluish tint.[5] In 2009, this field was advanced further by Wu and co-workers who integrated PV and PEC technologies in a single device, which is now termed a photovoltachromic cell (PVCC).[8] Their first device was effectively a back-to-back dye sensitized solar cell / electrochromic device, where the bias for the electrochromic switching is provided by the solar cell. The key advance here is that switching is controllable, and the solar cell can be used to generate power for an external circuit once switching is achieved. They demonstrated self-adaptive transparency up to 50% - only in the electrochromic central area - and maximum PCE below 1%. Although such PVCCs are one of the most promising device concepts for building-integrated PV,[9,10] their current PCE is not enough to offset the additional cost involved in adding the second device layer. Furthermore, they are prepared using liquid or gel electrolytes, which are a significant drawback for processing and durability.[11–13] To overcome this problem, several attempts have been devoted to the development of solid-state polymer electrolytes (SPEs) which can show good adhesion between the glass electrodes, high optical transparency, good mechanical properties, simple processability and, most importantly, no issues with leakage or evaporation over time.[14] This is analogous to the development of solid-state hole transporters for dye-sensitized solar cells. SPEs have been prepared with complexes of lithium salts (LiX) and high molecular weight polyethylene oxide (PEO).[15] Nevertheless,

most PEO-LiX SPEs show good ionic conductivity only when heated above 60°C,[16,17] which makes them unsuitable for room temperature applications such as PVCCs.

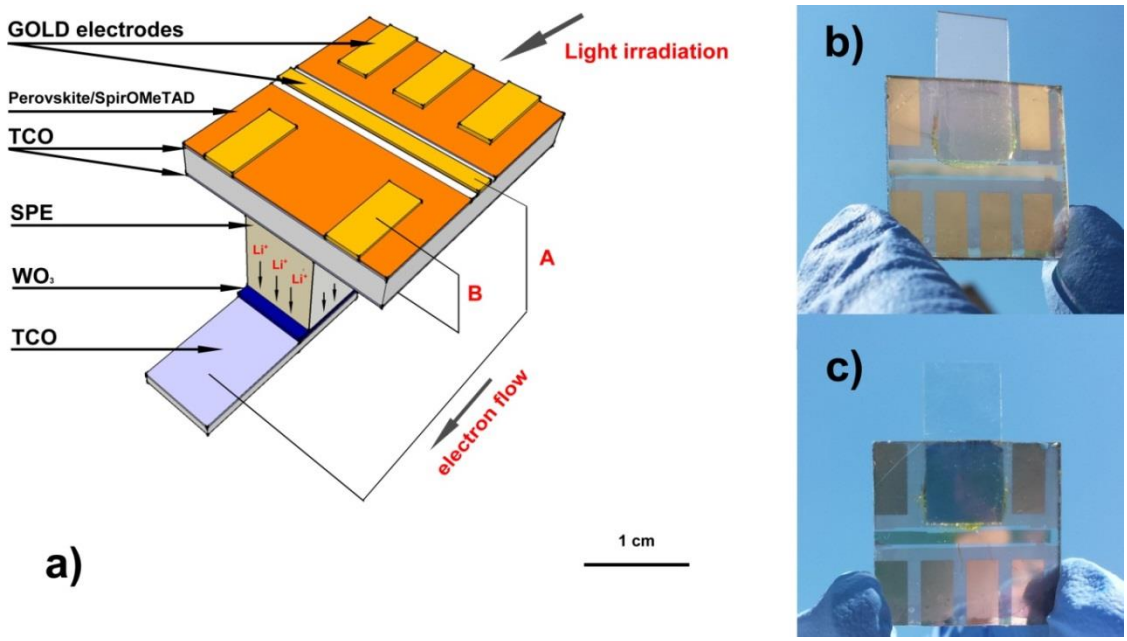

Figure 6.1: a) Axonometric view of the photovoltachromic device. Two external circuits connect the photoanode to the electrochromic electrode (A) and the gold cathode to the secondary electrode of the electrochromic device (B). Pictures of the device in bleached (b) and coloured conditions (c) are shown on the right end side. Schematic designed and photos taken by Alessandro Cannavale of the Unviersity of Salento, Italy.

In this chapter, a fully solid-state perovskite PVCC with self-adaptive transparency and a maximum PCE over 5% is reported. The device is realized by depositing the photovoltaic (PV) and the electrochromic (EC) layers on two separate glass slides. In Figure 6.1a) a scheme of this new device architecture is shown. The top glass slide has both sides coated with transparent conductive oxides (TCO), which work as independent electrodes for the PV and the EC cells, while the bottom glass slide has only one side coated with a TCO. The PV cell is made by a semitransparent $MAPbI_{3-x}Cl_x$ perovskite deposited on the top TCO glass. The EC layer is made by WO_3 deposited on the bottom TCO glass, and an SPE prepared with PEO-LiX and polyethylene glycol (PEG) is used as a glue to laminate the two glasses together and complete the EC cell. In Figure 6.1, pictures are also shown of the prototype device with the EC active area completely bleached (b) and coloured (c). To activate the colouring, the electrodes were connected as shown in Figure 6.1a) and the device exposed to solar light. Once the colouration has occurred, the PV cell can be used to

generate useful power for an external circuit. In a photovoltachromic module, it is imagined that there would be a switch to direct the output of the PV cell as required to either the electrochromic or the external circuit.

6.3 Semi-transparent and tinted devices

Semitransparent perovskite were prepared by controlling the film morphology in order to form an 'island-type' microstructure as described in the previous chapter. Dewetting of the perovskite film from the TCO glass was encouraged, causing it to form discrete micron-sized islands, indistinguishable to the naked eye. The islands are thick enough to be fully absorbing of incident light with energy above the bandgap of the perovskite semiconductor (~1.57eV). The combination of fully absorbing islands and fully transparent regions results overall in a homogeneous-looking, semi-transparent and neutral-coloured perovskite film (see Figure 6.1b and c). The semitransparent solar cell architecture is as reported in Chapter 5.

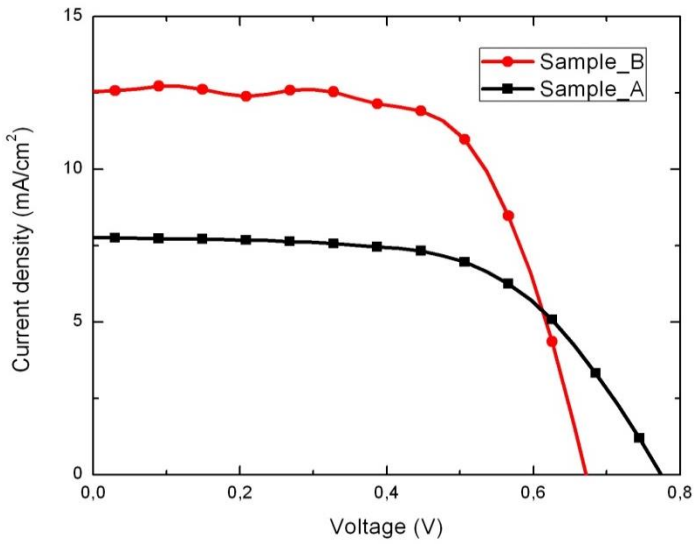

Figure 6.2: Current-voltage characteristics for the solar cell layers of the PVCC devices made with two different transparencies. Devices were measured under simulated 100 mW cm^{-2} AM1.5 illumination as detailed in the Experimental section.

	V_{oc} (V)	J_{sc} (ma cm^{-2})	FF	PCE (%)	AVT (%)
Sample A	0.77	7.8	0.59	3.7	26.1
Sample B	0.68	12.5	0.63	5.5	15.9

Table 6.1: Photovoltaic performance parameters of PVCCs with two different transparencies, showing performance parameters extracted form JV curves in addition to AVT.

Microstructured $MAPbI_{3-x}Cl_x$ perovskite films were fabricated with two different surface coverages, meaning that the ratio of transparent and fully absorbing areas was changed, controlling the overall macroscopic transparency. In Figure 6.2, the current-voltage characteristics of the PV component of two PVCCs with different transparency are shown (Sample A and B). The PV performance parameters and the average visible transmittance are summarised in Table 6.1. AVT is, as in the previous chapters, defined as the mean transmittance between 370 nm and 740 nm; in the non-coloured state (bleached) it was measured as 26.1 and 15.9 % for the electrochromic areas of Sample A and B respectively. It is noted that here light is passing through the solar cell active layer plus the electrochromic cell, but not the gold electrodes. As already observed in the previous chapter, the less transparent device (Sample B) displays significantly higher short-circuit current and an overall power conversion efficiency of 5.5%, compared to the more transmissive device with PCE of 3.7%.

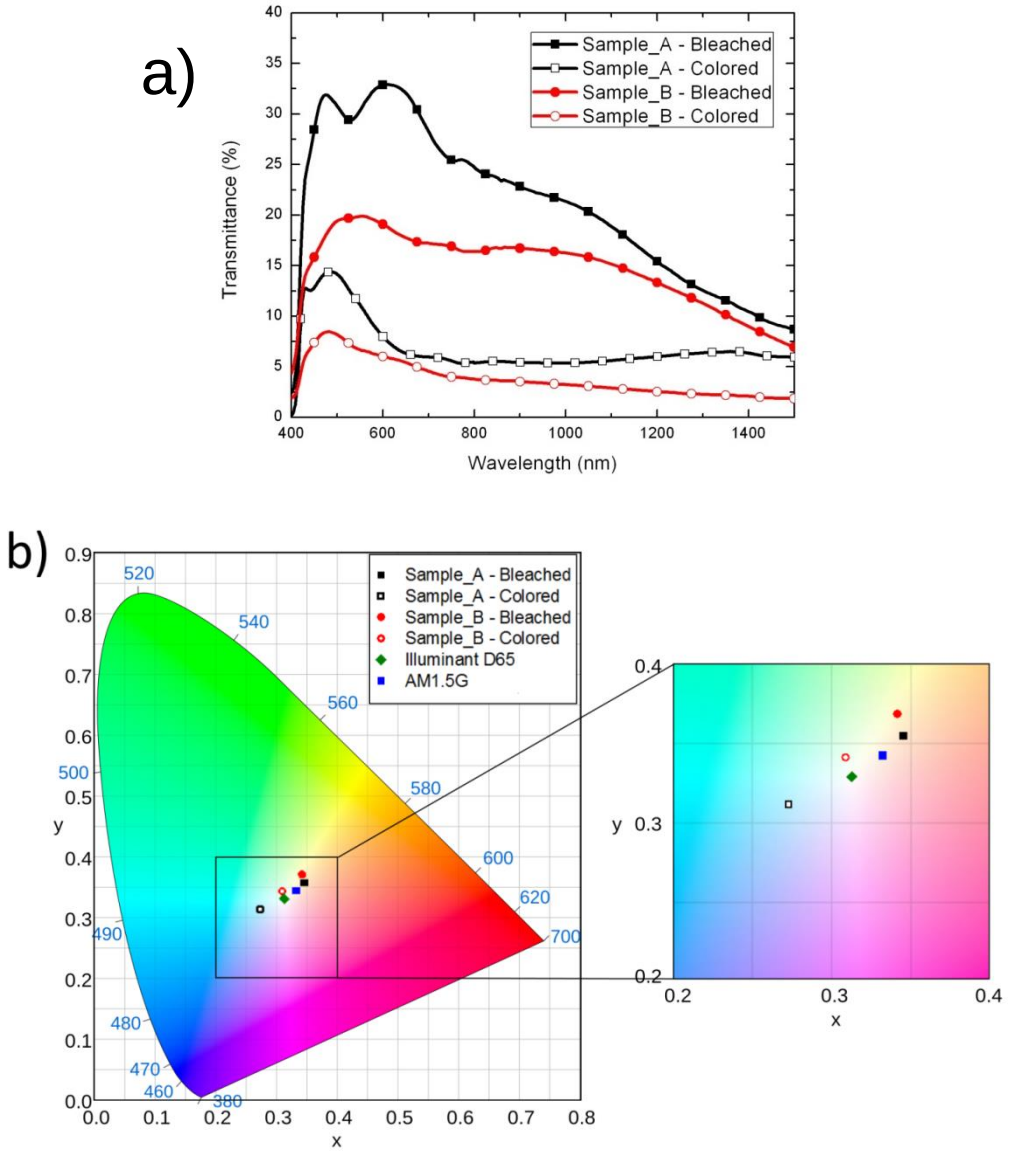

Figure 6.3: a) Transmittance spectra of complete PVCCs (Sample A and Sample B) in bleached and coloured conditions in a range of wavelengths between 400 nm and 1500 nm. b) colour coordinates of the films with transmittance spectra shown in (a) under AM1.5 illumination, plotted on the CIE xy 1931 chromaticity diagram, and the enlarged central region. Colour coordinates of the D65 standard daylight illuminant and AM1.5 illumination are also shown. Transmittance spectra taken by Alessandro Cannavale of the University of Salento, Italy.

Figure 6.3a) shows the bleached/coloured transmission spectra of the EC active area for Sample A and B. A maximum bleached/coloured modulation of 26 and 12% is observed at 635 nm for Sample A and B respectively. The modulation, averaged all over the visible spectra (370 – 740 nm), was also determined, and was found to be ~18 and ~10% for

Sample A and B respectively. The best literature values for purely electrochromic windows are now above 60%, with a high of 68% recently reported.[4] Self-powered PVCCs have been reported with up to 24% modulation over solar wavelengths.[14] Though the values attained here are not comparable to what is reported for the best electrochromic windows (power via an external circuit), they are an impressive result for self-powered devices.

The AVT after colouration was also calculated for the electrochromic area of both devices; sample A changes from AVT of 26.1% (bleached) to 8.4% (coloured), and sample B from 15.9% to 5.5%. These are very notable changes in AVT, going from obviously transparent to much more opaque. Clearly sample A, the more transparent perovskite sample, will make a more transparent window in the bleached state, but this is at the cost of photovoltaic performance.

In addition to modular transparency, neutral-colouring is particularly desired in glazing for building integration. To quantify the colour of the EC active area and the change it undergoes when transitioning from bleached to coloured, colour perception indices were calculated according to the CIE 1931 xy colour space standard.[18,19] Figure 6.3b) shows these colour coordinates of the transmission through the whole active region of the devices in both coloured and bleached states, compared to the reference daylight illuminant D65 and the AM1.5 spectrum. It is observed that the PVCCs in the bleached state have good colour-neutrality, lying well within the central region of the chromaticity diagram, close to the AM1.5 spectrum. In the coloured state, both devices shift towards the blue side of the colour plot. Sample A demonstrates a more extreme change than sample B, as would be expected for the more absorbing sample. Despite shifting towards a bluer colour perception, both devices still exhibit colour perception close to the centre of the plot, and thus have good colour-neutrality, which make them ideal candidates for building integration.

6.4 Colouration performance

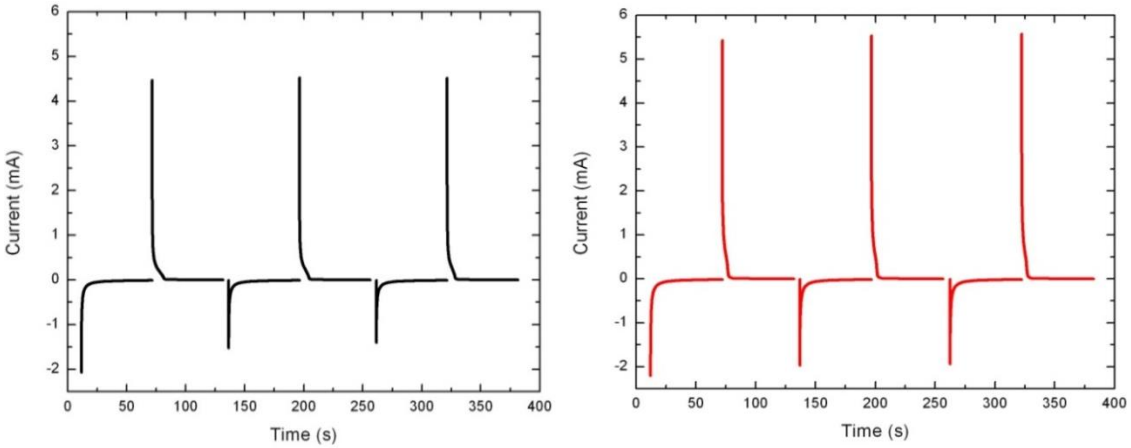

Figure 6.4: Chronoamperometric measurements for Sample A (left hand side) and Sample B (right hand side). Data taken by Pierluigi Cossari of the University of Salento, Italy.

Figure 6.4 shows the chronoamperometric (current-time) measurements of the EC cell in Sample A and Sample B. A voltage of -0.6 V was applied to the electrodes of the EC part of the device. An immediate spike of current is observed in both of the devices; this value decreases to roughly 30 μA in about 15-20 s, when the device reaches a stable colouration. Then, the bias was inverted and the bleaching was observed to take place with similar kinetics. Three complete cycles of colouring/bleaching are shown, demonstrating that the colouration process is extremely fast and reproducible in both samples. Such good EC behaviour is due to a careful design of the SPE composition (notably, the incorporation of PEG) and as a result the high ionic conductivity achieved at room temperature (1.25×10^{-5} S cm^{-1}, as determined by impedance spectroscopy- described in Section 6.6.5).

To establish if the semi-transparent solar cells provide enough power to drive the colouration, the power absorbed during the colouration process was also calculated, using the same chronoamperometric curves shown in Figure 6.4. For Sample A an initial value of 2.7 mW cm^{-2} was estimated (3.8mW cm^{-2} for Sample B), which decays to zero within 15-20 s, when the colouration is completed. Therefore, the power produced by the PV component (3.7 and 5.5 mW cm^{-2} under AM1.5 illumination for Sample A and B respectively) is thoroughly sufficient to drive the electrochromic component and the power produced by the PV device be used in an external circuit after only 20 s, once the colouration is completed.

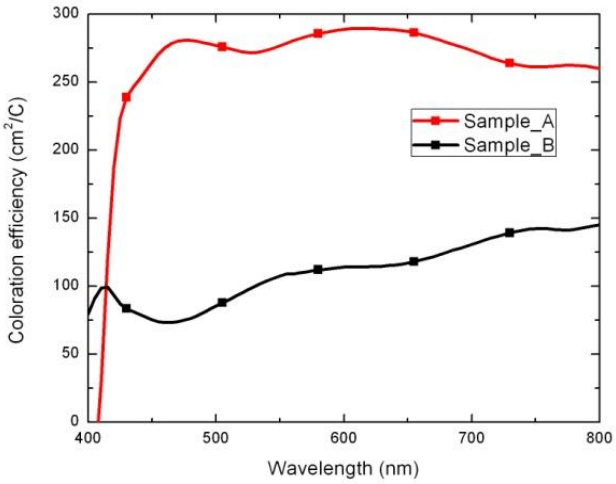

Figure 6.5: Colouration efficiency spectra of Sample A and Sample B. Data measured by Alessandro Cannavale of the University of Salento, Italy.

To evaluate the quality of the EC cells the colouration efficiency (CE) was measured, one of the most commonly used performance parameters.[20] A well-known expression relating the efficiency to the optical density was used to calculate CE, which in turn depends on the transmittances of coloured (T_c) and bleached states (T_b), and the inserted charge (Q), as follows:

$$CE = \frac{log\frac{T_b}{T_c}}{Q} \qquad \textbf{6.1}$$

The plot for the electrochromic performance is shown in Figure 6.5. At a wavelength of 620 nm, the colouration efficiency was determined to be 289 $cm^2\ C^{-1}$ for Sample A and 114 $cm^2\ C^{-1}$ for Sample B. The higher performance observed in Sample A is expected; it can be explained by considering the higher transparency of device A in the bleached state and the lower amount of charge absorbed by Sample A during the colouration (3.3 compared to 4.4 mC for Sample B). This is an impressive coloration efficiency; while in electrochromic devices, the highest reported coloration efficiencies at single chosen wavelength are ~760 $cm^2\ C^{-1}$, in integrated PVCC devices the reported values are less than 100 $cm^2\ C^{-1}$.[9] This thus represents a substantial improvement for the integrated devices.[21]

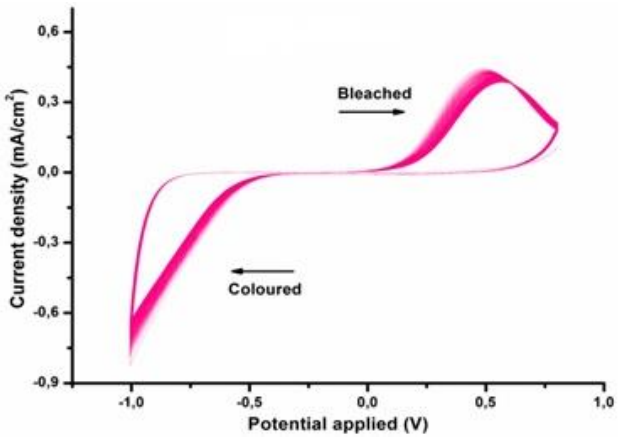

Figure 6.6: Cyclic voltammogram of the EC component of the PVCC showing 300 consecutive cycles. Data taken by Pierluigi Cossari of the University of Salento, Italy.

Figure 6.6 shows the cyclic voltammogram of the EC component of the PVCC. The colouring and bleaching associated with WO_3 reduction and oxidation were observed by polarizing between -1 and 1 V. A stable current response was achieved after 50 cycles and no significant changes were observed up to 300 cycles, which indicate good electrochemical reversibility and stability. It is noted here that the EC cell was assembled by making use of the SPE (see Section 6.6.3 for detailed formulation) as a glue to laminate the two glass electrodes; no additional sealing was used to protect the device from exposure to humid air.

6.5 Outlook and conclusion

In this chapter, perovskite PVCCs with self-adaptive transparency have been detailed. The combination of a semi-transparent perovskite photovoltaic and SPE electrochromic enables a fully solid-state PVCC with 26% AVT and 3.7% maximum PCE (or 16% AVT and 5.5% maximum PCE), that switches to an AVT of 8.4% (or 5.5%) upon self-activated tinting under illumination. The change occurs in only ~20 seconds of illumination, after which the power generated from the solar cell can be used in external circuits. This result represents a significant step towards the commercialization of building integrated PVCC, allowing efficient self-powered tinting windows with the additional possibility of delivering external power. All of the key components of the system are relatively cheap and the fabrication is compatible with a lamination process, which is well-known in the glazing industry.

6.6 Additional methods: PVCC device fabrication and testing

6.6.1 Electron beam deposition

Tungsten oxide layers (550 nm thick WO_3) were deposited by electron beam deposition on ITO/glass substrates (VisionTech 12 Ω/□). The vacuum chamber was initially evacuated to 10^{-6} mbar, and then pure dry oxygen was admitted through a needle valve. The pressure was maintained at 10^{-4} mbar throughout the process. The deposition rate was about 1.5 Å s^{-1}. During the deposition process, the chamber reached a temperature of about 215 °C. High vacuum e-beam deposition was also performed to obtain a secondary ITO conductive layer on the FTO glass used for the photovoltaic purposes. In more detail, a 150 nm thick Indium tin oxide ($Sn:In_2O_3$) was used as a conductive layer in order to control the electrochromic functionality of the device. In this case, the vacuum chamber was initially evacuated to 10^{-7} mbar and then a pure dry oxygen flux was admitted through a needle valve. The pressure was maintained at 10^{-4} mbar throughout the deposition. The deposition rate was ~0.5 Å s^{-1} and the substrate temperature was kept at 240°C during the process. Sheet resistance (20 Ω/□) was assessed by the four-probe van der Pauw technique.

6.6.2 Solid polymer electrolyte

The poly(ethylene oxide: poly(ethylene glycol:lithium iodide (PEO:PEG:LiI) electrolyte was prepared with ether-oxygen to lithium [EO]:[Li+] molar ratio of 4:1, whereas the PEO:PEG weight ratio was fixed as 40:60. A homogeneous mixture of PEG and lithium salt was obtained by stirring the desired concentration of polymer and lithium salt for a period of at least 6 hours in a dry argon-filled glovebox. PEO was then dispersed in PEG/LiI system by adding anhydrous acetonitrile and stirred until it dissolved in the mixture. Finally, the residual solvent was evaporated at room temperature and the polymer electrolyte was dried under vacuum for 72 hours.

6.6.3 Photovoltachromic device fabrication

A small amount of SPE was spread on the WO_3 coated TCO glass and pressed on the second glass to reproduce the architecture reported in Figure 6.1a. Mechanical pressure and mild vacuum was applied for 1 hours to laminate the two glass electrodes and remove any residual of air in the electrolyte.

6.6.4 Electro-optical characterization

Optical transmittance spectra of the short-circuited devices were observed by a VARIAN 5000 spectrophotometer in a wavelength range between 400 nm and 1500 nm. Full spectrum measurements were obtained by irradiating the short-circuited device using an array of seven white Luxeon LED (Cool White 6500 K, 7 LED 40 mm–1540 lm at 700 mA), operated by a Keithley source meter. During these measurements, the devices were connected as shown in Figure 6.1 using one photovoltaic pixel per time. Chronoamperometry measurements were collected with Autolab PGSTAT302N (Metrohm AG, the Netherlands) potentiostat.

6.6.5 Electrochemical characterization

Cyclic voltammetry and CA analysis of the EC device were performed on an Autolab PGSTAT 302N in the potential range of ±1V at a scan rate of 1mV s-1.

Electrochemical impedance spectroscopy (EIS) was carried out using an Autolab PGSTAT302N (Metrohm AG, the Netherlands) combined with a FRA32 frequency generator module by sweeping over 70 points in the frequency range from 10^{-1} – 10^{6} Hz with a root mean square (RMS) amplitude of 10 mV. The electrolytes with a diameter of 10 mm and a thickness of 50 µm were sandwiched between two stainless steel blocking electrodes separated by a Teflon ring. Impedance spectra were recorded after applying a colouration voltage of 1V for 10 min in order to reach a steady state. The ionic conductivity (σ) was calculated using the relation $\sigma = l/R_b A$, where l is the thickness of the polymer electrolyte film, A is the contact area between the electrolyte and the electrode, and R_b is bulk resistance obtained from the intercept of the semicircle with the real axis of the Z' versus Z'' Nyquist plot.

6.7 References

1. C. G. Granqvist, a. Azens, P. Heszler, L. B. Kish and L. Österlund, *Sol. Energy Mater. Sol. Cells*, 2007, **91**, 355–365.

2. A. Cannavale, F. Fiorito, D. Resta and G. Gigli, *Energy Build.*, 2013, **65**, 137–145.

3. R. D. Rauh, *Electrochim. Acta*, 1999, **44**, 3165–3176.

4. R. Baetens, B. P. Jelle and A. Gustavsen, *Sol. Energy Mater. Sol. Cells*, 2010, **94**, 87–105.

5. C. Bechinger, S. Ferrere, A. Zaban, J. Sprague and B. A. Gregg, *Nature*, 1996, **383**, 608–610.

6. U. O. Krašovec, A. Georg, A. Georg, V. Wittwer, J. Luther and M. Topič, *Sol. Energy Mater. Sol. Cells*, 2004, **84**, 369–380.

7. A. Georg, A. Georg and U. O. Kra, 2006, **502**, 246–251.

8. J. J. Wu, M. D. Hsieh, W. P. Liao, W. T. Wu and J. S. Chen, *ACS Nano*, 2009, **3**, 2297–2303.

9. A. Cannavale, M. Manca, F. Malara, L. De Marco, R. Cingolani and G. Gigli, *Energy Environ. Sci.*, 2011, **4**, 2567.

10. A. Cannavale, M. Manca, L. De Marco, R. Grisorio, S. Carallo, G. P. Suranna and G. Gigli, *ACS Appl. Mater. Interfaces*, 2014, **6**, 2415–2422.

11. A. Abate, A. Petrozza, V. Roiati, S. Guarnera, H. Snaith, F. Matteucci, G. Lanzani, P. Metrangolo and G. Resnati, *Org. Electron.*, 2012, **13**, 2474–2478.

12. A. Abate, A. Petrozza, G. Cavallo, G. Lanzani, F. Matteucci, D. W. Bruce, N. Houbenov, P. Metrangolo and G. Resnati, *J. Mater. Chem. A*, 2013, **1**, 6572.

13. M.-C. Yang, H.-W. Cho and J.-J. Wu, *Nanoscale*, 2014, **6**, 9541.

14. C. G. Granqvist, *Thin Solid Films*, 2014, **564**, 1–38.

15. M. J. Reddy, J. S. Kumar, U. V. Subba Rao and P. P. Chu, *Solid State Ionics*, 2006, **177**, 253–256.

16. P. Lightfoot, M. A. Mehta and P. G. Bruce, *Science*, 1993, **262**, 883–885.

17. A. M. Christie, S. J. Lilley, E. Staunton, Y. G. Andreev and P. G. Bruce, *Nature*, 2005, **433**, 50–53.

18. R. W. G. Hunt and M. R. Pointer, *Color Res. Appl.*, 1985, **10**, 165–179.

19. T. Smith and J. Guild, *Trans. Opt. Soc.*, 1931, **33**, 73–134.

20. A. Georg, A. Georg and U. Opara Krašovec, *Thin Solid Films*, 2006, **502**, 246–251.

21. G. Sonmez, H. Meng and F. Wudl, *Chem. Mater.*, 2004, **16**, 574–580.

7. FORMAMIDINIUM LEAD HALIDE: A BROADLY TUNABLE PEROVSKITE FOR EFFICIENT PLANAR HETEROJUNCTION SOLAR CELLS

The work presented in this chapter has been published and discussed in:

- G. E. Eperon, S. D. Stranks, C. Menelaou, M. B. Johnston, L. M. Herz and H. J. Snaith, "Formamidinium Lead Trihalide: A Broadly Tunable Perovskite for Efficient Planar Heterojunction Solar Cells*", Energy Environ. Sci.*, 2014, **7**, 982–988.
- M. R. Filip, G. E. Eperon, H. J. Snaith and F. Giustino, *Nat. Commun.*, "Steric Engineering of Metal-halide Perovskites with Tunable Optical Band Gaps", 2014, **5**, 5757.

7.1 Context and summary

Having established in the previous chapters that planar heterojunction perovskite solar cells, with a smooth and uniform perovskite film, will function most effectively, the focus of the thesis now shifts to understanding how to improve device efficiency by modifying and understanding the perovskite material itself. Most previous work on perovskite solar cells, including that in this thesis so far, has focused on methylammonium lead trihalide perovskites, with a bandgaps of ~1.57eV and greater. Here, the effect of replacing the methylammonium cation in this perovskite is explored, and it is shown that with the slightly larger formamidinium cation, formamidinium lead trihalide perovskites with a bandgap tunable between 1.48 and 2.23 eV can be synthesised. The 1.48 eV-bandgap perovskite is most suited for single junction solar cells; long-range electron and hole diffusion lengths are demonstrated in this material, making it suitable for planar heterojunction solar cells. Such devices are fabricated, and due to the reduced bandgap high short-circuit currents of >23mAcm^{-2} are achieved, resulting in power conversion efficiencies of up to 14.2%, the highest efficiency reported at this point for solution processed planar heterojunction perovskite solar cells. Moreover, this material exhibits increased thermal stability compared to the methylammonium based perovskite. Formamidinium lead halide is hence a promising and likely ultimately superior candidate for the highest efficiency perovskite solar cells.

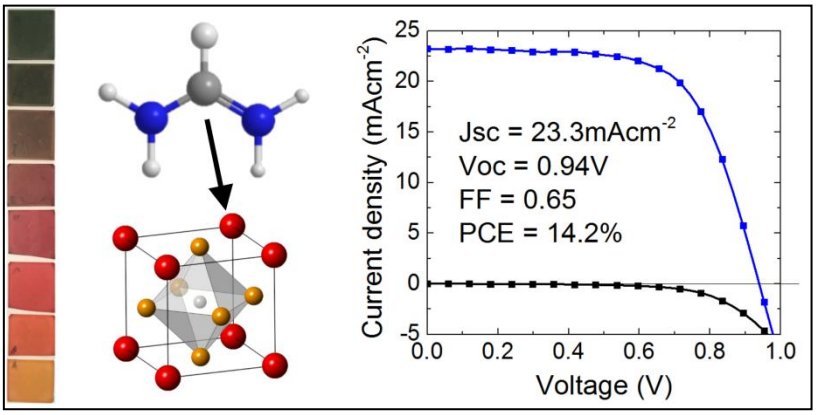

7.2 Introduction

The most studied perovskite material for solar cell applications, and that which the prior sections of this thesis have focussed on, is methylammonium lead halide. Previous studies have shown that by varying the halide composition between iodide and bromide in this material, the bandgap can be tuned between 1.57 and 2.3eV, enabling variation in colour and optimisation for applications in multi-junction solar cells.[1] However, it is known that the optimal bandgap for a single-junction solar cell is between 1.1-1.4eV, as discussed in Chapter 2. This is beyond the range of the methylammonium lead halide system.[2] In addition, for the bottom cell in a tandem architecture, the optimum band gap is around 1eV, giving good motivation to realise lower band gap perovskite absorbers.[2] As illustrated in Figure 7.1a, and discussed in more detail in Chapter 2, perovskites are defined as any compound which crystallises in the ABX_3 structure, consisting of corner-sharing BX_6 octahedra with the A component neutralising total charge. In the case of the organometal halide perovskites, A is an organic cation, B is the metal cation, and X a halide anion. Methylammonium lead triiodide, the perovskite of most recent interest, has a tetragonal perovskite structure arising from a distortion of the perovskite lattice.[3] It has been proposed that in this system, the organic A cation does not play a major role in determining the band structure, and acts to fulfil charge neutrality within the lattice.[4] Nevertheless, its size is important. A larger or smaller A cation can cause the whole lattice to expand or contract, and it causes bending of the X-B-X bond angle.[5] Changing the B-X bond length has been demonstrated to be important in determination of bandgap.[1] Motivated by this, an investigation into whether the bandgap could be tuned in a similar way by variation of the A cation size was carried out. Given a particular metal and halide, there is a relatively small size range allowed for the A cation, since it must fit between the corner-sharing metal halide octahedra. If it is too large, the 3D perovskite structure is unfavourable; lower-dimensional layered or confined perovskites will be formed.[3] If too small, the lattice would be too strained to form. A so-called tolerance factor has been defined previously, to describe the limits on ionic sizes of each component, as detailed in Chapter 2. The larger ethylammonium cation has been explored previously in solar cells, and was shown to form a wider bandgap perovskite due to a lower dimensional 2H-type structural rearrangement- it was too large to maintain the 3-dimensional ABX_3 lattice.[6]

In this chapter, the impact of tuning the size of the A cation is explored, in order to push the bandgap of the perovskite absorber further towards the infrared. It is found that an increase in the cation size results in a reduction in the band gap, and solar cells employing formamidinium lead triiodide are fabricated, that convert to current a greater proportion

of the sun's spectrum than the methylammonium analogue. High efficiency solution-processed planar heterojunction solar cells are fabricated, demonstrating power conversion efficiencies of up to 14.2%. This work represents the first known instance of formamidinium lead trihalide perovskite solar cells.

7.3 Replacing the A site cation

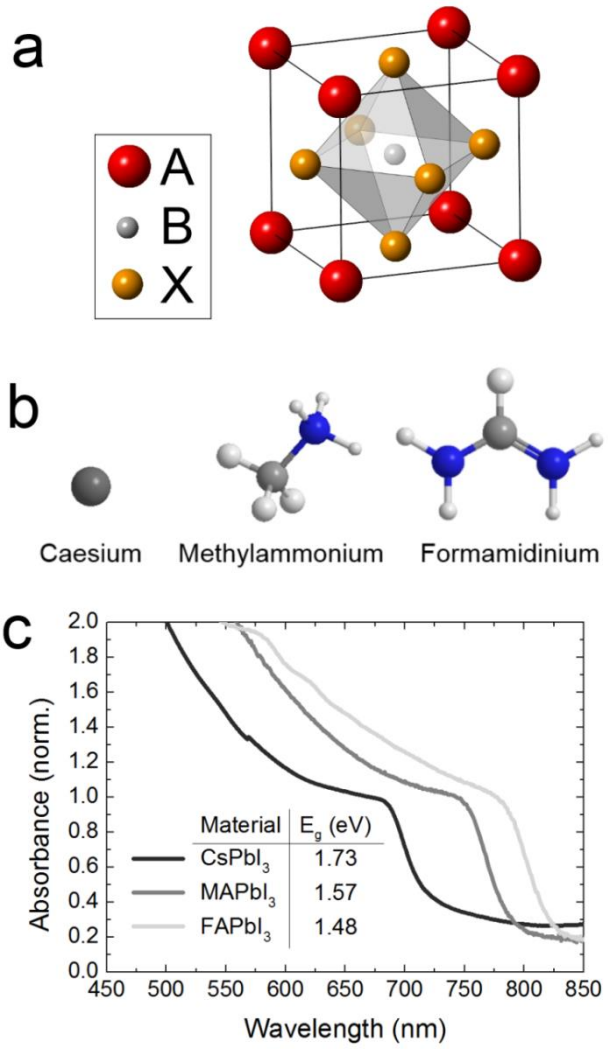

Figure 7.1: Tuning perovskite bandgap by replacing the A cation. a) The ABX_3 perovskite crystal structure. b) the atomic structure of the three A site cations explored. c) UV-Vis spectra for the $APbI_3$ perovskites formed, where A is either caesium (Cs), methylammonium (MA) or formamidinium (FA).

To investigate the effect of the A cation size upon the optical and electronic properties of the perovskite, perovskites were synthesised based on methylammonium lead triiodide, replacing methylammonium ($CH_3NH_3^+$)(MA) with caesium (Cs^+) and formamidinium

($HC(NH_2)_2^+$) (FA), illustrated in Figure 7.1b. Caesium has a smaller effective ionic radius compared to methylammonium, whereas formamidinium is slightly larger.[4] A single precursor solution was spin-coated onto substrates; the perovskite then formed upon heating. Full experimental details are provided in Chapter 3. Previous studies have reported the synthesis of these materials in crystalline form, but this is the first report of their thin-film synthesis.[7–10] The absorbance spectra of these materials is shown in Figure 7.1c.

It is observed that caesium lead triiodide absorbs up to a shorter wavelength, whereas formamidinium lead triiodide absorbs to a longer wavelength than methylammonium lead triiodide. It is noted that the $CsPbI_3$ was unstable in air, degrading to a non-perovskite phase in a matter of minutes, as discussed further in Chapter 9. Estimations of the bandgap from Tauc plots, as detailed in Section 3.4.2, gives values shown as an inset in Figure 7.1c. It is observed that as the A cation increases in ionic radius, and hence the lattice would be expected to expand, the bandgap decreases, causing a red-shift in the absorption onset. Just by replacing the methylammonium with the slightly larger formamidinium, we are able to shift the bandgap closer to the optimum for a single junction solar cell.[2] Therefore, this material is a likely candidate to be able to produce even more efficient solar cells than $MAPbI_3$.

7.4 Mixed halide compositions

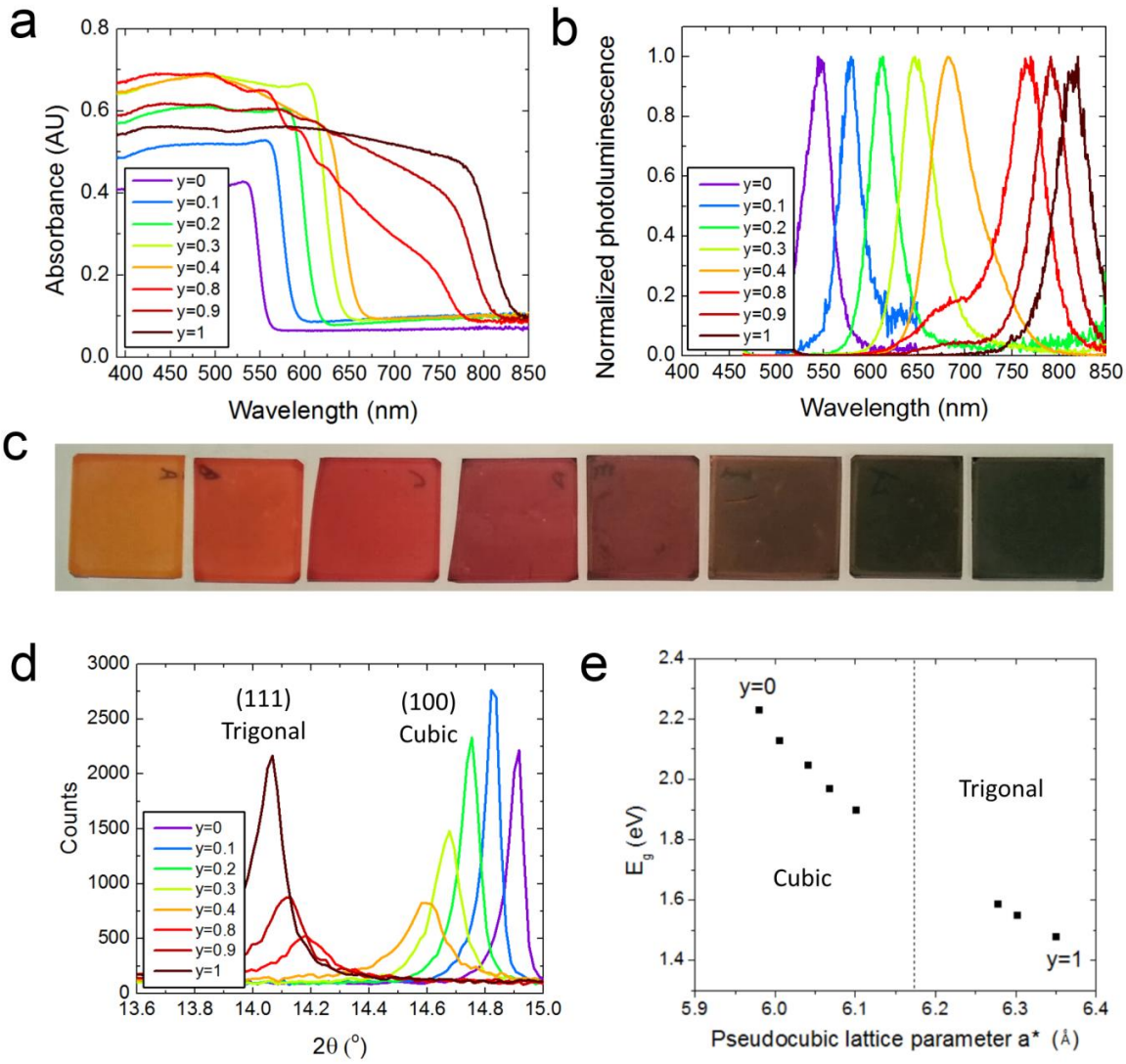

Figure 7.2: Tunability of the $FAPbI_{3y}Br_{3(1-y)}$ perovskite system. a) UV-Vis absorbance of the $FAPbI_{3y}Br_{3(1-y)}$ perovskites with varying y, measured in an integrating sphere. b) Corresponding steady-state photoluminescence spectra for the same films. c) Photographs of the $FAPbI_{3y}Br_{3(1-y)}$ perovskite films with y increasing from 0 to to 1 (left to right). d) XRD spectra of $FAPbI_{3y}Br_{3(1-y)}$ films showing the shift of the 100 (cubic) perovskite peak to the (111) trigonal peak as y decreases. e) Variation of bandgap with pseudocubic lattice parameter as determined from XRD spectra.

To explore the range of bandgap tunability of the formamidinium lead trihalide system, a range of formamidinium lead bromide-iodide mixed halide perovskites ($FAPbI_{3y}Br_{3(1-y)}$) was fabricated by gradually replacing iodide with bromide in the precursor solutions. It was possible to form most fractional mixtures, but it was not possible to form crystalline

phases, as determined by x-ray diffraction (XRD) data shown in Figure 7.3 for y=0.5, 0.6 and 0.7, so these are not considered in more detail here. The absorbance and photoluminescence from the perovskites in this series are shown in Figure 7.2a and Figure 7.2b respectively. Estimating the bandgap from Tauc plots, it was determined that the bandgap is tunable between 1.48 and 2.23eV, providing a whole range of coloured perovskites, as illustrated in Figure 7.2c. An increase in iodide fraction gradually red-shifts the bandgap. Photoluminescence peaks correspond well to the absorption onsets, suggesting the observed photoluminescence is predominantly from the bandgap rather than trap or sub-band states.[11] Similar to the methylammonium lead trihalide system previously studied,[1] analysis of XRD data (shown in full in Figure 7.3) shows that the perovskites transition from a cubic (for y<0.5, Br-rich) to a trigonal (y>0.7, I-rich) crystal structure, via a set of mostly amorphous phases. Figure 7.2d shows the shift of the [100] (cubic) to the equivalent [111] (trigonal) peak for these perovskites. A gradual shift in the lattice spacing upon increasing the iodide fraction is observed.

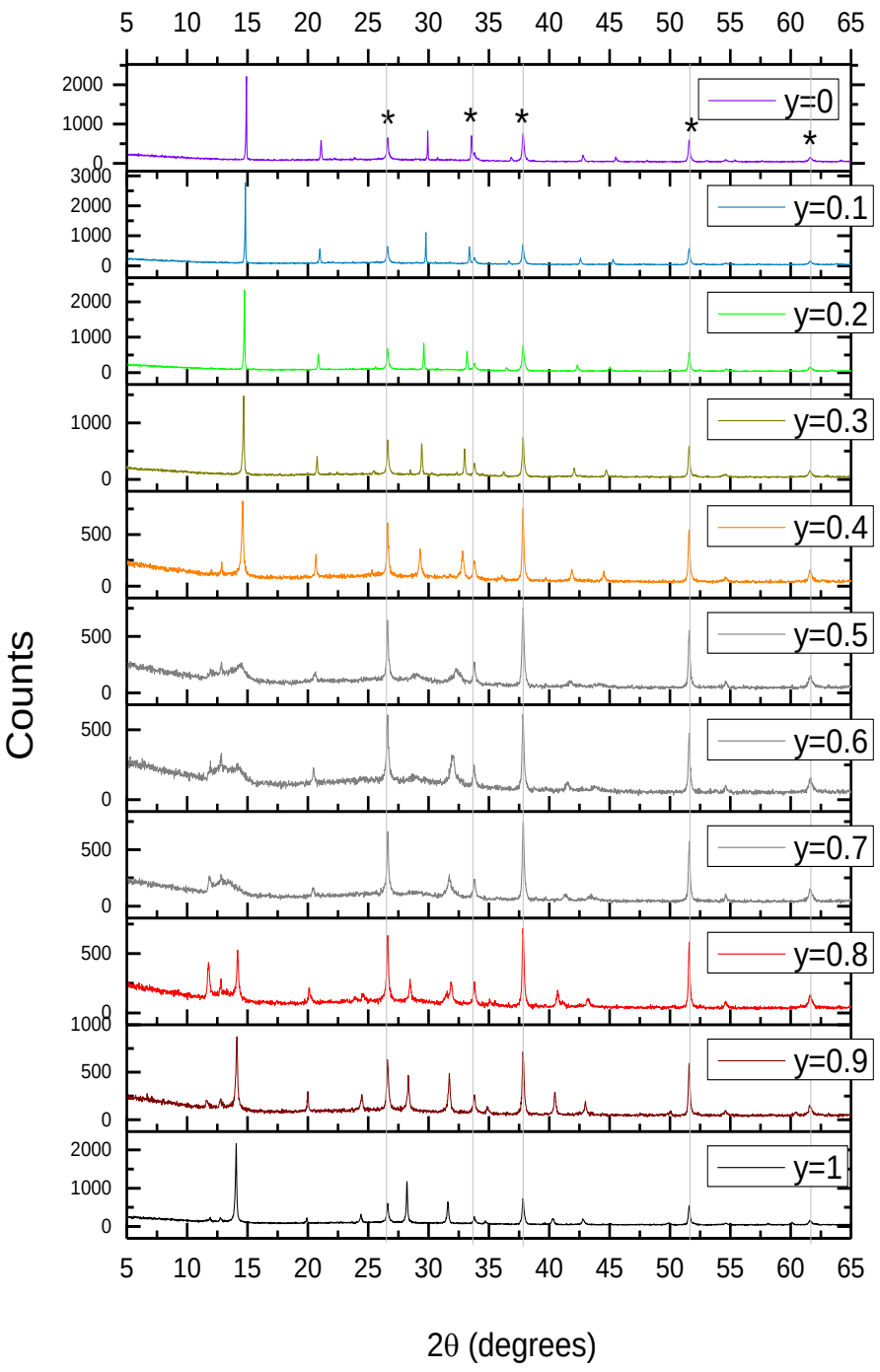

Figure 7.3: X-ray diffraction spectra for the whole range of $FAPbI_{3y}Br_{3(1-y)}$ materials, formed on fluorine-doped tin oxide-coated glass substrates. Peaks labelled with a * are assigned to the fluorine-doped tin oxide substrate. The films which produced mostly amorphous material are shown in grey.

Because the trigonal phase arises from a slight rotation of the adjacent PbX_6 octahedra, whilst maintaining corner-sharing, as shown in Figure 7.4, it is possible to define the trigonal phase by a pseudocubic phase, where the (100) spacing in the pseudocubic system replaces the (111) trigonal spacing, as previously described in the literature.[1,12]

The pseudocubic lattice parameters are then determined from lattice parameters **a** and **c** by:

$$\boldsymbol{a*} = \frac{\sqrt{2a^2}}{2} \; ; \; \boldsymbol{c*} = \frac{c}{2} \qquad 7.1$$

For a cubic lattice, **a*** and **c*** should be identical, so for the most accurate representation, **a*** and **c*** were determined in this way then averaged to get a single pseudocubic lattice parameter.

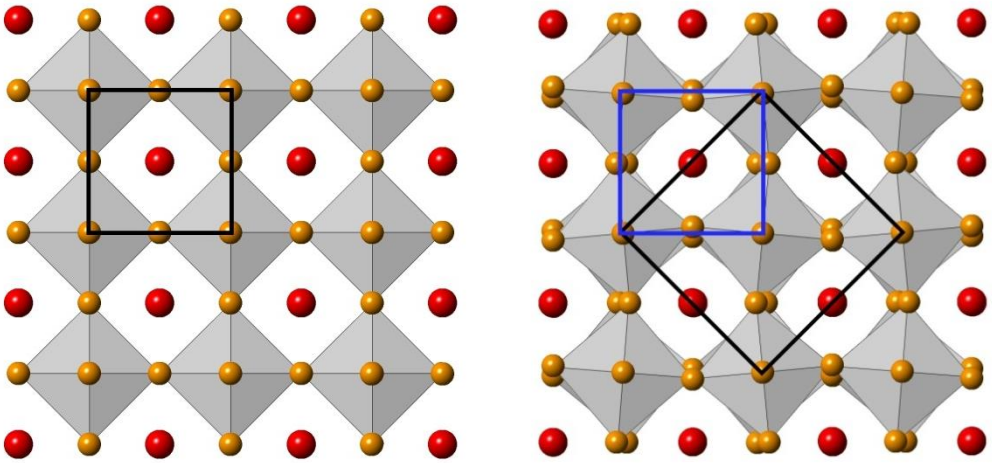

Figure 7.4: Cubic (left) and trigonal (right) lattices formed by the $FAPbI_{3y}Br_{3(1-y)}$ perovskites. The unit cell is shown in black. The pseudocubic lattice in the trigonal configuration is shown in blue. Red = A cation, yellow = halide, grey tetrahedra are centred on the metal cation.

The determination of the pseudocubic lattice parameter **a*** for the trigonal-phase perovskites, and cubic lattice parameter **a** (directly comparable to **a***) for the cubic perovskites enabled plotting the relation between bandgap and lattice spacing for this system. As shown in Figure 7.2e, it is observed that a larger pseudocubic lattice parameter results in a narrower bandgap. The relationship appears continuous across the phase change. This tunability demonstrates that the formamidinium system has wide flexibility; further investigation of the properties of the whole range of coloured perovskites may thus prove very interesting, specifically for optimising a wider band gap perovskite for a top cell in a tandem solar cell architecture. In this case, the bandgap of the top cell must be tuned to be the optimised value for a particular bandgap of bottom cell.[2] For a 1.1eV silicon bottom cell, a 1.7eV perovskite top cell would be ideal, for example.

7.5 Material properties

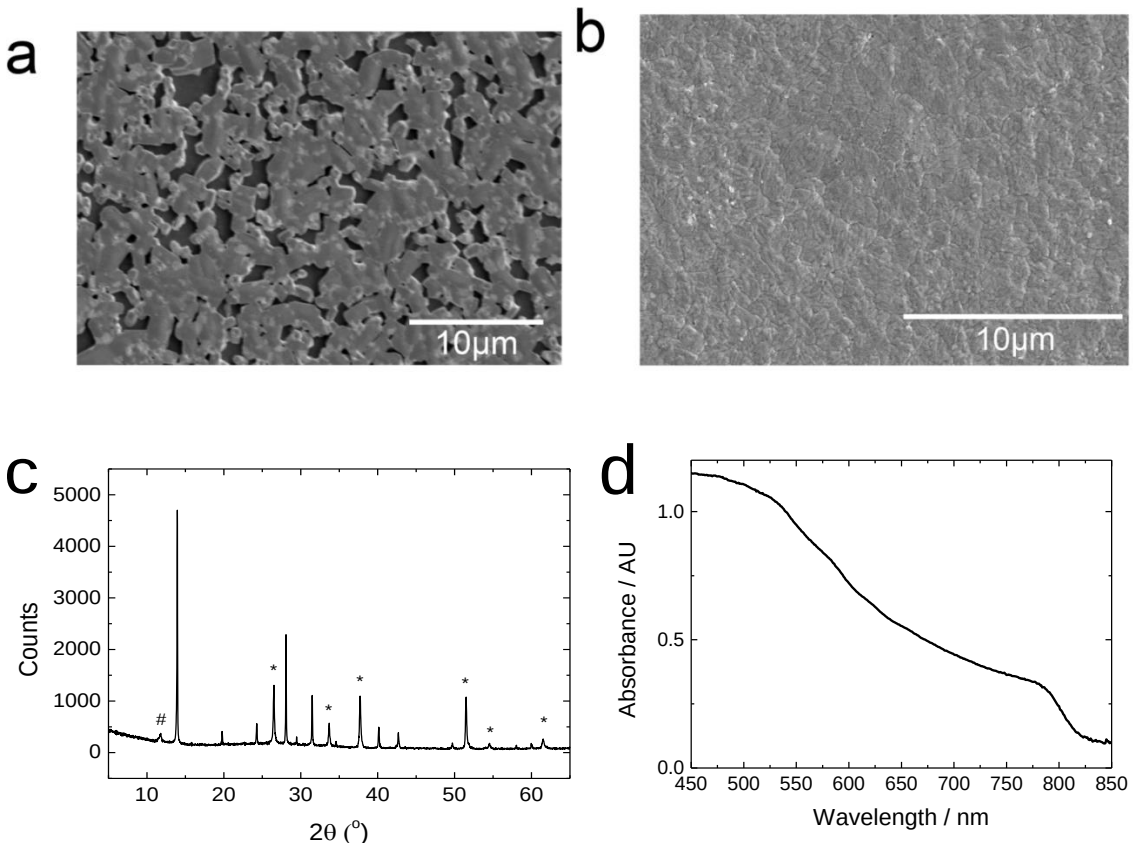

Figure 7.5: Material properties of $FAPbI_3$ films. Top view scanning electron micrograph of the sample morphology of a $FAPbI_3$ film formed from spin-coating the precursor solution with a) no addition of hydroiodic acid, and b) with adding a small amount of hydroiodic acid to the same precursor just before spin-coating. c) X-ray diffraction spectrum for a smooth and continuous $FAPbI_3$ film such as those used in quenching films. Peaks labelled with a * are assigned to the fluorine-doped tin oxide substrate, those with a # to PbI_2 impurities, and other peaks are assigned to the labelled reflections from a trigonal perovskite lattice with unit cell parameters a=b=8.99Å, c=11.0Å, in good agreement with the previous report on $FAPbI_3$[7]. d) Absorbance spectrum of a smooth and continuous 400nm thick film of $FAPbI_3$ prepared by adding HI. AU refers to absorbance units, which are dimensionless.

Formamidinium lead iodide shows a narrower bandgap than the commonly used methylammonium lead iodide, 1.48eV (~840nm absorption onset) compared to ~1.57eV respectively, and hence lies closer to that favourable for optimum solar conversion efficiencies. As detailed in Chapter 2, we should thus be able to attain higher photocurrents by harnessing more of the solar spectrum, provided the photogenerated

electrons and holes are suitably mobile and suitably long lived to be efficiently extracted from the solar cell. Previous reports on perovskite solar cells have explored four main architectures, as discussed in Chapter 2. Firstly, the 'sensitizing' architecture, where the perovskite simply acts as an absorber coating mesoporous TiO_2, with excited carriers injected into hole and electron transporting media for collection at the electrodes.[13–16] Secondly, the meso-superstructured architecture, where an inert scaffold forces electron transport through the perovskite itself.[13,17] Thirdly, the hole-conductor-free architecture, where in a similar way the removal of a separate hole transporter means that all hole transport occurs through the perovskite.[18,19] Finally, bulk thin-film planar heterojunction architectures have recently shown high efficiencies, as discussed in Chapter 4; here a bulk layer of perovskite is both absorber and long-range transporter of both charge species.[11,20,21] The thin-film and mesostructured approaches should ultimately provide the highest efficiencies, since the interfacial area at the heterojunction is minimised, where non-radiative recombination losses are most likely to occur. However, for a material to function well in the planar heterojunction configuration, it must be able to transport charge across film thicknesses greater than the absorption depth of a few hundred nanometers. To determine the optimum architecture for incorporation of $FAPbI_3$ into photovoltaic devices, whether thin-film, mesosuperstructured or sensitizing, time resolved photoluminescence quenching experiments were conducted using the technique described in detail in previous work, and summarised in Chapter 3, to obtain values for the electron and hole effective diffusion lengths.[11,22–24]. In brief, a hole (Spiro-OMeTAD) or electron (PCBM) quenching layer is spin-coated on top of a continuous thin film of the perovskite. Electrons or holes that diffuse into the boundary between perovskite and the quencher, transfer to the quencher and can no longer contribute to photoluminescence. By measuring the time-resolved photoluminescence decay rate with and without a quencher, and fitting the observed behaviour to a diffusion equation, a diffusion length can be estimated for the charge carrying species.[11]

Notably, it is important to carry out these measurements on very uniform and continuous thin films of the material in question. Spin-coating the formamidinium iodide plus PbI_2 precursor solution in DMF initially resulted in discontinuous perovskite films. However, as shown in Figure 7.5a and Figure 7.5b, it was found that by adding a small amount of hydroiodic acid (HI) to the stoichiometric FAI:PbI_2 1:1 perovskite precursor solution, extremely uniform and continuous films could be formed, with phase purity verified by XRD (Figure 7.5c), which is in good agreement with previous reports on single crystals of this perovskite.[7] We note that in these thin films, post annealing, we do not observe any significant presence of the previously reported hexagonal polymorph, a non-perovskite

'yellow phase'.[7] Moreover, realising a highly uniform coating is likely to have a beneficial effect on device performance, as concluded for the $MAPbX_3$ perovskite in Chapter 4. This addition of the acid to the formamidinium perovskite precursor solution provides a simple way to form a pinhole-free continuous film using conventional solution-processing. This method has not been reported previously. It is proposed that adding acid helps to solubilise the inorganic PbI_2 component, and so slows down crystallization of the film upon spin-coating, enabling a smoother film to be formed, without having any impact on the crystal structure, as verified by XRD. It was found that in the same way, addition of HI to a highly concentrated solution of lead iodide in DMF considerably enhanced its solubility (and incidentally, allowed the formation of very smooth films of PbI_2, which is normally challenging to achieve). This simple technique should prove useful as a general method for preparing very smooth hybrid organic-inorganic films, or preparing more concentrated precursor solutions.

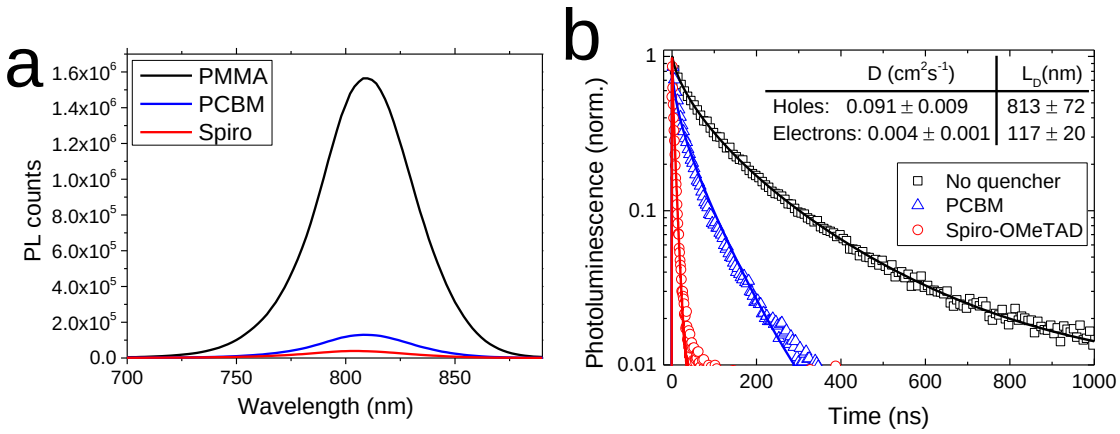

Figure 7.6: a) Steady-state photoluminescence spectra of a $FAPbI_3$ film of 400nm thickness coated in either an inert layer of polymethylmethacrylate (PMMA), the electron-quenching layer PCBM, and the hole-quenching layer Spiro-OMeTAD, demonstrating effective photoluminescence quenching for both holes and electrons with these layers. b) Normalised time-resolved photoluminescence intensity from films with and without electron and hole-quenchers, showing the stretched exponential fits to the decay curves. Diffusion coefficients (D) and diffusion lengths (L_D), extracted from the fitting, are shown in the inset. Errors quoted arise predominantly from film thickness variations.

It was verified that PCBM and Spiro-OMeTAD are effective quenching layers for electrons and holes respectively by measuring the steady-state photoluminescence spectra of perovskite films with these quenchers on top. As shown in Figure 7.6a, both quenchers are effective, however the PCBM does not entirely quench the PL from $FAPbI_3$, in contrast to

nearly complete quenching when coated upon $MAPbI_3$.[11] As shown in Figure 7.6b, by monitoring the time-resolved photoluminescence intensity at the peak wavelength (810nm), it was possible to estimate effective diffusion lengths for electrons and holes in this material, as 177±20nm and 813±72nm respectively. As shown in Figure 7.5d, films of a few hundred nanometers thickness have sufficient optical density to absorb most incident light in two passes, thus a thin-film planar heterojunction should be able to provide both efficient hole and electron extraction and light absorption, making this a suitable configuration for $FAPbI_3$ solar cells. It is noted that both the diffusion length for holes and electrons are significantly longer than those found in $MAPbI_3$, but shorter that those in the chloride-assisted $MAPbI_{3-x}Cl_x$ perovskite, which are over 1 micron for both electrons and holes.[11] Interestingly, there appears to be a significant imbalance in the electron and hole diffusion lengths. This arises from a lower determined diffusion coefficient for electrons, as shown in Figure 7.6b, rather than a reduced lifetime. There is not conclusive evidence for any particular mechanism giving rise to the imbalance, but it is proposed that by replacing methylammonium with formamidinium, the band structure of the perovskite is altered, possibly giving rise to an imbalance in the effective masses for electron and hole. This would in turn affect the diffusion coefficient and hence the diffusion length. It is also noted however, that the diffusion length modelling assumes perfect quenching, i.e. that once a charge species meets the interface with a quencher it transfers to the quencher with 100% efficiency and is not reflected. As the PCBM is not an ideal electron quencher for the $FAPbI_3$, as shown in Figure 7.6a, then the estimation of the electron diffusion coefficient and length is a lower limit.

7.6 Formamidinium lead halide solar cells

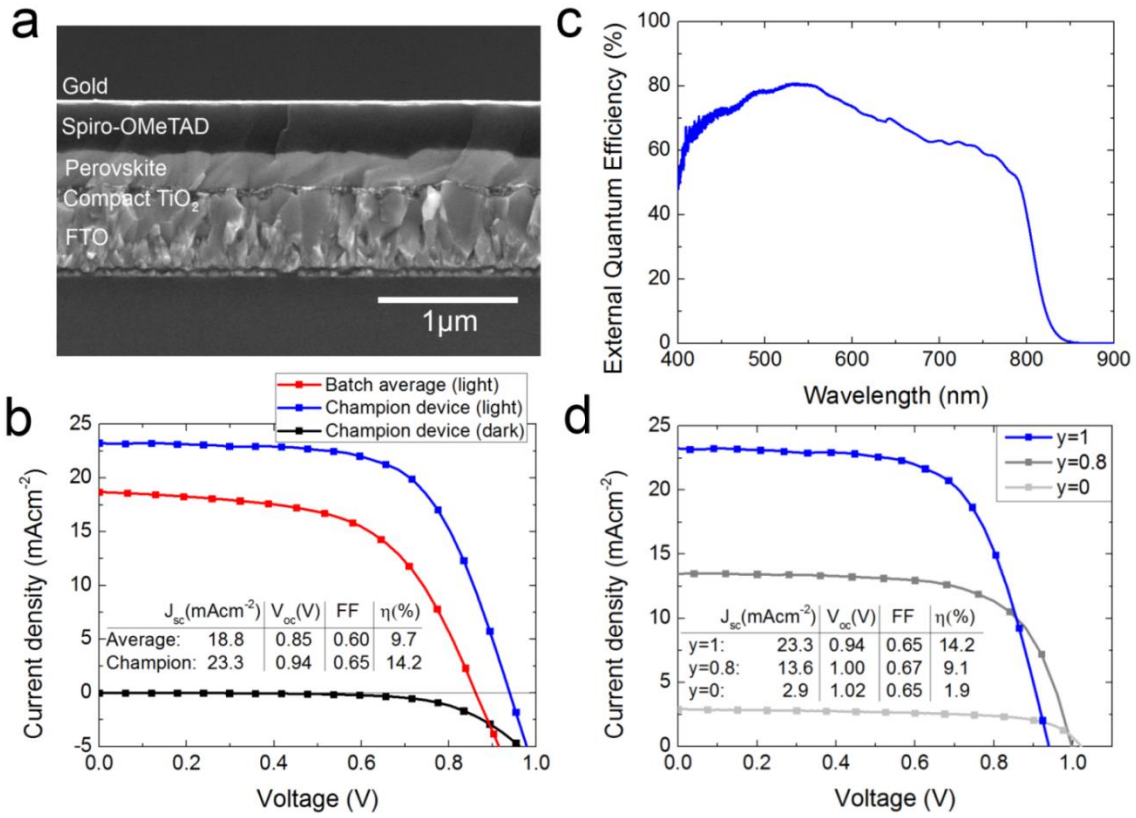

Figure 7.7: Planar heterojunction $FAPbI_3$ solar cells. a) Cross-sectional scanning electron micrograph of a representative $FAPbI_3$ device. b) Current-voltage characteristics of $FAPbI_3$ planar heterojunction solar cells under 100 $mWcm^{-2}$ AM1.5 illumination, showing both the mean current-voltage characteristics for the batch of 24 cells detailed in Table 7.1 and the current-voltage characteristics of the champion device fabricated. Performance parameters are shown as an inset. c) External quantum efficiency spectrum of a representative $FAPbI_3$ solar cell. d) Current-voltage charcteristics of $FAPbI_yBr_{3-y}$ planar heterojunction solar cells under 100$mWcm^{-2}$ AM1.5 illumination, showing devices with y=0.8 and y=0 compared to the champion $FAPbI_3$ solar cell. Performance parameters are shown as an inset.

Thin-film planar heterojunction solar cells with the $FAPbI_3$ perovskite were fabricated and optimised, using compact TiO_2 and Spiro-OMeTAD as electron- and hole-selective contacts respectively. The device architecture is shown in Figure 7.7a. Current-voltage characteristics of such devices were measured under simulated AM1.5 100$mWcm^{-2}$ sun light, and these characteristics are shown for the best device fabricated, and for the numerical mean of a 24-cell batch, in Figure 7.7b. Full details of device performance for the whole batch of such devices is detailed in Table 7.1 and Figure 7.8. Due to the high

short-circuit currents of over 23 $mAcm^{-2}$, power conversion efficiencies of up to 14.2% in the best performing devices were observed, which is a new record for solution-processed planar heterojunction perovskite solar cells. As shown in the EQE spectrum (Figure 7.7c), photocurrent is generated out to ~840nm, rather than only ~780nm achievable with the well-known $MAPbX_3$ material, due to the narrower bandgap.[15] The integration of the measured EQE spectrum over the solar spectrum estimates a short-circuit current density of $18.2mAcm^{-2}$, close to the average photocurrent generated from a typical cell. It is noted that this EQE spectrum was measured for a representative device from the batch, not the champion device.

No. cells	J_{sc} ($mAcm^{-2}$)	V_{oc} (V)	FF	PCE (%)
24	**18.8±3.3**	**0.85±0.08**	**0.60±0.09**	**9.7±2.6**

Table 7.1: Device statistics from a batch of 24 individual devices prepared using the optimised fabrication procedure, extracted from current-voltage characteristics measured under 100$mWcm^{-2}$ AM1.5 illumination. Errors are calculated from the standard deviation in the batch.

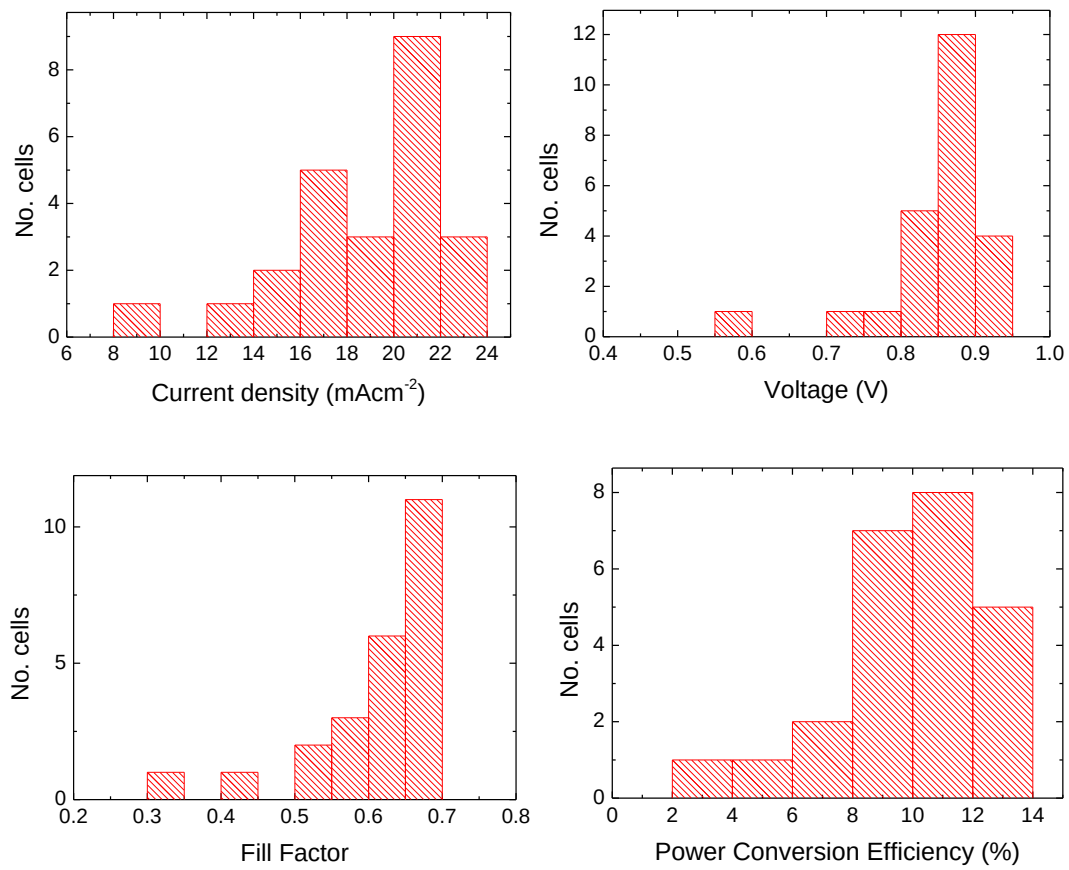

Figure 7.8: Histogram representation of the solar cell characteristics for the same batch of optimised devices as detailed in Table 7.1.

The high power conversion efficiency in this system can be explained by two main advantages of the $FAPbI_3$ perovskite. Firstly, via solution-processing with the hydroiodic acid additive it is possible to form a very uniform and continuous thin film, with very few pinholes or defects, which remains a difficult challenge for the $MAPbX_3$ films.[20] Uniform perovskite coverage is likely to lead to maximising the V_{oc} and FF, as discussed in Chapter 4. Secondly, the reduced bandgap of 1.48eV compared to ~1.57eV in the $MAPbI_{3-x}Cl_x$ perovskite allows absorption of photons over a greater proportion of the solar spectrum, and is closer to the ideal bandgap for a single-junction solar cell, which will lead to maximising the J_{sc}. Performing a quick calculation as detailed in Chapter 2, assuming 100% EQE, a J_{sc} of up to 29.2mAcm^{-2} could be attained with a 1.48eV material, as opposed to 26.3mAcm^{-2} for a 1.57eV material. This is a significant difference and shows the greater potential for the $FAPbI_3$ system. A corresponding drop in V_{oc} would be expected to accompany a smaller bandgap. However, the V_{oc} attained in the best $FAPbI_3$ planar heterojunction solar cells is 0.94V, compared to 0.97V observed in the best $MAPbI_{3-x}Cl_x$ solution-processed planar heterojunction solar cells. The reduction in bandgap from $MAPbI_{3-x}Cl_x$ to $FAPbI_3$ is ~0.09eV, whereas the V_{oc} only drops by 0.03V, so in these cells a

lower voltage loss from optical bandgap to V_{oc} (loss-in-potential) is observed than in the $MAPbI_{3-x}Cl_x$ cells – 0.54eV compared with 0.6eV. This implies fewer energetic losses, as a result of the highly uniform films or for another reason.

It is noted that by employing a meso-superstructured approach, even higher voltages of up to ~1.1V have been observed in the $MAPbI_{3-x}Cl_x$ system.[13] The origin of these higher voltages in comparison to the solution processed planar heterojunction devices are yet to be understood fully, but the loss-in-potential is only ~0.46eV, even lower than the loss in the $FAPbI_3$ cells. If this loss in the $FAPbI_3$ can be mitigated by, for instance, employing a mesostructure, a more appropriate choice or energetically tuning of the n- and p-type collection layers, or by enhancing the electron diffusion length, then even higher efficiencies should be possible with formamidinium lead trihalide.

Having fabricated high-efficiency $FAPbI_3$ devices, it was then of interest to observe how devices fabricated with the increased bromide fractions function. Having higher bandgaps, they should be able to generate higher open-circuit voltages, as previously shown with the $MAPbX_3$ system.[1,25] To explore this, planar heterojunction solar cells were fabricated in the same way with two further compositions of $FAPbI_yBr_{3-y}$ perovskites, y=0 ($FAPbBr_3$) and y=0.8 (a small replacement of iodide with bromide). Current-voltage characteristics of the best devices of these compositions fabricated are shown in Figure 7.7d, as compared to the best $FAPbI_3$ device. It is observed that by decreasing the iodide fraction (increasing the bromide fraction) from y=1 to y=0.8, we are able to generate slightly higher open-circuit voltages of 1.0V, accompanying a drop in photocurrent. This corresponds to a change in bandgap from 1.48eV to 1.57eV, so the increase in V_{oc} is more or less what would be expected, assuming no further energetic losses. Upon increasing the bromide fraction further by going all the way to $FAPbBr_3$, however, the V_{oc} increases only slightly further, to 1.02V. Here the bandgap is now 2.23eV, so the V_{oc} increase is much less than the bandgap increase. Something else must then be limiting the V_{oc}. This is most likely the HOMO level of the Spiro-OMeTAD hole transporter. Unless a different hole transport material were to be used, with a deeper HOMO level, the voltage of such devices is likely to be limited to ~1.02V.

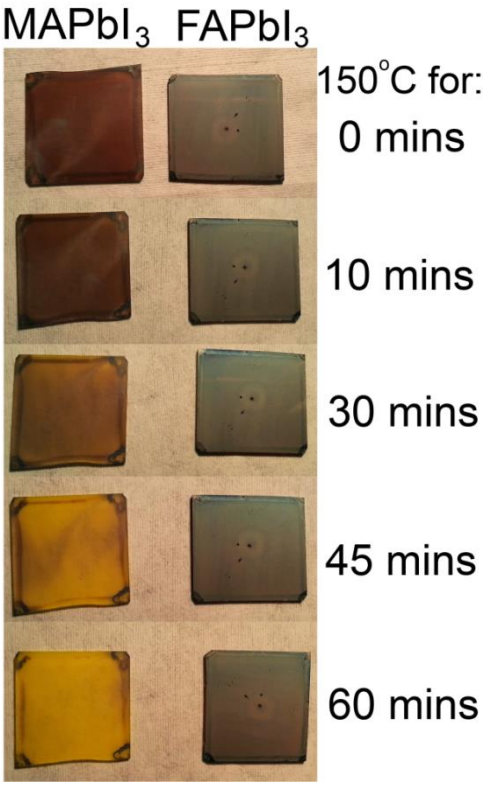

Figure 7.9: Thermal degradation of $MAPbI_3$ and $FAPbI_3$, when bare spin-coated films of each perovskite are heated in air at 150°C for the times indicated.

A fundamental property of the methylammonium lead iodide perovskite is that it is sensitive to degradation due to moisture and high temperatures.[1,7] Though this is likely to be manageable in manufacture, any modifications which enhance the robustness of the material will be advantageous. Some initial tests were carried out to determine how replacing the methylammonium cation with formamidinium affects these important properties. It was found that formamidinium lead iodide is more resistant when exposed to high temperatures in air than methylammonium lead iodide – it appeared fully stable without discolouration at 150°C in air, whereas the methylammonium-based perovskite discoloured after ~30 minutes, as shown in Figure 7.9.

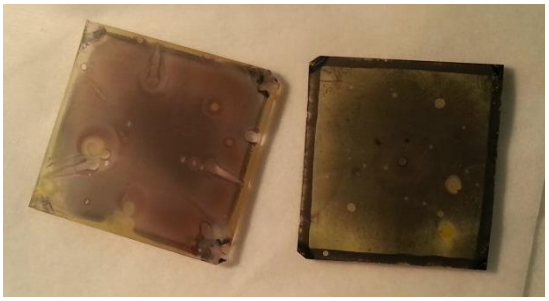

Figure 7.10: Films of $MAPbI_3$ (left) and $FAPbI_3$ (right) upon exposure to 80-100% relative humidity atmosphere for ~15 minutes at room temperature. The

atmosphere was created by pouring water onto a tissue in a sealed glass container with the films. Degradation is evident at an approximately equal rate in both films.

Exposing the perovskites to an extremely moist atmosphere, as shown in Figure 7.10, resulted in degradation of the formamidinium perovskite at a similar rate to the methylammonium perovskite. Both films discoloured significantly within 15 minutes. However, recent work on long-term stability of perovskite solar cells shows promise that with adequate encapsulation, similar devices to these can function continuously under illumination for thousands of hours, so this is unlikely to be a significant drawback to commercialisation of perovskite solar cells made with these materials.[15,26] Furthermore, the enhanced temperature stability of the $FAPbI_3$ is an extremely promising property, possibly indicative of better long-term thermal durability, and will be the subject of further investigations. It is worth mentioning that the international standards for commercialisation of solar cells require thermal stability at 85°C, and recent work has shown that $MAPbI_3$ is fundamentally unstable over long times at this temperature; the $FAPbI_3$ should be significantly more stable and be able to pass these tests.[27]

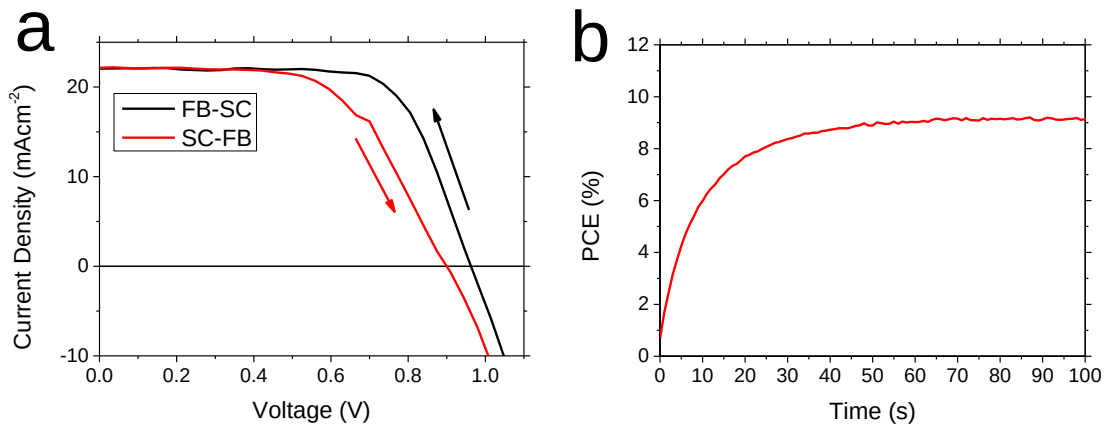

Figure 7.11: Hysteresis in $FAPbI_3$ planar heterojunction solar cells. a) Current-voltage scans for a typical device, measured at 0.38V/s scan speed. FB-SC refers to scanning voltage from forward bias to short circuit; SC-FB vice versa. The calculated efficiencies from the JV curve are ~14% and ~11% for FB-SC and SC-FB respectively. b) Stabilised power output measured holding the cell under AM1.5 illumination at 0.72V (MPP for the FB-SC scan). The cell stabilises at ~9% PCE.

As previously discussed, the issue of hysteretic current-voltage behaviour is a significant one in the methylammonium-based perovskites. In order to test if this issue was still present in FA-based devices, cells were scanned in both forwards and reverse voltage directions, and a stabilised power output also measured at the determined maximum

power point. Hysteresis data for a typical $FAPbI_3$ device is shown in Figure 7.11. It is clearly evident that hysteresis is still present in this material, in this architecture – it is not a unique feature of the $MAPbI_3$ material. Hysteresis will be discussed further in Chapter 9; here it can be concluded that solving this problem is integral to allowing the PCE of $FAPbI_3$ devices to stabilise at the highest values.

7.7 Outlook and conclusion

In this chapter, the effect of changing the size of the A cation in the organolead trihalide perovskite structure was investigated, and it was found that the bandgap can be tuned in this manner. It has been shown that replacing methylammonium with the larger cation formamidinium narrows the bandgap, enabling broad bandgap tunability with the mixed halide $FAPbI_yBr_{3-y}$ perovskite system between 1.48 and 2.23eV. Since $FAPbI_3$ has an optical bandgap of 1.48eV, it is closer to the ''ideal' single-junction solar cell bandgap (between 1.1-1.4eV). To determine the optimum device configuration, spectroscopic diffusion length measurements were carried out, and it was determined that $FAPbI_3$ has sufficiently long electron and hole diffusion lengths for planar heterojunction solar cells to be a suitable configuration. A novel method for fabricating very uniform smooth films of this perovskite, by adding hydroiodic acid, was developed, enabling high surface coverages necessary for the highest PCEs as discovered in previous chapters. Planar heterojunction solar cells were fabricated, and due to the reduced bandgap of $FAPbI_3$ very high short-circuit currents in excess of $23mAcm^{-2}$ were observed, and PCEs up to 14.2% were achieved, measured under simulated full sun light. Moreover, it was shown that the FA-based materials are more thermally stable than the MA-based materials, of high significance when considering commercialisation and real-world usage. These promising results firmly place the formamidinium metal trihalide perovskites as a contending class of materials for high efficiency solar cells and should provide the next steps towards commercialisation of high efficiency, high stability perovskite solar panels.

7.8 References

1 J. H. Noh, S. H. Im, J. H. Heo, T. N. Mandal and S. Il Seok, *Nano Lett.*, 2013, **13**, 1764–1769.

2 F. Meillaud, a. Shah, C. Droz, E. Vallat-Sauvain and C. Miazza, *Sol. Energy Mater. Sol. Cells*, 2006, **90**, 2952–2959.

3 D. B. Mitzi, *Progress in Inorganic Chemistry, Volume 48*, John Wiley & Sons, Inc, 1999.

4 I. Borriello, G. Cantele and D. Ninno, *Phys. Rev. B*, 2008, **77**, 235214.

5 M. R. Filip, G. E. Eperon, H. J. Snaith and F. Giustino, *Nat. Commun.*, 2014, **5**, 5757.

6 C. H. Nh, J.-H. J. Im, J. Chung, S. S. S.-J. Kim and N. N. N.-G. Park, *Nanoscale Res. Lett.*, 2012, **7**, 353.

7 C. C. Stoumpos, C. D. Malliakas and M. G. Kanatzidis, *Inorg. Chem.*, 2013, **52**, 9019–9038.

8 O. N. Yunakova, V. K. Miloslavskii and E. N. Kovalenko, *Opt. Spectrosc.*, 2012, **112**, 91–96.

9 D. M. M. Trots and S. V. V Myagkota, *J. Phys. Chem. Solids*, 2008, **69**, 2520–2526.

10 G. Murtaza and I. Ahmad, *Phys. B Condens. Matter*, 2011, **406**, 3222–3229.

11 S. D. Stranks, G. E. Eperon, G. Grancini, C. Menelaou, M. J. P. Alcocer, T. Leijtens, L. M. Herz, A. Petrozza and H. J. Snaith, *Science*, 2013, **342**, 341–344.

12 D. L. Proffit, H. W. Jang, S. Lee, C. T. Nelson, X. Q. Pan, M. S. Rzchowski and C. B. Eom, *Appl. Phys. Lett.*, 2008, **93**, 111912.

13 M. M. Lee, J. Teuscher, T. Miyasaka, T. N. Murakami and H. J. Snaith, *Science*, 2012, **338**, 643–647.

14 H.-S. Kim, C.-R. Lee, J.-H. Im, K.-B. Lee, T. Moehl, A. Marchioro, S.-J. Moon, R. Humphry-Baker, J.-H. Yum, J. E. Moser, M. Grätzel and N.-G. Park, *Sci. Rep.*, 2012, **2**, 591.

15 J. Burschka, N. Pellet, S.-J. J. Moon, R. Humphry-Baker, P. Gao, M. K. Nazeeruddin, M. Grätzel and M. Gratzel, *Nature*, 2013, **499**, 316–319.

16 A. Kojima, K. Teshima, Y. Shirai and T. Miyasaka, *J. Am. Chem. Soc.*, 2009, **131**, 6050–1.

17 J. M. Ball, M. M. Lee, A. Hey and H. J. Snaith, *Energy Environ. Sci.*, 2013, **6**, 1739–1743.

18 W. A. Laban and L. Etgar, *Energy Environ. Sci.*, 2013, **6**, 3249.

19 L. Etgar, P. Gao, Z. Xue, Q. Peng, A. K. Chandiran, B. Liu, M. K. Nazeeruddin and M. Grätzel, *J. Am. Chem. Soc.*, 2012, **134**, 17396–17399.

20 G. E. Eperon, V. M. Burlakov, P. Docampo, A. Goriely and H. J. Snaith, *Adv. Funct. Mater.*, 2014, **24**, 151–157.

21 M. Liu, M. B. Johnston and H. J. Snaith, *Nature*, 2013, **501**, 395–398.

22 G. Xing, N. Mathews, S. Sun, S. S. Lim, Y. M. Lam, M. Grätzel, S. Mhaisalkar and T. C. Sum, *Science*, 2013, **342**, 344–347.

23 P. E. Shaw, A. Ruseckas and I. D. W. Samuel, *Adv. Mater.*, 2008, **20**, 3516–3520.

24 D. Markov and P. Blom, *Phys. Rev. B*, 2006, **74**, 085206.

25 B. Cai, Y. Xing, Z. Yang, W.-H. Zhang and J. Qiu, *Energy Environ. Sci.*, 2013, **6**, 1480–1485.

26 T. Leijtens, G. E. Eperon, S. Pathak, A. Abate, M. M. Lee and H. J. Snaith, *Nat. Commun.*, 2013, **4**, 2885.

27 B. Conings, J. Drijkoningen, N. Gauquelin, A. Babayigit, J. D'Haen, L. D'Olieslaeger, A. Ethirajan, J. Verbeeck, J. Manca, E. Mosconi, F. De Angelis and H. Boyen, *Adv. Energy Mater.*, 2015, **Advance**, 1–8.

8. SEMI-TRANSPARENT NEUTRAL COLOURED SOLAR CELLS BASED ON FORMAMIDINIUM LEAD HALIDE PEROVSKITE

The work presented in this chapter has been published in:

- G. E. Eperon, D. Bryant, J. Troughton, S. D. Stranks, M. B. Johnston, T. Watson, D. A. Worsley and H. J. Snaith, "Efficient, Semitransparent Neutral-Colored Solar Cells Based on Microstructured Formamidinium Lead Trihalide Perovskite", *The Journal of Physical Chemistry Letters,* 2015, **6**, 129-138.

8.1 Context and summary

In this chapter the work in previous chapters is brought together. Using the semi-transparent microstructured solar cell concept developed in Chapter 5, the narrower-bandgap formamidinium lead iodide perovskite developed in Chapter 7 is incorporated into this architecture. This results in significantly high efficiencies per transparency. Furthermore, a novel transparent cathode is applied to the devices, enabling the fabrication of neutral-coloured semi-transparent full solar cells for the first time. Such devices demonstrate over 5% power conversion efficiency for average visible transparencies of almost 30%, retaining impressive colour-neutrality. This makes these devices the best-performing single junction neutral-coloured semitransparent solar cells to date. These microstructured perovskite solar cells are also shown to have a significant advantage over silicon solar cells in terms of performance at high incident angles of sunlight, making them ideal for building integration.

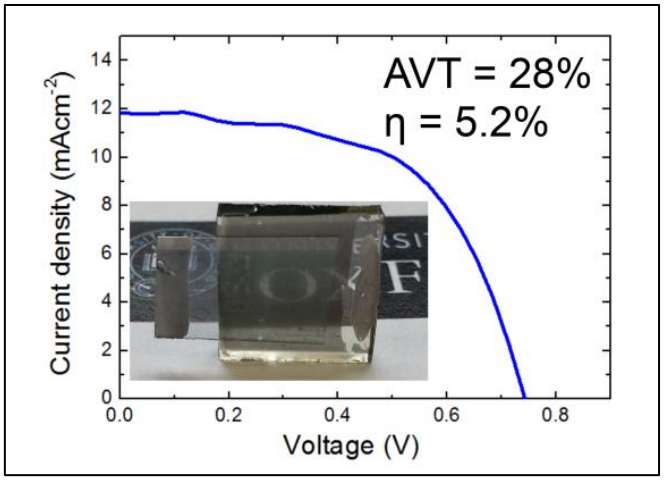

8.2 Introduction

In Chapter 5, the application of the most commonly studied $MAPbI_3$ perovskite was reported in neutral-coloured semitransparent solar cells for building-integrated photovoltaics.[1] Spontaneous dewetting of an excess-organic containing perovskite precursor dissolved in a low vapour pressure solvent enabled the formation of a microstructured array of perovskite "islands", which were able to generate respectable efficiencies despite comprising a discontinuous planar heterojunction architecture. The combination of fully absorbing islands and transparent regions allowed such films to be neutral-coloured and semi-transparent, with up to nearly 60% active layer average visible transmittance (defined as the mean transmittance of the film between 370nm and 740nm). However, in this first work on semi-transparent perovskite solar cells, it was not possible to employ a sufficiently transparent cathode that would retain the neutral colouration. In full devices, efficiencies of ~5% were achieved for an average visible transmittance of ~20%; however, this was with a semi-transparent gold cathode, which no longer provided neutral colour. It was concluded that the gold cathode was a key limiting factor – with a more transparent cathode, better AVTs should be achieved and also neutral colouration retained. More recently, others have reported on a semitransparent perovskite solar cell also employing a thin gold cathode, with 6.4% PCE and 30% full device AVT. However, they employed a thin but continuous layer of perovskite, giving a brown-yellow device.[2] As previously discussed in Chapter 5, other technologies have also achieved high efficiencies per transparency, most notably organic photovoltaics, but remain limited by low PCEs when neutral colour is attained.

Whilst most work has focused on the methylammonium lead iodide perovskite, $MAPbI_3$, in Chapter 7 of this thesis it was demonstrated that the methylammonium ($CH_3NH_3^+$) component can be replaced with formamidinium ($HC(NH_2)_2^+$), resulting in a slightly larger lead iodide-based crystal lattice, with the effect of narrowing the bandgap closer to that optimal for solar cells, from 1.57eV to 1.48eV.[3–5] Furthermore, it was observed that the $FAPbI_3$ perovskite is more thermally stable at raised temperature, more photostable under continual operation, and that it does not undergo a phase transition in the solar cell operating regime, which could be an issue for the $MAPbI_3$ perovskite.[3,5] Therefore, the $FAPbI_3$ perovskite has a number of highly advantageous characteristics for its use in solar cells.

In this chapter, two major improvements to the semitransparent perovskite solar cell are reported. $MAPbI_3$ is replaced with the advantageous $FAPbI_3$ in the microstructured architecture, which allows significantly higher efficiencies to be achieved for equivalent

transparencies. Such devices display very little JV hysteresis, and have high stabilised power output. Secondly, a novel ITO and precious metal-free transparent cathode is employed in such devices, allowing fully operating, completely neutral coloured semitransparent, perovskite solar cells for the first time.

8.3 Fabrication of microstructured $FAPbI_3$ via sacrificial component

$FAPbI_3$ was fabricated in the microstructured architecture by using a precursor containing excess of organic components, and in a low vapour pressure solvent, DMSO. This combination was previously found to produce a reasonably regular array of perovskite islands for $MAPbI_{3-x}Cl_x$ (see Chapter 5).[1] The presence of the excess organic allows morphological change during annealing.[6,7] Using a low vapour pressure solvent means that the perovskite starts to crystallise while the solvent is still present, and the combination of slow crystallisation and slow solvent removal results in the perovskite nucleating in a discontinuous island-type structure, effectively encouraging dewetting from the substrate. In the case of the organic excess MA perovskite previously studied, lead chloride is used as the lead source, and MAI as the MA and I source. It is assumed that the reaction progresses thusly:[8]

$$3MAI + PbCl_2 \rightarrow MAPbI_3 + 2MACl \qquad 8.1$$

The $MAPbI_3$ is the perovskite formed, and the MACl is predominantly removed via sublimation or degradation, which is experimentally observed to occur at temperatures greater than 80°C[8,9]. The notation $MAPbI_{3-x}Cl_x$ normally used for this fabrication route represents the fact that there may be a small residual amount of chloride left in the film, though it probably does not play a significant role.[10,11] In the case of the FA however, because the FA cation is larger, it is not so easily removed. Attempts were to produce similarly structured films in this manner, substituting MAI for FAI, but these were unsuccessful and the films did not result in the same morphology – they were very rough, discontinuous, and non-uniform. Likewise, using a stoichiometric 1:1 FAI:PbI_2 precursor in DMSO also produced very rough, non-uniform films. It appeared that the excess organic is critical to obtain the microstructuring. Therefore, a new route was taken to obtain microstructured films of $FAPbI_3$: MA was incorporated as a sacrificial component. It is assumed that the reaction progresses as shown below:

$$2MAI + FAI + PbCl_2 \rightarrow FAPbI_3 + 2MACl \qquad 8.2$$

Since FACl, being a larger molecule than MACl, requires higher temperatures to sublime than MACl, the MACl will be preferentially removed on heating at >80°C, leaving $FAPbI_3$ (or $FAPbI_{3-x}Cl_x$ to represent the fact there may be trace chloride remaining – here these are used interchangeably) behind. Films of this material were fabricated by dissolving the precursors in DMSO, spin-coating in a single step, and annealing first at 130°C for 20 minutes and subsequently at 170°C for 10 minutes. The first step was to remove the excess MACl in a similar manner to that used in Chapter 5, and the second step was to force the $FAPbI_3$ into its black, rather than yellow, phase, as in Chapter 7.[3,5] Films formed in this manner did indeed produce a material with a somewhat similar microstructuring as was observed in the $MAPbI_3$ material, as shown in Figure 8.1.

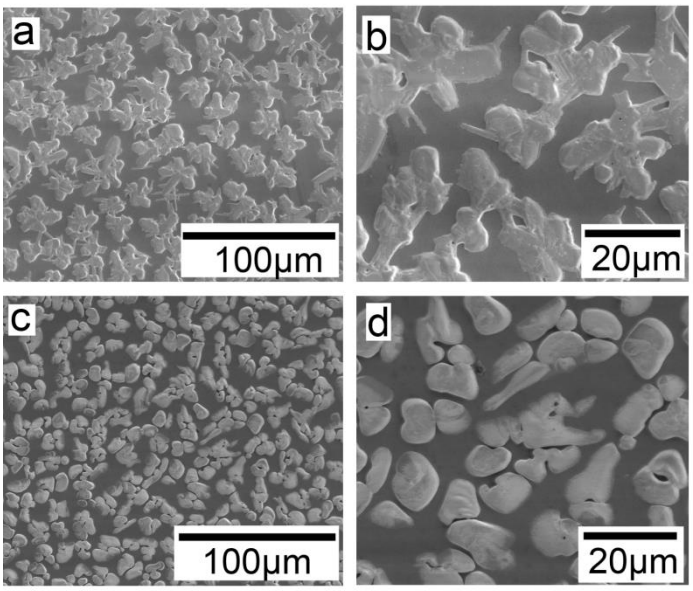

Figure 8.1: a) and b): different magnifications of FA-containing microstructured perovskite films produced from the precursors detailed in Equation 8.2 and annealed first at 130°C and then at 170°C. c and d: MA-containing films produced from the precursors detailed in Equation 8.1 and annealed at 130°C.

In order to confirm that the material produced is $FAPbI_3$, X-ray diffraction (XRD) measurements were carried out on the films, as shown in Figure 8.2.

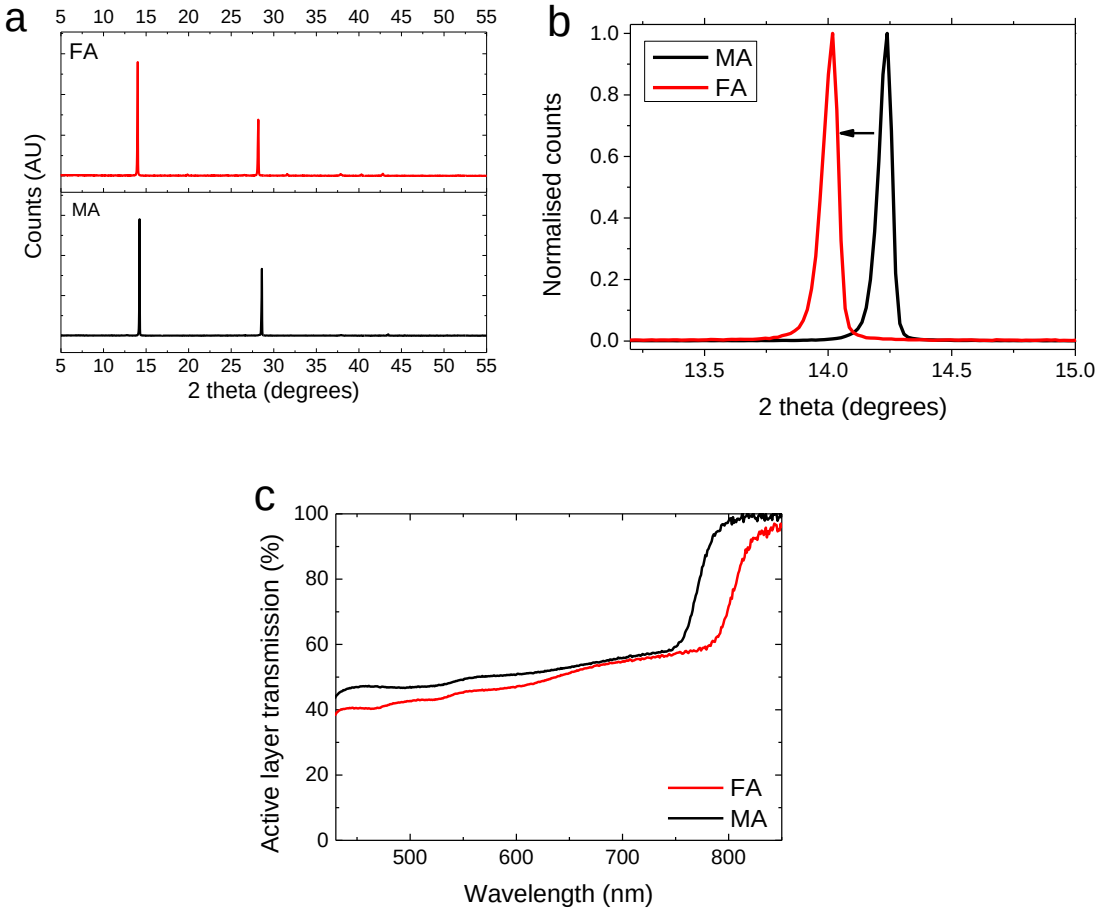

Figure 8.2: a) XRD spectra of the FA and MA films. Labeled peaks correspond to those indexed to the literature crystal structures of a tetragonal strcture with a=8.64Å, c=12.64Å for $MAPbI_3$ and trigonal structure with a=8.99Å, c=11.0Å for $FAPbI_3$. b) Zoom of the peaks at ~14° in the XRD spectra showing the shift from MA to FA. c) Transmittance spectra of the two materials. The data here shows the transmittance of the active layer, including Spiro-OMeTAD and the titania compact layer.

A material with highly oriented crystallinity (meaning that only the peaks associated with the preferred orientation are observed) is observed in the FA material, similar to that observed in the MA material. The peaks observed can be assigned to the (110)/(111) and (220)/(222) peaks of a tetragonal/trigonal lattice structure (with $\alpha=\beta=\gamma=90^o$ for the tetragonal, $\alpha=90^o$, $\beta=90^o$, $\gamma=120^o$ for the trigonal structure) respectively; the MA material agrees well with previous reports of a tetragonal material with a=8.64Å, c=12.64Å, and an obvious shift in 2θ is observed for the FA material (as shown for the peak at ~14° in Figure 8.2b), giving good agreement to a trigonal material with a=8.99Å, c=11.0Å, as previously reported for the black phase of $FAPbI_3$.[3,5,12,13] The change in phase between perovskites is

due to a very slight distortion of the perovskite lattice. No peaks corresponding to $MAPbI_3$ are seen in the FA material's spectrum, allowing it to be assigned unambiguously as almost pure black phase $FAPbI_3$. To further confirm the identity of the material, and to quantify the transparency, the transmittance of the materials was measured, as shown in Figure 8.2c). It is noted that since the application here is for semitransparent solar cells, spectra were taken of the whole active layer of such a device, which is compact TiO_2/perovskite/Spiro-OMeTAD. The method used to obtain the active layer transmittance is discussed in detail in Chapter 3. It is observed that whilst the MA material absorbs out to ~790nm, in accordance with a bandgap of ~1.57eV, the FA material absorbs out to ~840nm, in good agreement with the previously demonstrated bandgap of ~1.48eV.[3] it can thus be confirmed that the material is predominantly $FAPbI_3$; if there is any MA left, it has a negligible effect on the crystal structure and absorption spectrum. Furthermore, the FA material displays a quite flat transmission spectrum across the visible range, indicating that it is likely similarly colour-neutral to the MA material. Both materials formed in this microstructured way display a high transmittance, which is highly encouraging for their use in semitransparent solar cells.

8.4 $FAPbI_3$ microstructured solar cells

Having confirmed that it is possible to fabricate semitransparent microstructured arrays of $FAPbI_3$ islands, planar heterojunction solar cells were fabricated from such films, with the device structure shown in Figure 8.3a).

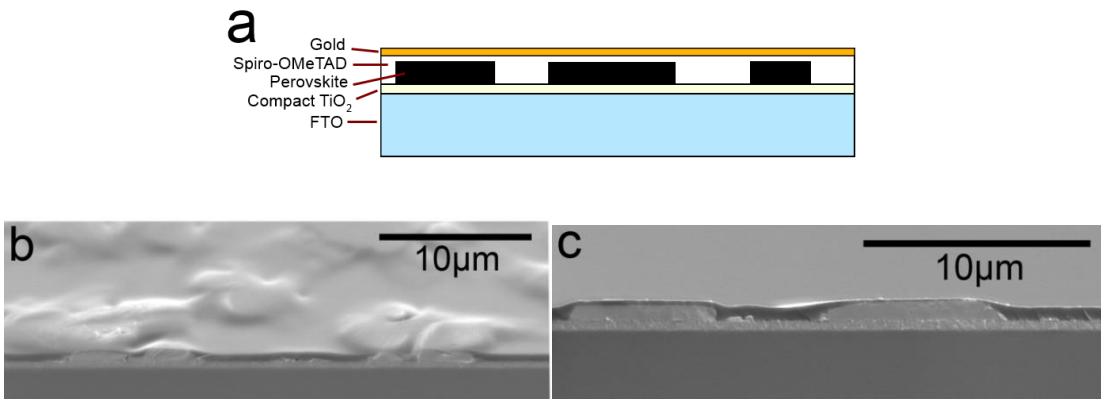

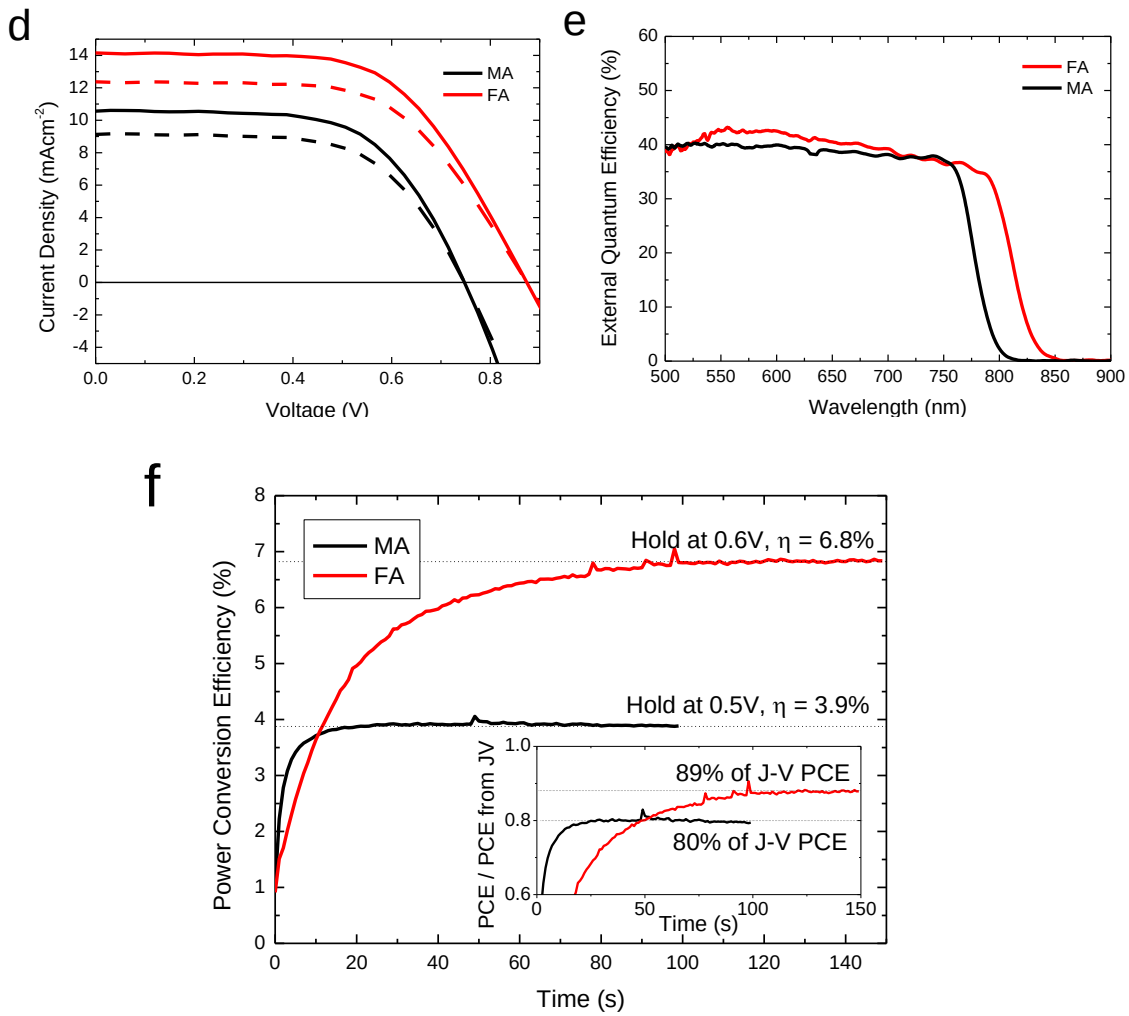

Figure 8.3: a) Diagram of the device architecture employed. b) Tilted and c) cross-sectional SEMs of a full semitransparent $FAPbI_3$ solar cell showing the islands of perovskite coated with Spiro-OMeTAD. d) JV characteristics of $MAPbI_3$ and $FAPbI_3$ solar cells, measured under simulated 100mWcm^{-2} AM1.5 illumination, for both the measured data (solid lines) and that calculated for just one light pass (dashed lines). e) EQE spectra for representative MA and $FAPbI_3$ solar cells. f) PCE extracted at maximum power point under 100mWcm^{-2} illumination over time, and in the inset, the same measurement plotted as a fraction of the PCE determined via a fast JV scan.

As discussed in previous chapters, due to the rectifying nature of the titania-Spiro-OMeTAD contact, such discontinuous devices are still impressively functional. Cross-sectional SEM images of such devices are shown in Figure 8.3b and c); the perovskite islands of ~ 900nm thickness are clearly observed, covered by a thin layer of Spiro-OMeTAD. In order to assess comparative performance of the FA films compared to MA films, thick gold electrodes were used as the cathode. Although transparency is then reduced, this was in order that that device performance was not limited by the electrode

initially. The current-voltage characteristics measured under simulated sunlight (AM1.5, 100mWcm^{-2}) illumination from the best-performing devices fabricated with each material are shown in Figure 8.3d), with full device parameters extracted shown in Table 8.1.

	J_{sc} (mAcm^{-2})	V_{oc} (V)	FF	η (%)	AVT (active layer) (%)	η_{MPP} (%)
FA	14.2	0.86	0.60	7.4	33.6	6.8
FA (1 pass)	12.4			6.4		
MA	10.6	0.64	0.54	4.9	40.5	3.9
MA (1 pass)	9.1			4.2		

Table 8.1: Table showing device characteristics of best $FAPbI_3$ and $MAPbI_3$-based semi-transparent solar cells fabricated with gold contacts. The data for 1 pass refers to the calculated corrected current from the same devices if light was not absorbed in the second pass reflected from the gold electrode, which is the data that would be important for a totally semi-transparent solar cell.

	No. devices	J_{sc} (mAcm^{-2})	V_{oc} (V)	FF	PCE (%)	Active layer AVT (%)
FA	21	13.0±2.1	0.75±0.17	0.40±0.18	4.3±2.6	33.6
MA	32	9.4±1.9	0.69±0.06	0.40±0.17	2.8±1.6	40.5

Table 8.2: Average solar cell performance parameters from a whole batch of FA-based and MA-based semitransparent solar cells, with errors determined via standard deviation, and representative AVT also shown for this batch of devices.

Data for both two passes of light (as measured due to the reflection from the gold contact) and for one pass of light (the best efficiency possible for such a device if it had a perfect transparent cathode, calculated as described in Section 5.8) is shown. The statistics for the whole batch fabricated is shown in Table 8.2. It is noted that the AVT of the FA films is a little lower than the MA films (33.6% compared to 40.5%), and furthermore the $FAPbI_3$ provides absorption over a greater fraction of the solar spectrum due to its reduced bandgap. Accordingly, as may be expected, it is observed that the photocurrent generated is higher than for the $MAPbI_3$. More surprising is the increase in V_{oc} that is observed with the $FAPbI_3$. Due to its reduced bandgap, it would be expected that if anything, the V_{oc}

would decrease. It has been experimentally observed that this increased voltage is reproducible, and its origin is currently unclear. It is possible that the higher-temperature anneal is beneficial to the compact titania, and allows for higher oxygen-doping. This would then raise the turn-on voltage of a Spiro-titania diode; as discussed in Chapter 4 any contact between Spiro-OMeTAD in the cell will act as a parallel shunt diode, so increasing the turn-on voltage of these diodes would have the effect of overall reducing the detrimental effect on V_{oc} that this normally has. The impact of the increased current and voltage in the $FAPbI_3$ compared to the $MAPbI_3$ is significant; power conversion efficiency increases from 4.9% to 7.4% for the best devices (2.8% to 4.3% on average across the batch).

The EQE of representative MA and FA cells is shown in Figure 8.3e). It is observed that the FA generates photocurrent up to ~840nm, and the MA up to ~790nm, in good agreement with the absorption spectra for the different perovskite materials.

It has been observed recently that such planar heterojunction perovskite solar cells are likely to exhibit hysteresis in their JV curves, as discussed in Chapter 2.[14] This can lead to exaggerated PCEs based on fast JV scans; accordingly, it is vital to also measure the stabilised power output of such devices. It has been suggested that $FAPbI_3$ might display less hysteresis compared to $MAPbI_3$, in which case its stabilised power output should be closer to its fast JV PCE.[5] To assess this, as shown in Figure 8.3f), the power output over time was measured while holding the devices at their maximum power point, as determined by the fast JV scan. Both the absolute PCE generated, and PCE as a fraction of that determined by the fast JV, are plotted in Figure 8.3f). It is observed that the $MAPbI_3$ semitransparent cell stabilises quickly, but only at 3.9%, or 80% of its PCE according to the fast JV scan. The $FAPbI_3$ cell takes longer to stabilise, but it then generates 6.8% PCE, which is 89% of its fast JV scan efficiency. These results are very promising for the $FAPbI_3$; they suggest that not only are the stabilised efficiencies significantly higher than a similarly transparent $MAPbI_3$, but also they exhibit a less severe hysteretic effect, meaning that the PCE extracted from a fast JV scan is closer to the stabilised PCE.

8.5 Incorporation of transparent laminated cathode

Having demonstrated that incorporating $FAPbI_3$ into the semitransparent microstructured perovksite solar cell architecture can lead to significantly enhanced efficiencies, the remaining challenge for semitransparent perovskite solar cells is then tackled; making the entire device fully semi-transparent, whilst retaining the neutral colouration. Whilst the FTO-coated glass (hereafter just FTO) is a reasonable transparent anode, the cathode is

more challenging. Previously, a thin gold contact has been relied upon as the semitransparent contact, but this has a detrimental effect on the transparency and neutral colouration. Recently, a transparent conductive adhesive laminate electrode based on a nickel mesh has been developed, which can be laminated onto the solar cell via application of a PEDOT:PSS-based pressure-activated conductive adhesive. This is described in greater detail elsewhere.[15] It provides a low-cost, transparent electrode with good colour-neutrality, and has been shown to be capable of replacing gold as an effective cathode in perovskite solar cells. It comprises a commercial nickel mesh embedded in a PET film, onto which a transparent conductive adhesive comprising a mixture of PEDOT:PSS and an acrylic glue is coated. This electrode is then pressure-laminated onto the solar cells at room temperature, after having spray-coated a thin layer of PEDOT:PSS on top of the Spiro-OMeTAD of the solar cells. This transparent laminated cathode (TLC) is applied to the $FAPbI_3$ semitransparent solar cells, to achieve fully semitransparent working perovskite solar cells with neutral colour for the first time.

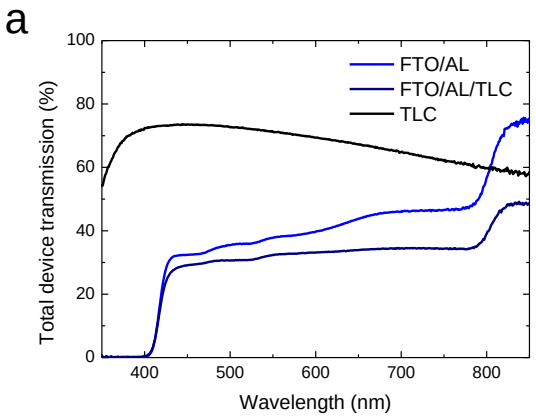

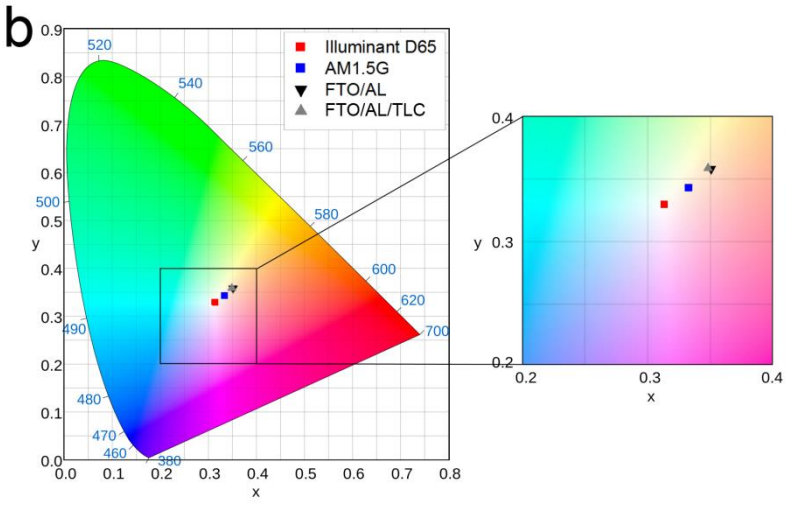

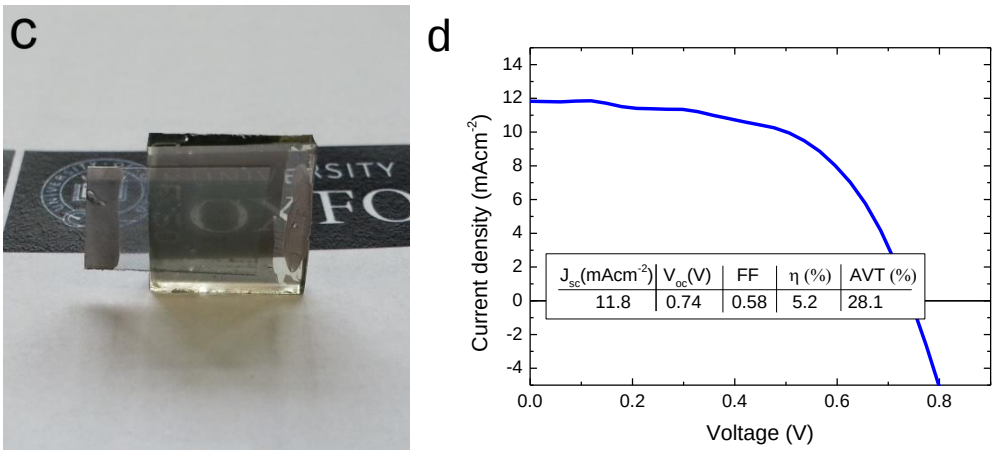

Figure 8.4: a) Transmission spectra of the structures FTO/Active layer, TLC on glass, and FTO/Active layer/TLC. b) colour coordinates of the films with transmittance spectra shown in (a) under AM1.5 illumination, on the CIE xy 1931 chromacity diagram, and the enlarged central region. Colour coordinates of the D65 standard daylight illuminant and AM1.5 illumination are also shown. c) Photograph of a fully semi-transparent $FAPbI_3$ device including the laminated transparent cathode d) Current-voltage characteristics of a fully semitransparent device such as depicted above. (University of Oxford logo reproduced with permission. Courtesy of University of Oxford.)

In Figure 8.4a), the transmission of the TLC alone, and the transmission of a full $FAPbI_3$ solar cell before (FTO/AL, where AL = active layer) and after the application of the TLC (FTO/AL/TLC), are shown. It is observed that the average visible transmittance is reduced from 34.2% to 28.1% upon application of the cathode. The flat transmission spectrum is retained, even enhanced. It is observed that the TLC on its own attenuates much more light than the increased attenuation when applied upon the perovskite cell. This is thought to be due to a large fraction of the attenuation with the TLC being reflection rather than absorption, which is predominantly absent at the AL/TLC interface in the complete stack. The colour-neutrality of the whole device is verified by calculating the colour perception indices according to the CIE 1931 xy colour space standard, as described in previous chapters. Transmitted light is represented by the product of the AM1.5 spectrum and the transmission of the sample in question. In Figure 8.4b), the colour coordinates of the active layer only (compact titania/perovskite/Spiro-OMeTAD), the active layer on FTO-glass, and the whole FTO/AL/TLC device are shown, compared to the reference daylight illuminant D65 and the AM1.5 spectrum. It can be observed that the films have excellent colour-neutrality, lying well within the central region of the chromacity diagram, close to the AM1.5 spectrum. Application of the transparent electrodes does not affect the colour

perception to any great extent, demonstrating that they are a suitable choice of transparent conductive electrode for the neutral-coloured $FAPbI_3$ semitransparent solar cell. A photograph of a neutral-coloured semitransparent $FAPbI_3$ device with both electrodes is shown in Figure 8.4c), exhibiting good visual transparency. Figure 8.4d) shows the current-voltage characteristics of the best-performing fully semi-transparent FTO/AL/TLC $FAPbI_3$ device fabricated. It displays a lower short-circuit current and open-circuit voltage than the equivalent devices with gold electrodes, though the current density is close to as expected with 1 pass of light. Accordingly, a PCE of 5.2% was obtained, for a neutral-coloured semitransparent solar cell with an AVT of 28%, with an active area of approximately 0.5 $cm^{-2,}$ masked to 0.0625cm^2.

A neutral-coloured perovskite device with 5.2% efficiency and complete device semitransparency of almost 30% represents a significant step towards the commercialisation of this technology. The efficiency/transparency ratio is almost as good as some of the recently reported single junction organic solar cells, despite the fact that the organic solar cell field is more than 20 years old.[16–18] These characteristics in fact make this one of the best performing neutral-coloured single junction semitransparent solar cells reported. However, the key advantage that the cells realised here have is in cost. The perovskite active material itself is comprised of readily available, cheap materials. Furthermore, in this chapter the possibility of replacing an expensive precious metal cathode with a cheap, and simple to process nickel-based mesh, has been shown. Neither is there any ITO in the device, a common concern due to the limited availability of indium. Fabrication of the whole device takes place via solution-processing at low temperatures and at atmospheric pressure; not a single vacuum process is required. This results in a semi-transparent solar cell which is extremely cheap, and the cost of coating such devices onto window glass would likely be less than the cost of the glass itself.[19] The limiting factors in the cost of the device now become the use of Spiro-OMeTAD as HTM and the high-temperature annealing for the titania compact layer. Replacement of Spiro-OMeTAD would also be advantageous for the AVT of such devices, as Spiro-OMeTAD absorbs strongly below 430nm, affecting the AVT somewhat. The titania compact layer is annealed at 500^oC, increasing the processing cost incurred in device production. Neither of these problems are insoluble however, and work in the perovskite solar cell community is well focussed on overcoming these limitations.[20–23]

It is observed that the efficiency of the $FAPbI_3$ devices drop upon use of the TLC. This mainly stems from a loss in V_{oc} and FF, which is possibly due to an increase in series resistance from the thick PEDOT:PSS/adhesive blend, and the fact that the HOMO of

PEDOT:PSS is typically higher than that of Spiro-OMeTAD, reducing the possible V_{oc}. Additionally, a significant drop in transmission is observed on application of the TLC. Therefore, it can be concluded that although the TLC provides good transparency and hole extraction, it is still not ideal. It can be expected that future developments in perovskite-compatible transparent electrodes will enable even higher PCEs from such semitransparent solar cells.

The TLC is mechanically flexible, meaning that by application of this to such semitransparent solar cells, the first steps towards a roll-to-roll processable semitransparent perovskite solar cell have been taken. If a flexible transparent substrate and anode were to be employed, for example ITO on PET, and combined with the TLC, it is apparent that such a device could be produced, further enhancing the commercial attractiveness of these solar cells for laminatable semitransparent PV foils.

8.6 Incident light angle dependence

For a building-integrated photovolatics to perform well all day, they must be effective in harvesting light that is incident at angles other than direct illumination. For the majority of the time, a window will be experiencing illumination angles significantly shallower than direct. Thererfore the angle-dependent short-circuit current generated by the $FAPbI_3$ and $MAPbI_3$ semitransparent solar cells were measured, in comparison to monocrystalline and polycrystalline silicon cells. Devices were illuminated with a laser with a small spot size to avoid errors due to variation of total incident power. To also represent power output expected from a working module as a function of angle to the sun, the data was multiplied by $\cos\theta$, to account for the reduced projected footprint of the solar cell with increasing angle. Figure 8.5 shows both the current generated from a small spot as a function of angle (solid lines) and multiplied by $\cos\theta$ to represent illumination area larger than the cell (dashed lines).

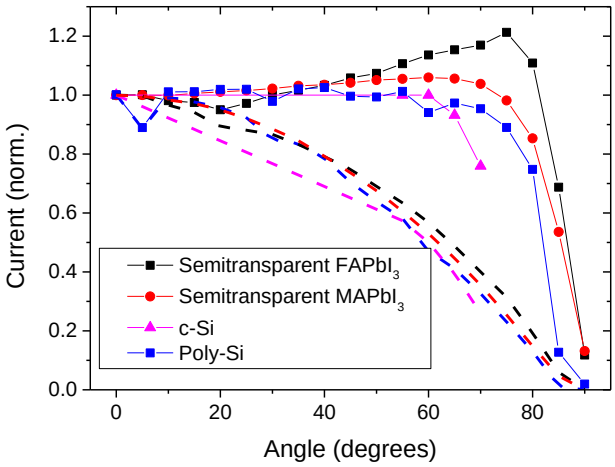

Figure 8.5: Angle-dependent photocurrent extracted from $FAPbI_3$ and $MAPbI_3$ semi-transparent solar cells, compared to that extracted from crystalline silicon (c-Si) and polycrystalline silicon (poly-Si) devices. 0° represents light incident at the normal; light incident at 90°is coming completely from the side of the device. Dashed lines take into account the reduced footprint of the solar cell with increased illumination angle to represent power output from a module in operation.

The semi-transparent FA and $MAPbI_3$ devices performed unprecedentedly well at lower light angles. At angles shallower than the normal, and right up to ~70° from normal, the $MAPbI_3$ devices generated even more power than they did at the normal. Even more impressively, the $FAPbI_3$ devices show a continuous *increase* in current generated as the device is angled away from the normal, and generate up to 1.2 times the current extracted from normal incident light at 75%. Notably, both technologies show a drop-off in current at higher angles than either silicon technology tested. c-Si begins to drop in current at ~60°, and polycrystalline silicon at ~65°, as compared to the MA at 70° and the FA at 80°. It is thought that at larger angles of incidence, light will be absorbed by the edges of the perovskite' islands', and can still be converted to current, as opposed to the smooth and flat silicon solar cells. At certain angles, a greater surface area of perovskite will in fact be illuminated due to the aspect ratio of the islands, hence the increase above the current displayed at 0°. The particular morphologies of the two perovskites are likely responsible for the distinction between their behaviours. In addition to the extra absorption from the edges of the islands, there could also be a waveguiding effect provided from the Spiro-OMeTAD, where light incident at shallow angles onto a point with no perovskite is redirected along the plane of the solar cell until it hits the side of a perovskite island. It is

likely that both of these effects combine to produce the beneficial angle dependence observed.

This demonstrates an important advantage of the semitransparent perovskites, and in particular the $FAPbI_3$, for building-integrated photovoltaics. If this aspect can be enhanced by careful design of the optical properties of each layer, then the semi-transparent perovskite cells may be ideal for BIPV in high irradiance locations, where the sun spends a large fraction of the day close to perpendicular.

The final concern when considering building-integration of solar cells, aside from efficiency, transparency, aesthetics and cost, is that of long-term stability. The methylammonium and formamidinium perovskites suffer from moisture-induced degradation, meaning that effective waterproofing or sealing is necessary for real operation.[3] For power-generating glass to be a viable installation, it must have a very long functional lifetime to avoid the necessity of replacing windows or window-coatings regularly. Furthermore, for the neutral-coloured application discussed here, one problem could be colour change under moisture degradation, to the yellow of lead iodide, the degradation product.[24] However, it has been shown that when sealed effectively, such devices can be stable for hundreds of hours under full spectrum sunlight.[25] Additionally, recently a water-resistant hole-transporting material replacement has been developed, which may be able to fully solve the issue of water-sensitivity.[24] Furthermore, others have demonstrated a screen-printable carbon back electrode/hole transporter configuration that enables long-term moisture stability.[26] These developments all point towards the possibility of perovskite solar cells that are stable in the long term, even in outdoor environments.

8.7 Outlook and conclusion

In summary, efficient semi-transparent perovskite solar cells were fabricated by a) incorporating the formamidinium cation into the microstructured architecture and b) application of a novel transparent cathode. The FA-based perovskite displayed higher solar cell performance parameters and lower hysteresis than the equivalent methylammonium-based devices, with an efficiency of 6.4% for a 34% AVT active layer. With the application of a transparent cathode, it was possible to fabricate completely semitransparent full working devices with impressively neutral-coloured transparency. From these, a power conversion efficiency of 5.2% was achieved from a device with an AVT of 28%. This is a significant improvement on previous reports, rendering the devices very commercially attractive for power-generating window applications. The angular

dependence of the semitransparent perovskite technologies demonstrated excellent performance at non-normal angles, surpassing commercially mature silicon technologies. These solar cells thus appear to be ideal for all-day operation in a building-integrated setting.

8.8 References

1. G. E. Eperon, V. M. Burlakov, A. Goriely and H. J. Snaith, *ACS Nano*, 2014, **8**, 591–598.

2. C. Roldan, O. Malinkiewicz, R. Betancur, G. Longo, C. Momblona, F. Jaramillo, L. Camacho and H. J. Bolink, *Energy Environ. Sci.*, 2014, **7**, 2968–2973.

3. G. E. Eperon, S. D. Stranks, C. Menelaou, M. B. Johnston, L. M. Herz and H. J. Snaith, *Energy Environ. Sci.*, 2014, **7**, 982–988.

4. N. Pellet, P. Gao, G. Gregori, T.-Y. Yang, M. K. Nazeeruddin, J. Maier and M. Grätzel, *Angew. Chemie Int. Ed.*, 2014, **53**, 3151–3157.

5. J.-W. Lee, D.-J. Seol, A.-N. Cho and N.-G. Park, *Adv. Mater.*, 2014, **26**, 4991–4998.

6. Y. Zhao and K. Zhu, *J. Phys. Chem. C*, 2014, **118**, 9412–9418.

7. V. M. Burlakov, G. E. Eperon, H. J. Snaith, S. J. Chapman and A. Goriely, *Appl. Phys. Lett.*, 2014, **104**, 091602.

8. A. Dualeh, N. Tétreault, T. Moehl, P. Gao, M. K. Nazeeruddin and M. Grätzel, *Adv. Funct. Mater.*, 2014, **24**, 3250–3258.

9. G. E. Eperon, V. M. Burlakov, P. Docampo, A. Goriely and H. J. Snaith, *Adv. Funct. Mater.*, 2014, **24**, 151–157.

10. S. T. Williams, F. Zuo, C.-C. Chueh, C.-Y. Liao, P.-W. Liang and A. K.-Y. Jen, *ACS Nano*, 2014, **8**, 10640–10654.

11. S. Colella, E. Mosconi, G. Pellegrino, A. Alberti, V. L. P. Guerra, A. Listorti, A. Rizzo, G. G. Condorelli, F. De Angelis and G. Gigli, 2014, **20,** 3532-3538.

12. C. C. Stoumpos, C. D. Malliakas and M. G. Kanatzidis, *Inorg. Chem.*, 2013, **52**, 9019–9038.

13. T. M. Koh, K. Fu, Y. Fang, S. Chen, T. C. Sum, N. Mathews, S. G. Mhaisalkar, P. P. Boix and T. Baikie, *J. Phys. Chem. C*, 2014, **118**, 16458–16462.

14. H. J. Snaith, A. Abate, J. M. Ball, G. E. Eperon, T. Leijtens, N. K. Noel, S. D. Stranks, J. T. Wang, K. Wojciechowski and W. Zhang, *J. Phys. Chem. Lett.*, 2014, **5**, 1511–1515.

15. D. Bryant, P. Greenwood, J. Troughton, M. Wijdekop, M. Carnie, M. Davies, K. Wojciechowski, H. J. Snaith, T. Watson and D. Worsley, *Adv. Mater.*, 2014, **26**, 7499–7504.

16. K.-S. Chen, J.-F. Salinas, H.-L. Yip, L. Huo, J. Hou and A. K.-Y. Jen, *Energy Environ. Sci.*, 2012, **5**, 9551.

17. A. R. B. M. Yusoff, S. J. Lee, F. K. Shneider, W. J. da Silva and J. Jang, *Adv. Energy Mater.*, 2014, **4**, 1301989.

18. C.-C. Chueh, S.-C. Chien, H.-L. Yip, J. F. Salinas, C.-Z. Li, K.-S. Chen, F.-C. Chen, W.-C. Chen and A. K.-Y. Jen, *Adv. Energy Mater.*, 2013, **3**, 417–423.

19. H. J. Snaith, *J. Phys. Chem. Lett.*, 2013, **4**, 3623–3630.

20. B. Conings, L. Baeten, C. De Dobbelaere, J. D. Haen, J. Manca, H. G. Boyen, C. De Dobbelaere, J. D'Haen, J. Manca and H. G. Boyen, *Adv. Mater.*, 2014, **26**, 2041–2046.

21. A. S. Subbiah, A. Halder, S. Ghosh, N. Mahuli, G. Hodes and S. K. Sarkar, *J. Phys. Chem. Lett.*, 2014, **5**, 1748–1753.

22. D. Liu and T. L. Kelly, *Nat. Photonics*, 2013, **8**, 133–138.

23. K. Wojciechowski, M. Saliba, T. Leijtens, A. Abate and H. J. Snaith, *Energy Environ. Sci.*, 2014, **7**, 1142.

24. S. N. Habisreutinger, T. Leijtens, G. E. Eperon, S. D. Stranks, R. J. Nicholas and H. J. Snaith, *Nano Lett.*, 2014, **14**, 5561–5568.

25. T. Leijtens, G. E. Eperon, S. Pathak, A. Abate, M. M. Lee and H. J. Snaith, *Nat. Commun.*, 2013, **4**, 2885.

26. A. Mei, X. Li, L. Liu, Z. Ku, T. Liu, Y. Rong, M. Xu, M. Hu, J. Chen, Y. Yang, M. Gratzel, H. Han, M. Grätzel and H. Han, *Science*, 2014, **345**, 295–298.

9. INORGANIC CAESIUM LEAD IODIDE PEROVSKITE SOLAR CELLS WITH CURRENT-VOLTAGE HYSTERESIS

The work presented in this chapter has been submitted for publication as:

- G. E. Eperon, G. M. Paternò, R. J. Sutton, A. Zampetti A. A. Haghigharad, F. Cacialli and H. J. Snaith, "Inorganic caesium lead iodide perovskite solar cells", 2015

9.1 Context and summary

The vast majority of perovskite solar cell research has focused on organic-inorganic lead trihalide perovskites. $CsPbI_3$ thin films were presented in Chapter 7, but they proved too unstable for fabricate devices from. In this chapter, working inorganic $CsPbI_3$ perovskite solar cells are presented for the first time. $CsPbI_3$ normally resides in a yellow non-perovskite phase at room temperature, but by careful processing control and development of a low-temperature phase transition route the material has been stabilised in the black perovskite phase at room temperature. Solar cell devices in a variety of architectures have been fabricated, with current-voltage curve measured efficiency up to 2.9% for a planar heterojunction architecture, and stabilised power conversion efficiency of 1.7%. The functioning planar junction devices demonstrate long-range electron and hole transport in this material, importantly demonstrating that there is nothing particularly special about the hybrid organic-inorganic nature of the more studied perovskites. Significant rate-dependent current-voltage hysteresis is observed in such devices, despite the absence of the organic polar molecule previously thought to be a candidate for inducing hysteresis via ferroelectric polarisation. Due to its space group and lack of a polar component, $CsPbI_3$ cannot be a ferroelectric material, thus the notion that ferroelectricity is required to explain current-voltage hysteresis in perovskite solar cells can be comprehensively dismissed. This report of working inorganic perovskite solar cells paves the way for further developments likely to lead to higher efficiencies, more stable devices, and new materials for inorganic perovskite solar cells.

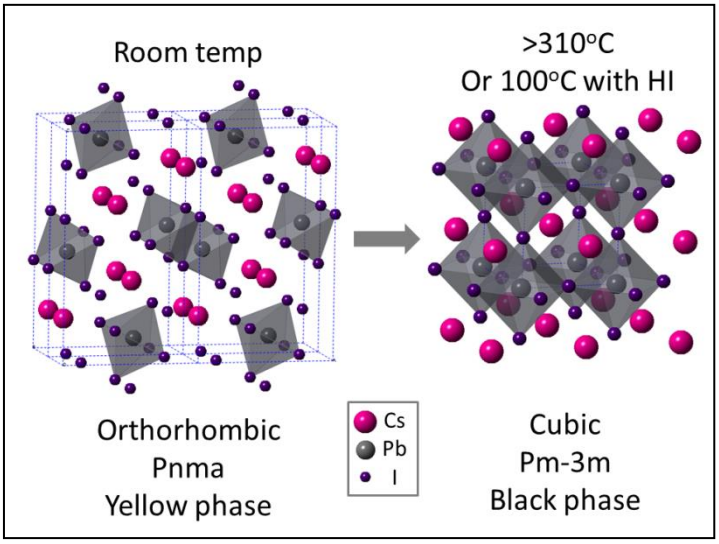

9.2 Introduction

As discussed and demonstrated in the prior chapters of this thesis, the most studied perovskite materials for solar cells, methylammonium lead triiodide and formamidinium lead triiodide exhibit long-range electron and hole diffusion lengths, low exciton binding energies, high carrier mobilities and suitable bandgaps for making solar cells and other optoelectronic devices.[1–5] Whilst the organic cation enables the stabilisation of the ABX_3 perovskite structure, one concern of these hybrid perovskites, when compared to conventional thin film compound semiconductors, *is* the inclusion of the organic cation: as shown in Chapter 7, the hybrid perovskites have considerably lower thermal decomposition temperatures (between 150 to 200°C in thin film) than conventional inorganic semiconductors. In addition, whilst these materials form high quality thin film semiconductors and subsequently high efficiency solar cells, in certain configurations they exhibit a current-voltage hysteresis on the timescale of seconds, making it easy to overestimate the actual power conversion efficiency of such devices and inhibiting the maximum performance being achieved.[6–8] Recently there has been much speculation about the origin of this hysteresis, with the two main suggestions being 1) that it is due to the motion of charged defects in solar cells under operating conditions, leading to beneficial or detrimental bias-dependent charge extraction efficiency,[9–11] or 2) that it is due to a ferroelectric polarisation, originating from aligned dipolar organic molecules in the lattice.[12–16] There is evidence for both theories and thus far no studies have conclusively ruled out either possibility. Ferroelectricity of the $MAPbI_3$ perovskite is thought to arise from alignment of the MA molecular dipoles throughout the lattice. Therefore, replacement of the polar organic molecule with a non-polar component would be an ideal test for the ferroelectric theory. If the polar organic molecule is responsible for the hysteretic effect, replacing it with a non-polar component should result in hysteresis-free devices. There have been reports of all inorganic caesium tin iodide perovskite solar cells, which do replace the organic component and also the lead cation.[17,18] However, the efficiencies are very low and these are fabricated on mesoporous titania, a structure that is known to mitigate hysteretic effects.[6] Additionally, fabrication of Sn-based devices remains challenging due to susceptibility for the Sn^{2+} ion to oxidize to Sn^{4+}.[19] Caesium lead iodide, the perovskite formed by substituting the organic cation in $MAPbI_3$ with caesium, has not yet been reported in functioning solar cells, likely due to the fact that the desired black (~1.73eV bandgap) cubic perovskite phase is not stable at room temperature at ambient conditions, making fabrication challenging.[20] The material generally transforms to the yellow NH_3CdCl_3 non-perovskite structure type at room temperature within a matter of minutes.[21] Solar cells with this yellow phase have been reported, but did not

function at more than 0.09% PCE.[22] In this chapter, by processing the material in a totally air-free environment, allowing stabilisation of it in its black phase, working caesium lead iodide solar cells are fabricated for the first time, and it is shown that such fully inorganic devices do display significant hysteresis in the current-voltage measurement. It can be comprehensively concluded that rotational alignment of the organic polar molecule in hybrid perovskite solar cells is not necessary for inducing current-voltage hysteresis. Moreover, the respectable starting performance of these inorganic perovskite devices shows that the hybrid nature of the previously explored perovskites is not critical to fabrication of working solar cells. The solar cells function even in a thin-film planar heterojunction architecture, demonstrating that this material has good ambipolar transport properties and a significant diffusion length despite the absence of the organic dipolar component.

9.3 Low-temperature fabrication and stabilisation of $CsPbI_3$

Caesium lead iodide ($CsPbI_3$) has been previously synthesised as single crystals and as nanocrystals, and as a dopant in methylammonium lead iodide films in solar cells.[20,22–26] It can be solution-processed in a similar manner to the hybrid lead halide perovskites; upon formation at room temperature it exhibits a yellow orthorhombic phase with wide bandgap, unsuitable for solar cell applications.[20] Upon heating, it can form a black cubic perovskite phase with an optical bandgap of ~1.73eV.[26] The phase transition has been reported to occur at temperatures of ~310°C.[20,25] However, upon cooling, this phase is unstable in ambient conditions at room temperature, returning to the yellow non-perovskite phase in a matter of minutes. Practically, it was found that when spin-coating a thin film of material, heating at temperatures of ≥335°C was necessary to form the black phase, and that after returning to the yellow phase when exposed to ambient conditions, re-heating would return it to the black phase. Notably however, it was found that when the film was never exposed to ambient air, it remained 'frozen' in the black phase even at room temperature, for a matter of weeks at least. The presence of atmospheric moisture appears to catalyse the phase transition in some way. Thus, by processing full devices in completely air-free systems, it was possible to fabricate thin films and full solar cell devices. Smooth and uniform thin films of black phase $CsPbI_3$were formed by spin-coating a 1:1 CsI:PbI_2 solution in DMF and heating to 335°C. However, 335 °C is still a relatively high temperature, rendering the conversion impractical for a number of device architectures and substrates, such as temperature-sensitive c-Si solar cells (relevant for tandem cell applications). However, it was found that by adding a small amount of hydroiodic acid, an additive commonly employed to enhance the solubility of perovskite

precursors allowing uniform film formation (as shown in Chapter 7),[2,27] to the precursor solution prior to spin-coating, it as possible to convert from the yellow to the black phase at only 100°C. Using this additive route, it was possible to form uniform and smooth thin films of black $CsPbI_3$ by spin-coating the precursor solution plus additive and annealing at 100°C for 10 minutes.

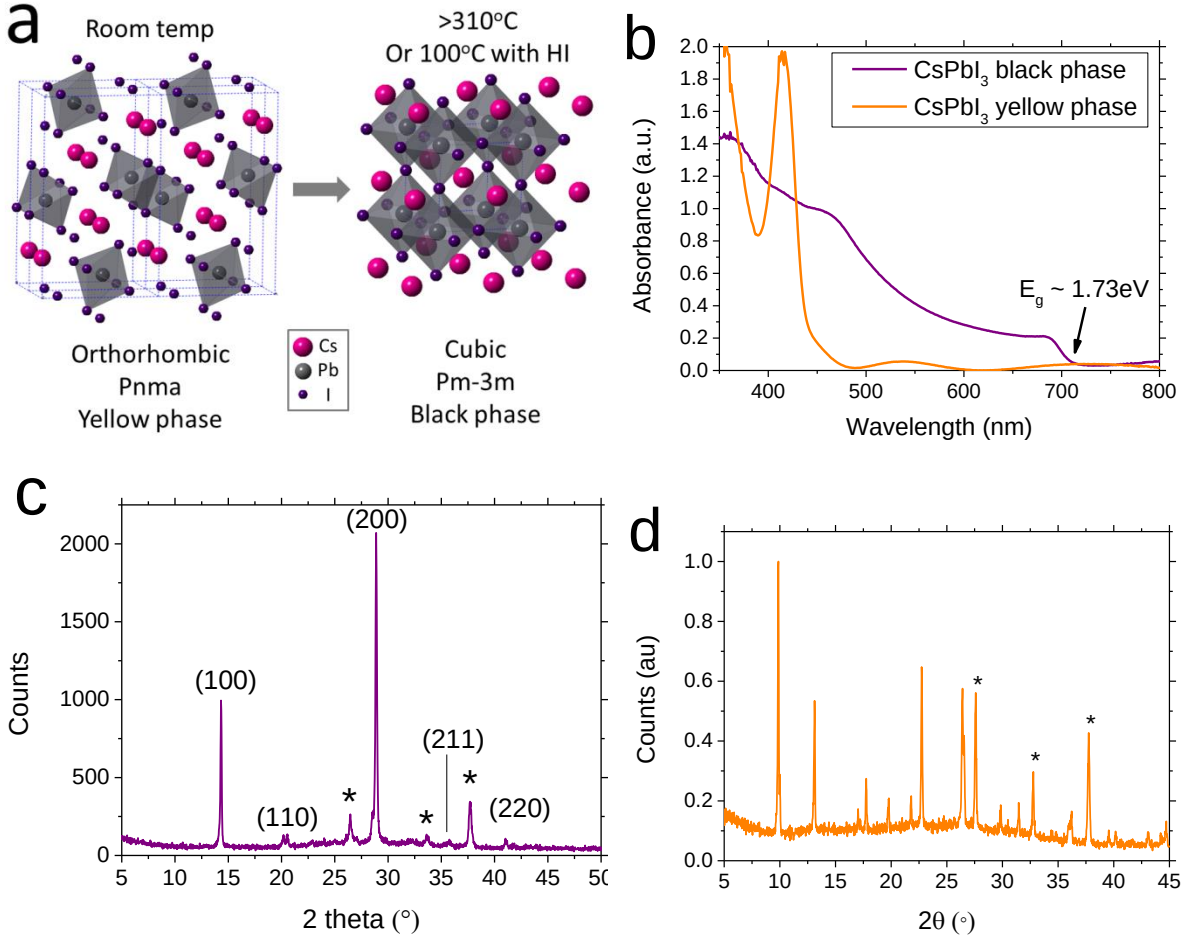

Figure 9.1: Material properties of $CsPbI_3$ a) Diagrammatic structure of $CsPbI_3$ phases20,23. b) Absorbance spectra of black and yellow phases of $CsPbI_3$ thin films. c) X-ray diffraction spectra (XRD) of $CsPbI_3$ thin film in black phase, with peaks assigned to a cubic (Pm-3m) lattice with a=6.1769(3)Å. Peaks marked with * are those assigned to the FTO substrate. The XRD was performed in air, with the perovskite film coated with polymethylmethacrylate (PMMA) to minimise exposure to air and inhibit the transformation into the yellow phase. d, XRD of yellow phase $CsPbI_3$.

Figure 9.1 shows the material properties of $CsPbI_3$ yellow and black phase thin films. The crystal structures of the yellow and black phases are shown in Figure 9.1a). Absorbance spectra (Figure 9.1b) agree with previous observations and indicate a material with

bandgap of ~1.73 eV for the black phase, and a material absorbing only below ~440 nm (2.82 eV) in the yellow phase. Refinement of x-ray diffraction data for the black phase (Figure 9.2c) indicates a cubic perovskite structure with lattice constant a=6.1769(3) Å and space group Pm-3m (no. 221).[20,23] It is noted that this is not a ferroelectric space group, so this material cannot sustain ferroelectricity in the classical manner- by distortion of the lattice.

The addition of HI did not result in any obvious changes to the optical properties of the material, as is shown in Figure 9.2; the absorption spectrum is essentially identical for the low and high temperature processed material. However, it was noticed that in addition to forming the black phase at lower temperature, the films processed with HI at low temperature were stable in the black phase for significantly longer when exposed to air than the high-temperature processed films – hours rather than minutes. This implies that the films processed with HI are producing a material with a more energetically favourable black phase – it requires less energy input to form it and it is more stable once formed. To further understand the role of HI, and the mechanism by which it allows us to form the black phase at a lower temperature, a more in-depth characterisation of the material formed with and without HI was carried out.

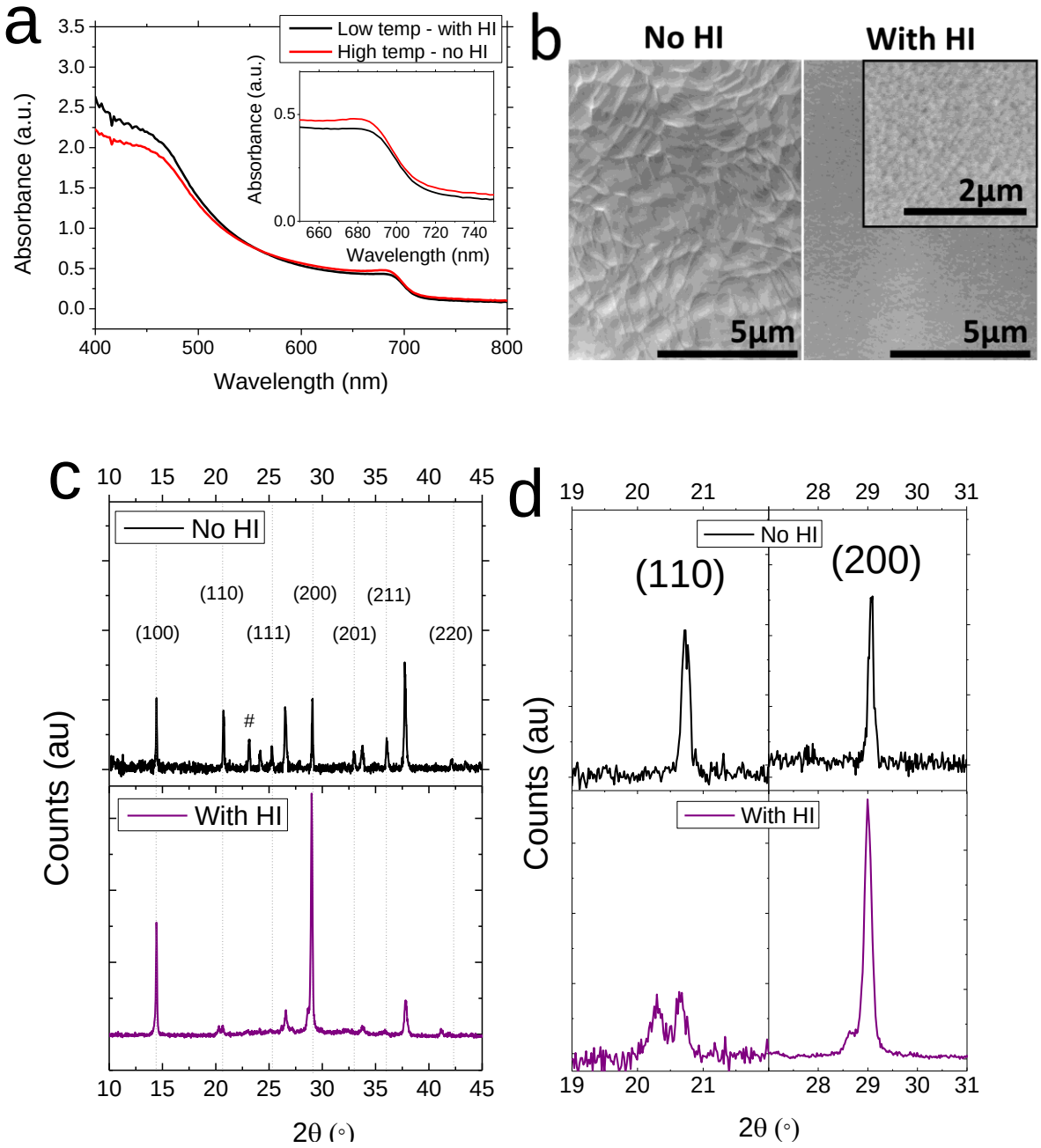

Figure 9.2: a) Comparison of absorbance spectra of films fabricated at low and high temperatures (with and without the hydroiodic acid additive) on FTO/compact TiO_2 substrate, which is representative of the morphology on all substrates. Inset: magnification of onset. b) Scanning electron micrographs of films fabricated without and witt HI additive, annealed at high and low temperature respectively. Inset: magnification of film fabricated with HI showing small grain size. c) Comparison of XRD spectra of films processed with and without HI. Assigned peaks are marked; peaks labelled with a # are assigned to some yellow phase present due to degradation in the film without HI (full spectrum of yellow phase in Figure 9.1). d)

Magnification of the (110) and (200) peaks to show peak splitting and shoulder in film processed with HI.

As shown in Figure 9.2b, scanning electron microscope characterisation of the surface of black phase films formed with and without HI (annealed at low and high temperature respectively), indicate a significant difference. Both films appear very uniform and smooth, but the grain size of the films formed without HI is very large, whereas with HI, the grains are significantly smaller – only on the scale of ~100nm, compared to almost microns in the film processed without HI. Comparing the X-ray diffraction spectra (Figure 9.2c and d), it can be noticed that although the overall majority crystal structure appears identical in the two films, there is a different degree of orientation (comparing the magnitude of the (100) and (200) peaks with the other peaks observed) – the film processed with HI has a more pronounced orientation. Moreover, looking closely at the (110) and (200) peaks (Figure 9.2d), a further difference becomes evident. The (110) peak is in fact split in the film processed with HI, appearing as a single peak only in the film processed without HI. This second peak cannot be assigned to any possible impurity, nor degradation to the yellow phase, the spectrum of which is shown in Figure 9.1d). The (200) peak exhibits a small shoulder in the HI processed film, and is a clear single peak in the film without HI. Peak splitting such as this is often related to the presence of strain in a crystal; thus it is proposed that the film processed with HI has a slightly strained crystal lattice.[28] This strain could then be responsible for allowing the lower temperature phase transition; strain has previously been observed to induce crystal phase transitions, and serves to completely shift the phase diagram for a material.[29–32] The role of HI in creating this lattice strain is likely related to formation of the smaller grains, which then causes the strain in the lattice. The small crystals presumably result from faster crystallisation from the solution containing HI, which could be due to the HI being driven off more rapidly than pure DMF, or reduced solubility of the precursors in a solution containing HI. It is noted that this would be opposite to the behaviour observed for $MAPbI_3$ or $FAPbI_3$, as detailed in Chapter 7, but given the replacement of the organic component with Cs, likely totally altering the solubility in different solvents, this would not be unprecedented. The evaporation of the HI during spin-coating could also be responsible for nucleating the material, providing a greater nucleation density and thus a larger number of smaller grains. HI clearly induces the formation of smaller grains, and this is likely responsible for stabilising the black phase at lower temperature. It is noted that in the previous report of $CsPbI_3$ nanocrystals, Protesescu *et al* observed that the smaller the nanocrystals, the more stable they were in the black phase, with the smallest nanocrystals being stable in the black phase for

months.[23] This fits well with the observations made here and reinforces this hypothesis, suggesting that the grain size is of critical importance for stabilisation of the black phase at low temperature.

9.4 $CsPbI_3$ solar cells

Having formed $CsPbI_3$ stably in the black cubic phase, and having ascertained that it can be maintained in this phase for a long period of time by processing in air-free environments, solar cell devices were fabricated. Solar cells were made in both the planar heterojunction and infiltrated mesoporous TiO_2 architectures, as planar heterojunctions will function only if the material is such that photoexcitation generates free carriers which are able to reach the opposite sides of the device before recombining. Infiltrating the perovskite into mesoporous titania allows materials with worse transport properties to function effectively, with the material acting as a sensitizer, and transferring photoexcited carriers rapidly into the mesoporous titania and hole transporting layer as appropriate. Additionally, the low temperature processing route allowed the fabrication of 'inverted' planar heterojunction devices, based on a PEDOT:PSS coated substrate with the n-type PCBM electron collection layer on top. Figure 9.3a shows diagrammatic representations of the different architectures employed.

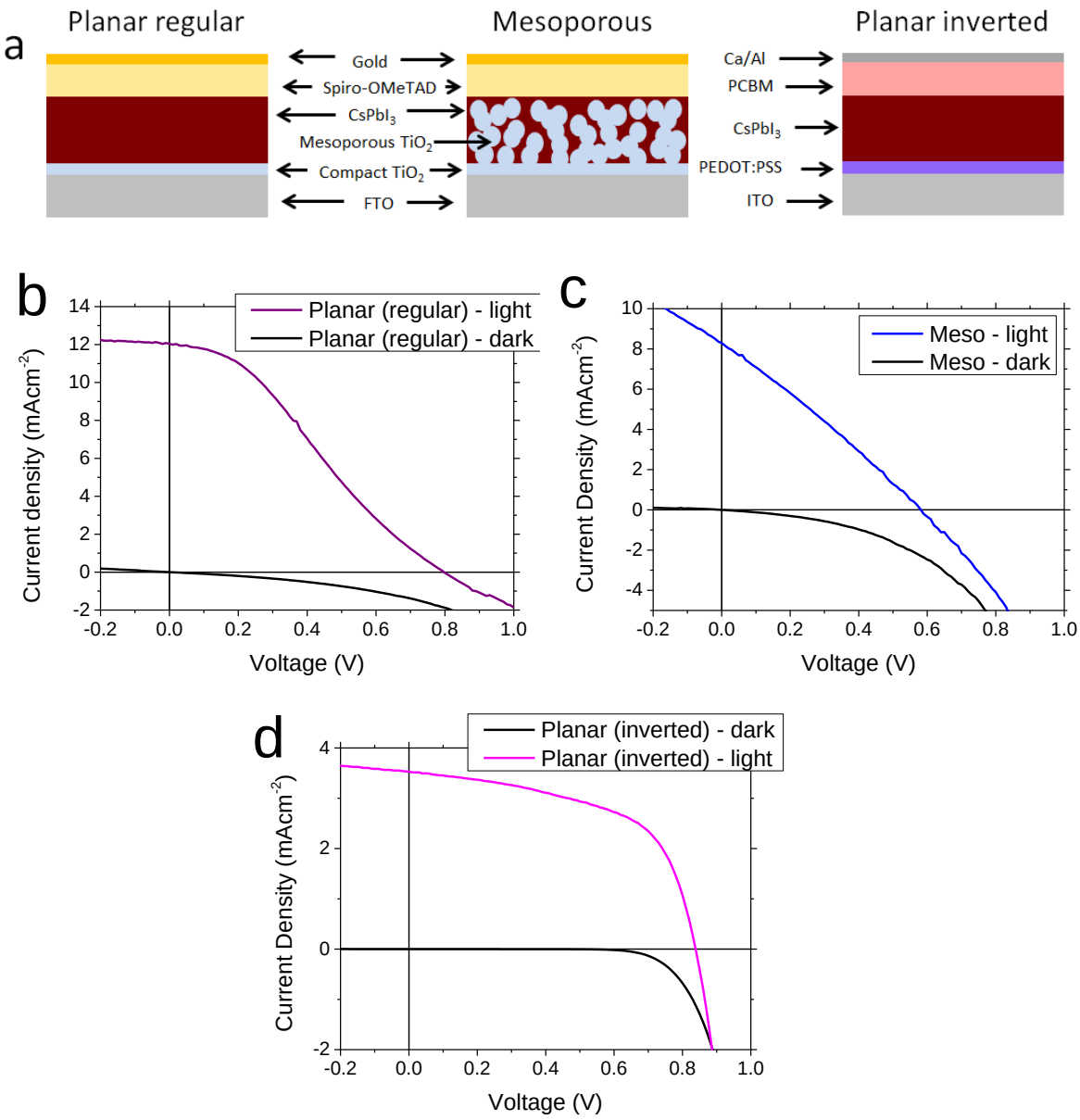

Figure 9.3: Solar cell properties. a) Schematic of the architectures used. Current-voltage characteristics measured under simulated AM1.5G illumination, scanning from forward to reverse bias at 0.1V/s, for regular planar heterojunctions (b), mesoporous titania based devices (c), and inverted planar heterojunctions (d). Devices were unencapsulated and were measured in vacuum conditions.

The perovskite, optionally infiltrated within a 400nm thick layer of mesoporous TiO_2, is sandwiched between electron-selective and hole-selective contacts of compact TiO_2 and Spiro-OMeTAD respectively for the 'regular' devices and PCBM and PEDOT:PSS for the 'inverted' devices. When not infiltrated, the perovskite was measured to have thickness of ~220nm. The Spiro-OMeTAD was doped with Spiro$(TFSI)_2$ and tert-butylpyridine; the Spiro$(TFSI)_2$ negates the normal requirement for doping via air exposure.[33] The current-

voltage (JV) characteristics, measured under AM1.5 illumination and scanning from forward to reverse bias, are shown in Figure 9.3b, c and d. The regular architecture planar perovskite solar cells are observed to generate up to 12mAcm^{-2} short-circuit current density, and an open-circuit voltage of ~0.8V. This results in 2.9% PCE for the fast JV scan. The mesoporous titania devices do not perform as effectively, generating lower open-circuit voltage, fill factor, and short-circuit current. This results in only 1.3% PCE. The planar inverted devices generate a lower current, but a good fill factor and open-circuit voltage, resulting in 1.7% PCE. High-temperature processed $CsPbI_3$ devices in the regular planar and mesoporous structures were also fabricated; these devices behaved very similarly to the low-temperature processed films. The planar regular devices and the mesoporous devices are clearly subject to imperfect shunt and series resistances, and possibly non-optimal interface contacts causing the s-shape of the planar device. Clearly, they are not optimised devices, but they do function. Further work will be necessary to understand the limitations of these initial devices, and fabricate high-efficiency solar cells. These will likely be enabled by optimising deposition techniques and annealing protocols, as has been responsible for the current high efficiencies of the more studied $MAPbI_3$ and $FAPbI_3$ devices.[27,34,35]

The fact that the planar devices function is integral to the understanding of this material. A functioning planar device means that because charges are extracted and a significant short-circuit current generated, carriers must be able to travel across the film before recombining. This implies that both electrons and holes must have a significant diffusion length in caesium lead triiodide. Moreover, it implies that the exciton binding energy is low enough that most excited carriers in the film are present as free carriers as opposed to excitons. The fact that the planar devices outperform the mesoporous devices indicates that transport in the perovskite is likely superior to transport in the mesoporous titania, and indicates that there is no need for the mesostructured approach for this all-inorganic perovskite.

9.5 Hysteresis in $CsPbI_3$ devices

As discussed in previous chapters, the issue of current-voltage hysteresis, with different JV characteristics exhibited at different scan speeds, is a critical issue in the hybrid organic-inorganic perovskite solar cells. Typically regular-structured planar devices display most hysteresis, with mesoporous titania-based devices and inverted devices mitigating the effects of hysteresis. The extent of hysteresis can be ascertained by measuring steady-state power output of the cell, which at maximum power point gives the real sustainable

efficiency of the device. Comparing this to the current-voltage sweeps allows us to quantify to what extent the PCE is artificially inflated in the JV scan due to the hysteretic effect. Accordingly, current-voltage characteristics for these fully inorganic perovskite solar cells were measured at different rates, and also the steady-state power output at V_{mpp} measured.

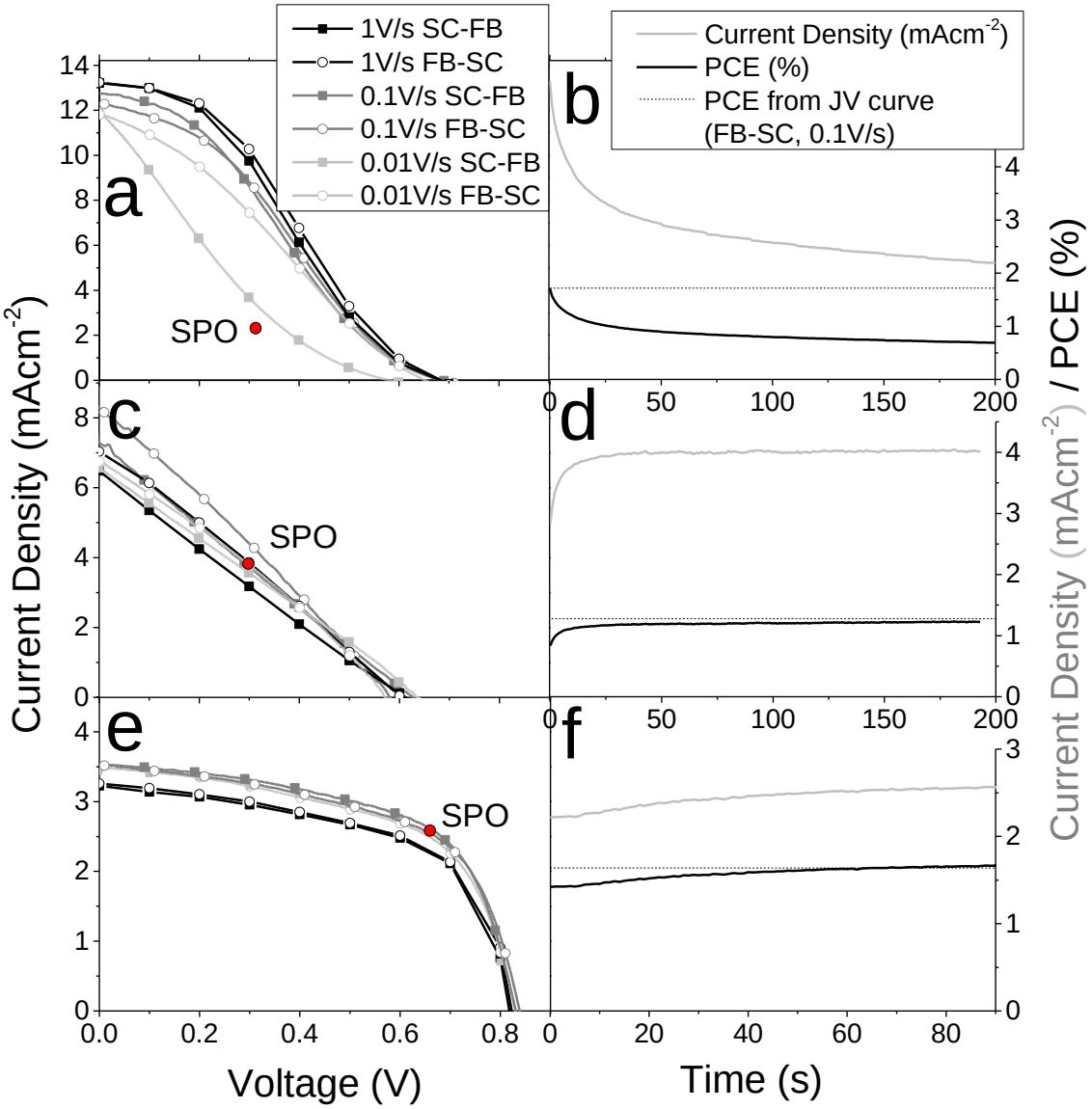

Figure 9.4: Hysteresis in inorganic perovskite solar cells. Current-voltage characteristics measured at different sweep rates for a) regular planar devices, c) mesoporous titania devices, and e) inverted planar devices. FB-SC = scanning from forward bias to short circuit, SC-FB vice versa. b), d) and f) show stabilisation of current density and hence PCE measured at the maximum power point determined from FB-SC scan at 0.1V/s, compared to the PCE extracted from that JV curve. The final stabilised power output (SPO) is marked on the JV plots as a red circle.

Current-voltage characteristics measured at different scan rates are shown on the left, and stabilised power measurements (holding at maximum power point) on the right hand side of Figure 9.4. It can be observed that the regular structure planar device (Figure 9.4a) shows large differences in its JV scans depending on scan rate. Faster scans appear to show in particular a superior fill factor, and more similar forward (SC-FB) and reverse (FB-SC) scans. At the slower scan speed, there is a very large difference in the forward and reverse scans. By measuring the stabilised power output (Figure 9.4b), it is shown that the stabilised value is significantly below that estimated from the JV scans; indeed, it is lower than any of the scans, no matter the rate or direction. Therefore, it can be concluded that the perovskite device in this architecture does display significant hysteresis, with the JV scans overestimating the PCE by a factor of more than 2. The mesoporous titania devices (Figure 9.4c and d) do also display some variation in hysteresis with scan rate, though not as notable as the planar devices. The stabilised power output rises to a value very similar to the estimated PCE from the JV scan, so it can be concluded that while there is some hysteresis in the current-voltage characteristics, it does not critically affect the steady-state response. In the case of the inverted devices, little hysteresis is observed in the JV curves. However, the scans at a very fast rate give a slightly lower short-circuit current density. The stabilised power output of these devices rises to almost exactly the same as the PCE estimated from the best JV curves, so there appears to be no artificial inflation of the PCE value in this case; hysteresis does not seem to affect these inverted devices detrimentally. It is noted that there was a similar degree of hysteresis observed in high- and low-temperature processed devices.

From these measurements several things can be concluded. Firstly, current-voltage hysteresis *is* present in $CsPbI_3$ devices. This effect is therefore not unique to the hybrid materials with a dipolar organic molecule. $CsPbI_3$ cannot be ferroelectric, either via dipole alignment or by classical lattice distortion, as it does not have a ferroelectric space group. Therefore the current-voltage hysteresis displayed here, and likely in other perovskite solar cells, is not a ferroelectric effect.

Secondly, it is observed that the planar regular device shows very significant hysteresis, and over-estimation of the PCE from the JV scans. On the other hand, the mesoporous titania based and inverted planar devices show little overestimation of the PCE, and much reduced hysteresis in the JV scans. This is in keeping with what has been observed previously for $MAPbI_3$ devices.[6,7] It is now generally thought that the hysteresis arises due to compensation of an applied bias with an internal built-in field, as shown diagrammatically in Chapter 2, Section 2.5.3.[9,36,37] This built-in field acts to reduce

recombination after the device has been held at forward bias (i.e. scanning FB-SC); it can allow even devices with poorly selective contacts to function well temporarily by biasing.[9] This allows carriers to be extracted before recombination, making the solar cell 'better' – this is the reverse scan with the higher efficiency. Devices with contacts that already rapidly extract charge before it recombines will not be so affected by the temporary built-in field, as it is not necessary for efficient extraction of charge. This is likely to be the case for the mesoporous and inverted devices. The large surface area of mesoporous titania allows rapid extraction of electrons, as does the PCBM in the inverted devices. However, the compact titania in the planar regular device is not as effective at extracting charge – there is even some evidence for an energy barrier that must be overcome by the temporary built-in field.[38] It requires the temporary enhancement gained by the device previously being at open-circuit conditions to function well (FB-SC in Figure 9.4a). Upon going back to short circuit, or holding at the maximum power point, the device behaves poorly again (SC-FB in Figure 9.4a). The hysteretic effect can be seen as changing the balance between recombination and charge extraction. To perform well, a device must extract charge efficiently before it recombines. This can either be achieved by having slow recombination or efficient contact materials. Pre-biasing temporarily reduces recombination by setting up an additional built-in field, physically separating photoexcited electrons and holes, so for a device with poor contacts, for short time after this, the device can function well but when the effect dissipates recombination critically impacts the device once more.

The dependence of hysteresis upon scan rate affords knowledge about the timescales involved in the hysteresis-inducing process. If the JV scan occurs on a timescale faster than the hysteretic effect, little difference will be observed in forward and reverse scans as the effect will not have had time to make a difference – the device is in the same 'beneficial state' throughout. If it occurs on a timescale slower than the hysteretic effect, little difference will also be observed, as the process has time to occur already and the device will be in effectively steady state at all points during both scans. It is when the JV scan happens on a timescale similar to the hysteretic effect that a large difference is observed in forward and reverse scans – in the forward scan the device is in the poor or 'un-assisted state' and in the reverse scan it is in the temporary 'beneficial state'. Figure 9.4a) shows that the hysteresis is most severe at the slowest rate of 0.01V/s. Faster than this, the JV curves show significantly higher PCE than the SPO, in accordance with being temporarily enhanced. Scanning slower was practically infeasible; based on the SPO measurement it can be assumed that it would take 10s of seconds at each point to reach steady state. From

the magnitude of hysteresis in the 0.01V/s scan, it can be concluded that in this device the hysteresis occurs on a timescale of seconds.

The main alternative to ferroelectricity proposed as a cause for the hysteretic effect is ion motion within the perovskite film. Charged defect ions could move to compensate an applied field, resulting in the built-in field via charge accumulation at the interfaces or doping of the film at either side. It has been shown that ions can move under bias in perovskite films, and there is mounting evidence that this is also the cause of the current-voltage hysteresis.[9,10,37] The results presented here agree well with this theory; the timescale of hysteresis observed is as expected for ionic motion, and the ferroelectric effect can be comprehensively ruled out.

Although the devices presented in this chapter are not the most efficient, with further optimisation it is likely that they could perform as well as the hybrid organic-inorganic materials. The fact that working $CsPbI_3$ devices have been fabricated suggests that there is no fundamental property of the hybrid organic-inorganic materials that allows them to work as efficient solar cells. It should be noted however that the maximum open-circuit voltage generated by these devices under full sun illumination is 0.85V and the material has an optical band gap of 1.73eV. Therefore the loss in potential or voltage-deficit, i.e. the difference in energy between the band gap and the open-circuit voltage, is relatively large at 0.88 eV. It remains to be seen if similarly small voltage deficits can be achieved as with the organic-inorganic perovskites (<0.4eV), at which point it could be claimed that the inorganic perovskites are just as effective as PV materials. To motivate such effort, these inorganic materials do not suffer from some limitations of the hybrid materials; notably the thermal stability of $CsPbI_3$ is much greater than that of the organic containing materials, where the organic component becomes volatile and easily removed at elevated temperatures. Whilst $MAPbI_3$ is known to degrade even when held at 85°C for long periods of time,[39] rendering it ultimately unsuitable for commercialisation, the black phase of $CsPbI_3$ is stable up to over 300°C – this is clearly a significantly more thermally stable material. If the ambient instability problems of these inorganic materials could be overcome, they could be a significantly more generally stable material allowing long-term efficient operation. Moreover, incorporating $CsPbI_3$ into high efficiency $MAPbI_3$ devices could lead to the optimum combination of high efficiency and good thermal stability. Significant further research into inorganic perovskite solar cells is expected to take place, likely to be accompanied by enhanced efficiencies and stability.

9.6 Outlook and conclusion

To summarise the work described in this chapter, working inorganic $CsPbI_3$ solar cells have been fabricated for the first time. By carrying out all processing in a totally inert atmosphere, and developing a low temperature phase transition route, it has been possible to stabilise $CsPbI_3$ films in the black phase at room temperature, and fabricate solar cells in a variety of architectures. Despite the fact that this material cannot be in any way ferroelectric, significant current-voltage hysteresis is observed in such devices, ruling out ferroelectricity as the cause of current-voltage hysteresis. Importantly, the fully inorganic materials such as this are much more thermally stable than the hybrid materials, which degrade under sustained heating at low temperatures. These therefore could represent the future of perovksite solar cells – it may be necessary to employ inorganic materials to pass necessary certification for commercialisation. The results presented in this chapter pave the way for further optimisation and stabilisation of the inorganic perovskite materials, with potential for more efficient and more stable devices than the hybrid materials currently displaying the highest efficiencies.

9.7 References

1 S. D. Stranks, G. E. Eperon, G. Grancini, C. Menelaou, M. J. P. Alcocer, T. Leijtens, L. M. Herz, A. Petrozza and H. J. Snaith, *Science*, 2013, **342**, 341–344.

2 G. E. Eperon, S. D. Stranks, C. Menelaou, M. B. Johnston, L. M. Herz and H. J. Snaith, *Energy Environ. Sci.*, 2014, **7**, 982–988.

3 V. D'Innocenzo, G. Grancini, M. J. P. Alcocer, A. R. S. Kandada, S. D. Stranks, M. M. Lee, G. Lanzani, H. J. Snaith and A. Petrozza, *Nat. Commun.*, 2014, **5**, 3586.

4 C. Wehrenfennig, G. E. Eperon, M. B. Johnston, H. J. Snaith and L. M. Herz, *Adv. Mater.*, 2014, **26**, 1584–1589.

5 T. Leijtens, S. D. Stranks, G. E. Eperon, R. Lindblad, E. M. J. Johansson, J. M. Ball, M. M. Lee, H. J. Snaith, I. J. McPherson, H. Rensmo, J. M. Ball, M. M. Lee and H. J. Snaith, *ACS Nano*, 2014, **8**, 7155–7174.

6 E. L. Unger, E. T. Hoke, C. D. Bailie, W. H. Nguyen, A. R. Bowring, T. Heumuller, M. G. Christoforo and M. D. McGehee, *Energy Environ. Sci.*, 2014, **7**, 3690–3698.

7 H. J. Snaith, A. Abate, J. M. Ball, G. E. Eperon, T. Leijtens, N. K. Noel, S. D. Stranks, J. T. Wang, K. Wojciechowski and W. Zhang, *J. Phys. Chem. Lett.*, 2014, **5**, 1511–1515.

8 J. a. Christians, J. S. Manser and P. V. Kamat, *J. Phys. Chem. Lett.*, 2015, **6**, 852–857.

9 Y. Zhang, M. Liu, G. E. Eperon, T. C. Leijtens, D. McMeekin, M. Saliba, W. Zhang, M. de Bastiani, A. Petrozza, L. M. Herz, M. B. Johnston, H. Lin and H. J. Snaith, *Mater. Horiz.*, 2015, **2**, 315–322.

10 Z. Xiao, Y. Yuan, Y. Shao, Q. Wang, Q. Dong, C. Bi, P. Sharma, A. Gruverman and J. Huang, *Nat. Mater.*, 2015, **14**, 193–198.

11 H. min Zhang, C. Liang, Y. Zhao, M. Sun, H. Liu, J. Liang, D. Li, F. Zhang and Z. He, *Phys. Chem. Chem. Phys.*, 2015, **17**, 9613–9618.

12 R. S. Sanchez, V. Gonzalez-Pedro, J. Lee, N. Park, Y. S. Kang, I. Mora-Sero and J. Bisquert, *J. Phys. Chem. Lett.*, 2014, **5**, 2357–2363.

13 J. M. Frost, K. T. Butler and A. Walsh, *APL Mater.*, 2014, **2**, 81506.

14 Y. Kutes, L. Ye, Y. Zhou, S. Pang, B. D. Huey and N. P. Padture, *J. Phys. Chem. Lett.*, 2014, **5**, 3335–3339.

15 S. Liu, F. Zheng, N. Z. Koocher, H. Takenaka, F. Wang and A. M. Rappe, *J. Phys. Chem. Lett.*, 2015, **6**, 693–699.

16 H.-W. Chen, N. Sakai, M. Ikegami and T. Miyasaka, *J. Phys. Chem. Lett.*, 2014, **6**, 164–169.

17 Z. Chen, J. J. Wang, Y. Ren, C. Yu and K. Shum, *Appl. Phys. Lett.*, 2012, **101**, 093901.

18 M. H. Kumar, S. Dharani, W. L. Leong, P. P. Boix, R. R. Prabhakar, T. Baikie, C. Shi, H. Ding, R. Ramesh, M. Asta, M. Graetzel, S. G. Mhaisalkar and N. Mathews, *Adv. Mater.*, 2014, **26**, 7122–7127.

19 N. K. Noel, S. D. Stranks, A. Abate, C. Wehrenfennig, S. Guarnera, A. Haghighirad, A. Sadhanala, G. E. Eperon, S. K. Pathak, M. B. Johnston, A. Petrozza, L. Herz and H. Snaith, *Energy Environ. Sci.*, 2014, **7**, 3061–3068.

20 C. C. Stoumpos, C. D. Malliakas and M. G. Kanatzidis, *Inorg. Chem.*, 2013, **52**, 9019–9038.

21 C. K. Møller, *Mat. Fys. Medd. Dan. Vid. Selsk*, 1959, **32**, no. 2.

22 H. Choi, J. Jeong, H.-B. Kim, S. Kim, B. Walker, G.-H. Kim and J. Y. Kim, *Nano Energy*, 2014, **7**, 80–85.

23 L. Protesescu, S. Yakunin, M. I. Bodnarchuk, F. Krieg, R. Caputo, C. H. Hendon, R. X. Yang, A. Walsh and M. V. Kovalenko, *Nano Lett.*, 2015, **15**, 3692–3696.

24 O. N. Yunakova, V. K. Miloslavskii and E. N. Kovalenko, *Opt. Spectrosc.*, 2012, **112**, 91–96.

25 C. K. Møller, *Nature*, 1958, **182**, 1436.

26 G. E. Eperon, S. D. Stranks, C. Menelaou, M. B. Johnston, L. M. Herz and H. J. Snaith, *Energy Environ. Sci.*, 2014, **7**, 982.

27 J. H. Heo, H. J. Han, D. Kim, T. K. Ahn and S. H. Im, *Energy Environ. Sci.*, 2015, **8**, 1602–1608.

28 H. W. Jang, S. H. Baek, D. Ortiz, C. M. Folkman, R. R. Das, Y. H. Chu, P. Shafer, J. X. Zhang, S. Choudhury, V. Vaithyanathan, Y. B. Chen, D. a. Felker, M. D. Biegalski, M. S. Rzchowski, X. Q. Pan, D. G. Schlom, L. Q. Chen, R. Ramesh and C. B. Eom, *Phys. Rev. Lett.*, 2008, **101**, 3–6.

29 A. J. Hatt, N. a. Spaldin and C. Ederer, *Phys. Rev. B - Condens. Matter Mater. Phys.*, 2010, **81**, 1–5.

30 Y. Tokura, *Science*, 2000, **288**, 462–468.

31 F. Tsui, M. C. Smoak, T. K. Nath and C. B. Eom, *Appl. Phys. Lett.*, 2000, **76**, 2421–2423.

32 Y. L. Li and L. Q. Chen, *Appl. Phys. Lett.*, 2006, **88**, 3–5.

33 W. H. Nguyen, C. D. Bailie, E. L. Unger and M. D. McGehee, *J. Am. Chem. Soc.*, 2014, **136**, 10996–11001.

34 N. J. Jeon, J. H. Noh, W. S. Yang, Y. C. Kim, S. Ryu, J. Seo and S. Il Seok, *Nature*, 2015, **517**, 476–480.

35 W. S. Yang, J. H. Noh, N. J. Jeon, Y. C. Kim, S. Ryu, J. Seo and S. I. Seok, *Science*, 2015, **348**, 1234–1237.

36 W. Tress, N. Marinova, T. Moehl, S. M. Zakeeruddin, M. K. Nazeeruddin and M. Grätzel, *Energy Environ. Sci.*, 2015, **8**, 995–1004.

37 Y. Zhao, C. Liang, H. min Zhang, D. Li, D. Tian, G. Li, X. Jing, W. Zhang, W. Xiao, Q. Liu, F. Zhang and Z. He, *Energy Environ. Sci.*, 2015, **8**, 1256–1260.

38 K. Wojciechowski, S. D. Stranks, A. Abate, G. Sadoughi, A. Sadhanala, N. Kopidakis, G. Rumbles, C. Li, R. H. Friend, A. K.-Y. Jen and H. J. Snaith, *ACS Nano*, 2014, **8**, 12701–12709.

39 B. Conings, J. Drijkoningen, N. Gauquelin, A. Babayigit, J. D'Haen, L. D'Olieslaeger, A. Ethirajan, J. Verbeeck, J. Manca, E. Mosconi, F. De Angelis and H. Boyen, *Adv. Energy Mater.*, 2015, **Advance**, 1–8.

10. THE IMPORTANCE OF MOISTURE IN HYBRID LEAD HALIDE PEROVSKITE THIN FILM FABRICATION

The work presented in this chapter has been published as:

- G. E. Eperon, S. N. Habisreutinger, T. Leijtens, B. J. Bruijnaers, J. J. van Franeker, D. W. deQuilettes, S. K. Pathak, R. J. Sutton, G. Grancini, D. Ginger, R. A. J. Janssen, A. Petrozza and H. J. Snaith, "The importance of moisture in hybrid lead halide perovskite thin film fabrication", *ACS nano*, 2015.

10.1 Context and summary

Moisture, in the form of ambient humidity, has a significant impact on methylammonium lead halide perovskite films, as mentioned in previous chapters. In particular, due to the hygroscopic nature of the methylammonium component, moisture has been observed to play a significant role during film formation. This issue has so far not been well understood, and neither has the impact of moisture on the physical properties of resultant films. It is of crucial importance, however, when considering scaling up production of perovskite films: what level of atmospheric control will be necessary? In this chapter, a comprehensive and well-controlled study is carried out on the effect of moisture exposure on methylammonium lead halide perovskite film formation and properties. It is found that films formed in higher humidity atmospheres have a less continuous morphology but significantly improved photoluminescence, and that film formation is faster. In photovoltaic devices, it is found that exposure to moisture, either in the precursor solution or in the atmosphere during formation, results in significantly improved open-circuit voltages and hence overall device performance. It is then found that by post-treating dry films with moisture exposure, photovoltaic performance and photoluminescence can be enhanced in a similar way. The enhanced photoluminescence and open-circuit voltage imply that the material quality is improved in films that have been exposed to moisture. It is determined that this improvement stems from a reduction in trap density in the films, which is postulated to be due to the partial solvation of the methylammonium component and 'self-healing' of the perovskite lattice. The work carried out in this chapter highlights the importance of controlled moisture exposure when fabricating high-performance perovskite devices, and provides guidelines for the optimum environment for fabrication. Moreover, it is noted that an unintentional water exposure is likely responsible for the high performance of solar cells produced in some laboratories, whereas counter-intuitively careful synthesis and fabrication in a dry environment will lead to lower-performing devices.

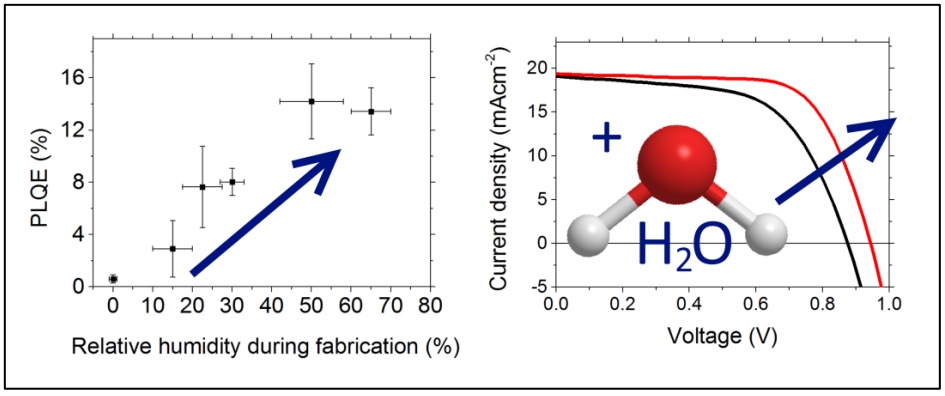

10.2 Introduction

Most work on perovksite solar cells has focused on optimising the solar cell constituents, namely the absorber material and charge-collection layers. The impact of environmental factors impacting the device fabrication, in contrast, has largely been neglected. Due to the general moisture-sensitivity of the perovskite material, in particular the effect of local humidity during the fabrication of perovskite films is an important factor, which merits further scrutiny. This variable is most often not sufficiently controlled, although recent reports indicate it may be critical in the formation of high-quality absorber films required for the most efficient devices.[1,2] Indeed, there is a wide variation of atmospheric conditions used between different research laboratories which are often not reported in the literature. Whilst it appears that many groups process their devices inside dry nitrogen-filled gloveboxes, many others fabricate devices in ambient conditions without controlling the humidity, which can vary strongly depending on the local weather conditions at the time. Recent reports have shown that this mostly uncontrolled variable could be crucial to attaining the highest efficiencies, so it is likely that a controlled humidity environment is a requirement for optimising device fabrication.[2–5]

Thus far there is only a fragmented understanding of the role of humidity with regards to device fabrication and performance due to a lack of thorough and comprehensive studies of this variable. In Chapter 4, it was noticed that the morphology of a perovskite film significantly depended on whether it was fabricated in air or a nitrogen atmosphere. In this chapter the fragmented understanding is remedied, by investigating in great detail the impact of moisture on perovskite film properties and photovoltaic performance. It is concluded that exposure to water at some point in the fabrication of the perovskite film is critical to attain the highest quality perovskite films, and that device performance improves accordingly.

10.3 Dry versus hydrated methylammonium iodide

When considering the role of moisture, it is important to distinguish between formation and degradation of the perovskite film. It appears that the presence of moisture influences the formation of the perovskite film during the crystallization phase but also has a deleterious effect on a fully crystallized film, leading to its degradation. It has been reported that prolonged exposure to moist air will degrade a methylammonium lead iodide perovskite film, and it was shown in Chapter 7 that a formamidinium lead iodide film discolours in very humid air too.[6–9] The mechanism of degradation is thought to involve the formation of hydrated intermediate structures ($MAPbI_3 \cdot H_2O$ and

$MA_4PbI_6{\cdot}2H_2O$), followed by total irreversible degradation to lead iodide. This is clearly of importance when considering the commercial lifetime of a perovskite solar cell exposed to atmospheric conditions. However, during fabrication the impact of moisture has also been reported to have a critical impact on the crystallization of perovskites. Ko *et al*, Raga *et al* and Pathak *et al* have reported that air-annealed perovskite films display higher efficiencies as compared to those annealed in nitrogen, although in these reports the humidity is not controlled, and it can therefore not unambiguously be determined whether oxygen or moisture are responsible for the improved performances.[3–5] The reason for these improvements is concluded to mainly stem from an increase in crystal size. You *et al* have reported that films annealed in controlled levels of humidity (though spin-coated in dry nitrogen) show a maximum performance at 20-40% relative humidity (RH), which in turn is linked to an improved morphology.[2] Notably, Bass et al report that in order to crystallize perovskite powders fully, exposure to moisture is crucial.[10] In this chapter, the impact of moisture during the preparation of perovskite films and devices is further explored, and it is demonstrated that it plays an important role for device performances. To carry out the experiments detailed herein, a humidity-controlled chamber was built, in which humidity can be regulated with a flow of dry nitrogen that passes through a water bubbler. A schematic of the humidity-controlled chamber is shown in Section 10.9.

An important point of discrepancy between reports of perovskite solar cells is in the preparation of methylammonium iodide (MAI). Throughout the published literature, different degrees of purity of MAI have been used. Many groups recrystallize and wash their MAI crystals to purify them, or use the as-formed crystals, but do not necessarily remove absorbed moisture from them by stringent vacuum drying or sublimation. Given that MAI is known to be hygroscopic, as with most alkylammonium salts,[11] MAI that is not treated to remove water will likely contain significant (but uncontrolled) amounts of absorbed water. In order to comprehensively study the impact of moisture on perovskite film formation and properties, here a precursor solution prepared from MAI that has been dried overnight in a vacuum oven and subsequently stored in a moisture-free glovebox was used, so it should be free of most absorbed moisture. It was found that MAI could be reversibly hydrated by exposure to air for a day or more, then vacuum dried at 40-50^{o}C to dehydrate. Approximately 7% by moles of MAI became hydrated quickly, corresponding to a ~1% weight increase. It is noted that in this report the chloride-assisted non-stoichiometric mixed halide precursor is used to form $MAPbI_3$ perovskite films, namely a precursor solution of 3:1 MAI to lead chloride by moles, normally termed $MAPbI_{3-x}Cl_x$. During annealing, it is expected that the excess organic and chloride will be removed.[12–15] This fabrication route is likely to be especially sensitive to moisture during the fabrication,

due to the large excess of the hygroscopic MA, and once formed it should behave similarly to $MAPbI_3$ formed via the myriad of other processing techniques.[16]

Initially, the properties of perovskite films prepared with dried and hydrated ('standard') MAI powders were compared. The standard MAI is the material normally used in our lab; it is purified after synthesis but not vacuum-dried, and stored in ambient air where it will readily absorb moisture. Films were fabricated from the two precursors in identical conditions, annealing the perovskite films at 90°C for 2.5 hours in a controlled humidity environment of 20% RH. In Figure 10.1a, it is shown that the morphology of perovskite films fabricated from the two precursors is similar. The surface coverages are quantified to be 70% and 72% for the standard and dried precursors respectively. Despite this, the photophysical properties of the films appear to be very different. In Figure 10.1b it is shown that the photoluminescence and photoluminescence quantum efficiency are significantly reduced for the dried precursor, and in Figure 10.1c, it is shown that the lifetime of excited species measured with time-resolved photoluminescence is significantly shorter.

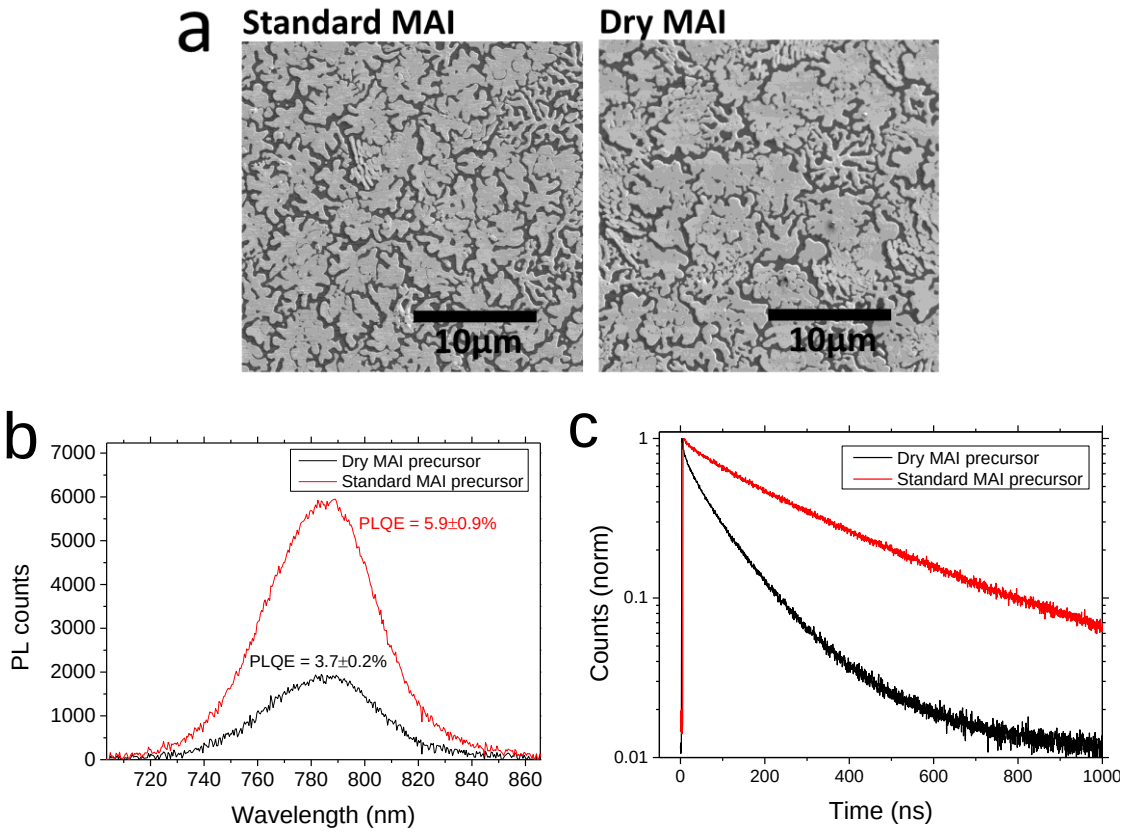

Figure 10.1: a) Scanning electron micrograph of the morphology of MAPbI3 films prepared from chloride containing precursors, using standard and dried MAI powders, in 20±5% RH conditions. b) Photoluminescence and photoluminescence

quantum efficiency, measured using an integrating sphere, for the standard and dried precursor perovskite films. PLQE was measured for at least 3 points on the sample and errors represent standard deviation. c) Time-resolved photoluminescence measured at 785nm, with excitation at 510nm, 3μJcm-2 per pulse, at 1MHz.

The striking difference in physical properties, despite the similar macroscopic morphologies, between the two precursors indicates that the beneficial effect of the absorbed moisture in the standard MAI is not based on a change in macroscopic morphology of the perovskite film. Previously, all differences observed in atmospheres with different relative humidities have been attributed to morphological considerations.

10.4 Annealing in different humidities

In order to pinpoint exactly how moisture affects the photophysical properties of a perovskite film, subsequently only the dry precursor solution was used for all further experiments. It is thus possible to explore the effect of exposing perovskite films, which have not already been exposed to water, to different levels of humidity at different stages of their formation.

The impact that exposure to moisture has on the morphology and physical properties of the perovskite was investigated by annealing films in a range of controlled humidity conditions. Typical literature reports indicate that annealing of this perovskite precursor takes ~2-2.5 hours to form the best perovskite films.[1,2,17,18]

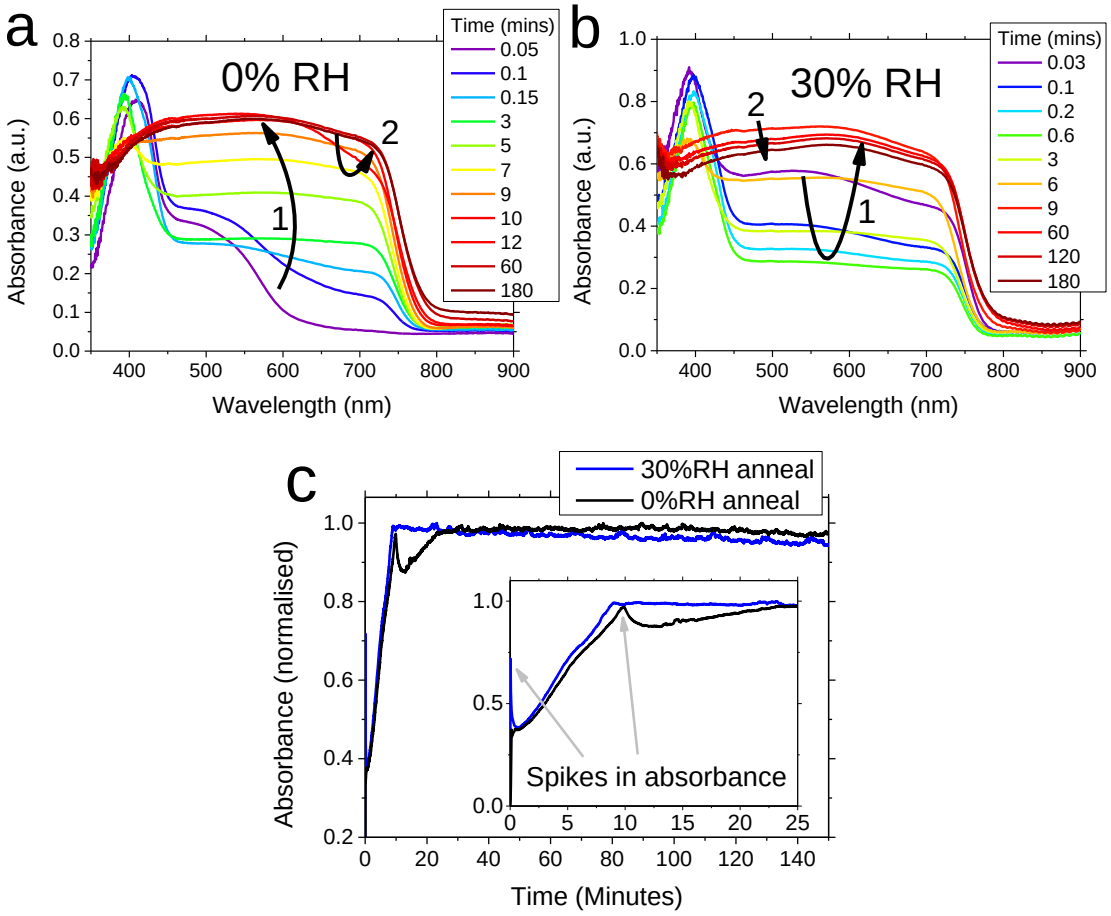

Figure 10.2: Impact of humidity on rate of perovskite film formation. In-situ absorbance of a film at different points during the annealing in a) 0% RH atmosphere and in b) 30% RH atmosphere. c) Trace of magnitude of absorbance at 700nm over time for both films. Inset: higher detail in the early time period of annealing. This data was collected by J. J. van Franeker and B. Bruijnaers of the Eindhoven Technical University, the Netherlands.

It was noticed that films changed colour more quickly in a moist atmosphere, in which they form the final dark film faster. This phase corresponds to the tetragonal $MAPbI_3$ perovskite structure. This was quantified by measuring the in-situ absorbance of a spin-coated perovskite film over time during the annealing process, while annealing in either dry nitrogen or nitrogen with 30% RH. The films were both spin-coated in a dry nitrogen-filled glovebox to exclude effects during the spin-coating process. It is noted that due to the measurement setup, the absorption measured represents two passes of light through the sample.

Firstly, considering the film annealed in 0%RH (Figure 10.2a), an initial peak is seen at approximately 410nm, and an absorption feature with onset of ~600nm. It is not entirely

clear which materials are present here but it is proposed that lead iodide is responsible for the ~410nm peak, having been previously observed in the initial stage via Raman studies,[14] and possibly a layered-type perovskite, forming due to the large MA excess, could provide the absorbance with onset ~600nm.This is likely to be the "precursor phase" that has been previously assigned through in-situ x-ray scattering experiments.[19] Upon annealing, the absorbance increases steadily and the characteristic tetragonal $MAPbI_3$ perovskite absorbance spectrum, with onset at ~780nm, is formed (feature 1 marked on Figure 10.2a). After ~10 minutes, the lead iodide peak has disappeared and the perovskite absorbance is maximised. However, a drop in absorbance at around 700nm is then observed, which subsequently increases again until about 30 minutes, after which time the absorbance remains unchanged up to 180 minutes of annealing (feature 2 marked on Figure 10.2a). In Figure 10.2c the absorbance at 700nm is plotted as a function of time. The gradual increase of absorbance in the initial phase ($t < 10$ min) and the subsequent decrease and re-increase ($10 < t < 30$ min) are clearly seen.

Considering the film annealed in 30%RH (Figure 10.2b), several differences are noticed. Firstly, as soon as the film is exposed to the moist atmosphere, the characteristic perovskite spectrum appears very rapidly (see inset of Figure 10.2c). Upon annealing, this decreases quickly before rising again (feature 1 marked on Figure 10.2b). The perovskite absorbance is fully formed by ~9 minutes, much faster than for the 0%RH annealed film, which takes ~30 minutes. There is no spike and drop as seen in the 0%RH annealed sample. Upon prolonged annealing, a drop in magnitude of absorbance in the 30%RH atmosphere is observed, likely indicating a degradation of the perovskite film (feature 2 marked on Figure 10.2a). This may well be correlated with the formation of the hydrated intermediate structure observed by Yang et al.[8]

It is noted that the absorbance spectrum being maximised does not correspond to the optimum curing conditions for the crystalline perovskite film. Upon being taken from the hotplate and transferred into ambient air, films that are annealed at 90°C for less time than ~ 2 hours degrade rapidly, forming a transparent material, indicating that there is likely to be a large excess of the hygroscopic MA component remaining; this observed degradation product is in keeping with the hydrated phase observed by Christians et al and Yang et al, and can be reversed on heating.[6,8] Additionally, it is noted that while the quick initial appearance of perovskite absorbance in the humid atmosphere, and subsequent decrease, and the possibly related 'spike' in perovskite absorbance in the 0% RH annealed film, are likely important, the significance of this feature is not fully understand, and further research on this is necessary. There is significant evidence that

intermediate or "precursor" phases are present in many different routes to process high quality perovskite films. [20–23]

The key conclusion of this experiment is that the final tetragonal $MAPbI_3$ perovskite phase forms faster in a more humid atmosphere. Firstly, the chemistry of the situation is considered. Methylamine and methylammonium halides are soluble in water - hygroscopic, in fact. On the other hand, lead halides, the other component present in the precursor, are insoluble or at best sparingly soluble in water. Therefore water acts as a partial solvent for the perovskite precursor – it can solubilise the organic component but not the lead halide. During formation of the perovskite film, in order to form a stoichiometric perovskite lead iodide and a stoichiometric amount of methylammonium iodide must be retained, and a large excess of methylammonium chloride lost, which is likely driven off as methylamine and hydrochloric acid.[24,25] Hence the reaction would be expected to be accelerated in the presence of moisture, due to the fact that methylamine and hydrochloric acid will form more readily via acid-base interaction with moisture, after which they will immediately vaporise, driving the reaction forward. This will allow loss of the methylammonium chloride with lower activation energy, and furthermore the ambient moisture will provide greater bulk mobility to the methylammonium component retained in the film, reducing the time needed for it to move to form the stoichiometric perovskite crystal. This is in keeping with the observations of Bass et al, who observed a rapid transformation of precursor powders to perovskite powder upon exposure to moisture – the water is solvating the methylammonium and allowing physical material flow to form the perovskite.[10]

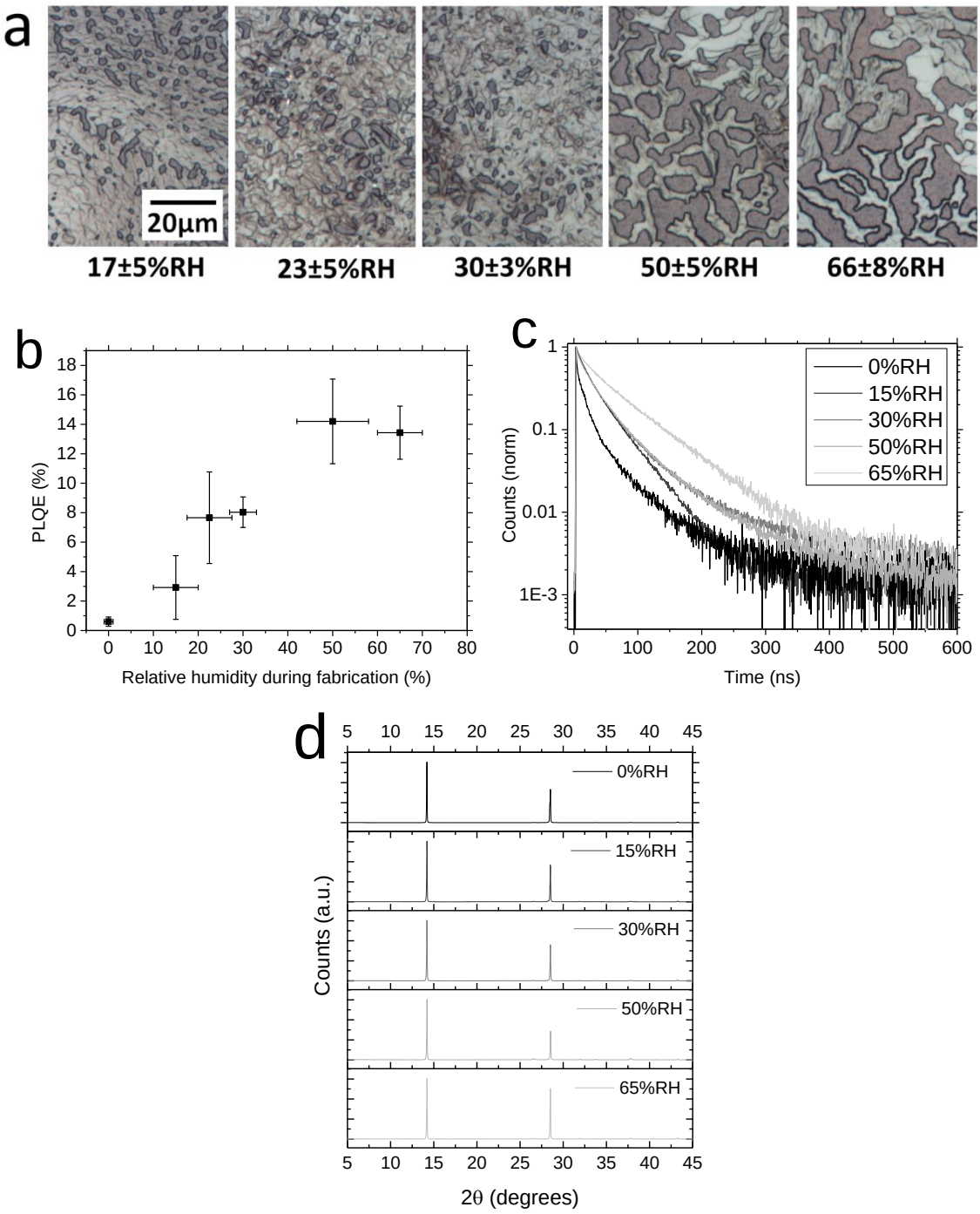

Figure 10.3: a) Optical microscope images of perovksite films prepared in different humidity atmospheres on compact TiO2-coated FTO substrates. The scale is the same in all images. Perovskite material is light in colour, bare substrate is darker. b) Photoluminescence quantum efficiency for perovskite films prepared in different humidity atmospheres. Data points are from the average of at least 3 measurements each, with error bars indicating standard deviation. c) Time-resolved photoluminescence measured at 785nm, with excitation at 510nm, 3µJcm-2 per pulse, at 1MHz, for films prepared in different humidity conditions. d) X-ray

diffraction data for perovskite films prepared in different humidity atmospheres. Films were annealed for 2.5 hours at 90°C.

The impact of a range of humidity levels on the final morphology of the perovskite films was then investigated, spin-coating and annealing using the dry precursor in different levels of RH. To investigate the morphology, films were fabricated on compact TiO_2-coated FTO glass substrates, as used in planar solar cell devices. Different to the inclusion of moisture in the MAI precursor, a significant change in morphology is observed on varying the atmospheric humidity, as shown in the optical microscope images in Figure 10.3a. It is observed that the best substrate coverage is attained at 30%RH and below, and it worsens with increasing humidity above this level.

Regarding the worsened coverage at higher humidities, there are a number of factors which could be influential. It can be envisaged that during the spin coating process, as the solvent (DMF) evaporates, the salts or complexes within the solution will start to crash out or precipitate onto the substrate. If the thin wet film is absorbing water as it is losing DMF, then the PbI_2 (or $PbCl_2$) will become increasingly insolubilized and likely to crash out at a faster rate than the MAI. This is likely to induce increased morphological inhomogeneity in the as cast film. It is known from the work in Chapter 4 that dewetting of the perovskite film into islands occurs due to the growth of large pinholes already present in the as cast films prior to crystallisation.[17,26] Hence, it can be inferred that the films cast in humid environments are likely to already have larger pinholes present directly after crystallization. If the inhomogeneity of the as-cast film is so extreme that there are regions of neat MACl (or MAI), then these regions could induce de-wetting of the perovskite film from the surrounding areas during crystallization. In addition, the rate of growth and extent of growth of pinholes will be dependent upon how kinetically mobile the components within the perovskite film are during crystallisation.[27] If hydration of the material increases the mobility of the ions within the crystalizing film, then this could enable more rapid growth of pinholes. A final consideration is the forces driving de-wetting; de-wetting occurs due to it being energetically favourable for the perovskite film to reduce its contact area with the substrate, at the expense of increasing its contact area with the environment within which casting is taking place. Having a humid environment is likely to alter both the surface energy of the compact TiO_2 substrate (it is noted that the same trend is observed on glass) and the perovskite/atmosphere interaction energy.

Beyond looking at the morphological influence of humidity, the photophysical properties were also measured, with films formed on glass immediately encapsulated with polymethylmethacrylate (PMMA) to inhibit contact between ambient moisture and the

films. Most striking is the effect of increasing humidity on photoluminescence quantum yield (Figure 10.3b). It is observed that films fabricated in higher humidity show increasingly higher PLQE. Films fabricated in a nitrogen-filled glovebox, never exposed to air or humidity, show almost no PLQE, which increases to over 14% for those fabricated in higher humidities. Furthermore, increasingly longer-lived photoluminescence decays were observed, meaning that the recombination lifetime of photogenerated charges increases upon an increase in humidity during fabrication (Figure 10.3c). Additionally, it is noted that the shape of the decay curves appears to change, which could either indicate a change in the dominating recombination process occurring in films fabricated in the different conditions, or change in the distribution of defects throughout the film.[28,29] It is also noted that morphology, in particular crystal size, does play a role in determining photoluminescence decay rates for these films, so this is likely to be relevant in addition to the atmosphere-induced changes in the absolute quality of the perovskite material.[30] Previously it has been shown that larger crystallites display slower recombination rates, however here it is not possible to accurately extract crystal size. X-ray diffraction spectra, shown in Figure 10.3d, for these films show that the highly oriented $MAPbI_3$ phase typical of the mixed halide precursor is formed for all of the humidities, with no significant impurities present. The enhanced photophysical properties can thus not be ascribed to the measurable formation of lead iodide, previously reported to cause a 'self-passivation' of perovskite crystallites when formed by over-annealing.[31] Furthermore, no formation of detectable crystalline hydrated intermediates is observed at these conditions.[9]

The strong increase in PLQE and radiative lifetime suggests that the material is suffering from fewer non-radiative losses when formed in higher humidity – implying that the material may be of higher quality i.e. having fewer defects. Superior performance may therefore be expected from a solar cell made from such a material with higher PLQE.

10.5 Device performance after humidity exposure

The most common device architecture employed in perovskite solar cells relies on a hole-transporting layer of Spiro-OMeTAD, doped with Li-TFSI, coating the perovskite. The doping is achieved by letting Li-TFSI oxidise Spiro-OMeTAD by being in contact with air for several hours, usually overnight.[32] However, it has previously been shown that Spiro-OMeTAD is permeable to water, and does not constitute a good moisture barrier.[7] Therefore, coating solar cells fabricated in carefully controlled humidity levels with Spiro-OMeTAD and subsequently leaving them overnight in air will likely result in ambient moisture permeating through the Spiro-OMeTAD layer and thus coming into contact with

the perovskite film, leading to uncontrolled effects of moisture on the perovskite absorber and thus invalidating the usefulness of the experiment.

As a means to prevent this uncontrolled exposure of the perovskite to moisture, a moisture-resistant hole-transporting layer was employed, comprising a composite of single-walled carbon nanotubes and PMMA or polycarbonate (PC). As previously demonstrated, the polymer matrix can block moisture ingress and subsequent degradation of $MAPbI_3$ perovskites. This makes it the ideal hole-transporting layer to prevent any ambient moisture ingress that may occur after the perovskite layer fabrication. From here, this layer, henceforth referred to as SWCNT-HTL, is employed, deposited immediately after perovskite annealing, in the relevant humidity atmosphere. In this way, the utmost care is taken to *never* unintentionally expose perovskite films to moisture at any stage of the fabrication process.

To determine whether the previous observation of enhanced PLQE when preparing perovskite films in a more humid environment, or with a moist (i.e. non-dried) precursor corresponds to improved device performance, perovskite solar cells were fabricated in carefully controlled conditions, immediately sealing with the SWCNT-HTL. Cells were fabricated with the dry precursor in a dry atmosphere, the dry precursor in a moist atmosphere (30±3% RH) and with the standard (moist) precursor in a dry atmosphere. Solar cells were also fabricated with the dry precursor in a dry atmosphere, with Spiro-OMeTAD as the hole-transporter, and left in ambient air overnight to test the hypothesis that moisture ingress through the Spiro-OMeTAD may have an effect. It is noted that cells fabricated with the SWCNT-HTL and a standard (not dried) perovskite precursor have shown open-circuit voltages and performances very similar to those fabricated with Spiro-OMeTAD, so it is plausible to compare devices made with the two hole transporters.[7,33] It is also noted that all solar cells discussed here are alumina-based meso-superstructured devices, with the device structure shown in Figure 10.4a. The alumina scaffold negates the detrimental effect of the worsened morphology at higher humidities – it acts to hold the perovskite precursor in place and so there is less unwanted contribution from pinholes reducing voltage, as has been discussed previously in Chapter 3.[17]

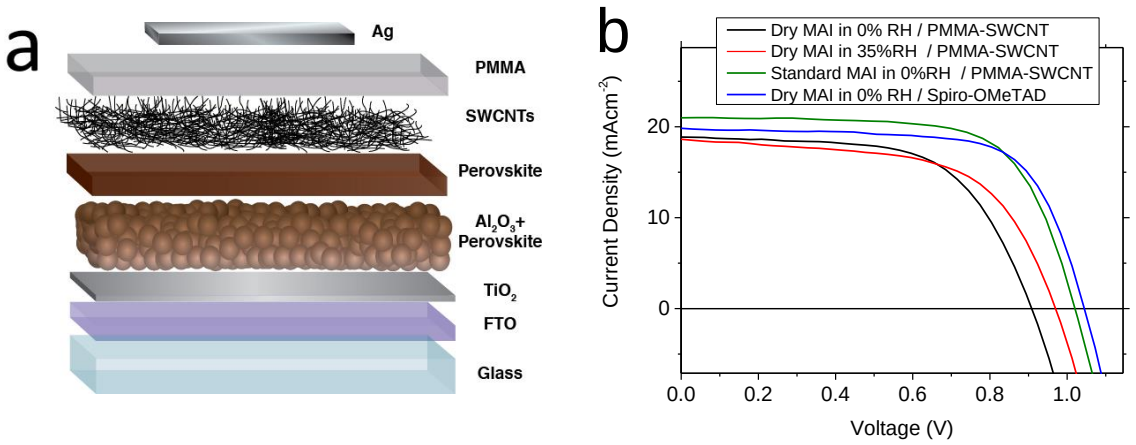

Figure 10.4: a) Schematic of the meso-superstructured solar cell architecture investigated. b) Current-voltage characteristics of meso-superstructured perovskite solar cell devices with and without exposure to moisture in a number of ways, measured under 100mWcm-2 AM1.5 simulated sunlight.

	J_{sc} (mAcm^{-2})	PCE from fast scan (%)	V_{oc} (V)	FF	SPO (%)
Dry MAI in 0% RH / SWCNT-HTL	17.7±0.9	8.5±1.2	0.87±0.02	0.54±0.04	5.7±0.2
Dry MAI in 0% RH/ Spiro-OMeTAD	17.5±1.5	11.7±1.5	0.98±0.05	0.67±0.03	7.2±2.1
Standard MAI in 0% RHF/ SWCNT-HTL	20.2±1.8	11.8±1.8	0.99±0.03	0.58±0.05	6.5±0.7 *
Dry MAI in 30% RH / SWCNT-HTL	16.0±1.5	8.7±1.6	0.95±0.03	0.56±0.05	4.0±0.3

Table 10.1: Average device performance data from at least 14 devices with perovskite films prepared with and without possible exposure to moisture in different ways – via exposure in the MAI, exposure during Spiro-OMeTAD doping, and exposure during annealing. SPO measurements taken from at least 4 stabilised devices.*this SPO was taken from a different set of devices with similar performance.

Figure 10.4b) shows current-voltage characteristics from champion cells made in each of these conditions. As these cells displayed hysteresis in the current-voltage characteristics, stabilised power output was also measured, which along with average device data is given in Table 10.1. Immediately, it is obvious that the impact of moisture is quite significant, especially with respect to the open-circuit voltage. Cells made without *any* exposure to

moisture show an open-circuit voltage of ~0.9V at best. In contrast, when employing the 'wet' standard precursor, annealing in a humid environment, or exposing to air with only Spiro-OMeTAD protecting them overnight, a large and significant increase in the open-circuit voltage is seen in all these cases. This corresponds to higher power conversion efficiency in most cases, both when measured in a fast current-voltage sweep and in terms of stabilised power output.

From these results, it can be concluded that exposure to moisture, which leads to a higher PLQE, also results in devices with a higher open-circuit voltage. This points towards humidity being correlated to a higher material quality. Improved PLQE indicates a reduction in non-radiative recombination; the improved V_{oc} correlates well with this observation, as a higher V_{oc} can be related directly to a higher PLQE. This stems from the reciprocity relation described by Rau et al, connecting V_{oc} and electroluminescence quantum efficiency, as discussed in Chapter 2, Section 2.6.[3,34,35] The latter in turn is correlated with the PLQE of the material.

It is noted that there is a previous report in which air exposure is shown to enhance the performance of a pre-doped Spiro-OMeTAD based device (so the oxygen-doping via ambient exposure was not required).[36] Therein, the authors propose that oxygen may passivate the perovskite surface. These results in contrast indicate that it is more likely that the observed improvements can be attributed to the contact with ambient moisture. You *et al*. have previously shown that oxygen does not have the same beneficial effect on photoluminescence properties as moisture;[2] to thoroughly test this possibility here, devices annealed in dry oxygen were also fabricated; these did not show the same enhancement in V_{oc} or PCE as the moisture-exposed films (see Table 10.2 for device data).

	J_{sc} (mAcm^{-2})	**PCE from fast scan (%)**	**V_{oc} (V)**	**FF**	**SPO (%)**
0%RH anneal	18.3±0.5	9.0±1.4	0.87±0.04	0.56±0.06	5.8±1.3
Oxygen anneal (0%RH)	17.6±1.1	8.6±1.2	0.87±0.03	0.56±0.04	4.6±0.23

Table 10.2: Average device performance data from at least 14 devices with perovskite films prepared with and without annealing in pure oxygen or nitrogen. SPO measurements taken from at least 4 stabilised devices.

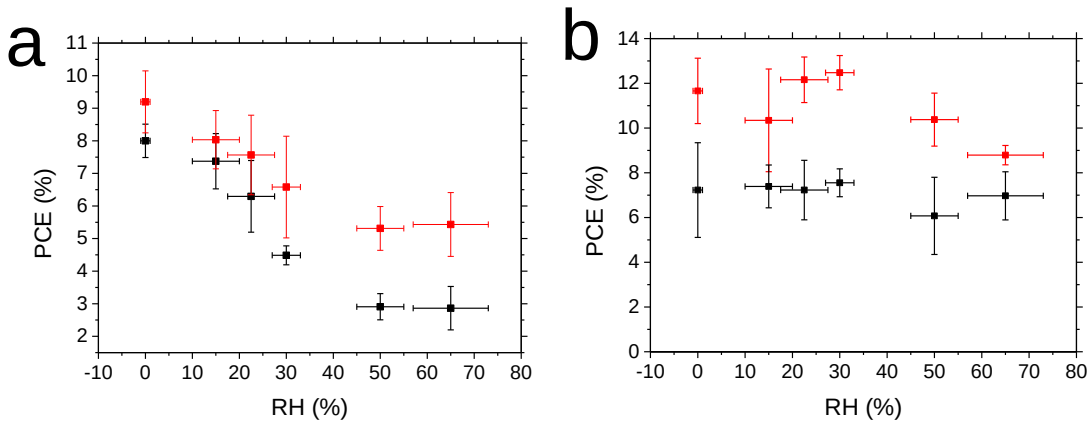

Figure 10.5: Average device data for Spiro-OMeTAD-based perovskite solar cells fabricated at different humidity levels. Stabilised power output (SPO) (black) and fast JV-scanned PCE (red) are shown a) for planar perovskite devices and b) for mesosuperstructured alumina-based devices. Error bars are given by standard deviation; each point for the fast JV PCEs represents at least 15 devices and for the SPO measurement at least 6 devices were held until steady-state efficiency was reached.

In order to understand how detrimental the morphological changes are, regardless of material quality, devices were also fabricated on both planar and mesostructured architectures in a range of humidities, using Spiro-OMeTAD as the HTL and leaving the devices to oxidise Spiro-OMeTAD in ambient atmosphere overnight, in the protocol typical for perovskite solar cell fabrication. Therefore they are likely to be affected by moisture exposure. Device data is shown in Figure 10.5; it is observed that planar devices function gradually worse when fabricated in higher humidity, with the lowest humidity being the best, whereas for mesostructured alumina cells, between 0% and 50%RH device performance is effectively constant, only dropping at humidities above this. This is an important observation for practical reasons: it means that planar devices are dominated by the worsened perovskite morphology, whereas for the mesostructured devices, fabrication is possible without deleterious impact at humidities of up to 50%, likely because the mesostructure holds the perovskite in place, preventing material de-wetting during spin-coating, and physically prevents shunt diode pathways.

10.6 Moisture post-treatment

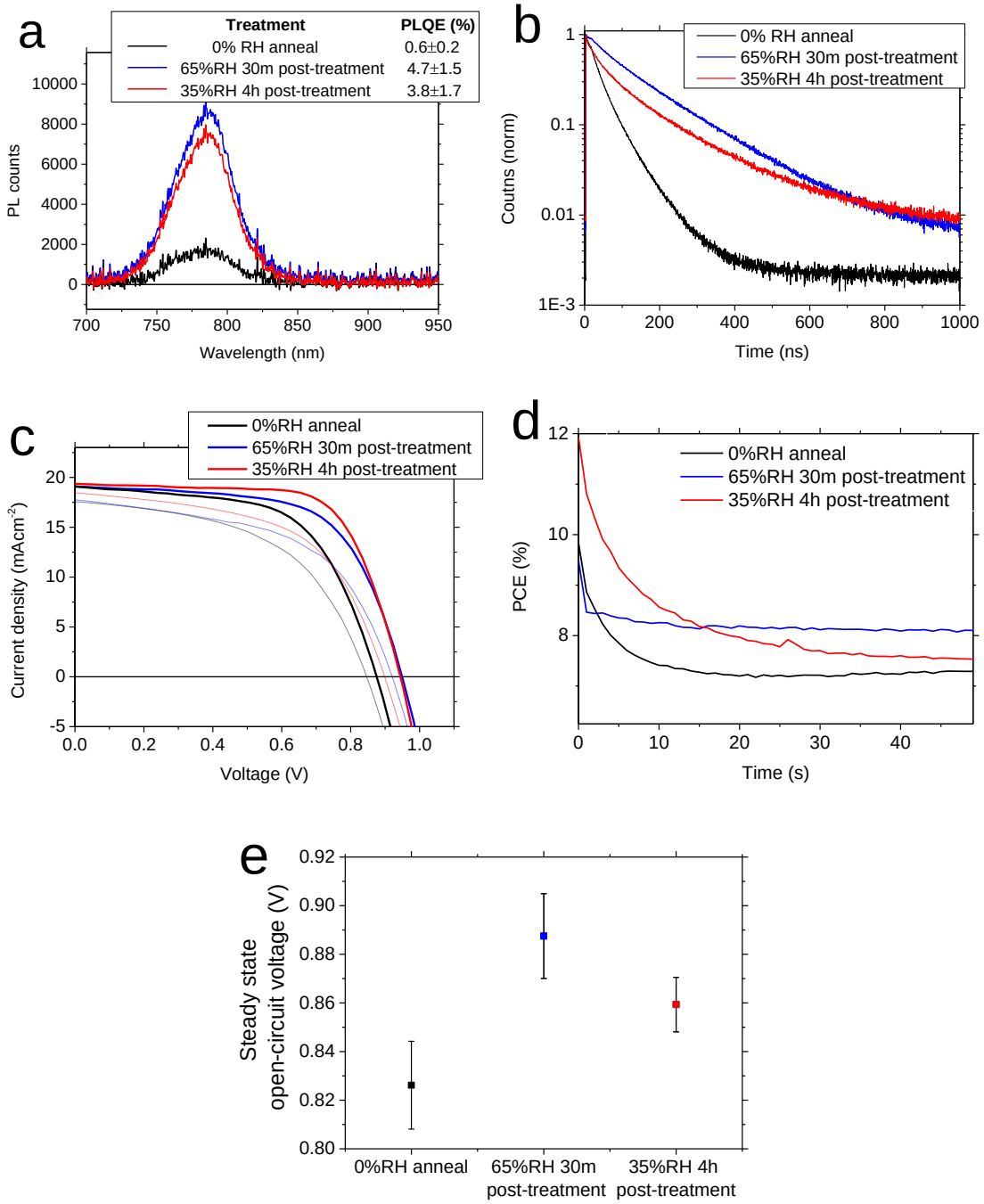

Figure 10.6: a) Photoluminescence and photoluminescence quantum efficiency, measured using an integrating sphere, for untreated and moisture-treated perovskite films. PLQE values averaged over at least 3 measurements are shown in the inset. b) Time-resolved photoluminescence of untreated and moisture-treated perovskite films, measured at 785nm, with excitation at 510nm, 3μJcm-2 per pulse, at 1MHz.c) Current-voltage characteristics of champion devices (bold lines) and average performance (pale lines) for perovskite mesostructured solar cells made

with moisture-treated and untreated perovskite films, made with a SWCNT-HTL. d) Stabilised power output measurements for representative 0%RH annealed and moisture post-treated devices. e) Steady-state voltage output under 1 sun illumination for moisture treated and untreated devices (average of 5 devices each).

Treatment	Jsc ($mAcm^{-2}$)	PCE from JV (%)	V_{oc} (V)	FF
0%RH anneal	17.5±0.8	7.9±1.9	0.85±0.05	0.55±0.07
0%RH anneal + 65%RH 30m post-treatment	17.8±0.9	9.1±1.9	0.92±0.07	0.55±0.08
0%RH anneal + 35%RH 4h post-treatment	18.5±0.6	9.4±1.9	0.90±0.06	0.57±0.09

Table 10.3: Average device characteristics extracted from current-voltage characteristics measured under AM1.5 100mWcm-2 illumination for the devices described in Fig.5. Averages taken for at least 20 devices per treatment.

Based on the results of moisture exposure, in particular the enhancement of V_{oc} for the Spiro-OMeTAD-based devices, it was realised that it may be possible to enhance the properties of a perovskite film with a moisture post-treatment. Perovskite films were made in an inert atmosphere, taking the utmost care never to expose them to water, and post-treated with water in different ways, subsequently sealing the films with PMMA immediately. It was found that the PLQE and photoluminescence lifetime of a film annealed in a dry atmosphere could intentionally be enhanced substantially by heating at 90°C in a 65±5% RH atmosphere for 30 minutes, or by simply leaving the film in 35±5%RH ambient air for 4 hours. The increases in PLQE and lifetime are shown in Figure 10.6a) and b) respectively. In particular, the enhancement in PLQE from 0.6% to 3-5% is notable. Photovoltaic devices were then made in 0%RH atmosphere, some were moisture post-treated in both ways, and immediately sealed with the SWCNT-HTL to test whether the PLQE enhancement did indeed correspond to better performance. The current-voltage characteristics of champion devices are shown in Figure 10.6c), and the average performances for the batch presented in Table 10.3. A significant increase in open-circuit voltage is observed with the moisture post-treatments, showing that the effect of fabricating films with unintentional moisture exposure has indeed been successfully replicated. PCE also increased correspondingly with the moisture treatments. Since these devices did display current-voltage hysteresis, stabilised power measurements are shown in Figure 10.6d), demonstrating that the moisture post-treatment does result in better stabilised power output than the control samples.

Because the most significant improvement is shown in the open-circuit voltage, to comprehensively demonstrate that voltages measured from current-voltage scans show reliable trends despite the current-voltage hysteresis, steady-state open-circuit voltages were measured for a number of devices under 1 sun illumination, as shown in Figure 10.6e). Devices were held at open circuit until the voltage stabilised (typically within 10-30 seconds). It was observed that the measured voltages are somewhat lower than the fast-scanned open-circuit voltage, but not significantly, and most importantly the trend still holds, showing that the moisture-treated devices do have a significantly better open-circuit voltage than the untreated ones. Taking all results into account, the 65%RH treatment seems somewhat more effective than the 35%RH treatment – open-circuit voltages are higher, stabilised PCEs are higher, and photoluminescent lifetimes and quantum efficiencies are somewhat higher. It is noted, however, that this treatment required the use of a specialised humidity chamber; the 4h 35%RH exposure can simply be done in normal lab conditions in many laboratories, and it provides a significant enhancement over the untreated samples.

It can thus confidently be concluded that some exposure to moisture enhances the PLQE of a $MAPbI_3$ perovskite film that has not previously been exposed to water. This can either happen unintentionally, as discussed in Figure 10.4, or intentionally as a post-treatment (see Figure 10.6). This PLQE enhancement correlates with an improved device performance, stemming mainly from an increased V_{oc}. The improved PLQE indicates a reduction in non-radiative recombination, which correlates with an improved V_{oc} as discussed earlier. Devices perform better when they have been exposed to some moisture, which highlights a clear conclusion of the work in this chapter: some moisture exposure (at some stage of the fabrication process) is important for attaining the highest performing perovskite solar cells. While only films produced from the non-stoichiometric precursor route have been measured, it is expected that this should generalise to perovskite films formed in other ways too. It is noted once more that the precise conditions in which the cells are processed, stored and tested are not diligently reported in the literature, and the study presented in this chapter suggests that all the highest efficiency cells reported thus far may indeed have a step in the process which involves exposure to an environment containing moisture.

10.7 Understanding the mechanism of moisture exposure

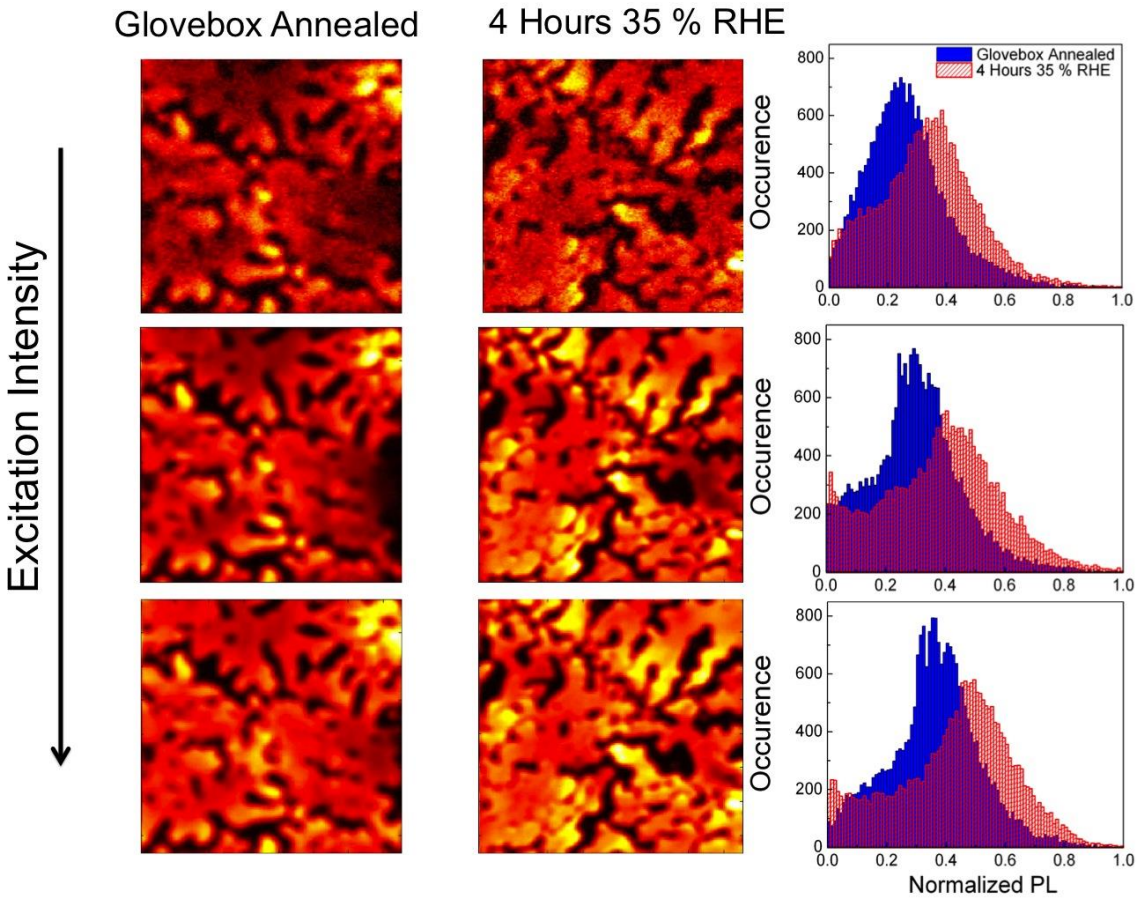

Figure 10.7: Photoluminescence intensity mapping on 0%RH annealed and 4h 35% RH post-treated perovskite films. Excitation intensity increases going from top to bottom. Photoluminescence intensity spatial maps are shown on left; scale is from black (no PL), through red, to yellow (high PL intensity). PL intensity distributions are shown on the right hand side. In all cases the field is 100x100µm. This data was collected by Tomas Leijtens of the Italian Institute of Technology, Milan.

It has recently become apparent that there is often significant inhomogeneity in the perovskite films.[29] In order to further investigate the role of the moisture treatments on film quality, photoluminescence mapping was carried out on treated and untreated films to establish whether there was a relation between low or high photoluminescence in particular regions of the film. The spatial photoluminescence intensity distribution was measured at three excitation powers (ranging from approximately 10^{15} – 10^{17} cm^{-3} steady state charge densities), which is shown in Figure 10.7. Under the lowest intensity, many 'dark' regions are observed in the 0%RH annealed sample. These are regions where there is likely to be more non-radiative than radiative recombination, which could be an

indication of a higher trap density in these regions.[29] In the 4h 35% RH treated sample, fewer dark regions are observed. To quantify this, photoluminescence intensity distributions were plotted (note that these are normalised to the maximum photoluminescence intensity). The 4h 35% treated sample is observed to have a distribution tending more towards the highest intensities than the 0%RH annealed sample, confirming the visual analysis that there are fewer 'dark' i.e. trap-dominated regions. To confirm whether the dark regions have a higher trap density, the excitation intensity can be varied.[29] If these regions are trap dominated because they contain a higher density of traps, an increase in excitation intensity will 'fill in' these traps, and the photoluminescence will increase and become more uniformly distributed towards the higher intensities.[28] For both samples, an increase in intensity is observed to reduce the number of dark regions and push the photoluminescence intensity distribution towards the higher end of the scale, with the moisture-treated sample having fewer darker regions in all cases. The shifts in distribution to the right with increasing intensity, which imply an increase in uniformity around higher PL, come from the fact that radiative recombination is expected to be bimolecular and should not depend strongly on location,[28,37] while the non-radiative decay is trap limited and will hence depend strongly on local trap densities.[29] This indicates that the higher excitation intensity is indeed allowing additional photoexcited carriers to fill in traps, and is good evidence that the enhancement in material quality that arises when the perovskite film is exposed to moisture is related to a reduction of trap density in the perovskite film.

Having demonstrated that there is an improvement in perovskite material quality with exposure to moisture, it now must be considered how such an improvement may arise. Firstly, it is important to consider if the improvement is related to the continued presence of moisture adsorbed onto or within the film, or as the hydrated phase, or if it is a permanent change in the material induced by a moist atmosphere. Previously it has been shown that the fully hydrated phases can revert to dehydrated perovskite simply by exposing to dry nitrogen at room temperature.[9] In order to test if the change observed is a permanent or reversible change, moisture post-treatments were carried out on perovskite films prepared in a fully dry atmosphere, and then dried some of them out again by heating at 65°C in a dry nitrogen atmosphere before sealing. In Figure 10.8, the time-resolved photoluminescence and PLQE of untreated films, moisture-treated films, and those that have been moisture-treated and then dried are compared. It is observed that the increased PL lifetime of films that arises upon moisture treatment is sustained after a post-drying step. The PLQE, increased by the moisture treatment, also does not return to the very low values of the films never exposed to moisture; within the error margins it

remains unchanged. It is thus concluded that the effect is not simply related to the formation of a layer of hydrated phase perovskite on the surface nor the continued presence of moisture within the film. Furthermore, it is a permanent change – moisture in some way affects the film in a way that is maintained even when moisture is removed. This implies that processing in a humid environment could be a commercially relevant method for improving the quality of perovskite films and not simply an academic curiosity.

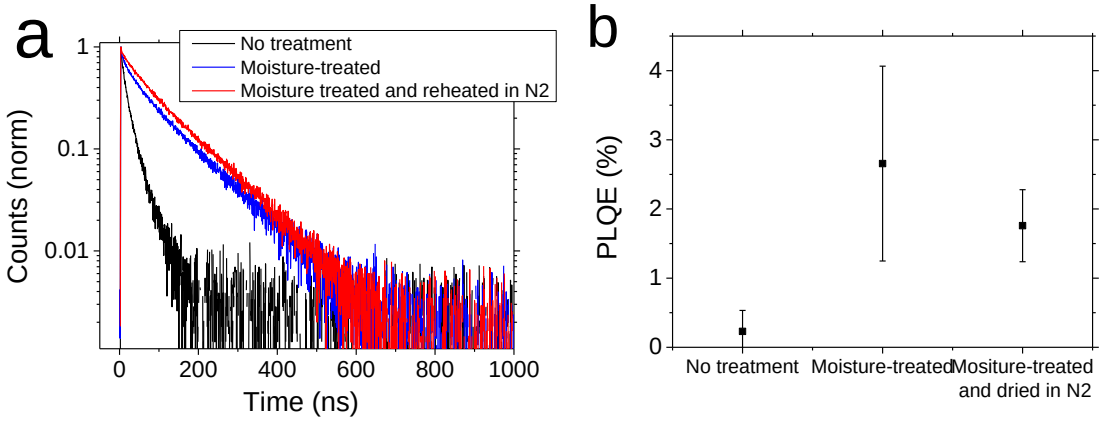

Figure 10.8: a) Time-resolved photoluminescence of untreated, moisture-treated, and moisture-treated and subsequently dried perovskite films, measured at 785nm, with excitation at 510nm, 3μJcm-2 per pulse, at 1MHz. b) PLQE of films treated in the same ways. PLQE measurements are averaged over 6 measurements for each treatment, error bars determined from standard deviation. Films were dried in nitrogen atmosphere under heating at 65°C for 1 hour.

Having established that moisture exposure irreversibly improves the perovskite film quality, which is inferred to be due to reducing trap state density, the question arises of how this occurs. Traps in the film can be caused by imperfections in the stoichiometry, such as excess (interstitial) or deficit (vacancy) methylammonium, iodide or lead atoms, or by other lattice defects. It could be suggested that the faster annealing means that the films made in the presence of moisture are subject to more annealing *after* the perovskite has finished forming, and that this enhances the material quality. In order to test this, experiments were carried out to show that annealing beyond a certain point, either by increasing temperature or annealing time, has no beneficial effect on the PLQE of the perovskite film (and is generally detrimental), so this hypothesis can be discarded (as shown in Figure 10.9). At high enough temperature, the films begin to turn yellow, indicating formation of lead iodide as the perovskite degrades by thermal sublimation of the methylammonium. The increase in PLQE is *only* observed when the film is exposed to moisture in some way. It is proposed that the presence of moisture affords the reactants

greater mobility, as also seen in the rate of formation of the perovskite film, allowing a higher quality film to result at a fixed temperature.

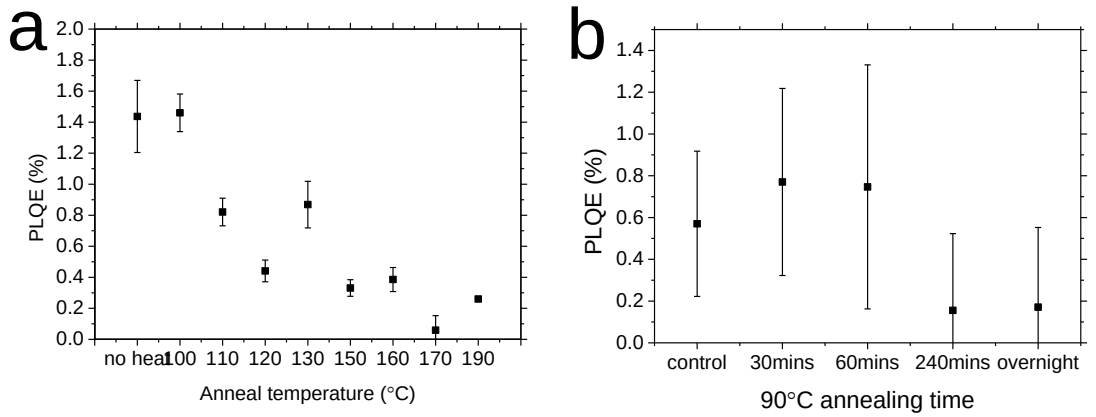

Figure 10.9: Investigation of whether further annealing can increase PLQE, replacing water treatment. a) PLQE as a function of temperature for a 15-minute post-anneal in nitrogen atmosphere. b) PLQE as a function of annealing time at 90°C. It is observed that neither increasing the annealing time nor the annealing temperature increase PLQE in the same way as the moisture treatments.

XRD spectra, shown in Figure 10.10, do not indicate any detectable presence of any crystalline material except $MAPbI_3$, so the changes cannot be ascribed to formation of significant hydrate phase or lead iodide at the surface. Furthermore, a significant change in the large-scale morphology or grain sizes is not observed upon post-treatments with water, as shown via scanning electron microscopy in Figure 10.10. The improvements cannot be ascribed to an improvement in large-scale crystal size or a macroscopic 'solvent-annealing' effect allowing whole grains to fuse.[2,38]

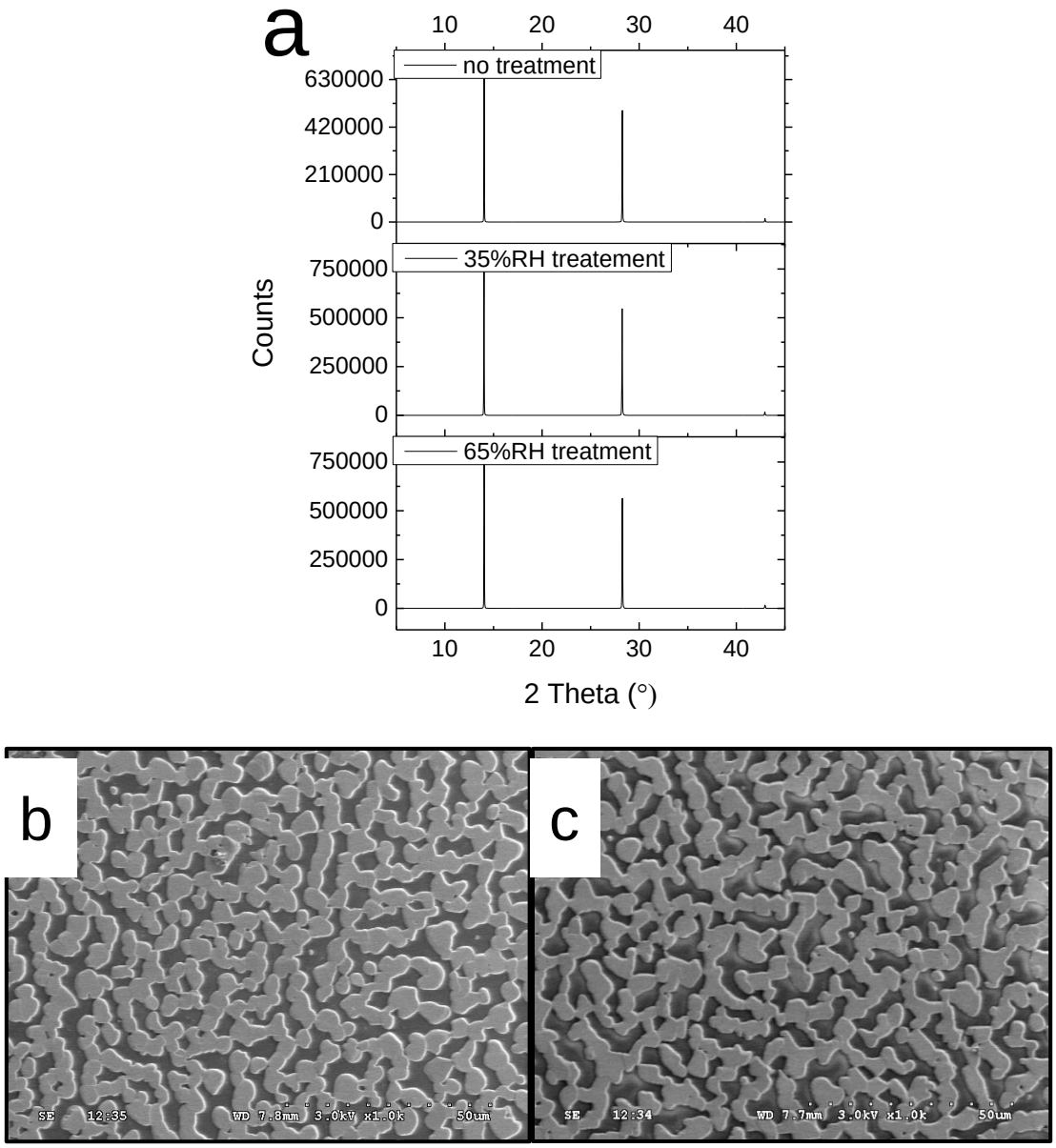

Figure 10.10: a) XRD spectra for films fabricated fully in nitrogen (0%RH) and post-treated at 35%RH for 4h at room temperature, or at 65%RH for 30 minutes at 90oC. The control film is never exposed to moisture. Bottom: Morphology after moisture treating perovskite films with 35%RH for 4h. b) Untreated films and c) treated films.

Therefore, having ruled out these options, the following hypothesis is proposed. The experiments performed show that moisture is able to solubilise and remove methylammonium from the perovksite lattice, and that a film annealed in the presence of moisture forms the perovskite structure faster, implying that water can facilitate the removal of the excess methylammonium in the precursor by partially solubilising it. Additionally, the reversible formation of a hydrated phase, with water weakly bound to

the methylammonium molecules, has been shown by others.[6] It is therefore proposed that water can solubilise the methylammonium (and possibly other components), affording it mobility within the crystal, and allowing any excesses to be removed and any deficits to be filled in, effectively 'healing' the perovskite structure and filling any trap states caused in this way. A reduction of these trap states results in less non-radiative trap-mediated recombination, and more radiative recombination. The material quality is improved, PLQE and photoluminescence lifetime increases, and the V_{oc} and thus PCE attainable in a perovskite solar cell increases.[34] This explanation builds upon that proposed by You *et al*, who suggested that the enhanced mobility of constituent ions in a moist atmosphere could lead to crystal reconstruction during annealing.[2] They however ascribe all observed benefits to the improved morphology; here it is clearly identified that there are more effects at play.

The next question is then whether the effects of the moisture post-treatment could be replicated with other polar solvents, for example isopropanol or ethanol, to allow use of a similar post-treatment within moisture-free atmospheres typically used for perovskite processing. In theory this should work in a similar manner, and this is currently under investigation.

It is noted that the perovskites incorporated into the standard solar cells made in our lab, and likely the labs of others, already either contain water from non-dried MAI or are unintentionally exposed to water via an overnight air exposure with only water-permeable Spiro-OMeTAD on top. Therefore, these cells do not suffer from the V_{oc} limitation and low PLQE that is observed when carefully avoiding water exposure. However, this may not be the case for all perovskite solar cells fabricated in all labs. Somewhat counter-intuitively, it is in fact the most carefully made solar cells, made in a glovebox, with purified and dried MAI, that will suffer from the lack of water exposure. Thus it is believed that the findings presented in this chapter will provide an extremely important route to improving the performance of such cells, and open the way for further studies of the exact mechanism for the improvement upon water exposure.

Furthermore, it is noted that, although an improvement is observed in device and film performance with the moisture treatments, they are far from perfect. V_{oc} is not improved to the extent that it is by using our 'standard' moist perovskite precursor, and PLQE remains far from the highest reported values. It is therefore concluded that other additional treatments are probably necessary for a perovskite film to achieve its full potential in a controlled manner. Some work has already been carried out to investigate what role additives, in the broadest sense, can have on the crystallisation and quality of

perovskite films, which is likely to be a promising avenue for increasing the PCE to the highest values possible.[39,40] As an aside, it is noted that Sn based perovskites, such as $MASnI_3$, degrade very rapidly when exposed to any atmosphere, and thus cannot benefit easily from this advantageous moisture exposure. Fully understanding the mechanism and replicating it with alternative less degrading solvents may thus prove to be critical to the advance of the Sn based perovskite.

10.8 Outlook and conclusion

In this chapter, the critical role of moisture exposure during metal halide perovskite thin film fabrication on the material quality has been demonstrated. Moisture exposure results in higher open-circuit voltage in photovoltaic devices, higher photoluminescence and longer photoluminescence lifetimes. It has been determined that this likely stems from a reduction in trap state density, which is postulated to be enabled by the partial solvation and enhanced mobility of the methylammonium component. It is noted that often moisture exposure can be unintentional, occurring during the Spiro-OMeTAD doping stage, or residually in the precursor solution. However, careful synthesis and fabrication in a dry environment will result in lower material quality and worse performing films. Guidelines for the optimum environment for film fabrication are provided, and it has been shown that a moisture treatment after film fabrication can improve film quality in the same way. These results are crucial for the understanding of the field in general and enabling the community to understand the best way in which to produce a perovskite film, and should pave the way for fabrication of high performing devices and further studies on the exact mechanism of improvement upon moisture exposure.

10.9 Additional methods: perovskite film and solar cell fabrication

To form perovskite films, initially glass slides were cleaned sequentially with acetone and isopropanol, and then treated with oxygen plasma for 5 minutes. The perovskite precursors were then spin-coated in the relevant atmosphere (either in a nitrogen-filled glovebox, for the 0%RH samples, or the home-made humidity controlled chamber in ambient air with humidity regulated by nitrogen flow through a deionised water bubbler) at 2000rpm for 60 seconds. The films were then immediately transferred to a hotplate at 90°C and annealed for 150 minutes followed by 120°C for 15 minutes.

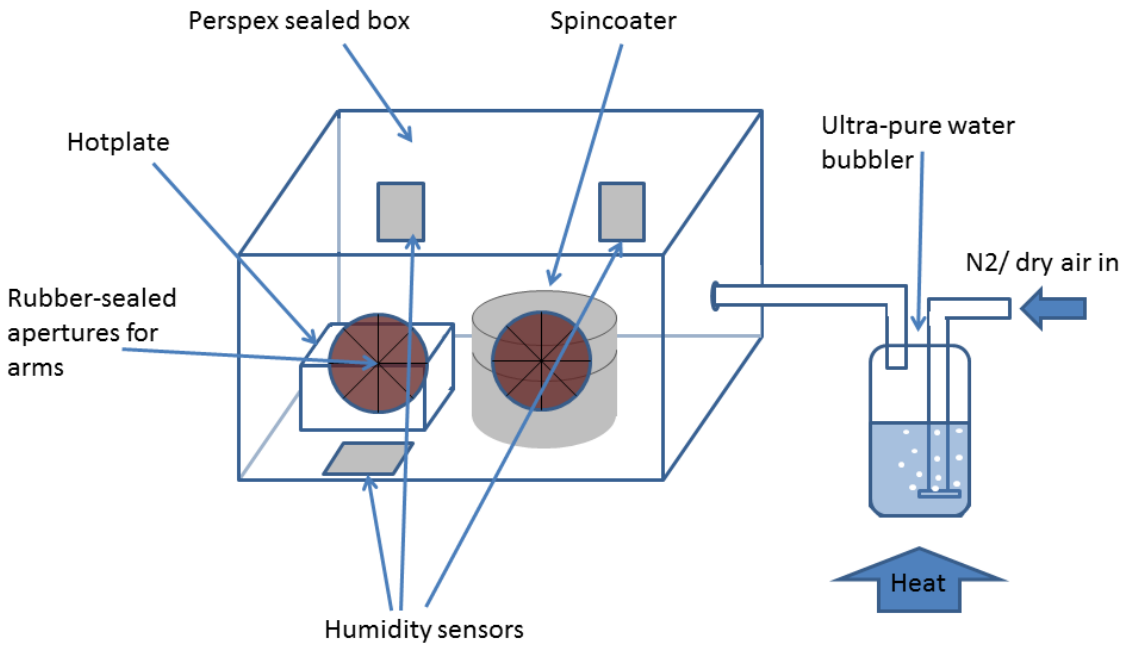

Figure 10.11: Schematic of the humidity-controlled chamber, with spincoater and hotplate inside. Humidity and temperature are measured on 3 separate accurate humidity sensors and averaged for readings. For dry atmospheres, N_2 or dry air is piped straight into the drybox without going through the bubbling system. To achieve very high humidities, it was found to be necessary to heat the water bubbler to encourage evaporation. The chamber does allow some escape of gas through the arm-holes so does not build up pressure above room pressure.

At this point any post-treatments were carried out: moisture post-treatments were carried out by heating at 90°C in an atmosphere of 60±5%RH for 30 minutes or by leaving at room temperature in a 35±5%RH atmosphere for 4 hours. Oxygen post-treatment was carried out by heating at 90°C within a sealed chamber that had been purged with oxygen.

Immediately after treatment, or annealing if untreated, films were spin-coated with PMMA in the relevant humidity atmosphere (nitrogen-filled glovebox for untreated, post-treated, and 0%RH films, and humidity controlled chamber for films annealed in different RH). This forms an effective moisture barrier whilst measuring – all measurements were carried out in air, and then films stored subsequently in a nitrogen-filled glovebox. Little change was observed during repeat measurements over a number of days of measuring and storage, indicating that the PMMA barrier is effective for protection during measuring. PMMA was dissolved in chlorobenzene at 50mg/ml and spin-coated at 1000rpm for 45s.

For mesosuperstructured device fabrication, substrates, TiO_2 compact layer and alumina scaffold were deposited as reported in Chapter 3. Devices were then transferred into the

relevant atmosphere (nitrogen-filled glovebox or humidity controlled chamber). The perovskite layer was then spin-coated (2000rpm for 45s) and annealed at 100°C for 120 minutes. After annealing, any post-treatments were carried out as previously described. Immediately after any treatments, the hole transport layer was deposited by spin-coating in a nitrogen-filled glovebox. For the moisture-blocking SWCNT-HTL, first the SWNT layer was deposited dynamically by slow drop-by-drop spin-coating (3000 rpm for 90 s), using 200µl of solution. The SWCNTs were functionalised previously with P3HT as described previously, and sonicated and purged with nitrogen before use.[7,33] This layer was followed immediately by the deposition of the PMMA or PC layer (30mg/ml in chlorobenzene), which was of thickness ~300nm. Spiro-OMeTAD layers and electrode evaporation were carried out as described in Chapter 3.

10.10 References

1. H. Zhou, Q. Chen, G. Li, S. Luo, T. -b. Song, H.-S. Duan, Z. Hong, J. You, Y. Liu and Y. Yang, *Science*, 2014, **345**, 542–546.

2. J. You, Y. (Michael) Yang, Z. Hong, T.-B. Song, L. Meng, Y. Liu, C. Jiang, H. Zhou, W.-H. Chang, G. Li and Y. Yang, *Appl. Phys. Lett.*, 2014, **105**, 183902.

3. S. Pathak, A. Sepe, A. Sadhanala, F. Deschler, A. Haghighirad, N. Sakai, K. C. Goedel, S. D. Stranks, N. Noel, M. Price, S. Hüttner, N. A. Hawkins, R. H. Friend, U. Steiner and H. J. Snaith, *ACS Nano*, 2015, **9**, 2311–2320.

4. H.-S. Ko, J. Lee and N. Park, *J. Mater. Chem. A*, 2015, **3**, 8808–8815.

5. S. R. Raga, M.-C. Jung, M. V. Lee, M. R. Leyden, Y. Kato and Y. Qi, *Chem. Mater.*, 2015, **27**, 1597–1603.

6. J. a. Christians, P. A. Miranda Herrera and P. V. Kamat, *J. Am. Chem. Soc.*, 2015, **137**, 1530–1538.

7. S. N. Habisreutinger, T. Leijtens, G. E. Eperon, S. D. Stranks, R. J. Nicholas and H. J. Snaith, *Nano Lett.*, 2014, **14**, 5561–5568.

8. J. Yang, B. D. Siempelkamp, D. Liu and T. L. Kelly, *ACS Nano*, 2015, **9**, 1955–1963.

9. A. Leguy, Y. Hu, M. Campoy-Quiles, M. I. Alonso, O. J. Weber, P. Azarhoosh, M. van Schilfgaarde, M. T. Weller, T. Bein, J. Nelson, P. Docampo and P. R. F. Barnes, *Chem. Mater.*, 2015.

10. K. K. Bass, R. E. McAnally, S. Zhou, P. I. Djurovich, M. Thompson and B. Melot, *Chem. Commun.*, 2014, **50**, 15819–15822.

11. B. Suarez, V. Gonzalez-Pedro, T. S. Ripolles, R. S. Sánchez, L. A. Otero and I. Mora-Sero, *J. Phys. Chem. Lett.*, 2014, **5**, 1628–1635.

12. W. Zhang, M. Saliba, D. T. Moore, S. K. Pathak, M. T. Hörantner, T. Stergiopoulos, S. D. Stranks, G. E. Eperon, J. A. Alexander-Webber, A. Abate, A. Sadhanala, S. Yao, Y. Chen, R. H. Friend, L. A. Estroff, U. Wiesner and H. J. Snaith, *Nat. Commun.*, 2015, **6**, 6142.

13. S. T. Williams, F. Zuo, C.-C. Chueh, C.-Y. Liao, P.-W. Liang and A. K.-Y. Jen, *ACS Nano*, 2014, **8**, 10640–10654.

14. G. Grancini, S. Marras, M. Prato, C. Giannini, C. Quarti, F. De Angelis, M. De Bastiani, G. E. Eperon, H. J. Snaith, L. Manna and A. Petrozza, *J. Phys. Chem. Lett.*, 2014, **5**, 3836–3842.

15. M. I. Dar, N. Arora, P. Gao, S. Ahmad, M. Grätzel and M. K. Nazeeruddin, *Nano Lett.*, 2014, **14**, 6991–6996.

16. L. Zheng, D. Zhang, Y. Ma, Z. Lu, Z. Chen, S. Wang, L. Xiao and Q. Gong, *Dalt. Trans.*, 2015, **44**, 10582–10593.

17. G. E. Eperon, V. M. Burlakov, P. Docampo, A. Goriely and H. J. Snaith, *Adv. Funct. Mater.*, 2014, **24**, 151–157.

18. P.-W. Liang, C.-Y. Liao, C.-C. Chueh, F. Zuo, S. T. Williams, X.-K. Xin, J. Lin and A. K.-Y. Jen, *Adv. Mater.*, 2014, **26**, 3748–3754.

19. K. W. Tan, D. T. Moore, M. Saliba, H. Sai, L. a. Estroff, T. Hanrath, H. J. Snaith and U. Wiesner, *ACS Nano*, 2014, **8**, 4730–4739.

20. M. Saliba, K. W. Tan, H. Sai, D. T. Moore, T. Scott, W. Zhang, L. a. Estroff, U. Wiesner and H. J. Snaith, *J. Phys. Chem. C*, 2014, **118**, 17171–17177.

21. D. T. Moore, H. Sai, K. W. Tan, L. a. Estroff and U. Wiesner, *APL Mater.*, 2014, **2**, 81802.

22. W. S. Yang, J. H. Noh, N. J. Jeon, Y. C. Kim, S. Ryu, J. Seo and S. I. Seok, *Science*, 2015, **348**, 1234–1237.

23. Y. Wu, A. Islam, X. Yang, C. Qin, J. Liu, K. Zhang, W. Peng and L. Han, *Energy Environ. Sci.*, 2014, **7**, 2934.

24. A. Dualeh, N. Tétreault, T. Moehl, P. Gao, M. K. Nazeeruddin and M. Grätzel, *Adv. Funct. Mater.*, 2014, **24**, 3250–3258.

25. E. L. Unger, A. R. Bowring, C. J. Tassone, V. Pool, A. Gold-Parker, R. Cheacharoen, K. H. Stone, E. T. Hoke, M. F. Toney and M. D. McGehee, *Chem. Mater.*, 2014, **26**, 7158–7165.

26. G. E. Eperon, V. M. Burlakov, A. Goriely and H. J. Snaith, *ACS Nano*, 2014, **8**, 591–598.

27. V. M. Burlakov, G. E. Eperon, H. J. Snaith, S. J. Chapman and A. Goriely, *Appl. Phys. Lett.*, 2014, **104**, 091602.

28. S. D. Stranks, V. M. Burlakov, T. Leijtens, J. M. Ball, A. Goriely and H. J. Snaith, *Phys. Rev. Appl.*, 2014, **2**, 34007.

29. D. W. de Quilettes, S. M. Vorpahl, S. D. Stranks, H. Nagaoka, G. E. Eperon, M. E. Ziffer, H. J. Snaith and D. S. Ginger, *Science*, 2015, **348**, 683–686.

30. V. D'Innocenzo, A. R. Srimath Kandada, M. De Bastiani, M. Gandini and A. Petrozza, *J. Am. Chem. Soc.*, 2014, **136**, 17730–17733.

31. Q. Chen, H. Zhou, T.-B. Bin Song, S. Luo, Z. Hong, H.-S. S. Duan, L. Dou, Y. Liu and Y. Yang, *Nano Lett.*, 2014, **14**, 4158–4163.

32. A. Abate, T. Leijtens, S. Pathak, J. Teuscher, R. Avolio, M. E. Errico, J. Kirkpatrik, J. M. Ball, P. Docampo, I. McPherson and H. J. Snaith, *Phys. Chem. Chem. Phys.*, 2013, **15**, 2572–9.

33. S. N. Habisreutinger, T. Leijtens, G. E. Eperon, S. D. Stranks, R. J. Nicholas and H. J. Snaith, *J. Phys. Chem. Lett.*, 2014, **5**, 4207–4212.

34. U. Rau, *Phys. Rev. B - Condens. Matter Mater. Phys.*, 2007, **76**, 1–8.

35. K. Tvingstedt, O. Malinkiewicz, A. Baumann, C. Deibel, H. J. Snaith, V. Dyakonov and H. J. Bolink, *Nat. Sci. Reports*, 2014, **4**, 1–7.

36. W. H. Nguyen, C. D. Bailie, E. L. Unger and M. D. McGehee, *J. Am. Chem. Soc.*, 2014, **136**, 10996–11001.

37. F. Deschler, M. Price, S. Pathak, L. Klintberg, D. D. Jarausch, R. Higler, S. Huettner, T. Leijtens, S. D. Stranks, H. J. Snaith, M. Atature, R. T. Phillips and R. H. Friend, *J. Phys. Chem. Lett.*, 2014, **5**, 1421–1426.

38. Z. Xiao, Q. Dong, C. Bi, Y. Shao, Y. Yuan and J. Huang, *Adv. Mater.*, 2014, **26**, 6503–6509.

39. N. K. Noel, A. Abate, S. D. Stranks, E. S. Parrott, V. M. Burlakov, A. Goriely and H. J. Snaith, *ACS Nano*, 2014, **8**, 9815–9821.

40. A. Abate, M. Saliba, D. J. Hollman, S. D. Stranks, K. Wojciechowski, R. Avolio, G. Grancini, A. Petrozza and H. J. Snaith, *Nano Lett.*, 2014, **14**, 3247–3254.

11. CONCLUSIONS AND OUTLOOK

The work presented in this thesis has been concerned with, in the broadest sense, controlling the physical, chemical and material properties of the perovskite active layer. It has focussed on pushing the boundaries of perovskite solar cell research further by tackling several challenges critical to the field. It has provided a new solar cell architecture, potential incarnations of the perovskite device suitable for building-integrated purposes, new absorber materials and insight into atmospheric interactions.

In Chapter 4, the role of the mesoporous layer typically employed in perovskite devices was understood, and the problems with planar devices, namely pinhole growth during annealing, realised. Because this should ultimately be a more efficient architecture, an investigation was carried out to understand how to control and prevent this dewetting behaviour, and using the results of this it was possible to attain uniform, high coverage perovskite films with efficiencies above 10%. Since the publication of the work in this chapter, a huge number of others have replicated these results and built upon them, propelling the efficiencies achieved with this perovskite in a planar device architecture to over 19% PCE.[1–6] This clearly highlights the importance of the work carried out; previously it was unknown whether the perovskites could function well in a thin-film architecture at all.

The perovskite solar cells are not yet as efficient as silicon modules, currently on the market, so other applications rather than simply competing for stand-alone high efficiency

modules were considered. The flexibility of solution-processing affords many more options than for high-temperature wafer processes. In Chapter 5, this problem was addressed. Building-integrated photovoltaics would be an ideal market for a low-cost flexible technology – but the most desired application here is as neutral-coloured semitransparent photovoltaic windows. In light of this, the dewetting that was minimised in Chapter 4 was then maximised, providing the ability to create a film of microstructured perovskite solar cell islands. Such films were neutral-coloured and with tuneable transparency. Furthermore, it was shown that even such discontinuous films were able to form respectably performing solar cells, and that additional aesthetic flexibility was available by incorporating a colour-tinting dye into the hole-transporting layer. This technology should prove important in the commercialisation of perovskite modules.

In Chapter 6, this concept was taken one step further; in order to allow in-situ switchable transparency levels of such a device, for controlling temperature and light levels in a building, cells such as this were sandwiched together with an electrochromic component – this allows tinting of glass from transparent to dark by application of an electric field. The photovoltaic component provides the electric component. Such devices then comprise a power-generating window with switchable tinting; after tinting has been switched, the solar cell part can continue to supply power to an external circuit, making this a powerful device, highly suited to building-integration.

In Chapter 7, the chemical composition of the perovskite was considered. The challenge here was that the methylammonium lead halide perovksite used thus far by the community has a bandgap of 1.57eV, whereas the optimum for solar energy conversion is between 1.1 and 1.4eV. By replacing components of the lattice, a new perovskite, formamidinium lead halide, was developed, with a bandgap tuneable between 2.23 and 1.48eV. Thus, the minimum bandgap is shifted closer to the solar cell optimum. Photophysical measurements on this material suggested it should perform effectively in thin-film architectures; devices were accordingly made in this architecture, which showed up to 14% PCE. This was the highest planar perovskite device performance at the time; since the publication of this work, formamidinium lead halide perovskites have shown up to an impressive 20.1% PCE, making it the world-leading perovskite material.[7] Following on from this development, and incorporating it into the semi-transparent device architecture, in Chapter 8 further advances in the efficiency of the semi-transparent device were reported. Furthermore, a novel transparent laminated electrode was employed, resulting in fully see-through devices retaining neutral colouration and reasonable efficiency.

The next challenge tackled was regarding the role of the organic cation in the hybrid perovskites, especially its relevance to device hysteresis. In Chapter 9, a novel deposition method for a fully inorganic $CsPbI_3$ perovskite was described, enabling for the first time working solar cells to be made with this material. They were demonstrated to still show respectable currents and current-voltage hysteresis in planar devices, meaning that the organic part of the typical perovskites is not solely responsible for a) allowing good transport and generation properties, or b) the appearance of current-voltage hysteresis, an ongoing question in the field. Although initial efficiencies are low, at around 3%, this perovskite is much more thermally stable than the hybrid materials; in order to pass the required international certification tests, cells must be operated for a long time at elevated temperature, and to pass this the organic component of the hybrid perovskites may need to be replaced. The inorganic perovskites may thus be the eventual future of the perovskite technology.

Finally, a critical issue which has so far not been well understood was tackled in Chapter 10. Atmospheric moisture is known to interact with the perovskite both during and after formation, but its effect has not been well understood. In this chapter, a well-controlled investigation into the morphological and photophysical properties of films exposed to moisture in a number of ways was undertaken. It was concluded that moisture can play a critical role during film formation, with a small amount of moisture providing mobility for the A site cation to move in the film, effectively self-healing any traps or defects as necessary. This was shown to result in superior optical properties and device performance. Most importantly, moisture in precursors or during fabrication is often not well controlled by groups working in the field – this work demonstrates that it is of crucial importance to do so.

Bringing all this work together, this thesis has presented several conclusions critical to advancing the future development of perovskite solar cells. The planar architecture and new materials should pave the way towards reaching the highest efficiencies, and the semi-transparent and photovoltachromic devices described present an ideal incarnation in which the current efficiency perovskite solar cells could be commercialised. Perovskites are cheap, easy to process, and certainly have high enough efficiency to be put into mass production. This leads to the next big challenge in perovskite solar cell research – stability. While the work in this thesis has briefly considered some aspects of long-term stability (better thermal stability with inorganic perovskites and formamidinium perovskites, better black-phase stability in $CsPbI_3$), this is a big problem to tackle, and one that will make or destroy the future of perovskite solar cells as useful in the real world. Work

published by the author of this thesis and others, during the production of this thesis, has demonstrated that to some extent the perovskite cells are capable of operating for hundreds of hours under load, but there is still a large efficiency drop over time.[8–12] The problem of fabricating cells which operate at high efficiencies for a long time will, in the author's opinion, be the next big push in the field of perovskite solar cells; once this is overcome, there is nothing stopping the technology from becoming widespread and helping to solve the world's energy crisis.

11.1 References

1. H. Zhou, Q. Chen, G. Li, S. Luo, T. -b. Song, H.-S. Duan, Z. Hong, J. You, Y. Liu and Y. Yang, *Science*, 2014, **345**, 542–546.

2. Z. Xiao, C. Bi, Y. Shao, Q. Dong, Q. Wang, Y. Yuan, C. Wang, Y. Gao and J. Huang, *Energy Environ. Sci.*, 2014, **7**, 2619.

3. J. H. Heo, D. H. Song, H. J. Han, S. Y. Kim, J. H. Kim, D. Kim, H. W. Shin, T. K. Ahn, C. Wolf, T.-W. Lee and S. H. Im, *Adv. Mater.*, 2015, **27**, 3424–3430.

4. M. A. Green, A. Ho-Baillie and H. J. Snaith, *Nat. Photonics*, 2014, **8**, 506–514.

5. C. Tao, S. Neutzner, L. Colella, S. Marras, A. R. Srimath Kandada, M. Gandini, M. De Bastiani, G. Pace, L. Manna, M. Caironi, C. Bertarelli and A. Petrozza, *Energy Environ. Sci.*, 2015, **Advance**.

6. Q. Dong, Y. Yuan, Y. Shao, Y. Fang, Q. Wang and J. Huang, *Energy Environ. Sci.*, 2015, **Advance**.

7. W. S. Yang, J. H. Noh, N. J. Jeon, Y. C. Kim, S. Ryu, J. Seo and S. I. Seok, *Science*, 2015, **348**, 1234–1237.

8. T. Leijtens, G. E. Eperon, S. Pathak, A. Abate, M. M. Lee and H. J. Snaith, *Nat. Commun.*, 2013, **4**, 2885.

9. K. Wojciechowski, T. Leijtens, S. Siprova, C. Schlueter, M. T. Hörantner, J. T.-W. Wang, C.-Z. Li, A. K.-Y. Jen, T.-L. Lee and H. J. Snaith, *J. Phys. Chem. Lett.*, 2015, **6**, 2399–2405.

10. J. Burschka, N. Pellet, S.-J. J. Moon, R. Humphry-Baker, P. Gao, M. K. Nazeeruddin, M. Grätzel and M. Gratzel, *Nature*, 2013, **499**, 316–319.

11. A. Mei, X. Li, L. Liu, Z. Ku, T. Liu, Y. Rong, M. Xu, M. Hu, J. Chen, Y. Yang, M. Gratzel, H. Han, M. Grätzel and H. Han, *Science*, 2014, **345**, 295–298.

12. X. Li, M. Tschumi, H. Han, S. S. Babkair, R. A. Alzubaydi, A. A. Ansari, S. S. Habib, M. K. Nazeeruddin, S. M. Zakeeruddin and M. Grätzel, *Energy Technol.*, 2015, **3**, 551–555.